Cairo University

STUDY OF DESIGN CONSIDERATIONS OF SENSING FOR MAGNETIC FIELD MEASUREMENTS

By

Mahmoud Said Yassin

A Thesis Submitted to the
Faculty of Engineering at Cairo University
in Partial Fulfillment of the
Requirements for the Degree of
MASTER OF SCIENCE
in
Advanced Materials

FACULTY OF ENGINEERING, CAIRO UNIVERSITY
GIZA, EGYPT
2021

List of Tables

List of Figures

List of Symbols

A	Coil Area
A	Domain Density
A	Magnetic vector potential
B	Magnetic Flux Density / Magnetic Induction
B^*	Hodgon Hysteresis Model Parameter
$B_+(H)$	Upper Branch of Chan-Vladimirescu Model
$B_-(H)$	Lower Branch of Chan-Vladimirescu Model
B_r	Remenant Magnetization
B_s	Saturation Magnetization
B_t	Strength of the measured magnetic field
B_x	External magnetic field in x direction
c	Nonlinear Parameter controls the topology of the potential function
c	Reversibility parameter
d	Material Thickness in Betotti's Hysteresis Model
d	Thickness of the sheet
D	Electric Induction
D_1	Hodgon Hysteresis Model Parameter
D_2	Hodgon Hysteresis Model Parameter
D_3	Hodgon Hysteresis Model Parameter
D_4	Hodgon Hysteresis Model Parameter
e	Electron Charge
E	Electric Field
f	Frequency
f_e	Excitation frequency
f (b)	Hodgon Hysteresis Model Parameter
f_L	Larmor Precessional frequency

F_L	Lorntz Force
g(b)	Hodgon Hysteresis Model Parameter
G	Gauge factor of the piezoresistor
G	Dimensionless constant
h	Plank's constant
H	Magnetic field
H_b	Value of H needed to reach saturation
H_{bias}	DC bias magnetic field
H_c	Coercive field
H_e	Effective magnetic field
H_{max}	Maximum magnetic field
$H_{stat}(t)$	The material's static Law
$H_{Total}(t)$	Total magnetic field
i_s	Current in the superconducting ring
I	Electric Current
I	Intensity of magnetization
I_{ac}	AC current
I_c	Critical current in superconductor
I_{dc}	DC current
I_{exc}	Excitation current
J	Conductive current density
J_e	External generated current density
k	Pinning parameter
K	Temperature dependent control parameter
l	Cell length
L	Inductance
L	Optical path length
L_y	Length of aluminum loop perpendicular to the magnetic field
m	Macroscopic magnetic moment

m_0	Orbital magnetic moment
m_s	Spin magnetic moment
M	Magnetization
M_{an}	Anhysteretic magnetization
M_0	Initial magnetization
M_s	Saturation magnetization
M_{irr}	Irreversible magnetization component
M_{rev}	Reversible magnetization component
n	Number of coil turns
n	Carrier density
n	Number of the step
n	The order of the central polynomial
$\widetilde{n_0}$	A term represents the microstructural information
$\tilde{n}$	Quantity represents the active magnetic objects
N_{sens}	Number of turns of sensing coil
N_{exc}	Number of turns of excitation coil
P	Polynomial
$\begin{cases} P_1 \\ P_2 \end{cases}$	Spin polarizations of the two ferromagnets at the Fermi surface
$\{P\}$	Set of parameters characterizing the microstructure and domain structure of the material
q	Charge of the current carrier
R	Resistance
R_a	Resistance when the two ferromagnets are antiferromagnetic
R_p	Resistance when the two ferromagnets are parallel
s (B)	Sign function
S	Magnetic core cross section
t	Layer thickness
$\begin{cases} t_1 \\ t_2 \\ t_3 \end{cases}$	Crossing times for Residence time difference readout strategy

$\begin{cases} T^+ \\ T^- \end{cases}$	Time intervals correlated to the interaction between excitation magnetic field and the coercive field of the ferromagnetic core
U(x)	Potential energy function
v	Velocity of the conductor
v	Voltage
V	Electric scalar potential
V	Verdet constant
V_0	Characteristic field represents the statistical distribution of the local coercive fields
V_{bias}	Bias voltage of the whetstone bridge
V_{ME}	Magnetoelectric coefficient
x(t)	Normalized Magnetization
ΔB	Variation of flux density
ΔH	Variation of magnetic field
ΔM	Variation of Magnetization
ΔR	Change in Resistance
θ	Phase difference between wave functions of electrons in pair
θ	Angle between direction of magnetization and direction of current
φ_0	Magnetic flux quantum
α	Domain coupling
α	Wall motion in Betotti's model
α	Frohlich model parameter
α_E	Magnetoelectric coefficient
β	Frohlich model parameter
β	Parameter representing wall motion effect
β	Angle of rotation
γ	Eddy current in Bertotti's model
γ_e	Gyromagnetic ratio of the electron
γ_p	Gyromagnetic ratio of the proton

ρ	Volume Charge density
ρ	Magnetoresistivity coefficient
σ	Electric conductivity
δ	The sign function in Bertotti's model
δ	Directional Parameter in J-A model
ϵ	Electric permittivity
ε_x	Longitudinal strain
η	Rayleigh Parameter
χ	Susceptibility
τ	System time constant
μ	Initial Permeability
μ_0	Permeability of free space
μ_m	Maximum Permeability
μ_r	Relative Permeability

Abstract

Recently, magnetic sensors have become vital in several applications. The development of magnetic sensors allows measuring magnetic fields at levels as low as few tens of femtotesla. There are a variety of magnetic sensors that can be used in many sectors, including geophysical survey, space observations, mobile phones, security monitoring, magnetic recording, terrestrial navigation, and biomedical diagnostics. Magnetometers can be categorized, according to their sensitivity, into high; medium and low. Magnetic sensors known as highly sensitive magnetometers can detect magnetic fields as weak as nanotesla.

Due to its usage in different applications, fluxgates sensors are the finest selection if measuring magnetic field in the nanotesla range is required. Fluxgate sensors measure the strength of an external magnetic field in certain direction i.e., they are vector magnetometers. The principle of operation of Fluxgate magnetometers based on manipulating a nonlinear soft magnetic material that is driven to saturation by an alternating excitation current and is modulated by the applied magnetic field to be sensed. The main part of fluxgate sensor is its core, i.e., the sensing element of the sensor. The nonlinear characteristics of core's magnetic material have a non-negligible influence on sensor's performance. Therefore, accurate modeling of the nonlinear hysteretic and the dynamic behaviors of the core's magnetic material is mandatory in order to predict the fluxgate sensor's behavior under variable operating conditions. For this reason, in this thesis we selected the Jiles-Atherton model, that it is extensively used in hysteresis modeling of magnetic materials, for modeling the fluxgate's magnetic core. Jiles-Atherton model was selected due to its meaningful physical parameters which make it convenient to represent hysteresis characteristic of the core's soft magnetic material.

Our work takes place in this context, as in this thesis, we propose comprehensive study to model the behavior of the fluxgate magnetic core, which explains how the current and magnetic distribution inside the core depends on both excitation parameters, and core's magnetic properties. This study will boost the fluxgate research to further improvement, and will assist the magnetometer's designers in choosing the appropriate operation conditions. In this thesis the finite element analysis was used to evaluate magnetic flux density, and current density distributions inside the fluxgate's core, taking into account hysteresis behavior of fluxgate core's magnetic material. Furthermore, in this thesis, we considered two core's design configurations, to be investigated, corresponding to different excitation mechanisms.

For each design configuration, detailed finite element study is presented to illustrate influence of frequency, core dimension, and excitation mechanism on current and magnetic distribution inside the sensor's core. The results presented in the thesis provide a performance map for tracking the operational behavior of the fluxgate core under various magnetic environments. Thus, this thesis fulfills the need to have a prior understanding through virtual prototyping (i.e. simulations) of the fluxgate core in order to guide the researchers to optimize the fluxgate sensor design without investing time and money to build physical prototypes.

Chapter 1 : Introduction

Magnetic field sensors become important in our daily lives and serve almost all industry sectors in assess and regulate hundreds of applications. *Figure 1-1* shows that the range of real magnetic fields of interest to be measured is enormous. Thus, there are several magnetic sensing approaches that are relying on wide range of phenomena that are based on physics and material science fields. A magnetic field sensor is a device or a system that can sense absolute intensity of magnetic field or one of its vector components. Essentially, all magnetic field sensors exhibit a variation in the device's physical attribute or characteristic. The existence of this variation relates the sensor's response to the measured magnetic field. Furthermore, this variation qualifies the magnetic field sensor for a certain application according to the required sensitivity. Therefore, magnetic field sensors can be classified according to their applications into three categories shown in *Table 1.1*. That is, it will be used to measure: i) fields greater than the Earth's magnetic field; ii) perturbations in the Earth's magnetic field; and iii) tiny variations in generated magnetic fields [1].
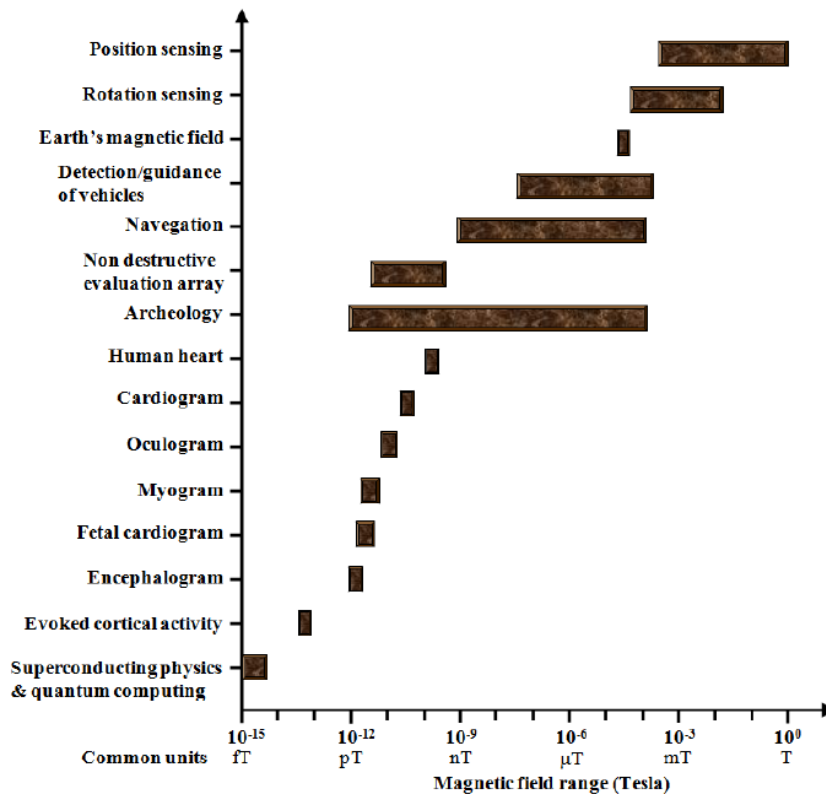
Figure 1-1: Magnetic fields' range of various sources and applications [2]

Table 1-1: Categories of magnetic sensors and their applications

Category	Definition	Major Applications
Category 1 Low resolution	Measuring field larger than Earth's magnetic	• Noncontact switching • Current measurement • Nondestructive inspection
Category 2 Medium resolution	Measuring perturbations in the magnitudes and/or direction of Earth's field	• Magnetic compass • Automobile industries • Traffic control
Category 3 High resolution	Measuring field differences due to induced permanent dipole moments	• Brain function mapping • Magnetic anomaly detection • Mineral prospecting

1.1. Fluxgate Magnetometer

Sensing low magnetic fields has always been an important function in a variety of applications. Therefore, several approaches have been proposed to sense magnetic fields in the range from 10^{-11} to 10^{-4} Tesla [3-4]. Despite all the attempts on other magnetic field sensors, fluxgate magnetometers remain one of the most reliable magnetic sensors due to their good linearity, proper direction sensitivity, comparative simplicity, and cost-effective operation [5].

In a certain range of measured intensities, fluxgates outperform other forms of magnetic field sensors. Their sensing range and their resolution fall in between low-cost solid state sensors and high-priced ultra-sensitive magnetometers based on quantum phenomena [6]. Fluxgates have a wide application range from accurate geophysical instruments to robust detection sensors for space and security applications [7-8]. With rapid progress of fabrication techniques and digitalization of electronic components, more needs to fluxgate sensors have been increased. Due to this demand, the treatment of fluxgate sensors nowadays focuses not only on describing various designs of the sensor, but also on exploiting various materials to be used as a core sensor [9-10].

The magnetic core of the fluxgate sensor is the main component that regulates measuring performance of the device. It is found that the design of the fluxgate's core usually limits usage of fluxgate to certain application [11]. Thus, it is vital to model the non-linear characteristics of the core's magnetic materials at different operating conditions in order to investigate the intensity of the induced signal, which in turn supplies information on the magnetic field to be evaluated.

Although there are extensive research on the fluxgate sensors [12- 15], this research field currently suffers from a lack of sufficient simulations of the phenomenon taking into account the nonlinear nature of the fluxgate sensing element, and the different design configurations.

1.2. Objective of the Research

If we look on the recent development of magnetic materials, fields, principles, and phenomena in practice, we can see an accelerating transition from the traditional use of ''bulk'' magnetic sensors in the industry to more sophisticated utilization of these

sensors in different applications [16]. This push of emerging applications for very small magnetic sensors leads to a strong desire for miniaturization of the fluxgate sensor. Furthermore, the progress of micromachined and semiconductor manufacturing technology has brought new chances to fluxgates sensors on a microscale, which is usually called as "micro fluxgates" [17-18]. The main goal was to transfer the advantages of the fluxgate from the macro to the micro scale. However, fluxgate miniaturization process is rather complicated, and not a straight forward matter.

The major issues encountered in sensor miniaturization are that when the dimensions of the sensor's dominant element "i.e. fluxgate core" decrease, the inherent nonlinear behavior of the magnetic core contributes in degrading the sensor's performance [19]. At the common fluxgate operating frequencies the hysteresis loss is the main contributor in the magnetic core loss, and the change in the hysteresis loop shape affects the fluxgate output [20] .Thus, modeling of hysteresis loops of the core's soft magnetic materials is important to understand the fluxgate sensing performance with different core structures. Moreover, the excitation current and frequency scheme need to be reinvestigated to assure the periodic saturation of the soft ferromagnetic core in order to obtain a good signal detection performance.

The design goal of a micro fluxgate, therefore, should focus on striking a balance among its effective parameters to ensure an optimal design with desired requirements. The balance can be done by the investigation of the various parameters that could affect the sensor operability. Thus, the main motivation of this thesis is the need to optimize sensor parameters, and to quantitatively predict the properties of the sensor from simulations made on the magnetic material core prior to the actual implementation of the fluxgate device. This is done through conducting the necessary simulations to study the behavior of the fluxgate magnetic core under various deign parameters (i.e. excitation current, core dimensions, frequency). Studying the effect of these parameters, taking into account an accurate modeling of the core's magnetic characteristics, paves the way to create a more reliable version of a fluxgate sensor's design in the microscale.

The motivation of this thesis is the need to optimize sensor parameters, and to quantitatively predict the properties of the sensor from simulations made on the magnetic material core prior to sensor design. Thus, this thesis provides a comprehensive detailed study for the fluxgate core behavior, which explains how the current and magnetic distributions inside the core relies on excitation current, frequency, and core dimensions. The detailed study conducted in this thesis will motivate enhanced designs and it will boost the research to further improvement.

1.3. Thesis Outline

The thesis comprises of seven chapters, the first chapter is an introduction; rest of thesis is arranged as follows:

Chapter (2) in this thesis provides an overview of theory of magnetism, and gives a general framework about different magnetic materials categories. Furthermore, the hysteresis loop, as one of the characteristics of the magnetic material, has been described; highlighting different approaches to model it, with an emphasis on the Jiles-Atherton model.

Chapter (3) in this thesis presents a comprehensive review of the various types of magnetic sensors. Several scalar and vector magnetometers have been discussed along with their theory of operations. Moreover, different designs of magnetic sensors have been presented, with a brief about its applications.

Chapter (4) focuses on the fluxgate sensor, with a description about its principle of operation. Categories of the fluxgate sensor have been demonstrated, with an illustration about the differences between them. Electronic circuits and readout strategies for the fluxgate sensor have been expressed as well in this chapter.

Chapter (5) outlines the theoretical background that governs the propagation of fields inside the fluxgate sensing element. After that, numerical simulations, using finite element method have been conducted to model one of the fluxgate's core configurations. Extensive studies have been made in this chapter to display fluxgate core's performance versus various working settings. The most dominant factors, that influence the fluxgate core's functionality, have been used to reveal their effect on the fields' distributions inside the fluxgate core. The results of the simulations have been discussed for each of the conducted studies.

Chapter (6) concerns with another set of simulations that deals with an enhanced configuration of the fluxgate core to improve its performance. Detailed studies have been done through the finite element tool COMSOL. The outcomes have been analyzed for several design parameters, with presenting the consequences of altering each parameter.

Chapter 7 summarizes the findings and presents the research' conclusions at the end of this thesis. Also, future work recommendations are offered.

Chapter 2 : Magnetism and Magnetic Materials

Magnetism is a quantum mechanical phenomenon. Magnetization of a magnetic material is caused by atomic current loops generated by three mechanisms [21]:

1. electron spin about its own axis;
2. orbital motion of the electrons around nucleus; and
3. motion of protons around each other in the nucleus.

This chapter provides details about the physical quantities that represent the magnetic behavior of the materials. Also, this chapter summarizes the basic characteristics of the common five categories of magnetic materials. Furthermore, since the precision of the magnetic core's mathematical model is critical during simulations, this chapter presents also the common approaches that model the hysteresis loop of the magnetic material. Moreover, further details are provided about the hysteretic behavior of the magnetic materials, with a focus on the selected Jiles-Atherton hysteresis model.

2.1. Magnetic Physical Quantities

A material consists of many atoms. An atom consists of a nucleus in the center and electrons rotating on orbits. The motion of electrons around the nucleus is equivalent to the flow of electric current in a microscopic resistanceless loop. The pattern of magnetic field induced by a loop current is similar to that exhibited by a permanent magnet. Therefore, the miniature current loop can be regarded as a magnetic dipole. Microscopic magnetic moment is vector quantity orthogonal to current loop plane, with intensity equal to product of loop current i and loop area $a_c = \pi r^2$. The average orbit radius is around 10^{-10} m. An electron generates the following magnetic moments [22]:

I. an orbital magnetic moment m_o because it rotates around the nucleus and

II. a spin magnetic moment m_s because it spins about its own axis while it orbits the nucleus.

Total magnetic moment of an atom can be defined as the vector sum of the atom orbital and spin magnetic moments. The magnetic moment of an electron is of the order 1000 times stronger than that of the nucleus. Therefore, total magnetic moment of an atom is dominated by sum of magnetic moments of its electrons. Finally, the macroscopic magnetic moment, m, of material, can be defined as vector sum of all microscopic magnetic dipole moments within the material [23].

Another quantity that should be described is magnetization *M*. Magnetization is a macroscopic vector physical quantity related to the magnetic dipole moments density per unit volume of material. If magnetic dipoles are aligned in one direction, they form a structure, and therefore induce a magnetic field. A set of magnetic dipoles points into the same direction is called a *magnetic domain*. A *magnetic domain* is a zone with uniform magnetization within a magnetic material. A magnetic domain acts like a small bar magnet. Large dipole moments are produced by domains as the vector sum of atomic moments. The domain moments, however, vary in direction from domain to domain, and the material as a whole has no magnetic moments. Typically, the magnetic domain contains from 10^{16} to 10^{21} atoms. The domains are divided from each other by

thin transition regions termed the *domain walls*, which are of the order of 100 to 150 atoms thick. In these domain boundaries, there is a gradual transition of spin orientation (*see Figure2-1*). The atomic magnetic moments reverse direction across magnetic domain walls. Magnetization process proceeds by motion of the domain walls. This process is discrete in the time domain and the space domain [24].
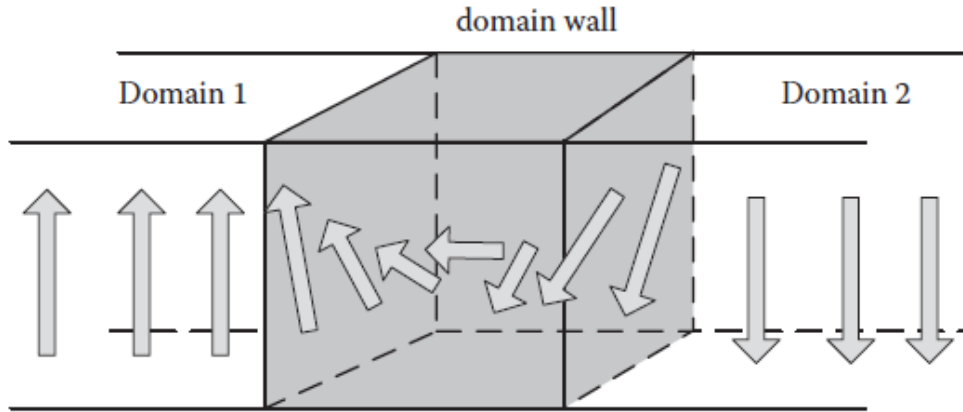
Figure 2-1: Magnetic behavior across domain wall

When a current travels across a relatively long conductive medium, a magnetic field, *H*, orthogonal to the circulating current's direction, is generated. Furthermore, the medium's response to this phenomenon is what is called the magnetic induction, also known as magnetic flux density, *B*, The magnetic flux density is proportional to magnetic field, *H* by:

$$B = \mu\, H \qquad\qquad (2\text{-}1)$$

Where μ is the material's permeability which corresponds to how much magnetic flux density B is induced within medium for a certain magnetic field H. usually permeability of material describes its *relative permeability* $\mu_r = \mu\,/\,\mu_0$, where μ_0, is permeability of vacuum (i.e., $\mu_0 = 4\pi \times 10^{-7}$ m kg s^{-2} A^{-2}). Dependence can be, therefore, written as

$$B = \mu_r\, \mu_0\, H \qquad\qquad (2\text{-}2)$$

The relative permeability is a measure of how much better a given material is than air for conducting magnetic flux. Another physical quantity that describes the magnetization processes is the susceptibility χ that links the magnetization M with the magnetic field H by:

$$M = \chi\, H \qquad\qquad (2\text{-}3)$$

Also, susceptibility and permeability of a medium can be related by:

$$\mu_r = \chi + 1 \qquad\qquad (2\text{-}4)$$

Now, when a magnetic field is applied to material, its response, i.e., its magnetic flux density can be written as:

$$B = \mu_0 \left(H + M\right) \qquad\qquad (2\text{-}5)$$

The component $\mu_0 \, \boldsymbol{H}$ in this relationship indicates the contribution of an external magnetic source, whereas the component $\mu_0 \, \boldsymbol{M}$ reflects the internal contribution of the magnetized medium. Therefore, the medium can show flux density response, even there is no applied magnetic field, due to its intrinsic magnetization (either spontaneously or due to previous magnetizing) [25]. Finally, it should be highlighted that there are three common systems of units used to describe the magnetic physical quantities. The Gaussian or cgs system, as well as two MKS unit systems, Kennelly and Somerfield, are the three unit systems. *Table 2-1* summarizes the essential equations and units of these systems. Magnetic unit philosophy differs between the cgs and SI systems. The cgs system relies on magnetostatics and "magnetic pole" principle, whereas SI system relies on electrodynamic approach to magnetism, and electric currents concept [26]. In this thesis, the physical quantities will be described according to *Table 2-2*, while *Table 2-3* summarizes the conversions between the different magnetic units.

Table 2-1: Principle Unit Systems Currently Used in Magnetism

Quantity		*SI (Sommerfield)*	*SI (Kennelly)*	*EMU (Gaussian)*
Field	*H*	A/m	A/m	oersteds
Induction	*B*	tesla	tesla	gauss
Magnetization	*M*	A/m	_	emu/cc
Moment	*m*	Am^2	Weber meter	emu
Intensity of Magnetization	*I*	_	tesla	_
Field Equation		$B = \mu_0 \left(H + M\right)$	$B = \mu_0 H + I$	$B = H + 4\pi M$
Note: The intensity of magnetization *I* used in the Kennelly system of units is merely an alternative measure of the magnetization *M*, in which tesla is used instead of A/m. Under all circumstances therefore $I = \mu_0 M$				

Table 2-2: The Physical Quantities used in This Thesis

Quantity	*Symbol*	*Unit*
Magnetic Field	H	[A/m]
Magnetic Flux Density, magnetic induction	B	T
Magnetization	M	[A/m]
Magnetic Moment	m	[Am^2]
Susceptibility	χ	[-]
Permeability	μ	[-]

Table 2-3: Conversions for common magnetic units

	Tesla (T)	(A/m)	Gauss (G)	Oersted (Oe)
A/m	1.256×10^{-6}	1	12.56×10^{-3}	12.56×10^{-3}
Oe	10^{-4}	79.6	1	1
T	1	7.96×10^{5}	10^4	10^4
γ	10^{-9}	7.96×10^{-5}	10^{-5}	10^{-5}
G	10^{-4}	79.6	1	1

2.2.   Magnetic Materials

Empirically, magnetic materials can be categorized based on their induced magnetization response to external magnetic field. This categorization can be done through the consideration of the microscopic mechanisms that govern the material's behavior when magnetic field is applied. Based on this, there are five categories of magnetic materials, which are as follows [27]:
(i) Diamagnetic materials;
(ii) Paramagnetic materials;
(iii) Ferromagnetic materials;
(iv) Antiferromagnetic materials;
(v) Ferrimagnetic materials

2.2.1.   Diamagnetic materials

In diamagnetic materials, the magnetic effects are weak. If no magnetic field is applied, the orbital and spin magnetic moments cancel each other and the net magnetic moment is zero. An applied magnetic field makes spin moment slightly exceed orbital moment ($m_s > m_o$), resulting in a small net magnetic moment. The small magnetic moment causes small dipole alignment, which produces a small magnetic field. This field opposes the applied magnetic field, causing repulsive effect and slightly reducing the total magnetic field. That is why diamagnetic materials show negative and small magnetic susceptibilities ($\chi \cong -10^{-5}$). Also, a diamagnetic material has a relative magnetic permeability that is slightly below one ($\mu_r < 1$). Diamagnetism occurs only if a magnetic field is present. When the applied field is reduced to zero, alignment of dipoles disappears. In other words, the magnetic behavior of diamagnetic materials is completely reversible, and if the applied magnetic field is not present, random magnetic moment orientation is restored. [28].The diamagnetic materials include bismuth (Bi), diamond (C), lead (Pb), and mercury (Hg).

2.2.2.   Paramagnetic materials

The magnetism of paramagnetic materials arises from partial alignment of magnetic dipole moments inside the material, which are randomly directed when there is no presence of magnetic field. When magnetic field is zero, the individual dipoles are oriented randomly and the net internal magnetic field is zero. When an applied field exists, the magnetic dipoles are aligned in applied field direction. Degree of alignment of the dipoles increases as the magnitude of applied field increases. Therefore, paramagnetism occurs only in presence of magnetic field. When the applied field is reduced to zero, alignment of dipoles disappears and the dipoles are randomly oriented [29]. Paramagnetic materials have a positive and small magnetic susceptibilities between $+10^{-6}$ and $+10^{-2}$. Also, Paramagnetic material has a relative magnetic permeability that is slightly above one ($\mu_r > 1$). The paramagnetic materials includes calcium (Ca), magnesium (Mg), niobium (Nb), platinum (Pt), titanium (Ti), and tungsten (W).

2.2.3. Ferromagnetic materials

A ferromagnetic material has a large magnetic moments that arises from the spin moments m_s (i.e. $m_s \gg m_o$). If there is no applied magnetic field, the magnetic domains are oriented in random directions and produce internal magnetic field in random directions. Since various domains have random directions, the net magnetic field is zero. When there is an applied magnetic field, domains tend to align in applied field direction and produce very strong internal magnetic field, which adds to the external field. The degree of alignment increases when the magnitude of the external field increases. As a result, ferromagnetics have a large and positive magnetic susceptibility in the range from 1 to 1, 000, 000, resulting in $\mu_r > 1$. The relative permeability of ferromagnetic materials is a function of both applied field and previous magnetic history (i.e. Material's hysteresis loop). This means that when there is no applied magnetic field, some magnetic domains remain aligned in same direction as before in presence of the applied field [30]. The main materials that show ferromagnetism behavior are the three metals; iron (Fe), cobalt (Co), and nickel (Ni).

2.2.4. Antiferromagnetic materials

In antiferromagnetic materials, the magnetic moments of adjacent atoms are aligned in opposite directions and are about equal in magnitude when there is no applied magnetic field. Thus, net magnetic moment is zero in presence of an external magnetic field. That is means that even an external magnetic field has a small effect on the material magnetic properties, resulting in relative magnetic permeability μ_r slightly greater than unity. Thus, Antiferromagnetic materials have a very low magnetic susceptibility [31]. Antiferromagnetic materials such as Cerium (Ce), Neodymium (Nd), Erbium (Er), Europium (Eu), and Samarium (Sm).

2.2.5. Ferrimagnetic materials
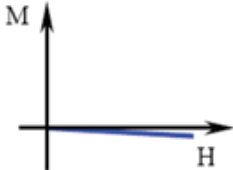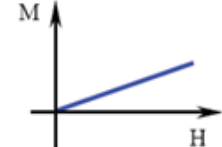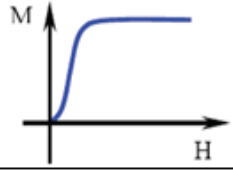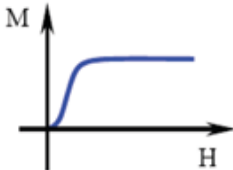
Ferrimagnetic materials, such as chromium (Cr) and manganese (Mn), have strong coupling forces between atomic dipole moments, yet these coupling forces cause antiparallel alignments of electron spins. Therefore, the spin magnetic moments which are very large in magnitude, are greatly unequal, and vary in direction from atom to atom when there is no applied magnetic field, causing no net magnetic moment. If a magnetic field is present, magnitudes of the magnetic moments become unequal and thier directions alternate, causing a net nonzero magnetic moment. However, magnetic flux density induced in ferrimagnetic materials is smaller than that in ferromagnetic materials, due to the partial alignment. The relative permeability of ferrimagnetic material is much higher than unity ($\mu_r \gg 1$). But when ferrimagnetic materials are heated above their Curie temperatures, the spin directions become random and the ferromagnetic material becomes paramagnetic [32].

Magnetic materials classification is summarized in *Table 2-4*, and their magnetic orders are shown in *Figure 2-2*. In conclusion, magnetic behavior of magnetic materials can be characterized by the corresponding values of χ and μ_r as follows:

I. Diamagnetic; χ is small and negative, and μ_r slightly less than 1.

II. Para- and antiferromagnetic; χ is small and positive, and μ_r slightly greater than 1.

III. Ferro- and ferrimagnetic; χ and μ_r are large and positive, and both are functions of H.

Table 2-4: Types of Magnetic Materials [33]

Material Type	Atomic / Magnetic behavior	
Diamagnetism	Atoms have no magnetic moments	
Paramagnetism	Atoms have randomly oriented magnetic moments	
Ferromagnetism	Atoms have parallel aligned magnetic moments	
Antiferromagnetism	Atoms have anti-parallel aligned magnetic moments	
Ferrimagnetism	Atoms have mixed parallel and anti-parallel aligned magnetic moments	
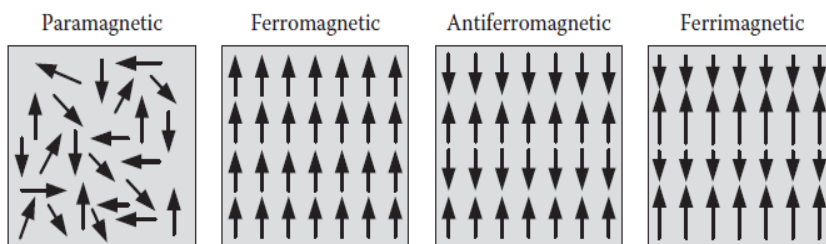
Figure 2-2: Various kinds of magnetic orders of the magnetic materials

2.3. The Hysteresis

Basically, relative permeability μ_r is suitable parameter for defining characteristics of magnetic materials since it informs about relation between two main magnetic characteristics: flux density B and magnetic field H. However, in reality, description of magnetic behavior can be complex, as relation between B and H is, at most cases, nonlinear for the magnetic materials. For this reason, the permeability actually depends on the instant value of magnetic field at certain working point. Accordingly, a specific

value of permeability can give information only about a specific operating point. Therefore, during any design approach, it is convenient to define nonlinear magnetization curve as a representation of magnetizing process inside the material. The nonlinear magnetization curve of a magnetic material is called the hysteresis [34]. The magnetic hysteresis refers to the fact that when a magnetic material is field cycled (i. e., the magnetic field H rises then falls), two non-overlapping curves connects magnetization with magnetic field, i.e. M (H) emerge. Another representation of the magnetic hysteresis involves rather the magnetic flux density B versus H since it is B that is, in fact, measured.

A ferromagnetic material has a "memory" because it stays magnetized after external field is vanished. In ferromagnetics, process of repeated magnetization and demagnetization in an AC magnetic field is only partially reversible. The induced magnetization does not vanish even after the removal of the magnetic field. Demagnetization involves either reversing the spins in magnetic domains or moving the domain walls. The B –H curve is a nonlinear and multivalued function, which exhibits saturation, as shown in *Figure 2-3*.

When magnetic field H is increased, magnetic flux density B also increases. At high values of H, the core magnetization approaches its saturation value, corresponding to full alignment of magnetic moments, and magnetic flux density B reaches the saturation induction or flux density value B_s. When magnetic field H is reduced, many domains tend to remain aligned due to frictional forces resisting the domain movement. Hence, the magnetic field must be reduced significantly before the domains begin to return to their initial unaligned arrangement. When the magnetic field H become zero, magnetic flux density B does not become zero because domains remain partially aligned and the core retains some residual magnetic flux density known as residual flux density, residual magnetism, or remnant magnetization B_r. To reduce B to zero, a negative or reverse magnetic field intensity, called coercive field $H = H_c$, must be applied. If magnetic field intensity is further decreased, magnetic flux density also decreases and reaches the saturation value $-B_s$. When magnetic field intensity is increased, magnetization curve follows a different path. At $H = 0$, $B = \pm B_r$ and at $B = 0$, $H = \pm H_c$. Therefore, the magnetization curve is not fully reversible [35].
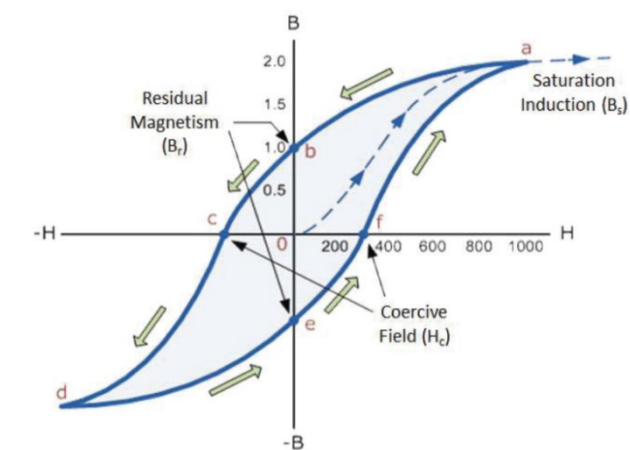
Figure 2-3: Magnetic hysteresis loop

The shape and size of the hysteresis loop is of significant importance, as the area within a loop of a material defend as magnetic energy losses per unit volume per cycle

[36]. Hysteresis loop is produced by measuring magnetic flux of magnetic material whereas magnetizing field is changing [37]. Modeling of the hysteresis loop of the magnetic material is crucial for optimal design of any device that uses this material [38-39]. The purpose of the proposed magnetic hysteresis models is to develop equations that realizes magnetic flux density depending on an applied magnetic field, B(H) [40-41]. Numerous attempts have been made to build a hysteresis model, but they can be classified into two kinds of models: physics-based and phenomenon-based models. Physics-based models consider the micro-mechanism of the hysteresis curve [42-44], while phenomenon-based models just consider the external behavior of magnetization produced by applied magnetic field while not the inherent magnetization mechanism [45-47]. We will explain below some of the most common models.

2.3.1. Rayleigh Model

Rayleigh model is one of the oldest developed magnetic hysteresis models. It connects magnetic flux density and magnetic field by [48]:

$$B = \mu_{in} H + \frac{1}{2} \eta H^2 \tag{2-6}$$

Where μ_{in} is the initial permeability and η is the Rayleigh parameter. For an external sinusoidal magnetic field with maximum H_{max}, the general equation of the model is:

$$B = (\mu_{in} + \eta H_{max})H \pm \frac{1}{2} \eta (H^2 - H_{max}^2) \tag{2-7}$$

The negative sign in equation (2-7) relates to falling field and positive sign corresponds to raising field. As a result "±" could be written as sign function. Rayleigh hysteresis model has small number of parameters and is simple to be constructed; nonetheless, it can be applied only for low applied magnetic fields. Also, this model ignores saturation state, and the hysteresis loops must be centered and elliptical [49].

2.3.2. Frohlich Model

Frohlich model is also an analytical model that has two parameters f_1 and f_2 to describe the hysteresis curve depending on material's characteristics as follows [50].

$$B = \frac{H}{f_1 + f_2 |H|} \tag{2-8}$$

Afterwards, the original model was extended to represent the hysteresis loop by:

$$B = \begin{cases} \frac{(H - H_c)}{f_1 + f_2 |H - H_c|} & for\ H > 0 \\ \frac{H + H_c}{f_1 + f_2 |H + H_c|} & for\ H < 0 \end{cases} \tag{2-9}$$

Where $f_1 = H_c \left(\frac{1}{B_r} - \frac{1}{B_s}\right)$ and $f_2 = \frac{1}{B_s}$ \qquad (2-10)

Frohlich model is based on mathematical representations as Rayleigh model, and has no physical aspect. It represents saturation states but in limited applications [51].

2.3.3. Chan-Vladimirescu Model

This model represents the hysteresis using polynomial approach. It assumes that hysteresis is made up of upper and lower branch corresponds to falling and rising applied magnetic fields H respectively. These branches are represented by two expressions named "branch equations" [52]:

$$B_+(H) = B_s \frac{H+H_c}{|H+H_c|+H_c \left(\frac{B_s}{B_r}-1\right)} \qquad H < 0 \ (upper \ branch) \qquad (2\text{-}11)$$

$$B_-(H) = B_s \frac{H-H_c}{|H-H_c|+H_c \left(\frac{B_s}{B_r}-1\right)} \qquad H > 0 \ (lower \ branch) \qquad (2\text{-}12)$$

The initial magnetization curve is computed by averaging the two equations as:

$$B_{mag}(H) = \frac{B_+(H)+ B_-(H)}{2} \qquad (2\text{-}13)$$

Chan-Vladimirescu model needs 3 parameters to model the hysteresis curve; *Hc (Coercive field), Br (Residual flux density) and Bs (Saturation flux density)*. However, this model built on static behavior of magnetic material, and can not deal with dynamic conditions [53].

2.3.4. Hodgdon Model

Hodgdon model represents the hysteresis curve by a differential equation that relates change of magnetic field to the change of magnetic flux [54].

$$\frac{dH}{dB} = h_m * s(B) * [f(B) - H] + g(B) \qquad (2\text{-}14)$$

where h_m is constant, and $s(B)$ is sign function:

$$s(B) = \begin{cases} +1 & if \ B > 0 \\ -1 & if \ B < 0 \end{cases} \qquad (2\text{-}15)$$

f (B) and g (B) are two functions define what is called Hodgdon "*material functions*" [55] and given by:

$$f(B) = \begin{cases} D_1(B + B^*) - D_2 B^* & if \ B < -B^* \\ D_2 B^* & if \ |B| \le B^* \\ D_1(B - B^*) + D_2 B^* & if \ B > B^* \end{cases} \qquad (2\text{-}16)$$

$$g(B) = \begin{cases} (1 + D_3)D_2 & if \ |B| \le B^* \\ D_1 & if \ |B| > B^* \end{cases} \qquad (2\text{-}17)$$

where D_1, D_2, D_3, and B^* are model parameters. Afterwards, other complex trigonometric functions were also presented by Hodgdon for achieving better accuracy in modeling the hysterics curve [56].

2.3.5. Polynomial Model

Polynomial model is a static mathematical model that is proposed to model the very low coercive field materials. Here the hysteresis curve is represented by a piecewise polynomial approach based on spline function. The saturation state is represented by polynomial of the first order and slope μ_0. Moreover, the central region of the hysteresis loop is represented by an rth order polynomial, as seen in *Figure 2-4*. The mathematical representation of the hysteresis model can be written as [57]:

$$B = \begin{cases} \mu_0 \ (H - H_b) + P(H_b) & if \ H \geq +H_b \\ P(H) & if \ |H| < \ H_b \\ \mu_0 \ (H + H_b) - P(H_b) & if \ H \leq -H_b \end{cases} \tag{2-18}$$

Where P is a polynomial in R such that: $P(X) = \sum_{i=0}^{n} p_i \, X^i$, and H_b is the value of H needed to reach saturation. The number of parameters and accuracy of this model relies on the rth order of the polynomial. So, if the order of the polynomial is n=5, four parameters (p_1, p_3, p_5 and H_b) can be used to represent the hysteresis curve. Therefore, the static behavior of each material determines the choice of the polynomial order since different magnetic materials can be represented by different polynomial orders [58].
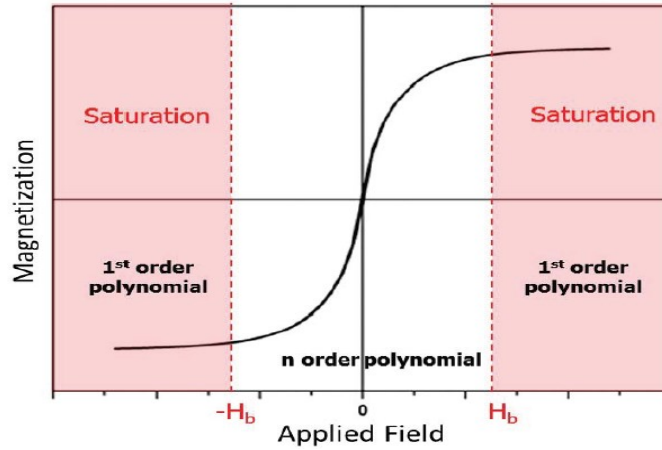
Figure 2-4: The Polynomial model

2.3.6. Dynamic Static Feedback Model (DSF Model)

The model's idea is based on representing the different hysteretic effects created in magnetic materials by static and dynamic losses. This is done using a 1st order differential equation:

$$H(t) = \ H_{stat}\big(B(t)\big) + D_s \frac{dB(t)}{dt} \tag{2-19}$$

where *H(t)* is magnetic field, *B(t)* is average flux density and H_{stat} *(B)* is what is called material's static law [59]. The DSF model requires also a parameter D_s that represents the wall motion effects, and a static magnetic model that defines the material's static characteristics. The DSF model can be used in the cases of low losses. On the other hand, the frequency range that can be represented by this model is limited [60].

2.3.7. Bertotti's Model

Bertotti's model represents the hysteresis curve based on its dynamic and static contributions in losses. In this model, a term defined as magnetic objects is used to describe the magnetic domains behavior inside the material. Each of these statistically independent magnetic objects corresponds to collection of interacting magnetic domain walls. Thus, magnetization process in a material can be defined in terms of $\tilde{n}$ simultaneously active magnetic objects, where term $\tilde{n}$ defined as [61]:

$$\tilde{n}(H_{exc}, \{M_c\}) = \tilde{n}_0 + \frac{H_{exc}}{V_0} \tag{2-20}$$

$\tilde{n}$ is function of both excitation field H_{exc} and the set {M_c} of factors that characterize material's microstructure and domain structure. The term $\tilde{n}_0$ describe the microstructural information of the material, as it refers to the limiting number of simultaneously active magnetic objects. Furthermore, the term V_0 describes the statistical distribution of the local coercive fields inside the material. As a result, the total magnetic field can defined as [62]:

$$H_{Total}(t) = H_s(B(t)) + b_{m1}\frac{dB(t)}{dt} + b_{m2} * b_{m3} * \left|\frac{dB(t)}{dt}\right|^{1/2} \tag{2-21}$$

Where b_{m1}, b_{m2}, and b_{m3} are eddy current, wall motion, and sign coefficients respectively. b_{m1} depends on material's conductivity σ and material thickness *d*. b_{m2} is a function of characteristic field V_0.

$$b_{m1} = \frac{\sigma d^2}{12}, \quad b_{m2} = \sqrt{\sigma g V_0 s_m}, \quad b_m = sign(\frac{dB}{dt}) \tag{2-22}$$

Where *g* is dimensionless coefficient ($g \approx 0.136$), and s_m is term called the magnetic cross section as proposed by Bertotti.

All the above mentioned models have several drawbacks including their robustness and reliability. Beside that most of them does not take into consideration the inherent physics of material's behavior and can't cope with its dynamic change with frequency [63]. Due to the advances made in developing the Micro-magnetic theory, and understanding the concepts of macroscopic magnetization that relates microstructural features of magnetic materials with macroscopic magnetization curves, Four models: Landau-Lifshitz , Preisach , Stoner-Wohlfarth, and Jiles-Atherton, were developed and still being the most used to analyze and illustrate the Hysteretic behavior of several magnetic materials [64].

The Landau-Lifshitz model was created to represent individual magnetic moments behavior under influence of magnetic field. In the presence of a magnetic field, magnetic moments rotate, at least at the macroscopic level. Therefore, Landau-Lifshitz

model was implemented by applying this concept at microscopic level of individual magnetic moments. However, while developing the model, it was not quite clear at which scale these moments are [65]. Because the Landau-Lifshitz model is a continuum model, the described moments are not individual "atomic" moments, but they are also not domains. However, magnetic material behavior can then be computed by integrating rotation process throughout material's volume. A main issue with utilizing this model is that it demands a precise calculation of a huge number of distribution function parameters, which makes it difficult to be applied on large simulations due to the processing time as the computations have to be done on huge number of individual magnetic moments [66].

The Stoner-Wohlfarth model was developed to express the reorientation of magnetic moments of individual domains by coherent rotation or flipping of all moments within domain [67]. This model, unlike the Landau-Lifshitz model, does not account for individual moments. Although that Stoner-Wohlfarth model initially supposed that there were no magnetic interactions between magnetic domains, the model was later enhanced to involve the coupling between magnetic domains. Afterwards, the effects of anisotropy on the orientation of magnetization were implemented in this model [68].

The Preisach model describes the magnetic hysteresis on the macroscopic scale. The concept of this model based on considering the magnetic hysteresis to be the sum of a sequence of switching events that arise at the microscopic level in a magnetic material [69]. The model's key assumption is that each magnetic domain in the material has the same magnetization but distinct switching fields. As a result, the hysteretic characteristic of the material can be defined as volume fraction of magnetic domains with certain combination of switching fields [70].

The Jiles-Atherton model was created using the statistical thermodynamic principles at a multi domain microscopic level. The concept of this model is based on the process of domain boundary movement that is described by the Langevin-Weiss theory [71]. The orientations of magnetic moments are assumed to be statistically distributed at this model. Thus, the Magnetic properties can be computed by integrating the moment distribution over all possible orientations. The Jiles-Atherton model also includes magnetic moment coupling concept in the form of an internal magnetic field proportional to magnetization, which tends to align moments in a domain parallel to one another [72]. The following section will go through the main Jiles-Atherton model concepts in further details.

2.4. Jiles–Atherton Model of Hysteresis

During the numerical simulations, the accuracy of a modeling the nonlinear hysteretic behavior of the fluxgate core is vital in providing relevant precise results about the magnetization process. In this thesis, Jiles–Atherton Model was selected to model nonlinear behavior of fluxgate magnetic core. The macroscopic Jiles-Atherton (J-A) hysteresis model is one of the best model that describe magnetic hysteresis of a material. Its advantages include the relative accuracy and its mathematical expressions that can be implemented in finite element analysis tools. This makes it one of the commonly used hysteresis model in several approaches [73]. J-A model creates the possibility of modeling the characteristics of magnetic components during its operation, when magnetic cores are magnetized by current wave forms [74].

The Jiles-Atherton model is inspired from physical mechanism of magnetic hysteresis, in which it is supposed that magnetic material consists of number of magnetic domains and that a number of pinning sites (i.e., nonmagnetic inclusions, impurities, dislocations, vacancies, structure defects, and inhomogeneous stress regions) are uniformly distributed throughout the volume of the material, determining the magnetic hysteresis [75]. Hence, as shown in *Figure 2-5*, the magnetization mechanism is determined by two processes: domain walls movement and magnetic moments rotation within each magnetic domain. When magnetic material is subjected to applied magnetic field, magnetic domains will be affected, firstly, by wall displacements. These magnetic domains, whose magnetization points toward the same direction as applied field, will expand while the neighboring magnetic domains will shrink or disappear. At certain point, when the applied field increases, domains start to rotate [76].According to J-A theory, the change in magnetization, M, of a magnetic material can be calculated from microstructural domain processes that participates in reversible M_{rev} and irreversible M_{irr} changes in magnetization [77]

$$\Delta M = \Delta M_{irr} + \Delta M_{rev} \tag{2-23}$$

(a)

(b)
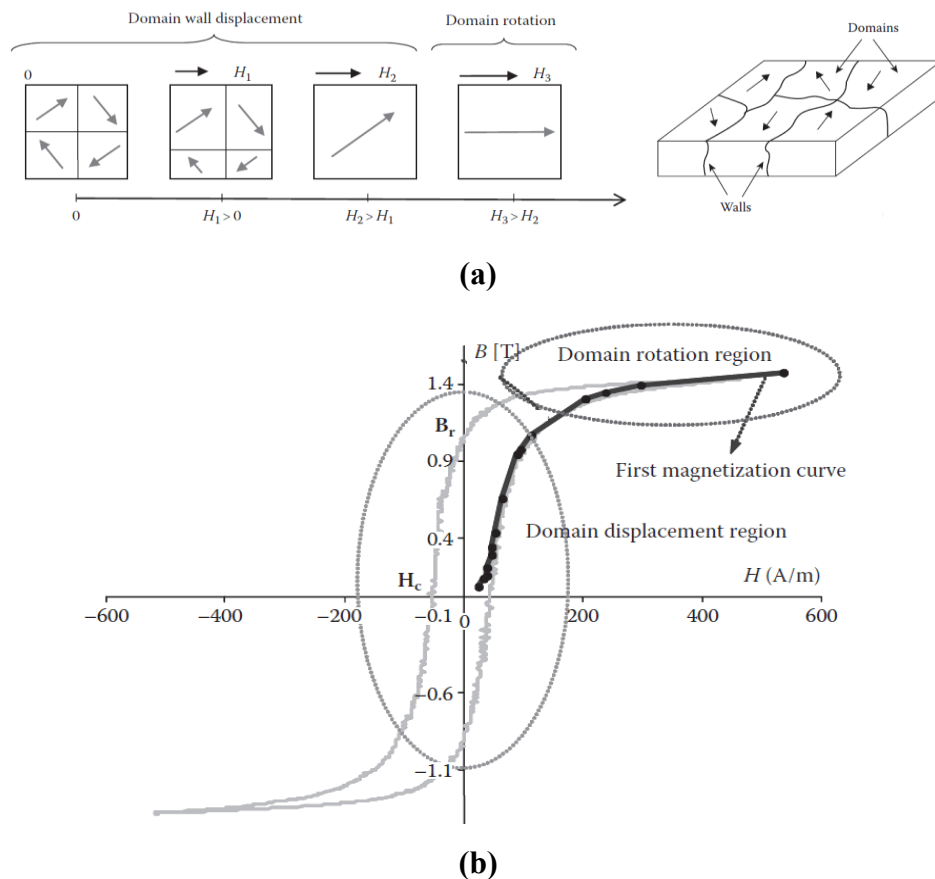
Figure 2-5: (a) Domain wall displacement and rotation for an applied magnetic field, (b) Hysteresis loop and the magnetization regions

Before proceeding further, it is important to describe the origin of irreversible and reversible magnetic components as shown in *Figure 2-6*.

A. Reversible magnetic component

The reversible magnetization component results from the impact of reversible bending of domain walls. At low applied magnetic fields, the magnetic domain boundaries will expands. And since this is reversible magnetic regime, if magnetic field decreases again, magnetization will be back to its initial state following the same route. This mainly arises from the magnetic domain wall displacement which is reversible in nature [78].

B. Irreversible magnetic component

The irreversible component of magnetization is mostly attributed to pinning of magnetic domain walls. At high applied magnetic fields, the magnetic domain walls will depinn and will be free to move. And since this is an irreversible magnetic regime, if magnetic field decreases again, the magnetization due to magnetic field variation will not follow the same route. Although this regime corresponds to free domain wall movement, at higher magnetic fields, the magnetization will change via magnetic moment rotation [79].
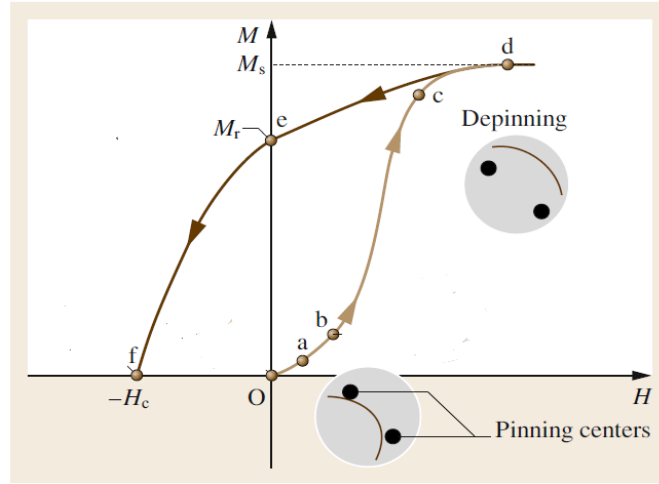
Figure 2-6: Reversible and irreversible regime of the magnetization against the magnetic field. At reversible regime the domain walls are pinned by impurities and bend under the strength of *H*, whereas at irreversible regime depinning of the domain walls occurs

The changes in the reversible and irreversible magnetization components as a function of magnetic field can be described by ordinary differential equations as follows [80]:

$$\frac{dM_{irr}}{dH_e} = \frac{(M_{an} - M_{irr})}{k\delta} \tag{2-24}$$

$$M_{rev} = c(M_{an} - M_{irr}) \tag{2-25}$$

Where δ is the directional parameter that describes the ascending and descending part of the hysteresis curve. k and c are the model parameters. Another model parameter α exists in the definition of the effective field term, *He = H + α M,* that defines the contributions of the magnetic interactions between domains and the applied

magnetic field. M_{an} is the anhysteretic magnetization. The anhysteretic magnetization is the magnetization of an ideal magnetic material which does not contain any pinning sites and therefore, its magnetization curve does not show hysteresis *"see Figure 2-7"*. At this case, the magnetization is made only via the rotating magnetic moments mechanism [81]. In practice a point on the anhysteretic curve is attained by applying a known DC bias magnetic field and then by superimposing upon it a strong alternating magnetic field of low frequency, whose magnitude is gradually reduced to zero. The value of anhysteretic magnetization for the given value of H_{bias} is obtained as the amplitude of the alternating field reaches zero. For the description of anhysteretic magnetization Jiles and Atherton have applied the modified Langevin function [82]:

$$M_{an} = M_s \left[\coth\left(\frac{H_e}{a}\right) - \frac{a}{H_e} \right]$$

(2-26)
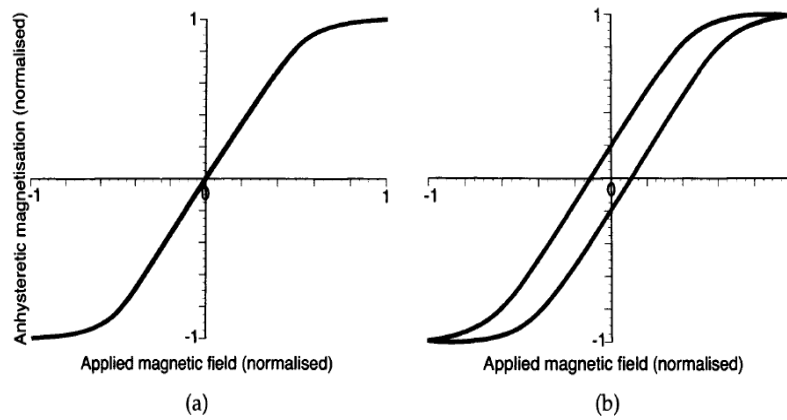
Figure 2-7: (a) Typical anhysteretic magnetization curve with no hysteresis, (b) The corresponding hysteresis curve

where two new model parameters were introduced: a and M_s, where M_s is saturation magnetization of material. The five descriptive parameters of Jiles-Atherton model have physical meaning, which imposes an advantage to the model [83].The description of each of the five parameters are as follows:

I. Spontaneous magnetisation (M_s): The spontaneous magnetization is generated in presence of applied magnetic field due to parallel alignment of magnetic moments inside magnetic domains. Saturation is achieved when spontaneous magnetization of all magnetic domains is parallel to the applied magnetic field as if there is a one domain in the material.

II. Pinning parameter (k): The pinning parameter can be considered as a microstructural quantification of the material's coercivity. It is representation of pinning density and pinning site energy.

III. Domain density (a): The domain density is a parameter that defines the number of magnetic domains inside the material. It affects the hysteresis curve slope and therefore it can be considered as a representation of the material's permeability.

IV. Domain coupling (α): The domain coupling parameter defines the indirect magnetic coupling between the material's domains. It is proportional to the remnant magnetization point in the hysteresis behavior.

V. Reversibility parameter (c): The reversibility parameter is proportional to the reversible domain wall bending and motion. In other words, it is related to the reversible magnetization component.

Furthermore, *Figure 2-8* illustrate the five microstructural parameters of the J-A model. It can be seen that *Ms* affects the maximum value of magnetization; while *a* influences the knee region of the loop. Furthermore, *α* mainly affects the slope dB/dH in the region around the coercive point, while k and c mainly influences the coercive field amplitude, and value of the derivatives at the points close to the coercive field.
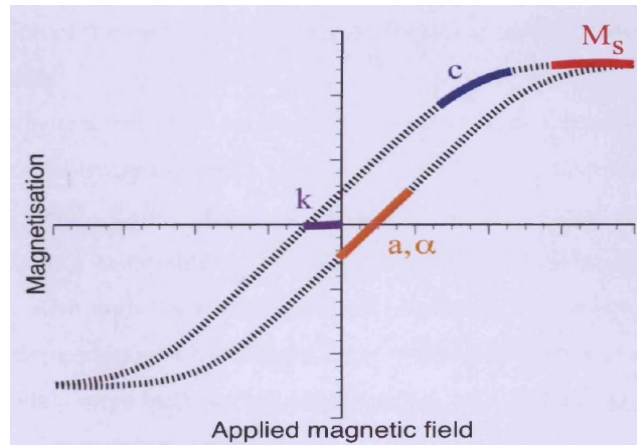
Figure 2-8: The five descriptive parameters of J-A model, and their influence on the respective specified regions of the hysteresis curve

Several attempts have been conducted to analyze effects of the five J-A model parameters on hysteresis loop [84-86], and it was concluded that (*see Figure 2-9*):
   • Variations of variable *k* dilate the loop and change the coercive field.
   • Changes in parameter *α* modify the loop rectangularity and change the remnant induction or magnetization.
   • Variations on *a* modifies the loop shape.
   • Changing *c* modifies the initial magnetization which is related to the reversible magnetization.

Table 2-5 summarizes the effect of the five J-A model parameters on hysteresis curve. Here "↑" and "↓" indicates increasing and decreasing respectively, while "–" represents no effect or a small effect. Determination of Jiles-Atherton model parameters concerns with identifying the five coefficients iteratively from the experimental hysteresis loop [87-88]. However, it should be highlighted that Jiles-Atherton model equations is a nonlinear differential equations that does not have a certain analytical solution. Thus, there is no available direct method to compute the Jiles-Atherton model's parameters based on the measured hysteresis loops [89-90]. Instead, determination of J-A model's parameters can be done by applying an iterative procedures based on numerical methods [91].
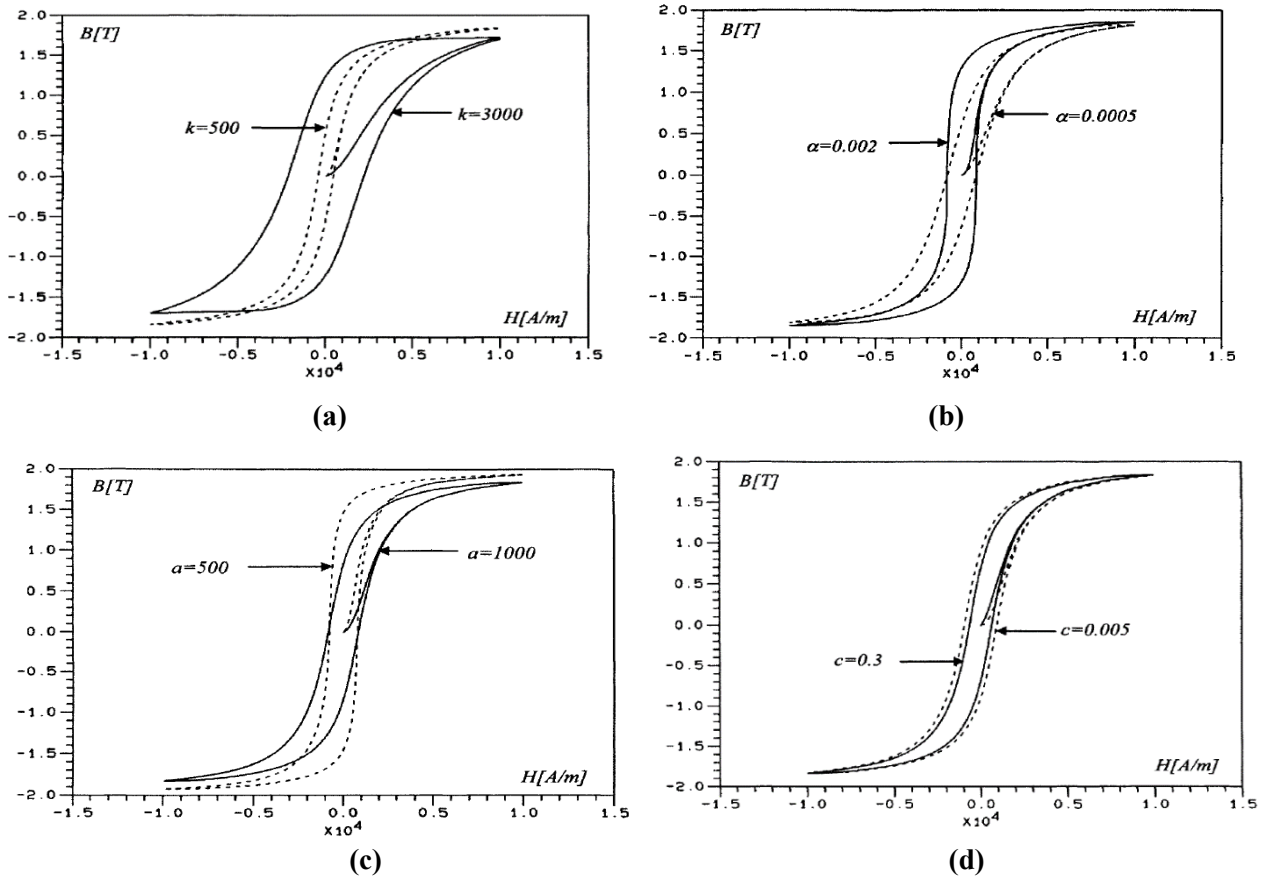
Figure 2-9: Hysteresis loops for (a) different k values, (b) different α values, (c) different a values, and (d) different c values.

Table 2-5 Effect of the J-A parameters on the Hysteresis Curve

Parameter	Physical Impact	Remanence	Coercive Force	dB/dH at Coercive Point	Loop Area	Maximum Magnetization
M_s [A/m] ↑	saturation magnetization	↑	—	↑	—	↑
α ↑	represents interdomain coupling	↑	—	↑	—	—
a [A/m] ↑	quantifies domain walls density	↓	—	↓	—	—
c ↑	describes magnetization reversibility	↓	↓	—	↓	—
k [A/m] ↑	quantifies average energy required to break pining site	↑	↑	—	↑	—

However, the iterative algorithms can be, to some extent, subtle to the chosen initial values of model parameters and also pattern of evolution of model's equations. Thus, in some cases, it may not converge and also can get trapped in local minima [92]. To avoid these drawbacks, determination of hysteresis model's parameters could be done using optimization algorithms such as genetic algorithms [93], particle swarm [94], differential evolution [95], simulated annealing [96]. Recently, these proposed intelligence optimization methods succeed to find the values of the Jiles–Atherton

model parameters that have a proper agreement with experimental hysteresis loop [97-98].

2.5. Magnetic Materials: Properties and Classification

Magnetic properties of materials are affected by both material's composition and microstructure [99]. Those properties that depend mainly on composition of particular alloy are the intrinsic or the structure insensitive properties. These properties are not changed considerably during the manufacturing process of the magnetic material. Resistivity and Curie temperature are among the fundamental intrinsic properties [100]. On the other hand, extrinsic or structure sensitive properties depends on the microstructure's features of the particular alloy. Microstructural features include grain size, defect concentrations, magnetic domains and domain walls. The structure sensitive properties can be adjusted through material's processing via mechanical and thermal treatments [101]. The key extrinsic magnetic properties are the permeability, and coercivity of the material.

Beside these properties, and based on hysteresis curves of magnetic materials, the wide variety of magnetic materials can be classified into two types: the magnetically hard (hard to magnetize and demagnetize) and the magnetically soft (easy to magnetize and demagnetize). Soft magnetic materials have a relatively high magnetic permeability while also having low coercivity. Furthermore, their B-H curve exhibits relatively narrow hysteresis loop. The soft magnetic materials can be magnetized with relatively low magnetic field. They are utilized mainly in approaches that require the previously described magnetic properties, and those applications that involve a change in magnetic induction such as transformers, motors, relays, and solenoids, magnetic sensors [102-103]. Fe-Cr alloys, Fe-Co alloys, Fe-Ni alloys, and Fe-Al-Si alloys are examples of soft magnetic materials. The impact of alloying ferromagnetic elements such as Fe, Co, and Ni is the most beneficial since they show high magnetic permeability, low coercivity, and increased electrical resistivity [104].

Hard magnetic materials are distinguished by their ability to retain high remanence or residual magnetization even after a relatively high magnetic field is applied and then removed. This type of magnetic materials has relatively high coercivity values; usually between 5 and 900 kA.m^{-1} and their B-H curve exhibits relatively wide hysteresis loop (see Figure 2-10). In practice, hard magnetic materials are alloys that, when magnetized, keep their magnetization for long periods of time after magnetizing field is removed; as a result, they are employed in production of permanent magnets such as Platinum-cobalt, Samarium-cobalt (Sm-Co), platinum-iron, and Neodymium iron boron (Nd-Fe-B) magnets [105].
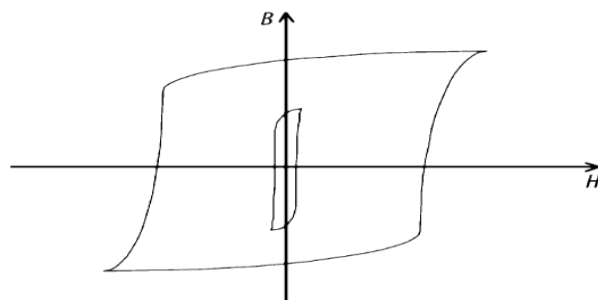
Figure 2-10: Hysteresis curves of hard and soft magnetic materials

Chapter 3 : Review of Magnetic Sensors

Sensing magnetic fields can be done by several ways. Magnetic sensors are defined here as sensors that are associated, in one way or another, with the laws and effects of magnetic fields. Therefore, this category of sensors covers those sensors in which specific material characteristics are altered in presence of magnetic field [106]. Magnetic sensing approaches explore a wide variety of concepts and phenomena based on material science and physics research fields. Beside this, Magnetic sensors are further classified into two types: scalar magnetic sensors and vector magnetic sensors [107]. Vector magnetic sensors detect the magnitude of the field just in their sensitive direction, whereas scalar magnetic sensors detect the overall magnitude of the field. Figure 3-1 shows sensing ranges of the main magnetic field sensors. In this chapter, a review will be offered about most common magnetic sensors nowadays, includes the initial sensor structure, the output signal nature, key aspects, and sensor's application areas.
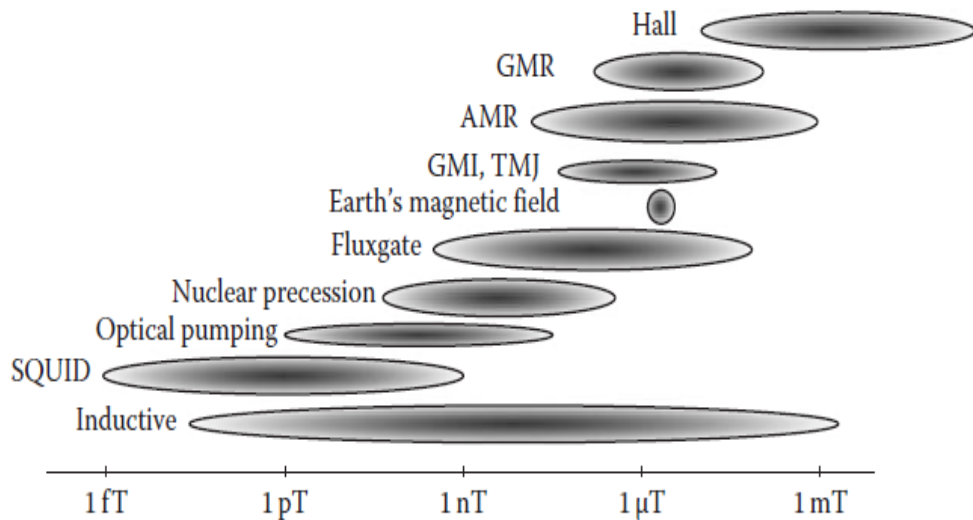
Figure 3-1: The working range of common magnetic field sensors

3.1. Search Coil Magnetometer

The concept of operation for the search-coil magnetometer is based on Faraday's law of induction. *Figure 3-2* presents the simplest design for the coil-based sensor. When the magnetic flux B through a coiled conductor varies, a voltage v induced between its leads; which is proportional to rate of change of the flux.

$$v = -n_t a_c \frac{dB}{dt} = \mu_0 n_t a_c \frac{dH}{dt} \tag{3-1}$$

Where a_c is coil area, n_t is coil's number of turns and μ_0 is permeability of vacuum. Magnetic flux inside the coil will vary if the coil is in varying magnetic field, if the coil is moved through nonuniform magnetic field, or if the coil is rotated in

uniform magnetic field. If magnetic field is varying as sinusoid $B = B_m \sin wt$ the induced voltage is: $v_{ind} = -2\pi n_t a_c f B_m$. The output signal sensed by a search-coil magnetometer is influenced by rate of change of magnetic flux through the coil, coil area, number of coil turns, and permeability of material [108].
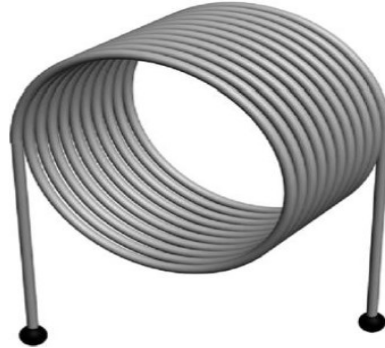
Figure 3-2: A simplest design for the coil-based sensor

The search coil magnetometer senses only varying magnetic field but it cannot sense DC magnetic fields. Theoretically, search coil magnetometer can measure magnetic fields as low as 20 fT (2 x 10^{-5} nT). Their typical frequency ranges from 1 Hz to 1 MHz [109]. For search coil magnetometer, sensitivity of sensor relies on coil dimensions; therefore, sensor should be relatively large to achieve high sensitivity. Coil diameter should be as large as feasible in case of an air coil. As a result, sensors with a diameter of more than one meter and a weight of hundreds of kilograms are needed for geophysical applications. Also, we may require search coil magnetometer for space investigations with length of about one meter [110].

For example, a three-axis search coil magnetometer was designed for space research at the scientific satellite DEMETER with number of turns of 12,200 [111]. The output signal of sensor depends on derivative of magnetic field. Therefore, it is vital to have integrating amplifier at sensor's output, and this can add noise to the output. The main applications for this types of sensor nowadays is its usage in harsh environments, i.e. stray magnetic field detection (i.e. possibly dangerous for health) [112]. It can be used also in detecting electromagnetic pollution.

3.2. Hall Effect Magnetometer

The Hall Effect magnetometer is one of the commonly used magnetic field sensors. The main concept of this magnetometer relies on Hall Effect as follows: when a current i passes inside thin conductive material sheet that is penetrated by magnetic flux density B, a voltage v is formed orthogonal to both current and field [113] (see *Figure 3-3*):

$$v = \frac{iB}{C_d q d}$$
(3-2)

where q is charge of the current carrier, C_d is carrier density and d is sheet thickness. For Hall Effect sensors, semiconductors can be used instead of metallic conductors. Because a semiconductor has fewer conduction electrons than metal, electrons in semiconductor have significantly higher drift velocity than those in metal if total current through it is the same. Practically, the electrons in semiconductors encounter a larger force as a result of their faster velocity, and the Hall voltage rises. Low-cost Hall effect sensors are commonly made of silicon. However, a more sensitive Hall Effect magnetometers can be made of gallium arsenide (GaAs), indium arsenide (InAs) and Indium antimonide (InSb). The common range of Hall Effect magnetometers is from several mT to several T, and the useful frequency range from DC to several tens of kHz [114].

Beside their basic structure, Hall effect sensors have the benefit of being compatible with microfabrication processes. Hall effect devices can be made with the common CMOS technologies, and the sensor's signal conditioning circuitry can be integrated easily with Hall effect sensor [115]. A large offset voltage at the device's output is the fundamental drawback of Hall effect sensors. The non-symmetric shape of sensor arising from misaligned layers during manufacturing, carrier concentration gradients, surface imperfections, and contact resistance changes are the main causes of this offset. For silicon Hall effects, the offset voltages can reach up to 10 mT. Another issue related to Hall Effect magnetometer is that the magnetic flux also penetrates the area enclosed by the sense wires. As a result, a voltage is induced in this area, and this limits the ability of the sensor to detect fast alternating magnetic fields. Most of the Hall sensors is used in automotive applications (i.e., ignition control, AntiBlock System, ABS). It is also used for the current control in contactless DC motors with permanent magnet [116].
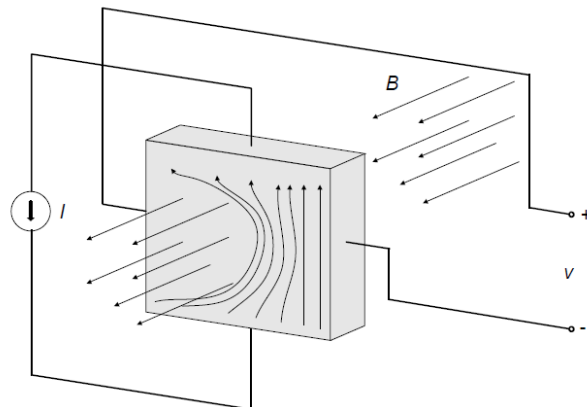
Figure 3-3: An applied magnetic field is presented, that causes the current *i* to experience a force. As a result, the density of conductive carriers is larger near one edge of the sheet, and a voltage potential *v* is induced.

3.3. Magnetoresistive magnetometers

Magnetoresistance magnetometers based on the concept that applied magnetic field can cause change in resistance (ΔR) of certain material. At this case, the magnetoresistance MR can be expressed as ΔR/R where R is the resistance when

magnetic field is zero [117]. MR values are given as percentage change in resistance per Tesla or as voltage change out per volts in per change in field.

ΔR/R is usually small. As a result, the change in DC voltage is small as well. Therefore, a bridge circuit is commonly used in order to mitigate DC offset at the output. This chapter will examine three basic types of magnetoresistance magnetometers with different mechanisms: anisotropic magnetoresistance (AMR), giant magnetoresistance (GMR), and magnetic tunnel junction (MTJ) [118].

3.3.1. Anisotropic Magnetoresistance Magnetometers

Anisotropic Magnetoresistance AMR sensors use material, whose resistance is influenced by the angle between current flow direction and magnetization. Generally, for ferromagnetic materials; the resistance decreases when the magnetization direction rotates away from current flow direction, and resistance has the smallest value when magnetization is orthogonal to current flow direction. Change in resistance can be defined as square of cosine of angle between current flow direction and magnetization [119]. *Figure 3-4* demonstrates basic principle of an AMR sensor. Supposing that the external field is in *y* direction, the magnetization rotates out of *x* direction by an angle Θ between magnetization direction and current direction, for which the change of resistance is: $\Delta R/R = -\Delta\rho/\rho \sin^2\Theta$,where $\Delta\rho/\rho$ is a magnetoresistivity coefficient.
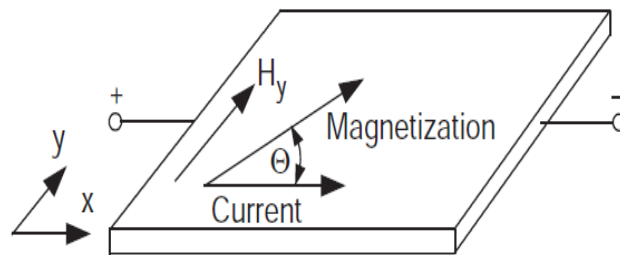
Figure 3-4: The basic principle of an AMR sensor

Thin films with an easy axis in the external magnetic field direction and thickness of about 50 nm show better AMR performance [120]. Because of these demands, AMR magnetometers are usually deposited on substrates using sputtering or evaporation process. In most cases, a thermal annealing step is required to improve the magnetic easy axis properties. The main drawback of AMR magnetometers is their relative small change in resistance (i.e. is less than 4%.) when magnetic field is applied. Another problem in AMR sensor is that, while magnetization spins in the applied magnetic field direction, it does not always point in the same direction as the field since its direction is governed by a number of factors. [121]. One factor is film geometry, where a long thin film, retains magnetization in the film plane and make it point along the film's length. Another factor is the easy axis that is controlled by applied magnetic field during film deposition.

Because AMR sensor's response is unipolar for magnetization rotation, switching the applied field's direction has no effect on the ferromagnetic thin film's resistivity value. To make the AMR magnetometer sensitive to magnetic field direction, a sequence of aluminum bars placed onto a ferromagnetic sheet so that current are forced

to pass at a 45° angle to field direction (*Figure 3-5*). This structure gives a low impedance route for the current and guides it to pass at 45° to the initial magnetization M_0 [122]. *Figure 3-6a* illustrates the relation between change in resistance $\Delta R/R$ and angle θ between current and magnetization. *Figure 3-6b* illustrates the current and magnetization direction at the ferromagnetic sheet. The magnetization M direction can be defined according to external magnetic field H_{ext}, and initial magnetization direction M_0. If H_{ext} is applied, the resulting magnetization M changes its direction, and the angle between current and magnetization changes, and so does the ferromagnetic sheet's resistance. As the current has a 45° offset towards the initial magnetization M_0, the external field H_{ext} can be defined if it is negative or positive according to a bias from this offset. Furthermore, using constant current helps in achieving linearity in the output for specific range of negative and positive magnetic field values.
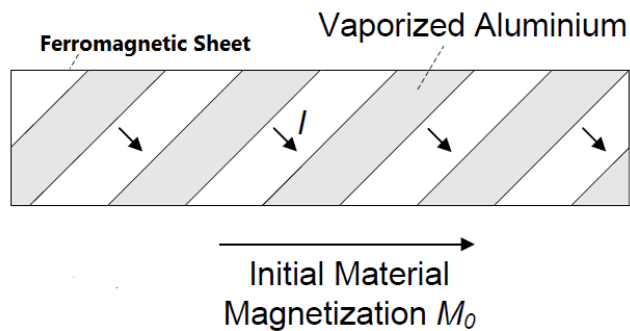
Figure 3-5: Aluminum is embedded into the ferromagnetic sheet in a 45° angle against the initial magnetization
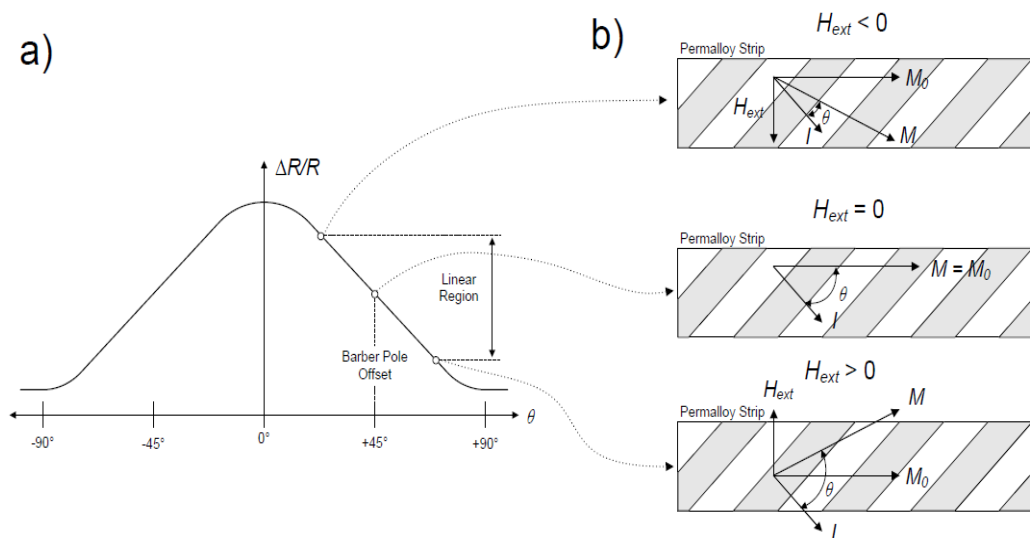
Figure 3-6: The angle between the magnetization and the current flowing through the ferromagnetic material controls the change in resistance. An external magnetic field can change material's magnetization

Because of its simple form, AMR magnetometers are commonly employed in read heads of data storage devices, and position sensing applications. They can detect magnetic fields up to 200 µT at frequencies ranging from DC to several megahertz [123]. AMR magnetometers are much more sensitive than Hall sensors, however, Due

to the thermal annealing process that contributes in producing the ferromagnetic thin film, the AMR magnetometers are difficult to be implemented with CMOS technology; instead magnetometer and electronics are implemented separately and integrated afterwards.

3.3.2.　Giant Magnetoresistance Magnetometers

The Giant magnetoresistance (GMR) Effect is another used approach to sense magnetic fields. Here, the magnetic field has an effect on resistance R of GMR magnetometer. A four-layer arrangement consisting of two thin ferromagnets separated by conductor is used to create GMR. The fourth layer is an antiferromagnet that is used to pin one of ferromagnetic layers from rotating [124].

The four-layer structure of GMR sensor is illustrated in *Figure 3-7*. The free magnetic layer magnetization is directed by the applied magentic field. The resistance R perpendicular to the layers is considerable if the free ferromagnetic layer is magnetized in opposite direction as the pinned layer (*Figure 3-7b*). When applied magnetic field aligns the free layer magnetization in the same direction as the pinned layer, the resistance is minimal (*Figure 3-7c*). The concept behind the change in the resistance R can be illustrated as follows. If the magnetizations of the two ferromagnet layers are parallel, electrons can move more readily between the layers. This is because when magnetizations are parallel, electrons experience less scattering while transitioning between the electronic band structure states of the ferromagnet layers.
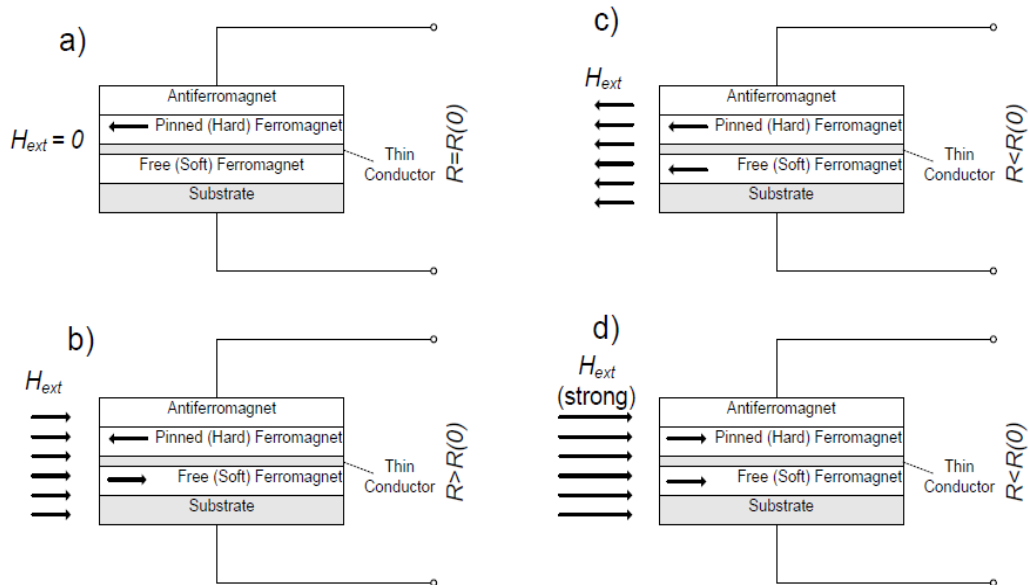
Figure 3-7: The GMR Effect's basic operating concept.

Change in resistivity between parallel magnetizations case and antiparallel magnetizations case can reach 12.8% compared with 2-4% for AMR magnetometer [125]. In other words, there is a potential to sense magnetic fields about four times less than those sensed with AMR magnetometers. That is why GMR magnetometers have been used to enhance the read heads performance in the data storage devices. GMR performance relies on the layers thickness. The change in layer thickness produces

different resistance proportional to the applied magnetic field. Generally, layers should be less than 10 nm [126].

The variety of materials that are used for GMR magnetometer help to get different ranges of operation and sensitivity values for the magnetometer. The sensor can be manufactured in an area of ~100 μm^2, and the manufacturing process is compatible with CMOS technology. The GMR magnetometer is used in many applications such as non-destructive material test, magnetic reading heads, and position sensing [127]. The current GMR magnetometers can measure fields as small as 10 nT. The main drawback of the GMR is that a relatively high applied field can unpin the pinned ferromagnetic layer and consequently change magnetometer response.

3.3.3.   Magnetic tunnel junction magnetometers

Magnetic tunnel junctions (MTJ) or spin dependent tunneling (SDT) magnetometers have similar structure as the GMR magnetometer. They also include two ferromagnetic layers separated by an ultra-thin interlayer. An antiferromagnetic layer also helps to pin the magnetization of the adjacent ferromagnetic layer from rotation. However, there are two main differences when compared to the GMR magnetometer. The first difference is that the interlayer here is an insulator (i.e., metal oxide). The second difference is that, in SDT magnetometers, the current flows due to the tunneling through the nonconducting separation layer. Thus, in the MTJ magnetometer, the electrons move from layer to the other through the insulator layer. This is why this magnetometer is called tunneling magnetoresistance [128].

Figure 3-8 shows the structure of a MTJ sensor. If no magnetic field is applied, the two ferromagnetic layers exhibit anti-parallel magnetization. This arrangement results in a low tunneling probability and, as a result, a greater resistance value. On the other hand, a parallel magnetization causes a high tunneling probability and lower resistance value.
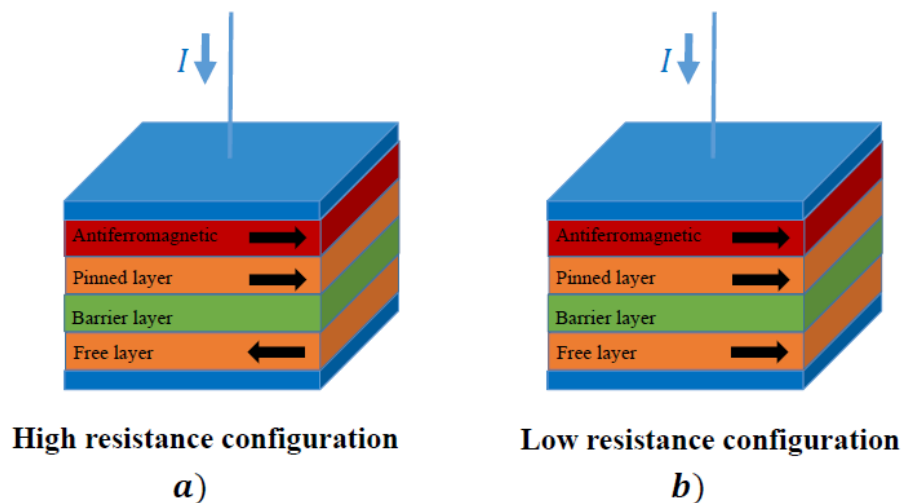
Figure 3-8: MTJ sensor structure

The magnetoresistance ratio MR or ΔR/R of the MTJ sensor is given by [129]:

$$\Delta R/R = (R_a - R_p)R_p = 2P_1P_2(1 - P_1P_2) \qquad (3\text{-}3)$$

P_1 and P_2 are spin polarizations of the two ferromagnet layers, while R_a and R_p are resistances of the antiparallel ferromagnets case and the parallel ferromagnets case, respectively. Such magnetometers have relatively large magnetoresistance (about 40%) for relatively weak magnetic field [130]. Thus MTJ magnetometers are much more sensitive than AMR and GMR magnetometers and can be made smaller than GMR sensors. However, its implementation is technically challenging while depositing the tunnel junctions. This is because the insulating layer should be thin, i.e., about 1 nm, to have an improved performance [131]. MTJ devices were acquired for reading heads, and also considered as the key element in nonvolatile random access memory (NRAM).

3.4. Giant Magnetoimpedance magnetometers

Giant magnetoimpedence (GMI) magnetometers are based on dependence of conductor impedance on applied magnetic field [132]. Compared to other magnetoresistance magnetometers, GMI can be defined as a complex impedance structure. To utilize the GMI effect to measure magnetic fields, GMI sensor may be put in an oscillator structure. By this way, the impedance of the GMI sensor will affect the oscillator frequency [133]. Furthermore, the implementation of sandwiched magnetic layers as the GMI structure enhances the magnetometer performance, but, at the same time, this will increase the manufacturing complexity [134]. The GMI magnetometer exhibits a relatively high impedance ratio that could reach several hundred %. Thus, The GMI magnetometers are more sensitive than AMR and GMR sensors. This contributes in using the GMI magnetometer in biomedical applications, and automation industry [135].

3.5. Fiber-optic magnetometer

Fiber-optic magnetometer employs a Mach–Zender interferometer using two glass fibers arrangement as shown in *Figure 3-9*. In this arrangement, a laser produces light that reaches a beam splitter. The light then propagates into the two fibers, and detected by a photodetector at each fiber end. For magnetic field sensing, one of the fibers will be either wrapped around or coated with magnetostrictive material, whose dimensions change according to magnitude and direction of its magnetization [136]. Therefore, fiber length alters if magnetostrictive material is magnetized by an applied field. Due to change in the fiber length, light propagates through the fiber will be out of phase with light coming from the reference fiber. The two light beams interference makes light level at the photodetector to differ by a value that is dependent on the phase difference. It was demonstrated that path length changes of about 10^{-13} m can be recognized with this type of sensors [137]. Electroplating magnetostrictive materials onto fibers has been illustrated, and the sensitivity range of the fiber-optic magnetometer from 10^{-2} to 10^6 nT. The fiber-optic magnetometer may be used to detect either constant fields or varying fields with frequencies below 60 kHz [138]. A common length for this magnetometer can be about 1m long, and may be used to in submarine detection, and ships traffic exploration.
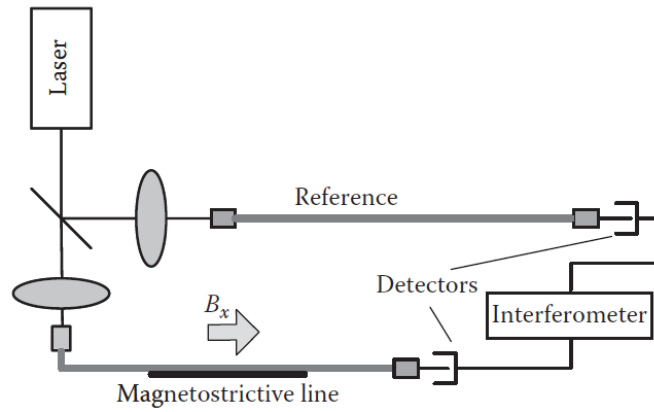
Figure 3-9: The fiber-optic magnetometer

3.6. Magnetoelectric Magnetometer

Another technique for sensing the magnetic field at certain direction is through the magnetoelectric (ME) effect [139]. The magnetoelectric effect is the change in electric field of material when a magnetic field is applied. *Figure 3-10* illustrates a basic structure of a magnetostrictive/piezoelectric composite *ME* magnetometer. It consists of interlayer layer of piezoelectric material between two layers of magnetostrictive material. By this configuration, the strain of the magnetostrictive layer is coupled to the piezoelectric layer. In the presence of magnetic field, the change in the dimensions that is induced in magnetostrictive layer due to magnetic field is converted into a voltage in piezoelectric layer. Electric field (E) resulted from applying a constant magnetic field (H_{dc}) can be written as:

$$E = \alpha_E H_{dc} \qquad (3\text{-}4)$$

where α_E is the Magnetoelectric coeffcient. Moreover, the voltage that is induced at the surfaces of a piezoelectric layer of thickness of d can be defined as [140]

$$v_{ME} = d\, E = \alpha_E\, d\, H_{dc} \qquad (3\text{-}5)$$

The Magnetoelectric voltage coefficient $\partial V_{ME}/\partial H$ dependes on the applied magnetic field H_{dc}. Magnetoelectric magnetometer has a simple structure, and a small size. A magnetoelectric magnetometer consists of two layers of a magnetostrictive material (TERFENOL-D) sandwiched between piezoelectric layer of a material (Pb $(Mg_{1/3} Nb_{2/3})$ O_3 $PbTiO_3$) has the ability to sense changes in the magnetic field in the pT range [141].
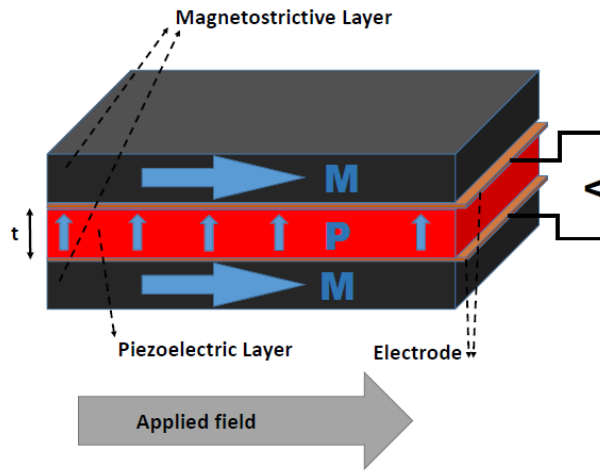
Figure 3-10: Schematic diagram of magneto-electric sensing element

3.7. Magneto-Optical Magnetometer

Magneto-optical magnetometer exploits Faraday Effect to sense magnetic field. Faraday Effect describes the phenomena of rotation of a polarized light plane when it passes across magnetic material. Faraday effect arises from that material's refractive index is different depending on weather the electrons precess about the magnetic field in the opposite or same direction [142]. The effect is highest if propagation direction of the light aligned with the applied magnetic field.

Generally, polarized light consists of two circularly polarized waves; clockwise (CW) and counterclockwise (CCW). The polarization plane rotates due to change in relative phases of CW and CCW waves. *Figure 3-11* illustrates the structure of magneto-optical magnetometer. The polarized light is propagated through a fiber to the magnetometer. Then, when magnetic field is present, polarization direction is rotated by an angle β which is related to the applied magnetic field with Verdet constant V_d [143]:

$$\beta = V_d l. B \tag{3-6}$$
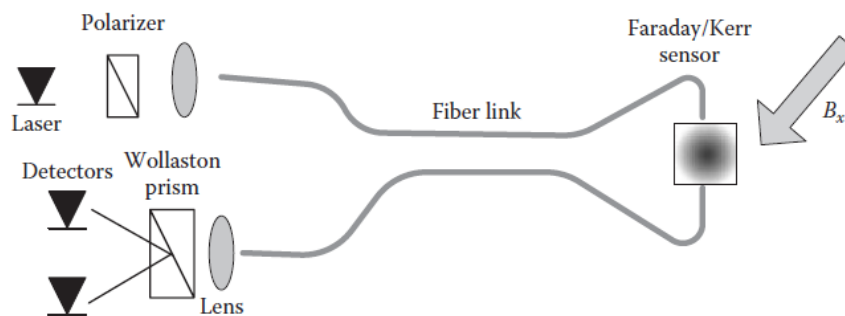
Figure 3-11: The basic circuit of magnetooptical magnetometer

After Wollaston prism, the phase difference between the two circularly polarized beams, after they gone across the magnetically optic material, are detected. Phase

difference can be defined as $2BVl$, where l is the optical path length in the magnetically optic material. At the detector, the phase difference causes interference fringes that can be measured as a ratiometric quantity. Typical magneto-optic materials for magnetic field detection are terbium gallium garnet, and yttrium iron-garnet (YIG). The magneto-optical magnetometer has a very fast response time. Therefore, these magnetometers are used to measure extremely high fields of short duration (e.g., a contactless current sensors in high voltage lines) [144].

3.8. Magnetotransistors and Magnetodiodes

A magnetodiode is, in principle, a diode. However, here, the *p* region is separated from *n* region by undoped silicon layer. The device is based on a sapphire substrate, on which silicon is deposited, and then silicon dioxide is deposited afterwards. If a negative potential is present at metal contact on the n-doped area and a positive potential is present at metal contact on the p-doped area, holes in the *p*-type area and electrons in the *n*-type area will be injected into the undoped silicon layer. Total current will be sum of electrons current and holes current [145].

Some of the carriers will recombine, especially those near silicon-silicon dioxide interface or silicon-sapphire interface. As a result, the material's resistance rises due to the loss of charge carriers. When there is no magnetic field, Recombination at both interfaces leads to resistance. When magnetic field is applied orthogonal to travel direction of charge carriers, it deflects holes and electrons either up or down, according to field direction.

Because they are going in opposing directions, both holes and electrons are deflected in the same direction. As a result, if magnetic field deflects the charge carriers down, the material's resistance rises; if it deflects them up, the resistance falls. [146]. Magnetodiode response to magnetic field is around ten times higher than Hall effect magnetometer response.

The Magnetotransistor is simply a version of an *npn* transistor. The difference is that instead of one collector for the transistor, there are two at the magnetotransistor. [147]. When there is no applied magnetic field, the charge carriers arrive in equal amounts to both collectors. If there is an applied magnetic field orthogonal to charge carriers' travel direction, they will be deflected toward one collector or the other, according to magnetic field direction. The voltages from the two collectors are fed to difference amplifier, which produces an output proportionate to the applied magnetic field. [148]. This is called the Suhl effect, where an applied magnetic field induces a variation in travelling carriers' trajectory, causing difference in current distributions recorded between collector outputs. Magnetotransistor response is assumed to be 100 times more than Hall-effect magnetometer [149].

3.9. The SQUID magnetometer

The Superconducting Quantum Interference Device (SQUID) magnetometer is based on the interactions of magnetic fields and electric currents that occur if specific materials are cooled down to their superconducting transition temperature. These materials become superconductors at this temperature and lose resistance to electric current flow. For a superconducting ring sample, a current is induced in the ring if a magnetic flux becomes threaded across the superconducting material ring. Generally,

the current could continue to flow forever if there are no any other disturbances. The induced current magnitude can be considered as sensitive indication to magnetic flux density. Typically, the magnetic flux across the superconducting ring is quantized [150], and can be represented by the relation:

$$\psi + 2\pi \frac{\varphi_{in}}{\varphi_0} = 2\pi z \tag{3-7}$$

where φ_0 is magnetic flux quantum. The angle ψ is phase difference between wave functions of electrons in pair, and z is the step number. The magnetic flux quantum (fluxon) relies only on physical constants, i.e., $\varphi_0 = \frac{h}{2e} = 2.067833667 \times 10^{-15} \, Wb$, where h is Planck's constant; and e is electron charge. For a ring of 1 cm^2 cross section, flux quantum equals to flux density of 2.067×10^{-11} T. Thus, SQUID magnetometer is usually employed for very low magnetic fields sensing [151]. For SQUID, the current inside the ring can be determined as:

$$i_s = I_c \sin \left(\frac{2\pi\varphi_{in}}{\varphi_0} \right) \tag{3-8}$$

The current I_c is a parameter defined as the *critical current*—if the current overcomes this value, the superconducting effect disappears. If a ring of an inductance L is placed in external magnetic φ_{ex} field, the internal flux is $\varphi_{in} = \varphi_{ex} - Li_s$, [152] and

$$\varphi_{in} = \varphi_{ex} - LI_c \sin \frac{2\pi\varphi_{in}}{\varphi_0} \tag{3-9}$$

Typically, the SQUID's output is triangle wave with each cycle equivalent to magnetic flux quantum. Therefore, the external magnetic field can be computed in terms of the number of cycles. Currently, SQUIDS are used for measuring very weak magnetic fields produced by various organs of living objects (e.g., human brain or heart) in biomagnetic studies [153]. It can be also used for measurements of samples' magnetic properties that are either small or very weak magnetically. Direct measurements of magnetic properties of thin films are one of the applications of SQUID magnetometers. SQUID also a promising candidate to be involved in quantum computing experiments [154].

3.10. Resonant Magnetic Field Magnetometers

The resonant magnetic field magnetometers based on Lorentz force operation principle. Lorentz force actuates a resonant structure, increases its displacement, causing a bending in its planar frame [155]. A resonant structure exhibits an amplified response when frequency of the applied excitation source is equal to resonant frequency(ies) of the structure. Therefore, a resonant sensor employs a structure that operates at one of these frequencies (typically first frequency or vibration mode is the commonly used) [156]. *Figure 3-12a* shows a clamped-clamped beam resonant structure. When the beam is experienced an excitation source at frequency equivalent to its first resonant mode, it will have a maximum deflection at its midpoint as shown in *Figure 3-12b*. The excitation source for resonant magnetic field sensors can be a

Lorentz force that arises because of the interaction between applied magnetic field and alternating excitation current. At this case, an aluminum sheet is put on clamped-clamped beam surface and excitation current i with frequency equivalent to first beam-resonant frequency flows inside it (*Figure 3-12c*). By this configuration, a Lorentz force (F_L) is induced when the beam experienced a magnetic field. This force can be defined as [157]:

$$F_L = i\, H_x\, L_y \qquad\qquad (3\text{-}10)$$

where L_y is the length of aluminum sheet in the orthogonal direction of magnetic field. Here, Lorentz force works as an excitation source, creating an amplified deflection on midpoint. Beam deflection magnitude relies on Lorentz force magnitude, which is related to excitation current and the applied magnetic field. This deflection can be sensed via piezoresistive, optical, and capacitive sensing techniques.
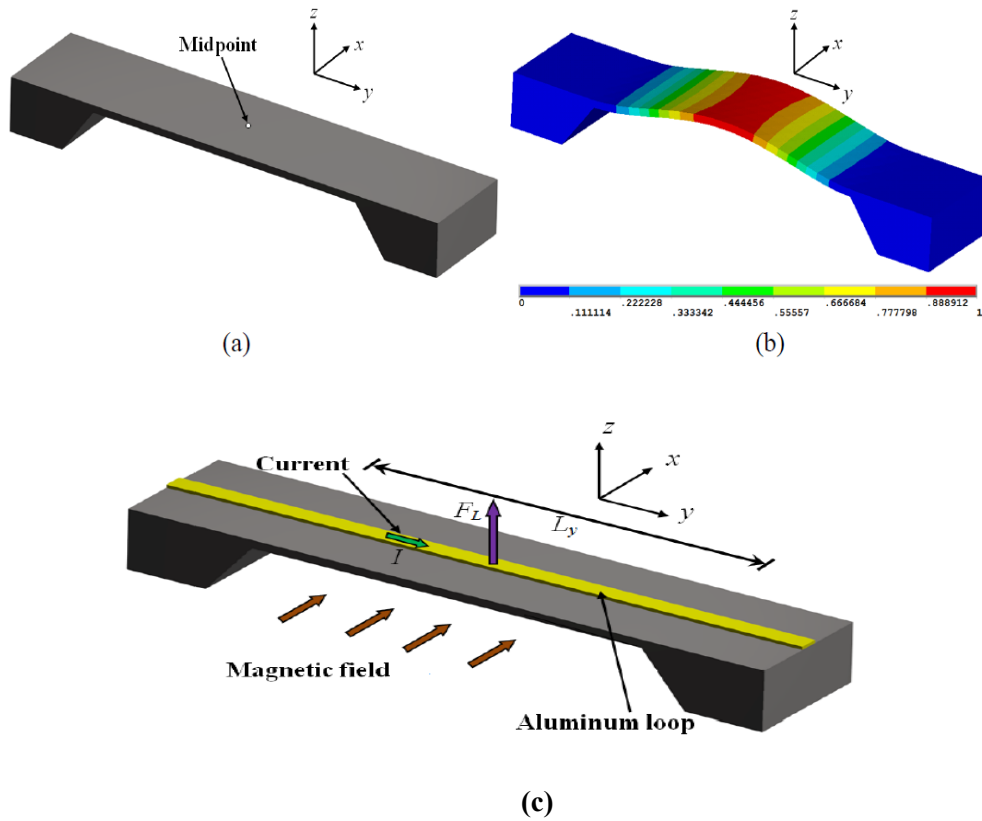
Figure 3-12: (a) Resonant structure beam, (b) its first vibration mode, and (c) the force generated upon it

Figure 3-13 depicts resonant magnetic field magnetometer with piezoresistive sensing. Two U-shaped clamped-free microbeams are joined to silicon substrate to form the structure. The magnetometer employs piezoresistive sensing using Wheatstone bridge. It includes two active piezoresistors (put on the microbeams) that can shift their resistance values, and two passive piezoresistors (deposited on the substrate) that have fixed value resistances [158]. Excitation current is flowing through the aluminum sheet

at microbeams' resonant frequency. If the structure is subjected to applied magnetic field, a Lorentz force is generated, and induces longitudinal strain (ε_x) on the two active piezoresistors causing their resistance values to change as [159]:

$$\Delta R = G_p \, \varepsilon_x \, R \tag{3-11}$$

where ΔR is change in resistance of each active piezoresistor, G_p is piezoresistors gauge factor, and R is resistance of each piezoresistor. Variation in active piezoresistors' resistance induces an output voltage (V_{out}) at Wheatstone bridge, defined as:

$$V_{out} = \frac{\Delta R}{2R + \Delta R} \, V_{bias} \tag{3-12}$$

where V_{bias} is bias voltage of Wheatstone bridge. Accordingly, magnetic field amplitude is acquired via output voltage of the Wheatstone bridge. Advantages of using Piezoresistive sensing include simplicity, and conformity with MEMS technology [160].
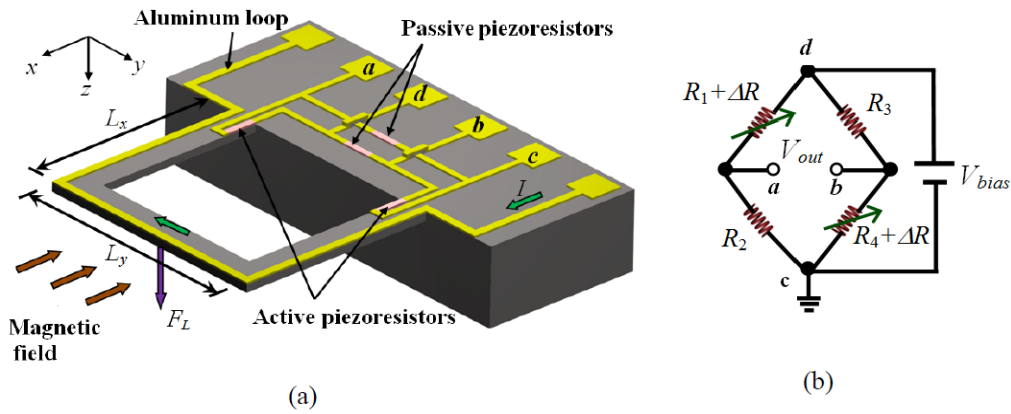
Figure 3-13: (a) Resonant structure for magnetic field sensing using piezoresistive elements, and (b) the Wheatstone bridge [158]

Figure 3-14 shows resonant magnetic field magnetometer with optical sensing. The structure composed of rectangular microbar supported by four microbeams. An alternating current i is applied at resonant frequency in the presence of magnetic field, resulting in Lorentz force that deflects the microbar. This deflection is detected optically by using laser, as the deflection of the reflected light beam is measured using position sensitive detector. By this way, deflections are related to the applied magnetic fields [161]. Advantages of using optical readout technique are electronic circuitry reduction and light weight. However, optical sensing can require complex manufacturing processes [162].
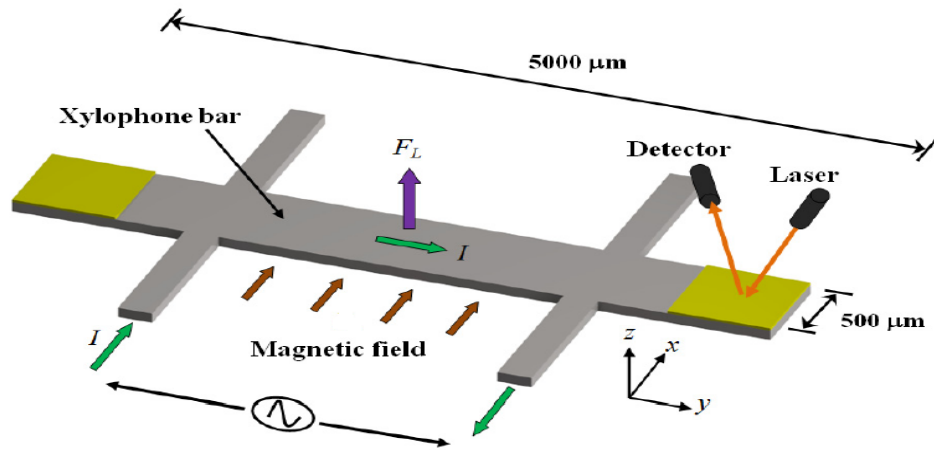
Figure 3-14: Resonant structure for magnetic field sensing using optical readout technique

Figure 3-15 shows resonant magnetic field magnetometer with capacitive sensing technique. It includes movable conducting microbeam, movable comb, and fixed finger electrodes. The Lorentz force is induced on the conducting beam as an alternating current goes across it while a magnetic field is applied. Accordingly, the movable electrodes will shift their distances with respect to fixed electrodes and capacitance value will change. Thus, magnetic field is sensed using the capacitance variation [163]. The capacitive readout technique could suffer from parasitic capacitances at the connecting leads, and this can affect the output measurements. Additionally, capacitive sensing demands complicated electronic circuits [164].
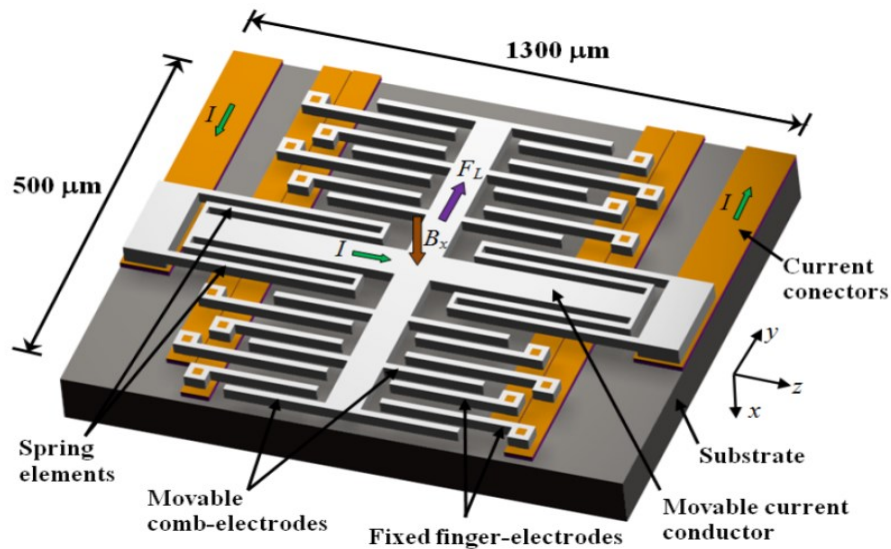
Figure 3-15: Resonant structure for magnetic field sensing based on capacitive variation technique

3.11. Fluxgate Magnetometer

Fluxgate magnetometer principle of operation relies on the variation of the magnetic material's permeability of its core. The permeability of the magnetometer's core is taken into a dynamic state by an ac current applied to the sensor. At a dynamic state, the fluxgate core's permeability is sensitive to an applied magnetic field and changes with it. Permeability variation associated with variation in the applied magnetic field affects magnetic flux inside fluxgate core. The changes of magnetic flux are detected through an induced voltage, where its value is related to ambient magnetic field and represent magnetometer output [165].

Fluxgate basic scheme, is illustrated in *Figure 3-16*, includes an excitation (driving) coil and sensing (pick-up) coil, wrapped around high permeability soft magnetic core that represents fluxgate's sensing element. The excitation current I_{exc} flows inside the excitation coil generates magnetic field that saturates soft magnetic material of the magnetometer core (i.e., the core reaches its saturation magnetization in both directions). Meanwhile, the external magnetic field B_{ex} is guided inside the core creating a high magnetic flux because of high permeability of the soft magnetic material. Thus, permeability of the fluxgate magnetic core is modulated during its operation, which creates changes in the flux, and hence the gated flux induces voltage in the sensing coil V_{out}. That why this device is named as "fluxgate" as the device's sensing element gating flux "in and out" of the sensing coil. A basic formula for fluxgate output voltage is [166]

$$V_{out} = -N_s S \mu_0 H \frac{d\mu_r(t)}{dt} \tag{3-13}$$

where N_s is number of turns of pick-up coil, S is core's cross-section, H is the measured field, and μ_r is relative permeability of the core.
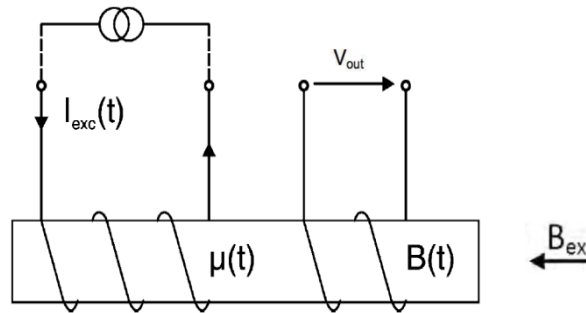
Figure 3-16: The basic structure of fluxgate magnetometer

Fluxgate sensors sense magnetic fields between 10^{-10} to 10^{-4} T with a proper linearity. They are suitable for measurements with resolution on the order of 1 nT [167]. Fluxgate magnetometers are approximately five orders of magnitude more sensitive than other solid-state magnetic sensors, such as Hall-effect magnetometers. In contrast to induction magnetometers, which only detect field changes, fluxgate magnetometers can detect the dc magnetic field as well. Furthermore, Fluxgates also measures magnetic field direction, compared with scalar measurements of nuclear resonance magnetometers. When compared to optical-fibre magnetometers, fluxgate magnetometers are more sensitive to measured field and less susceptible to vibration

fluctuations. Also, Fluxgate magnetometers are significantly less expensive than (high sensitive) SQUID that suffers from the bulk size and the need to liquid helium for cooling [168]. Fluxgate sensors are employed in geophysical studies, as it is used for measuring Earth's magnetic field variations. Portable Fluxgate sensors contribute in detection of local magnetic field anomalies through field and airborne measurements. Fluxgate sensors are commonly used in cars and aircrafts industries. The fluxgate principle is also employed for indirect measurement of current flow in pipelines; determine the ferromagnetic bodies' location, detection of submarines and missile guidance [169]. When compared to other magnetometers, the fluxgate sensor shows to be better to achieve accurate vector magnetic field measurements, due to its endurance versus magnetic shocks. The main drawback of fluxgate magnetometer is the challenges that face the manufacturing of its sensing element and the associated coils [170].

3.12. Total Field Magnetometers

Unlike vector magnetometers, which sense only magnetic field component that lies along the sensitive axis, total field magnetometer senses total magnetic field, regardless of direction [171]. Total field magnetometers take advantage of the fact that splitting between some nuclear or electron spin energy levels is related to magnetic field magnitude. There are two main designs of the total field magnetometers: nuclear precession magnetometer and optical pumping magnetometer [172]. The nuclear precession magnetometer depends on that hydrogen atom nucleus, a proton, has magnetic moment related to angular momentum of its spin. As angular momentum is quantized, magnetic moment of the proton may only have certain values that are multiples of fundamental unit called nuclear magneton. Gyromagnetic ratio (γ_p) of the proton is defined as ratio of magnetic moment to spin angular momentum. It is a constant with value $\gamma_p = 2.67513 \times 10^8$ s^{-1}T^{-1} [173].

Figure 3-17 shows the operation of the nuclear precession magnetometer. It consists of a container filled with proton-rich liquid. Around the container, a magnetizing solenoid and a sensing coil are wrapped. The same solenoid can be used alternately for magnetizing and sensing. When current in the solenoid is switched on, it generates magnetic field of order of 100 mT that is around 2000 times higher than Earth's field. As a result, magnetic field causes an alignment of protons magnetic moments along the axis of the solenoid. After magnetic field is switched off, magnetic moments of the proton spins react to the force applied on them by the Earth's magnetic field. Like child's top spinning in the gravity field, magnetic moments of the proton precess about the ambient magnetic field direction, with rate known as Larmor precessional frequency f_L. Magnetic moments precession induces current in the sensing coil. The induced signal is amplified electronically and the processional frequency is then computed. The measured magnetic field is proportional to the processional frequency, and is given by [174]:

$$B_t = \frac{2\pi}{\gamma_p} f_L \qquad (3\text{-}14)$$
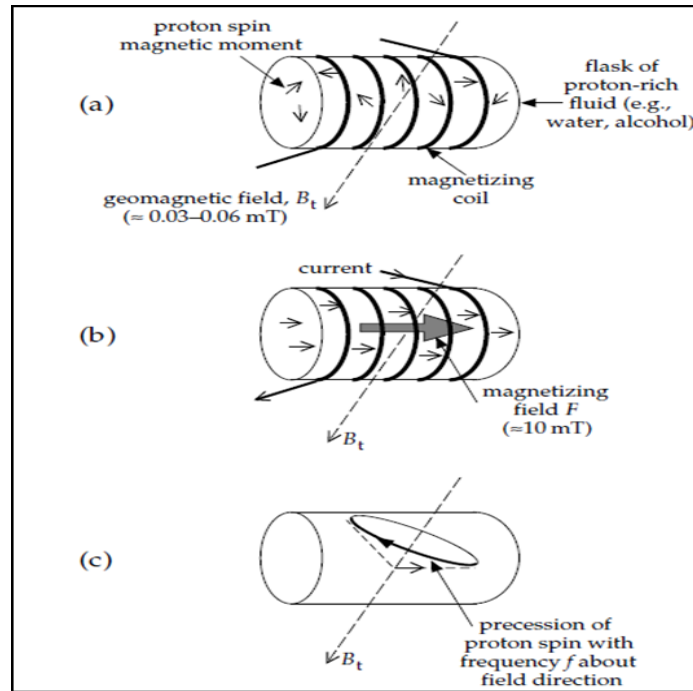
Figure 3-17: (a) Nuclear precession magnetometer components, (b) Current in the coil creates a field F that aligns protons spins, (c) As field F is off, proton spins precess about the magnetic field producing current in the coil at Larmor precessional frequency [175]

Optically pumped magnetometer is another design of the total field magnetometers. The operation principle relies on quantum-mechanical model of the atom [176]. The electrons of an atom occupy concentric shells around nucleus with different energy levels, where electron lowest energy level is its ground state. According to an applied magnetic field, magnetic moment associated with electron spin can be either parallel or anti-parallel, where the electron energy is different in each case. This causes splitting of the ground state into two sublevels with slightly different energies. This energy difference is proportional to magnetic field strength. Energy levels splitting in the presence of a magnetic field is called the Zeeman effect [177].

Optically pumped magnetometer utilizes Zeeman effect in vapors of elements which have only a single valence electron in the outer most energy shell. *Figure 3-18* shows a schematic representation of an optically pumped magnetometer. A polarized light propagates via an absorption cell that contains helium vapor and falls on a photodiode that senses the light intensity. At the Earth's magnetic field electrons precess about direction of the field with Larmor precessional frequency. At one part of the processional cycle an electron spin is nearly parallel to field direction and one half-cycle later it is almost anti-parallel [178]. This is sensed by photodiode and converted to a current. Strength of the measured magnetic field B_t that causes the ground state splitting is proportional to Larmor frequency, and is defined as [179]:

$$B_t = \frac{2\pi}{\gamma_e} f_L \qquad\qquad (3\text{-}15)$$

γ_e is defined as the electron gyromagnetic ratio, which is almost 1800 times larger than γ_p, the proton gyromagnetic ratio.
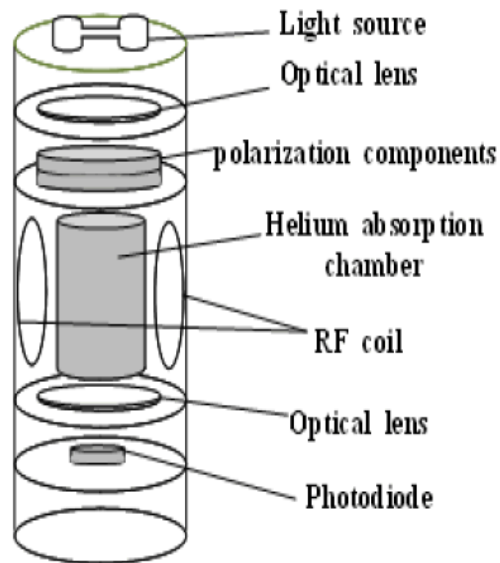
Figure 3-18 Structure of helium optically pumped magnetometer

Chapter 4 : Fluxgate Magnetometer

Fluxgates are magnetic field sensors that have a wide range of applications where determining magnetic field along a certain direction is required. As the name implies, all forms of fluxgates are relies on the magnetic flux gating inside its sensing element to produce output related to applied magnetic field. Therefore, sensing element of the fluxgate, i.e., its core, contains a high permeability soft magnetic material which is periodically saturated by an excitation current at certain frequency. Although the operating concept of fluxgate magnetometer appears to be uncomplicated, several details are critical, and should be put into consideration to attain a satisfactory sensor performance in general.

In this chapter the principle of operation of the fluxgate sensor will be analyzed. Then, the mechanisms which generate the sensor's output signal will be explained. Next, a few details about electronic circuits of fluxgate sensors will be discussed. After that, the main configurations of the fluxgate sensors will be detailed, along with their most used geometries.

4.1. Principle of Operation

The fluxgate operation principle can be illustrated with the simple layout in *Figure 4-1*. This fluxgate magnetometer immersed in an external magnetic field with two coils around its sensing element. If there is no external magnetic field, magnetometer reading corresponds exclusively to the magnetic field produced by the excitation coil at certain frequency. In practical, the magnetometer output is voltage equal to sum of several odd harmonics of excitation frequency. If external magnetic field is applied, even harmonics are added to magnetometer reading as well. As a result, these even harmonics amplitudes can be utilized to represent the external magnetic field intensity [180].
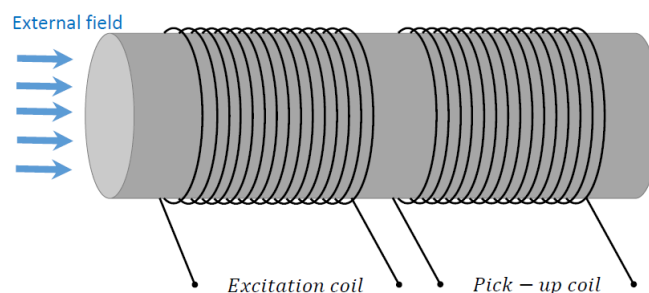
Figure 4-1: Basic configuration of a fluxgate magnetometer

Responses of fluxgate magnetometers are limited by the excitation parameters that are provided to its sensing element and the dimensions of its sensing element including the geometrical aspects of the soft magnetic material inside the core. The induced voltage V_{out} in pick-up coil that is produced due to variation of the magnetic flux (B) can be defined generally as [181]:

$$V_{out} = -\frac{dB}{dt} = -N_s S \frac{dB(t)}{dt} = -N_s S \frac{d}{dt}\left(\frac{\mu\, N_e\, I_0 sin(2\pi f_e t)}{l_c}\right) \qquad (4\text{-}1)$$

where N_s is number of turns of the pick up coil, , S is sensing element cross section, N_e is number of turns of excitation coil, l_c is excitation coil length, μ is magnetic permeability, and $I_0 sin(2\pi f_e t)$ is sinusoidal excitation current at frequency f_e.

It should be noted here that the fluxgate's output relies on the magnetic field's derivative, dB/dt, rather than the magnetic field itself. As a result, the fluxgate's output is frequency dependent. Also, it should be highlighted that the above equation $V = f(B)$ did not involve material features (i.e. the nonlinear magnetic features of the ferromagnetic core material). Thus, another equation can be used to represent output signal of fluxgate as [182]:

$$V_{out} = \frac{N_s S \, \mu_0 \mu_r \, dH(t)}{dt} + \frac{N_s S \, \mu_0 H d\mu_r(t)}{dt} \qquad (4\text{-}2)$$

Where μ_r is relative permeability, μ_0 is vacuum permeability, N_s is number of turns in pickup coil, S is core's cross sectional area, and H is the field in the core material. The fundamental induction effect is represented in the first term in equation (4), and, here, it is considered as a source of interference. Fluxgate operation depends on the second term, which describes variation of core permeability due to nonlinear magnetic nature of the soft magnetic material. The output of the fluxgate is always extracted from the second harmonic component. Thus, the fluxgate is commonly named as the second harmonic fluxgate magnetometer.

However, it should be highlighted that the second harmonic readout strategy is not the only extraction technique used for fluxgate output. Recently, a time domain readout strategy for extracting the fluxgate output is introduced. The working principle of this technique exploits the inherent nonlinear nature of the ferromagnetic core dynamics; represented by the hysteresis loop. Therefore, before proceeding in explaining the new readout strategy named "residence times difference", an insight of the hysteresis behavior from the energy standpoint, should be provided. Hysteretic behavior can be represented as consequence of minimum energy movement versus magnetic field. In *Figure 4-2*, field is cycled in a clockwise manner, and minimum energy is shown for several field values, where hysteresis is described to be result of asymmetric behavior of energy versus magnetization as the field is cycled [183].

A simplified layout of Residence Times Difference (RTD) fluxgate magnetometer with two-coil assembly is illustrated in *Figure 4-3*. A time-periodic magnetic field H_e will be induced, when a time-periodic current I_e flows in the excitation coil. Here, the dynamical response of the fluxgate's core (i.e., sensing element) is originated from a bistable potential energy function $U(x)$. The double-well potential energy function is tightly connected to micromagnetic phenomena and is, generally, calculated by estimating collective motion of core's domain wall; the dynamics can be represented via the potential energy function [185]:

$$U(x) = \frac{x^2}{2} - \frac{1}{c_n}\ln cosh\, [c_n(x + H_e(t) + H_x)] \qquad (4\text{-}3)$$

where H_e describes the sinusoidal excitation magnetic field and H_x describes the applied magnetic field to be sensed. Here, $x(t)$ represents normalized magnetization, while c_n is a nonlinear parameter that controls potential function $U(x)$ topology.
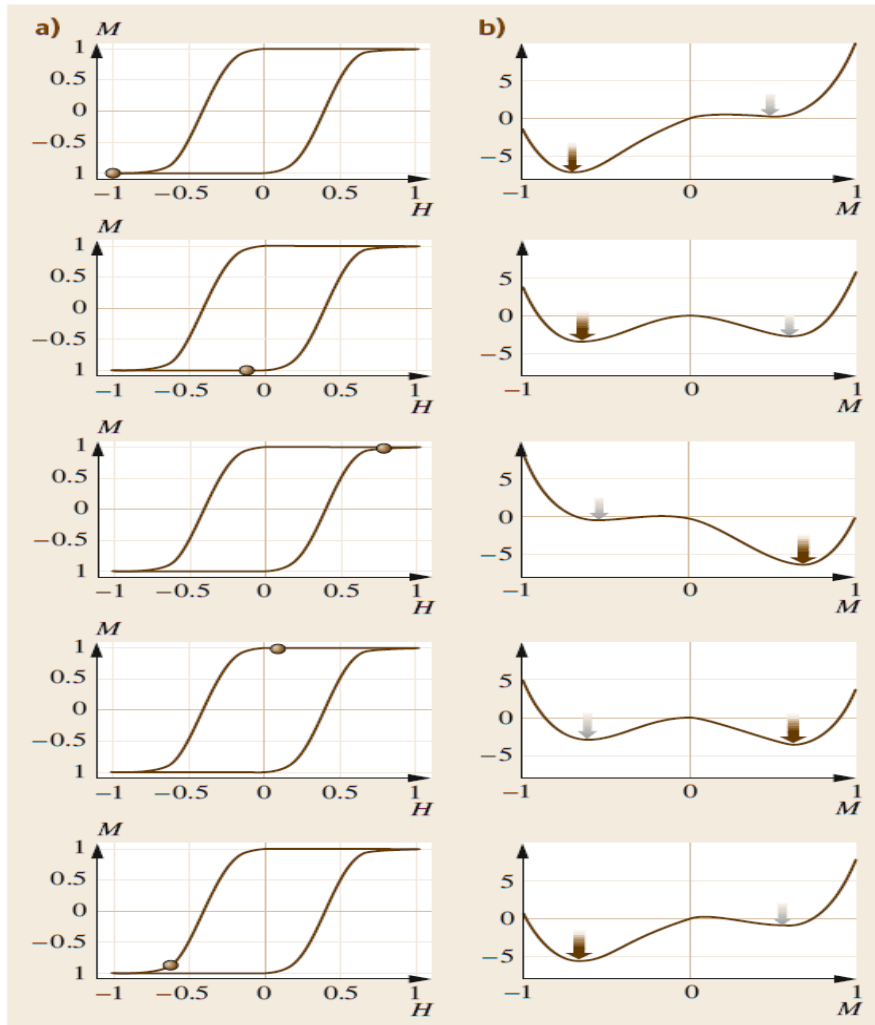

Figure 4-2: (a) Hysteresis loop, and (b) energy as a function of magnetization. When field changes along the hysteresis loop, represented by the round spot, in a clockwise manner, the energy varies its form and its absolute minimum, represented by the thick arrow, moves consequently [184].
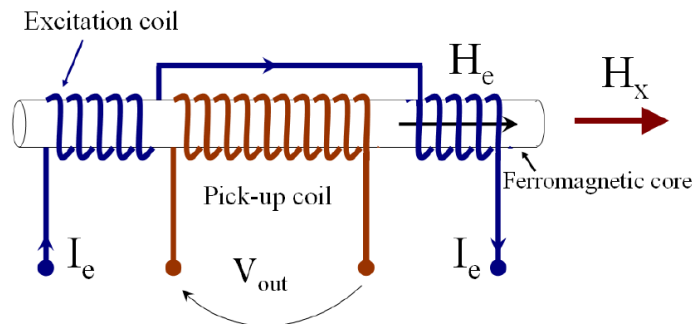

Figure 4-3: Residence Times Difference (RTD) fluxgate magnetometer

Thus, dynamical behavior of (normalized) magnetization $x(t)$ inside fluxgate's core can represented as partial derivative of double-well potential energy function with respect to magnetization x:

$$\tau \frac{dx}{dt} = -x + tanh\left[\frac{x+H_e(t)+H_x}{Q}\right] \equiv \frac{\partial U(x,t)}{\partial x} \qquad (4\text{-}4)$$

where τ is time constant of the system, and Q is the temperature dependent control parameter. *Figure 4-4* depicts a qualitative relation between hysteresis loop and potential energy function $U(x)$. For soft magnetic core, two saturation states of hysteresis loop correspond to two stable states of potential function $U(x)$.

In order to switch magnetization of the core from one steady state to the other, resultant field inside the core $H(t) = H_e + H_x$ have to go over the positive and negative coercive fields (Hc and $-Hc$), so that magnetization x moves between its stable saturation states. At least, time-periodic excitation field $H_e(t)$ must have intensity just enough to trigger the switching between the steady states in the absence of any external magnetic field. Time intervals when magnetization parameter "resides" in the two stable states are known as "residence times" [186]. Residence times difference concept is built on observation of these time intervals (i.e., the residence times) that core magnetization spends in the two stable states (i.e., the two saturated states of the core's hysteretic loop). Residence time differences can be calculated from pickup coil voltage, which is related to the first time derivative of the magnetic flux (whose form is a two-state waveform, i.e., a square wave) and, hence, corresponds to a "spike train". The RTD-fluxgate readout strategy depends on utilization of information provided by time position of spikes in output voltage signal [187].
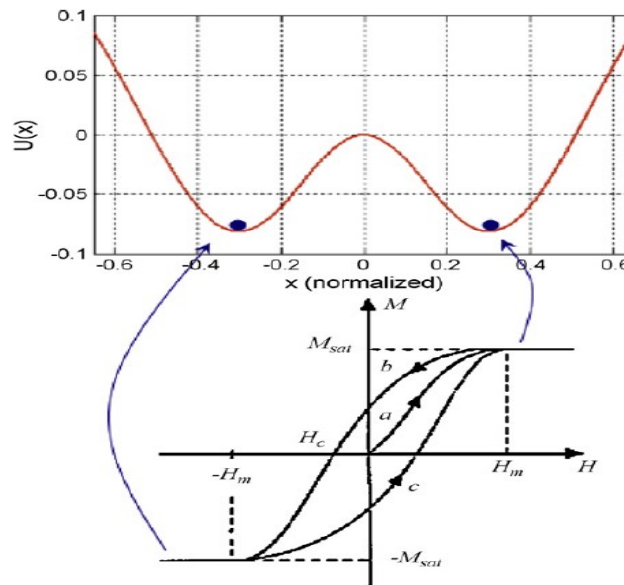
Figure 4-4: The two stable states of magnetization along the potential function and the hysteresis loop

In order to clarify RTD readout concept, *Figure 4-5* illustrates time intervals, $T+$ and $T-$, corresponds to the interaction between excitation magnetic field (H_e) and coercive field ($\pm H_c$). They are known as Residence Times, and stand for the times spent

by core magnetization in the two (stable) steady states. As a result, residence time in right well $T+$ of potential $U(x)$ can be described as the time interval elapsed between crossing of upper Hc level (at time t_1) and the successive crossing of lower Hc level (at time t_2). Residence time in left well $T-$ is described as the time interval between lower threshold crossing (time t_2) and upper threshold crossing in the next period of bias signal (at time t_3).
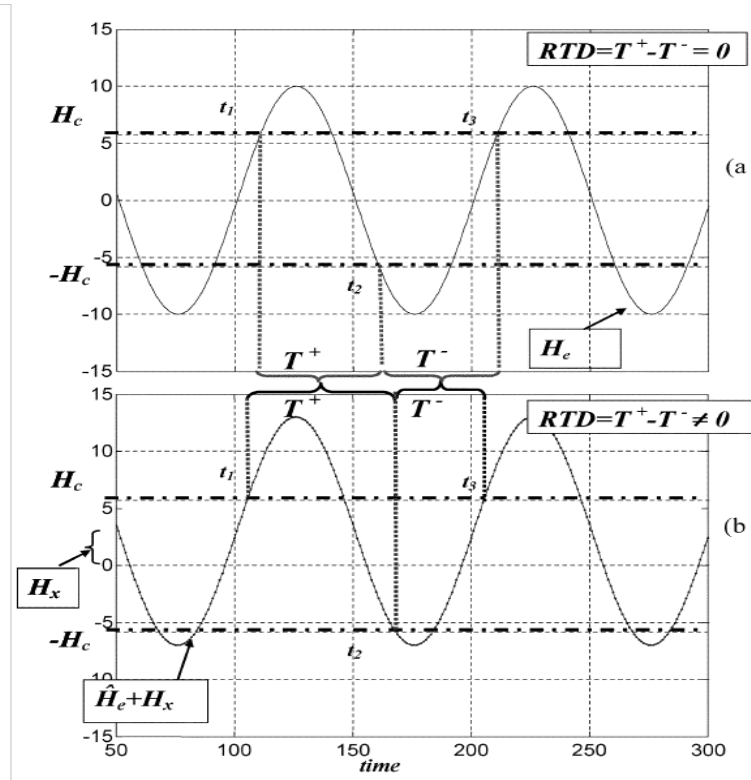
Figure 4-5: RTD fluxgate readout strategy [188]

The Residence Time Difference is the quantity $RTD = T^+ - T^-$. If there is no external magnetic field, hysteresis loop (or the corresponding potential energy function) is symmetric and two identical residence times are attained leading to RTD = 0. Then, presence of external magnetic field causes skewing of hysteresis loop with direct impact on residence times; they become non-identical, i.e. RTD $\neq$ 0. To develop an expression for the time interval $RTD = T^+ - T^-$, expressions for T^+ and T^- are required. Considering residence times definition, the threshold crossing times t_1, t_2, and t_3 can be defined as [189]:

$$t_1 : H_x + H_e(t_1) = H_c \tag{4-5}$$

$$t_2 : H_x + H_e(t_2) = -H_c \tag{4-6}$$

$$t_3 = t_1 + \tau \tag{4-7}$$

For a sinusoidal magnetic field of magnitude $\widehat{H_e}$ and frequency $1/\tau$, we obtain:

$$H_x + \widehat{H_e} \sin(wt_1) = H_c \qquad\qquad (4\text{-}8)$$

$$H_x - \widehat{H_e} \sin\left(w\left(t_2 - \tfrac{\tau}{2}\right)\right) = -H_c \qquad\qquad (4\text{-}9)$$

where $w = 2\pi/\tau$. The residence times in the steady stables states can be defined as:

$$T^+ = t_2 - t_1 = \frac{1}{w}\left[arcsin\left(\tfrac{H_c + H_x}{\widehat{H_e}}\right) - arcsin\left(\tfrac{H_c - H_x}{\widehat{H_e}}\right)\right] + \tfrac{\tau}{2} \qquad\qquad (4\text{-}10)$$

$$T^- = t_3 - t_1 = \frac{1}{w}\left[arcsin\left(\tfrac{H_c - H_x}{\widehat{H_e}}\right) - arcsin\left(\tfrac{H_c + H_x}{\widehat{H_e}}\right)\right] + \tfrac{\tau}{2} \qquad\qquad (4\text{-}11)$$

Then RTD can be defined as:

$$RTD = \frac{2}{w}\left[arcsin\left(\tfrac{H_c + H_x}{\widehat{H_e}}\right) - arcsin\left(\tfrac{H_c - H_x}{\widehat{H_e}}\right)\right] \qquad\qquad (4\text{-}12)$$

Figure 4-6 depicts the relation between double-well potential energy function and Residence Times Difference concept, while *Figure 4-7* elucidates typical output voltage time evolution. The major advantage of the RTD readout concept is translation of external magnetic field information from amplitude domain to time domain, which enhances the efficiency of signal processing due to the intrinsic digital form of the readout signal [190].
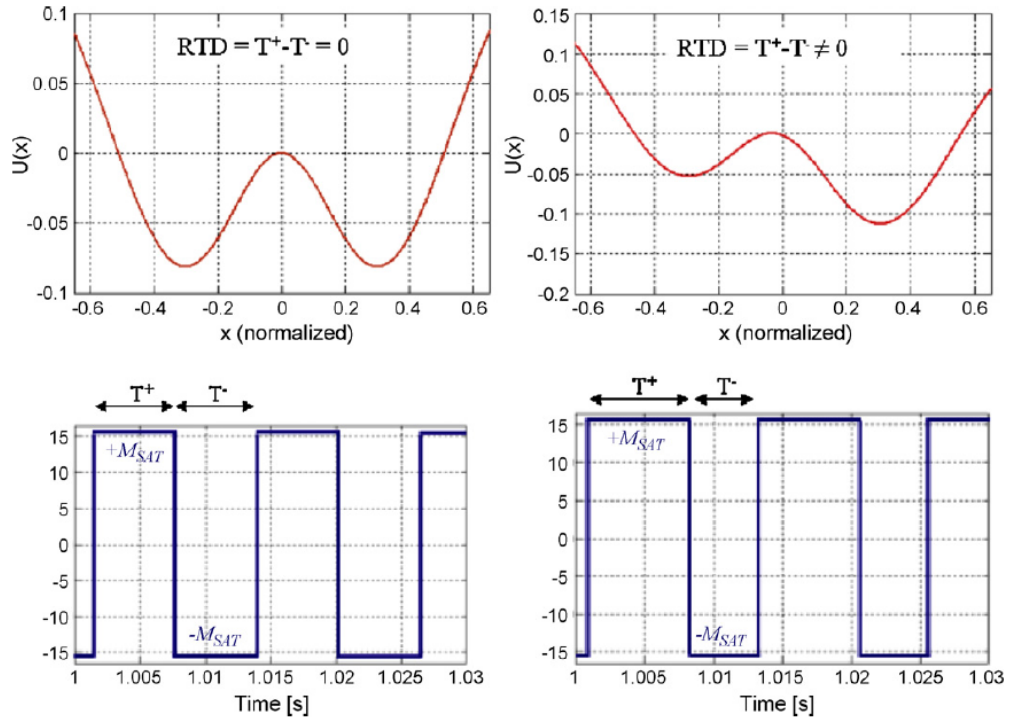
Figure 4-6: Residence Times Difference readout, and the associated double-well potential energy function
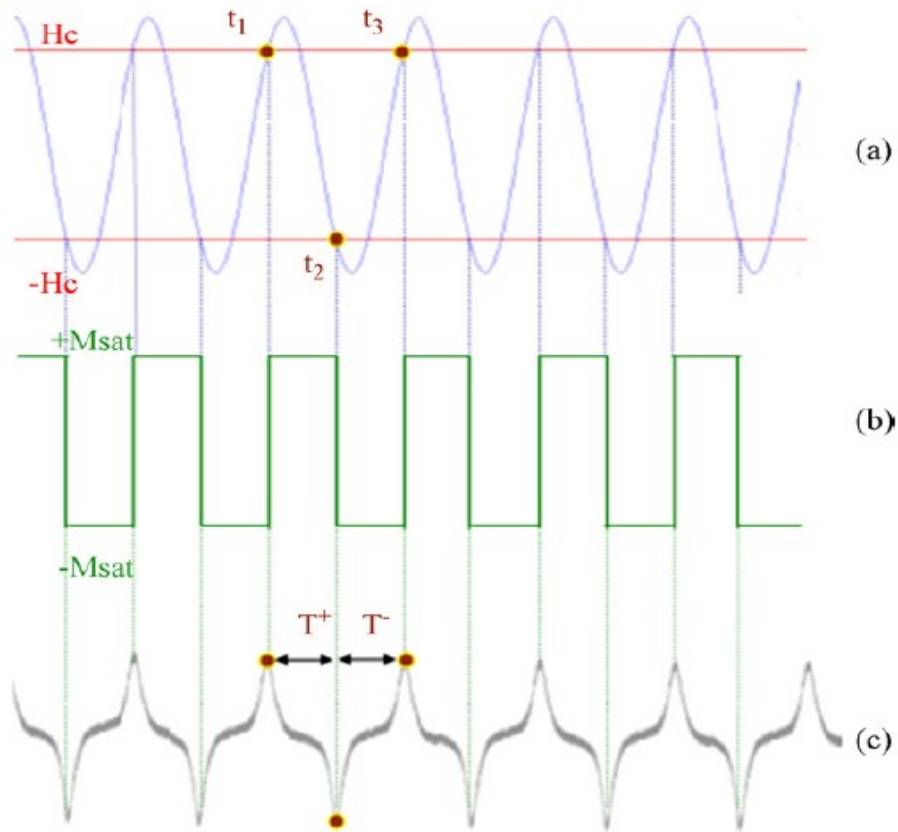
Figure 4-7: RTD mechanism: (a) coercive field Hc representation; (b) corresponding magnetization; (c) associated output

4.2. Electronic Circuits of Fluxgate Sensors

Figure 4-8 depicts a block diagram of a 2nd harmonic fluxgate magnetometer [191]. Signal frequency from generator is reduced to $f/2$ frequency drive the excitation coil. Driver circuit generates appropriate waveform of excitation signal. After amplification and filter (to eliminate parasitic signals such as odd harmonics), output signal from sensing coil is delivered to phase-sensitive detector (PSD), for noise rejection; where signal from the generator is used as reference signal for PSD [192]. Despite that block diagram in *Figure 4-8* appears to be uncomplicated, several factors, that have major impact on output performance, should be taken into account such as:

• Matching between excitation coil and generator (frequency, capacitance value of the driving coil, wave shape). For example, *Figure 4-9* illustrates effect of parallel capacitor on driving signal [193].

• Matching between amplifier and sensing coil (influence of capacitor, tuned or un-tuned output, etc.) [194].

Recently, it was settled that analog domain have nearly reached the end of their improvement whereas digital domain has the potential to create totally new possibilities for the second-harmonic fluxgate circuit. Thus, in recent years, ,there is a trend to move the excitation and detection circuits from the analogue to the digital domain, while reducing the analogue components interfaced with the fluxgate magnetometer. The

inherent flexibility in the digital design provides the opportunity of enhanced signal processing, and low power consumption for the digital fluxgates. Examples of digitalization of fluxgate magnetometers are:

1. An analog to digital converter (ADC) involved at analog magnetometer output [195].

2. A digital–analog configuration where part of analog components serve as an element of digital conversion of magnetic field into bit stream [196].

3. All digital configuration where after analog amplification, output signal is processed digitally.
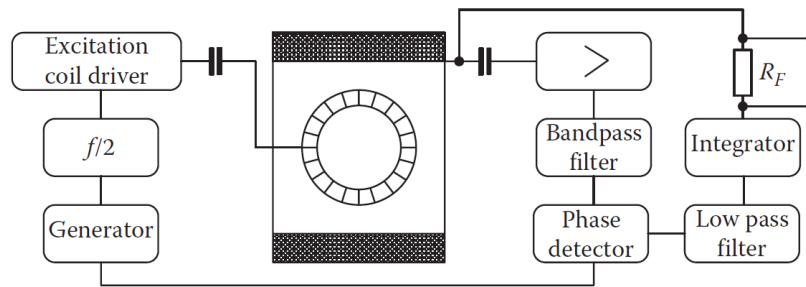
Figure 4-8: A 2nd harmonic fluxgate and the associated circuitry
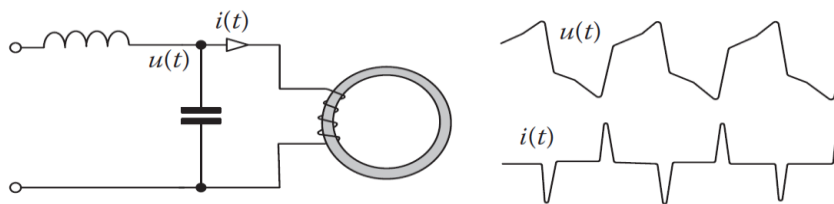
Figure 4-9: Effect of parallel capacitor on the driving signal

Most of analog components can be replaced by equivalent digital components. For example, PSD can be replaced by digital multiplier (mixer), the same employs to filters [197]. *Figure 4-10* describes an example of the merit of digital processing over the analog way. Typically, output signal when there is no magnetic field has to be zero whereas output signal when magnetic field applies should have even harmonics only. However, in circuitry implementations, odd harmonics do not compensate totally, and the zero-field signal become distorted because of coupling between excitation and pickup coils (the left bottom in *Figure 4-10*). Consequently, signal for magnetic field presence will be distorted (the left top in *Figure 4-10*). By digitally subtracting the zero-field signal, we can get undistorted signal (signal on the right in *Figure 4-10*). This process is difficult to be done with analog circuit but digitally, we could eliminate parasitic elements correlated with pre-stored zero-field signal. Other examples for processes that can be done digitally are: enhancement of noisy signal by using moving average digital filter, remove average value (offset), change online operating conditions, linearity enhancement, magnetometer calibration, statistical analysis [198].
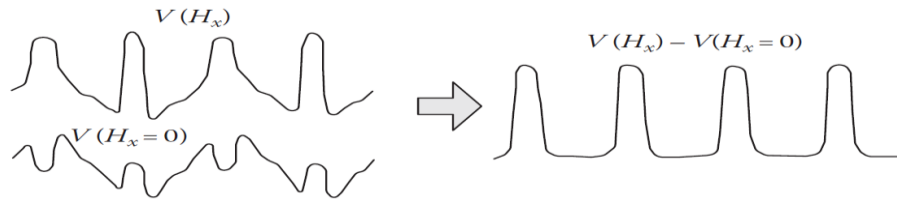
Figure 4-10 Recovery of the output waveform by digital subtraction

Figure 4-11 shows a block diagram of fluxgate magnetometer, where part of the circuit is analog. Generally, replacement of analog components and the digitization makes the sensed signal considerably insensitive to electro-magnetic interference, and more resistant against the supply voltage fluctuations [199].
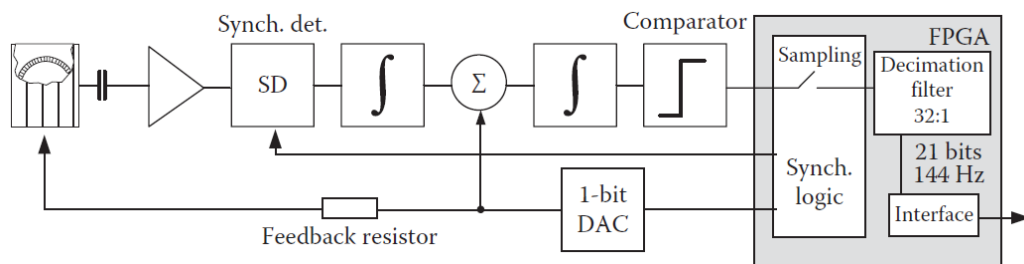
Figure 4-11 Block diagram of fluxgate magnetometer

Figure 4-12 shows a proposed design of a digital fluxgate sensor, where the design is implemented on FPGA, without the need to separate ADC or DAC chips [200]. The amplified output signal of fluxgate converted to digital form by analog to digital converter and then the next functions are performed digitally. The capacity of modern FPGA chips gives the ability to embed the processing electronics into the same chip as the magnetometer electronics (i.e., the field measurement extraction) to the digital domain [201]. Furthermore, replacing analog components by digital processing in an FPGA enhances measurement stability as it ensures accurate field vector timing relative to system clock, regardless of range and sampling rate [202].
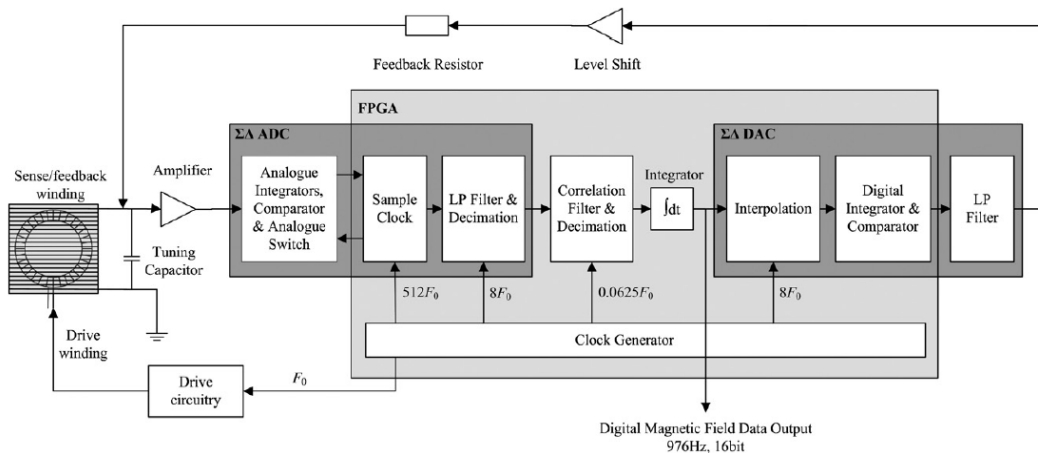
Figure 4-12: Example of digital fluxgate magnetometer

4.3. Fluxgate Configurations

One of the key points in fluxgate operation is that when the fluxgate soft magnetic core is excited periodically, its permeability varies greatly with the level of applied magnetic field *H*. In this context, it should be noted that permeability is not the slope dB/dH of the Hysteresis curve, but rather the slope of line from origin to certain point on the curve. Two values of interest are usually mentioned, initial permeability μ and maximum permeability μ_m, which are illustrated in *Figure 4-13*, and represents the typical variation of permeability with magnetic field for a soft magnetic material. The slope of the B-H curve dB/dH is defined as the differential permeability [203].
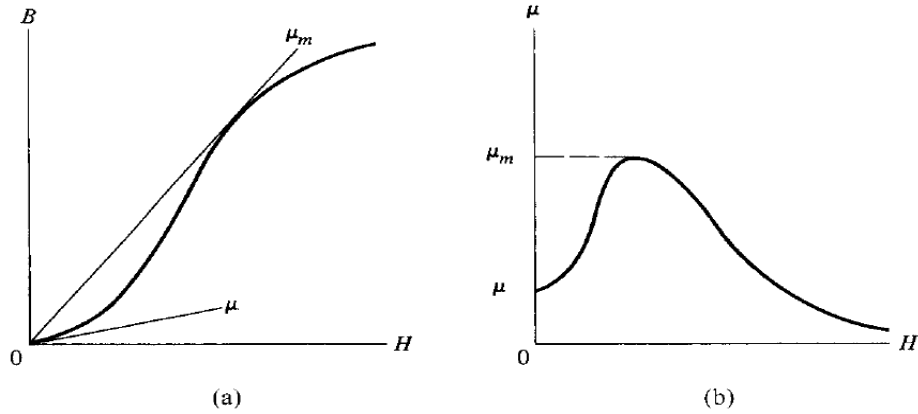
Figure 4-13: (a) flux versus field curve of a soft magnetic material and, (b) equivalent variation of permeability with magnetic field

The magnetic flux inside the core's cross section *S* can be defined as:

$$B(t) = \mu_0 \, \mu_r\big(H(t)\big) \, H(t)S \tag{4-13}$$

where $\mu_r\big(H(t)\big)$ is time varying permeability. Then, time derivative of the flux is:

$$\frac{dB(t)}{dt} = \mu_0 S \left[\mu_r\big(H(t)\big)\frac{dH(t)}{dt} + \frac{d\mu_r\big(H(t)\big)}{dt} H(t) \right] \tag{4-14}$$

which can be written more explicitly as:

$$\frac{dB(t)}{dt} = \mu_0 S \left[\mu_r\big(H(t)\big)\frac{dH(t)}{dt} + \frac{d\mu_r\big(H(t)\big)}{dH(t)}\frac{dH(t)}{dt} H(t) \right] \tag{4-15}$$

Basically H(t) has two components: the excitation field; and the external field to be sensed. In this context, Fluxgate configurations are classified according to the relative direction of excitation field with respect to external field to be sensed as shown in *Figure 4-14*. For parallel fluxgate configuration, both excitation and external fields have the same direction. However for the orthogonal fluxgate configuration, excitation field is orthogonal to external field. This leads to a different gating mechanisms, and sensor structures for each configuration [204].
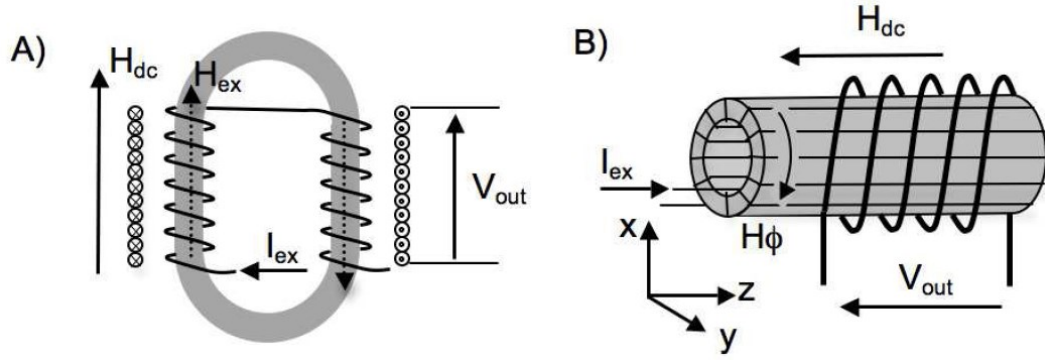
Figure 4-14: Structure of parallel (A) and orthogonal (B) fluxgates configurations

4.3.1. Parallel Fluxgate Configuration

For the parallel fluxgate sensor, the permeability inside the soft magnetic core is modulated according to the relation $\mu_r = dB/\mu_0 dH$. Since the alternating excitation field H_E modulates the core permeability periodically, the gating mechanism in parallel fluxgates depends on changes in *dB/dH*. The magnetic field around the core *H(t)* is the scalar sum of excitation and measured fields as :

$$H(t) = H_E(t) + H_M(t) \tag{4-16}$$

The excitation frequency is usually chosen at higher frequency than the measured field. The change in flux can be written as [205]:

$$\frac{dB}{dt} = \mu_0 S \left[\mu_r(t) \frac{dH_E(t)}{dt} + \frac{d\mu_r(t)}{dt} \left(H_E(t) + H_M(t) \right) \right] \tag{4-17}$$

Parallel fluxgates can be divided according to their core geometry to three categories; rod core, ring core, and racetrack core. Rod core sensors have an open magnetic path, while both ring and racetrack cores have closed magnetic path.

Figure 4-15a shows the single rod core fluxgate, which contains two coils wound around the core, i.e. excitation and pick up coils. However, this structure is rarely used, as the excitation signal induces a strong first harmonic component on the pickup coil. In order to remove this component, double-rod core geometry is employed. Double rod sensors have two types; Forster type with two excitation coils, and two pickup coils anti serially connected. The other type is called Vacquier type (see *Figure 4-15b*).

(a)

(b)
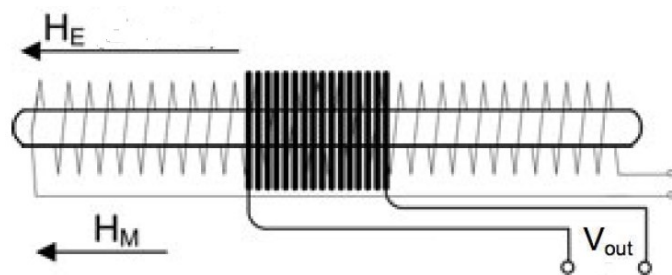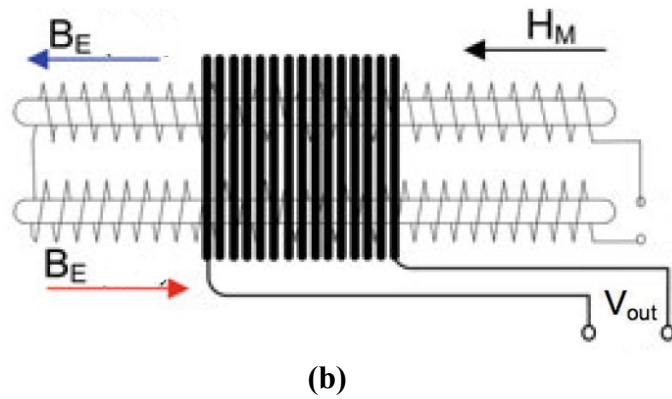
Figure 4-15: (a) Single rod-core. (b) double-rod core fluxgates

This structure consists of two core components, each with its own excitation coil that generates an excitation field in opposing directions. Both cores share a single pick-up coil, which subtracts the flux created by excitation coils. An advantage of double-rod structure, unlike ring-core structure, is that the sensing direction is well defined by the core direction [206]. In ring core fluxgate type, excitation coil is wound circumferentially around a ring core. Pick-up coil is wound diametrically on the bobbin and is used to sense magnetic field parallel to its plane (see *Figure 4-16a*). The ring core geometry produces closed magnetic path for excitation field, which provides the symmetry needed to suppress undesired excitation signal. However, this type has a lower sensitivity compared to the rod core design [207]. Racetrack sensors can be regarded as hybrid core with a combination of rod and ring cores. The racetrack shaped sensors benefits from its closed loop geometry and so, they have high sensitivity and resistance to orthogonal fields [208]. *Figure 4-16b* shows an example of the racetrack sensor.

(a)   **(b)**
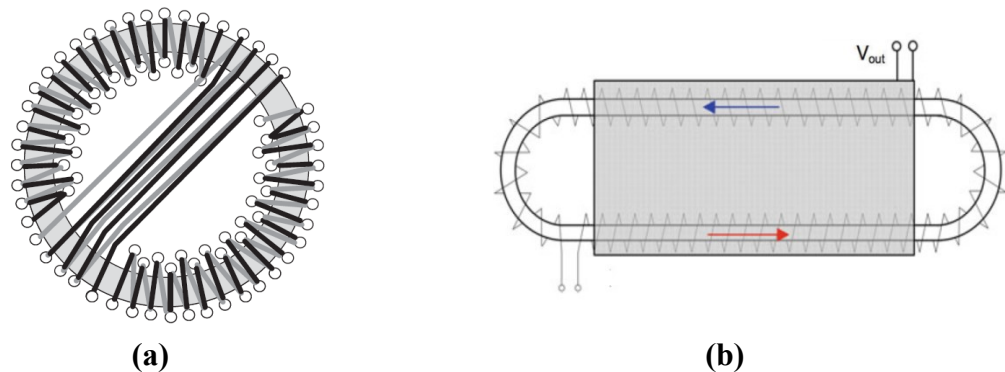
Figure 4-16: (a) Ring-core fluxgate (b) Race-track fluxgate

4.3.2. Orthogonal Fluxgate Configuration

The excitation coil in a parallel fluxgate is wound around the core to generate an excitation field that is parallel to the measured field. On the other hand, an orthogonal fluxgate, in its simplest form, is made up of a cylindrical soft magnetic core surrounded by toroidal excitation coil. Periodic excitation of the magnetic core causes its magnetization to rotate between the excitation field and the measured field. The rotation of magnetization induces second harmonics, in the sensing coil, with amplitude

proportional to the measured field, obtaining the same functionality as parallel fluxgate. However, in this configuration, the measured field still in the axial direction of the core, but the excitation field created by the toroidal coil is in the circulatory direction. In other words, the excitation field lays in a plane that is orthogonal to the sensed direction, (i.e., the core's axis). That is why this type of fluxgate is named orthogonal, as the excitation and sensed field are mutually orthogonal.

It should be highlighted that stating that the excitation field is orthogonal to measured field does not mean that excitation field is linear. Actually, it is always perpendicular to measured field along the whole circumference. As a result, the total magnetic field for the orthogonal configuration can be defined as vector sum of excitation and measured magnetic fields:

$$H(t) = H_E(t) + H_M(t) \tag{4-18}$$

Therefore, the alternating flux inside the core can be re-written as:

$$\frac{dB}{dt} = \mu_0 S \left[\frac{d\mu_r(H(t))}{dH(t)} \frac{dH_E(t)}{dt} H_M \right] \tag{4-19}$$

Thus, the orthogonal gating characteristic is markedly different from the parallel gating characteristic, where the permeability is modulated according to the relation $\mu_r = B/(H - H_c)\mu_0$. Also, for the orthogonal fluxgate, the flux and the field may not be in the same direction inside the core. Therefore, the gating mechanism in orthogonal fluxgates depends on changes in $B/(H-H_c)$, where H_c is the coercive field [209]. At this standpoint, it will be more illustrative to describe the magnetization mechanism, inside the orthogonal fluxgate sensing element, through a 2D vector plane. *Figure 4-17* depicts working principle of orthogonal fluxgate magnetometer [210]. The change in magnetization with magnetic field "i.e., hysteresis curve" can be described as:

$$\Delta B = \mu_0(H + M) \tag{4-20}$$

The symbol Δ reflects local variation of the value around given point on hysteresis curve of the core. Magnetization of soft magnetic material as a function of magnetic field can be defined as:

$$\Delta M = \chi \, \Delta H \tag{4-21}$$

Where χ being the susceptibility of the material. A simplified hysteresis curve shown in *Figure 4-17a* will be considered in this analysis. The magnetization of the soft magnetic core reaches its maximum value M_{sat} twice for each period of the excitation. When there is no external field, vector M is in the excitation field direction. However, when an external field is applied, vector M consists of two mutually orthogonal components, M_{exc} and M_{ext}, which result from excitation field and external field, respectively. As excitation field H_{exc} rises, M_{exc} component of vector M starts to rise (y-axis in *Figure 4-17b*) up to specific value equal to M_{sat}, which is the highest possible magnetization inside fluxgate core. For further rise in total field inside the core, the amplitude of M can not rise anymore and the only effect of rising H is to rotate M along the circumference (i.e., M= M_{sat}), which is represented by the dashed circle in *Figure 4-17b*.
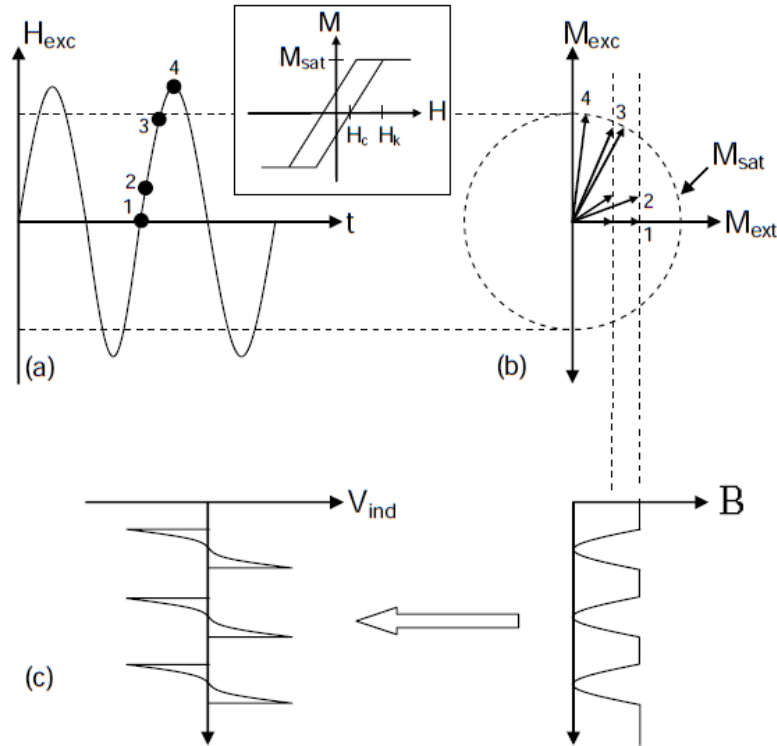
54

Figure 4-17: Working principle of orthogonal fluxgate magnetometer

When magnetic field reaches certain value H_k, corresponds to saturation magnetization M_{sat}, M_{ext} component of vector **M** forces to decrease. When magnetic field starts to decreases again, M_{ext} component starts to increase again, and returns back to its initial value. This cycle creates periodic change in the flux B that produces voltage in sensing coils (*Figure 4-17c*). When external magnetic field direction is reversed, M_{ext} becomes negative and the induced voltage phase is shifted by Π rad. This implies that orthogonal fluxgate is capable of differentiation between positive and negative external fields. Actually, real component of the second harmonic of induced voltage is utilized in order to consider the voltage phase, and hence distinguish the sign of the magnetic field [211].

The point that circumferential cross section of the orthogonal fluxgate core is itself a closed magnetic path gives orthogonal fluxgates an advantage over parallel fluxgates. In this case, to have closed magnetic path, we do not need to employ ring or race-track shaped structures as what is typically done for parallel fluxgates. Instead, orthogonal fluxgates have different core geometries. The first geometry is shown in *Figure 4-18*, where toroidal coil is wounded around a cylinder to provide an excitation field in the circumferential direction. The toroidal coil provides large excitation field, which is essential for a proper functionality of a fluxgate [212]. However, this structure is difficult to be implemented, as the manufacturing of a toroidal coil around a cylinder is not compatible with the standard fabrication process. For this reason, another structure was proposed to use micro magnetic wires. The progress in the manufacturing techniques helps in the ability to produce magnetic microwires with a small diameter (10-200 μm) and soft magnetic behavior [213]. Thanks to this, the orthogonal fluxgate structure in *Figure 4-19* has been proposed, which employs a soft magnetic wire as a

core. In this structure, the soft magnetic wire operates as both magnetic core, and an excitation element, where the excitation current injected directly in the soft magnetic microwire to generate a circular magnetic field inside it. As a result, this structure eliminates the need to an excitation coil, which simplifies the fluxgate structure, and attracts new interests to orthogonal fluxgates when miniaturization of magnetic sensors is required [214].
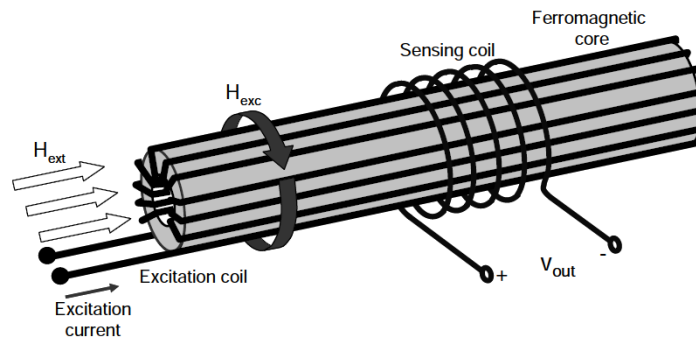
Figure 4-18: Orthogonal fluxgate structure based on soft magnetic material cylinder
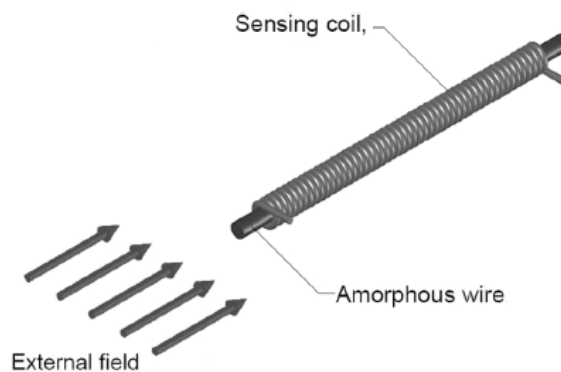
Figure 4-19: A wire core orthogonal fluxgate

One of benefits of using microwire as a fluxgate core, aside from removing the excitation coil, is the quite small wire diameter "i,e., ~μm". A small diameter is beneficial not just for downsizing, but also for enhancing spatial resolution in magnetic field measurements. For example, assuming magnetic field in the x direction. Parallel fluxgates adopt either race-track or ring structure where two sections of the core are sensitive in external magnetic field direction [215]. These two sections will sense different fields H_{XA} and H_{XB}, as shown in *Figure 4-20*. As the pick-up coil collects flux from both sections, the total sensed magnetic field will be average of H_{XA} and H_{XB}, with is no way to differentiate them. As a result, spatial resolution of Parallel fluxgates is restricted by its core width. On the other hand, the limiting dimension of spatial resolution of orthogonal fluxgate is the microwire diameter. This means that it is possible to sense magnetic field in single spot, and this make spatial resolution of orthogonal fluxgates much higher than that achieved by parallel fluxgates "i,e., up to

two orders of magnitude". That is why orthogonal fluxgate magnetometers considered as a high potential candidate to be used in applications such as magnetic imaging [216].
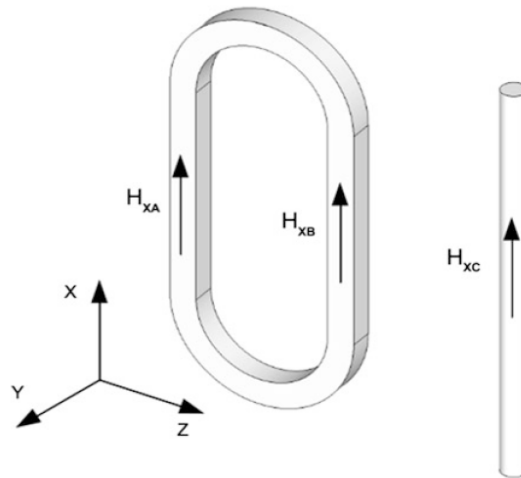
Figure 4-20: Spatial resolution of parallel (left) and orthogonal fluxgates (right)

4.4. Fundamental Mode Orthogonal Fluxgate

The fundamental mode fluxgate, which was recently developed, provides new opportunities for improving orthogonal fluxgates with wire cores. The sensor's structure is similar to wire core orthogonal fluxgate; except that a dc component is added to the ac current in order to excite the core (see *Figure 4-21*). Adding a dc component to the ac-bias current turns the bipolar excitation form of the microwire core into a unipolar form. Furthermore, the dc bias shifts the core magnetization state away from magnetization reversals regime where the main magnetization mechanism is the wall movement, to another regime where magnetization varies only by coherent rotation as shown in *Figure 4-22*.
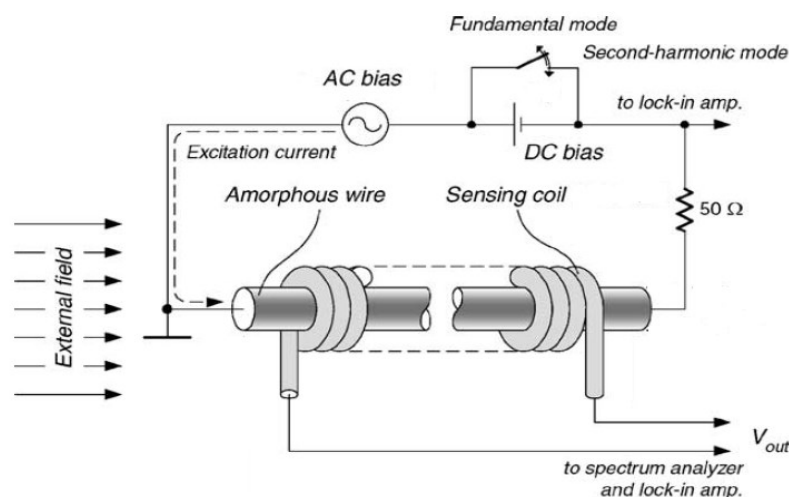
Figure 4-21: Second harmonic and fundamental modes orthogonal fluxgate employing a wire core

In this operation mode, the fundamental, rather than the second harmonic, gives information about the measured field, as fundamental component of the induced voltage at the pick-up coil indicates the presence of the measured magnetic field, and its magnitude depends on hysteresis loop of the microwire core [217]. Orthogonal fluxgate based on this operation mode can show higher sensitivity compared to conventional orthogonal fluxgate. Also, a high value of dc bias reduces core's vulnerability to irregular magnetic domain wall motion that is caused by magnetization pinning sites. This leads to suppression of magnetic noise created in the fluxgate core [218].
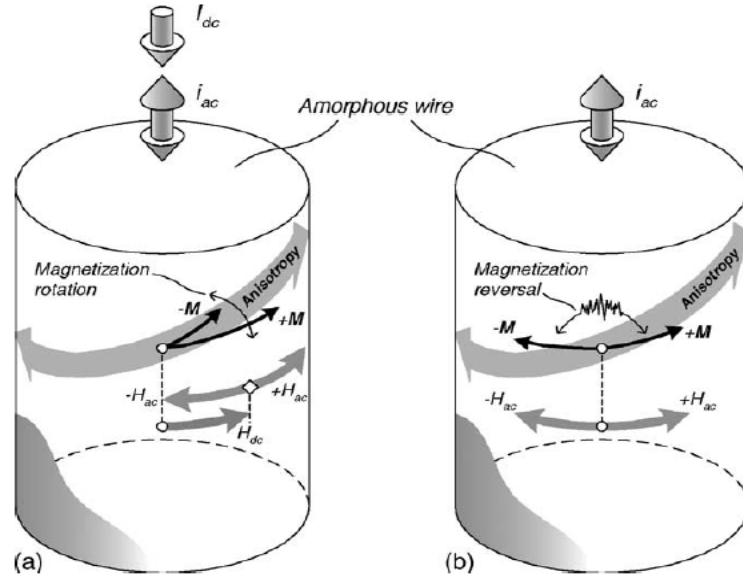
Figure 4-22: (a) Fundamental mode and (b) second harmonic mode magnetization behavior

In order to further explain the fundamental operation mode *Figure 4-23* and *Figure 4-24* illustrates the analysis of magnetization behavior to understand the position it needs to minimize its total energy. If we assume an orthogonal microwire core excited by an $I_{ac} + I_{dc}$ current. This in turn produces circular magnetic fields $H_{ac} + H_{dc}$. When there is no applied magnetic field the net magnetization M will lay on the circumferential direction too (see *Figure 4-23*).

Now, if an applied magnetic field H_Z is present in the axial direction, magnetization will deviate away from circumferential direction by an angle ϱ between φ direction (where $H_{ac} + H_{dc}$ lays) and Z direction (where H_Z lays) (see *Figure 4-24*). The angle ϱ relies on the magnitude of both $H_{ac} + H_{dc}$ and H_Z. Thus, ϱ is larger when H_Z is larger, while ϱ is lower when $H_{ac} + H_{dc}$ is larger. As a result, the net magnetization position can be defined through minimizing the total energy [219]:

$$E = -\mu_0 M(H_{ac} + H_{dc}) \cos \varrho - \mu_0 M H_z \cos \left(\frac{\pi}{2} - \varrho\right) \qquad (4\text{-}22)$$

M usually lays on φ direction, and ϱ changes can be predicted with respect to circumferential magnetic field. As H_{ac} become minimum, the circumferential field will be $H_{dc} - |H_{ac}|$ and ϱ become maximum. While as H_{ac} become maximum, the

circumferential field will be $H_{dc} + |H_{ac}|$ and ϱ become minimum. In presence of external magnetic field H_Z, projection of M on Z-axis M_Z will oscillates with the same frequency as H_{ac}. As a result, when external magnetic field H_Z is zero ϱ value become zero, as there is no field to deviate M away from the circumferential direction. As the value of H_Z increases, the deviation of M from the circumferential direction increases as well [220].

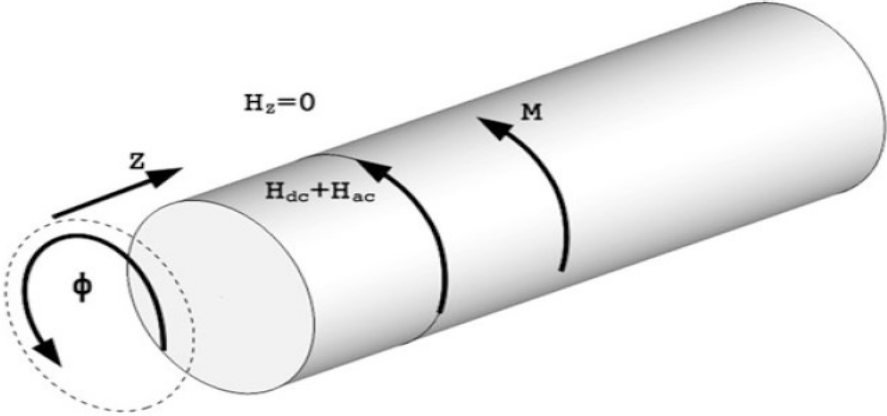**Figure 4-23 Magnetization and magnetic field in fundamental mode operation without external magnetic field**
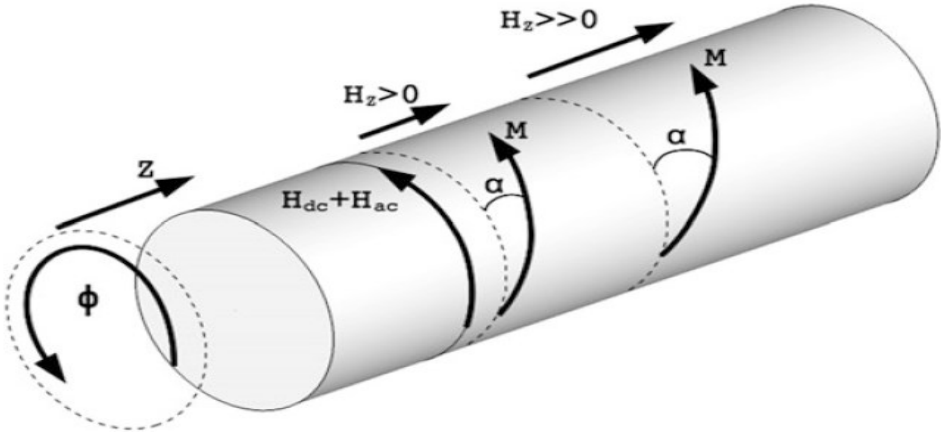

Figure 4-24 Magnetization and magnetic field in fundamental mode operation against two different external magnetic field values

Chapter 5 : Soft Magnetic Microwire Based Orthogonal Fluxgate Core: Simulations and Results

During the various attempts to develop fluxgate magnetometer designs, it was realized that the fluxgate core's factors are the key for an enhanced sensor performance. The soft magnetic core of the fluxgate should fulfill certain requirements arising from its principle of operation; these requirements can be fulfilled by the investigation of the several parameters that affect the sensing element of the fluxgate. The evaluation of core performance is a multi-disciplinary subject, involving the nonlinear behavior of the core material, core geometry, and the electromagnetic response of the core due to the excitation conditions. In this chapter, the fluxgate core is modeled numerically using finite element analysis method. First, the electromagnetic equations describing the phenomena are presented, then the required finite element method equations are conducted. Then, different factors have been tested through conducted simulations to reveal the effect of each design parameter on the fluxgate sensing element.

5.1. Formulation

In order to describe the electromagnetic response of the fluxgate core, the governing equations must be known. Maxwell's equations in differential forms in the time domain at any point in space and at any time are given by:

$$\nabla \times H = J + \frac{\partial D}{\partial t} \tag{5-1}$$

$$\nabla \times E = -\frac{\partial B}{\partial t} \tag{5-2}$$

$$\nabla . D = \rho \tag{5-3}$$

$$\nabla . B = 0 \tag{5-4}$$

Where J is conductive current density (corresponding to motion of charge) is source of EM fields, and ρ is the volume charge density is a source of the electric fields. E is electric field, and D is electric induction. In low-frequency cases, it can be assumed that $\left|\frac{\partial D}{\partial t}\right| \ll J$, and equation (5-1) can be written, approximately, as

$$\nabla \times H = J \tag{5-5}$$

Now, the magnetodynamic fields can be defined via Maxwell's equations as [221]:

$$\nabla \times H = J \tag{5-6}$$

$$\nabla \times E = -\frac{\partial B}{\partial t} \tag{5-7}$$

$$\nabla . B = 0 \tag{5-8}$$

The magnetodynamic field description via electromagnetic equations has certain features. The time variable has to be involved in the equations. Also, the magnetic flux density B and electric field intensity E induced by flux density variation are in different planes. As a result, rigorous solutions for magnetodynamic problems are very difficult to be obtained. In order to solve such problems, approximations, in most cases, are used, and, generally, the solution techniques need to be adapted to the characteristics of the problem [222]. Therefore, constitutive relations equations should be obtained to get a closed system that takes into account the material characteristics, as:

$$B = \mu H \tag{5-9}$$

$$D = \epsilon E \tag{5-10}$$

$$J = \sigma E \tag{5-11}$$

where μ, ε, and σ are magnetic permeability, electric permittivity, and electric conductivity, respectively, for linear materials. However, in our cases, the fluxgate soft magnetic core considered as a nonlinear material. Nonlinearity here is not only that the current intensities affect the material's magnetic properties, but also the history of the field distribution is taken into account as well (i.e., Hysteresis effect). Thus, another form of constitutive relation for the magnetic field can be written as

$$B = \mu H + B_r \tag{5-12}$$

where B_r is remnant magnetic flux density, i.e., the magnetic flux density when no magnetic field is applied. The penetration of fields in nonlinear magnetic material is a very complex problem, where analytical solutions are difficult to obtain [223]. Thus, several numerical techniques have been proposed to solve such a problem using Maxwell's time-dependent partial differential equations formulation [224]. The finite element method (FEM) proved to be a powerful numerical technique that is used to analyze partial differential equations in arbitrarily shaped materials. Finite element methods extensively applied in electromagnetic problems and proven to be a useful technique to solve certain types of problems taking into account nonlinearities of the medium [225]. In this thesis, the calculation of electric and magnetic fields inside the core's geometry is done using finite element models developed in COMSOL Multiphysics [226]. Here, the numerical formulations of the proposed models are not directly described in terms of electric or magnetic fields. However, they are presented through different potentials that propose some advantages in the computational aspects. In our case, the problem is formulated in terms of electric scalar potential V, and magnetic vector potential A, which can be defined as:

$$B = \nabla \times A \tag{5-13}$$

$$E = -\nabla V - \frac{\partial A}{\partial t} \tag{5-14}$$

Here magnetic flux density B and electric field E are linked to magnetic vector potential A and to electric scalar potential V. The main advantage of using electric scalar potential V in numerical procedures is that there is only one unknown at each

point of the studied domain, instead of the three unknowns in terms of E. The magnetic vector potential A is used extensively for solving magnetodynamic problems. Although the potential A does not have a definitive physical meaning, using A in the problem formulation make it possible to impose a physical condition on the domain borders (i.e., boundary conditions) compared to using the magnetic field as variable. Thus, in our simulations, using the definitions of potentials, the analysis of magnetic and electric field is done using the equation [227]:

$$\sigma \frac{\partial A}{\partial t} + \nabla \left(\mu_0^{-1} \nabla A - M \right) - \sigma \, v_c (\nabla A) + \sigma \, \nabla V = J_e \tag{5-15}$$

where J_e is an external current density, and v_c is conductor velocity. Taking divergence of equation (5-15) obtains:

$$\nabla . \left(-\sigma \frac{\partial A}{\partial t} + \sigma \, v_c \, (\nabla A) - \sigma \, \nabla V + J_e \right) = 0 \tag{5-16}$$

Equations (5-15) and (5-16) form system of equations for the two potentials A and V. In order to account for nonlinear magnetic features of the fluxgate's sensing element, it was vital to involve a hysteresis curve in COMSOL to present the relative permeability of soft magnetic material as function of magnetic flux density. Choosing an accurate model to represent the magnetic hysteresis loop is important to obtain relatively precise results. Thus, in this thesis, The Jiles-Atherton model is chosen for representing soft magnetic micro wire structures, due to its meaningful parameters that reflects the physical processes behind the magnetic hysteresis loop, and its ability to be implemented in finite element computations [228]. Here, we used the Jiles-Atherton hysteresis model with its five descriptive parameters to reproduce the magnetic hysteresis behavior of fluxgate core. In COMSOL, The effective magnetic field H_e, that describes the field that is expected to affect the magnetic moments on a microscopical level, is defined through the α parameter as:

$$H_e = H + \alpha . M \tag{5-17}$$

The maximum magnetization parameter M_s contributes in calculating the slope that determines the anhysteretic part of the material behavior through the formula for anhysteretic magnetization [229]:

$$M_{an} = M_s . Lan(a^{-1} . H_e) \tag{5-18}$$

Where a is the domain density, and $Lan(x) = \coth(x) - \frac{1}{x}$ is the langevin function. Using the defined quantities, the main equation of the Jiles-Atherton model that describes the magnetization M is [230]:

$$\frac{dM}{dt} = \max \left(X . \frac{dH_e}{dt}, 0 \right) . \frac{X}{|X|} + c . \frac{dM_{an}}{dt} \tag{5-19}$$

Where c is the reversibility parameter, and the auxiliary vector X is defined as:

$$X = k^{-1}(M_{an} - M) \tag{5-20}$$

Where *k* is the Pinning parameter.   The above mentioned equations are governing equations which will be solved by finite element COMSOL multiphysics.

5.2.   Micro Wire Based Fluxgate Core Modeling and Simulation

In our first model, the fluxgate core consists of a single magnetic microwire. The excitation current is injected directly (i.e., flows) into the wire, generating the circumferential magnetic field. For fluxgate operation, the excitation current, the wire diameter, and the frequency are the main factors that influence its performance. All these factors are mutually dependent on each other. As in this thesis, we don't address the noise and sensitivity prospective, our problem concerns with describing the current density *J*, and magnetic flux *B* inside the microwire core. Excitation of the core by different mechanisms was modeled by finite element method to identify necessary excitation current for a given material hysteresis and different core dimensions to provide information about actual magnetic flux distribution and density inside the core. Current density distribution inside the core was modeled when an ac current feed the soft magnetic core with different amplitudes and frequencies to demonstrate the response of the different parts of the core when the excitation current increases. Furthermore, the effect of adding dc bias with different amplitudes to the ac excitation mechanism was investigated to illustrate how this will affect the distribution of fields inside the core.

In this thesis, as the fluxgate core's structure has no geometrical variation in the direction orthogonal to the plane of study, this provides the problem to be solved with less physical memory and processing power of the personal computer. This is why we didn't apply 3D geometries simulations in this thesis. Instead, the use of two-dimensional description was adopted to model the fluxgate core. Thus, we take the solution domain as a 2D planar circle that corresponds to the microwire cross section as illustrated in *Figure 5-1*. Also, a region outside the materials' domains is defined as a free air surrounding the core. After modeling the geometry of the core, *Magnetic Fields* interface is added under the *AC/DC* branch for the physics selection of the model. After adding physics for the model, we assign boundary conditions to the core. The magnetic continuity is employed for all boundaries except for boundaries at the edges of the solution medium, which are defined as magnetically insulated. After defining the governing physics and boundary conditions, a mesh is generated for the whole model in order to discretize the domain geometry of the core into triangular elements. After building the model, many FEM simulations were conducted with different core radius values that are submitted to different excitation current amplitudes, and different frequencies. These studies are used in this thesis to show the effect of excitation frequency and amplitude on the field's density distribution along the wire cross section. The detailed analysis of fields due to the investigated design parameters is presented in the next sections.
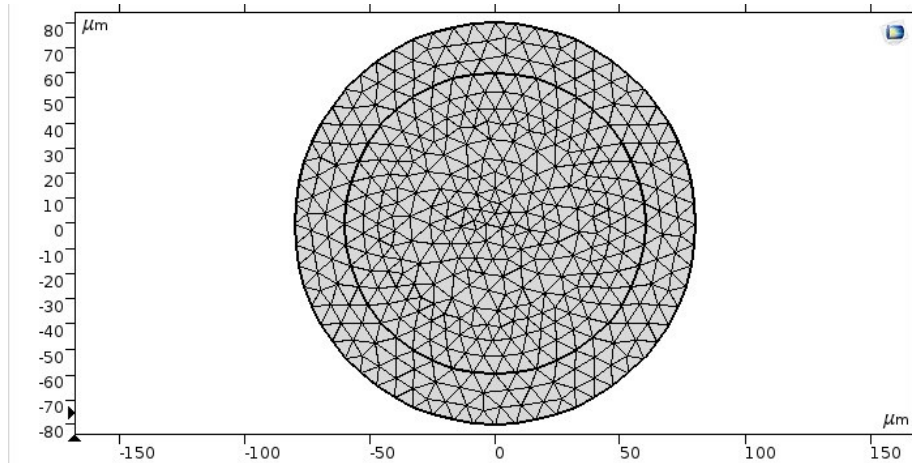
**Figure 5-1: COMSOL solution domain for the first configuration**

5.3. Analysis of the Results

Recent research for developments of fluxgate sensors tends to employ a micro fluxgate magnetometer with high-performance to be compatible with many applications that require very small sensor size [231-232]. This is strongly in favor of orthogonal fluxgates that have a sensing mechanism independent of excitation mechanism due to the orthogonality of excitation and measured magnetic fields. Therefore, excitation mechanism can be designed, and afterwards, the measuring range is adjusted independently [233]. Moreover, in the microwire fluxgate structure, there is no need for excitation coil, as the excitation field is induced by current passing inside the microwire. Thus, fluxgate magnetometer structure is further reduced which will be a benefit in the fabrication process, and make it applicable to considerably reduce the size of the fluxgate for approaches that require sensor miniaturization.

For instance, it can be assumed that miniaturization of the fluxgate concerns only with increasing the compactness of its dimensions. Unfortunately, the miniaturization process of fluxgate magnetometer is rather complicated than assumed. It was found that as the fluxgate's dimensions decrease, the magnetic noise increases considerably, while the operation range and the sensitivity decreases as well. These drawbacks can limit the applications of the micro fluxgate sensor, and require a different insight about the fluxgate's design considerations. It was found that in the case of small sized cross section area of magnetic core, high frequency operation is favorable to restore the high sensitivity of the magnetometer. Increasing frequency of the excitation current helps to enhance the dynamic performance of the core as $dH_{exc}/dt \sim f$ [234]. Thus, the **first** study to be conducted in this chapter is the effect of frequency on the microwire core. The radius of the magnetic core is chosen to be 20 μm, and the core is surrounded by air. The current flow through the cross section of the core has an intensity of 20 mA at a certain frequency. *Figure 5-2* illustrates the effect of excitation frequency on current density, and magnetic flux distribution.
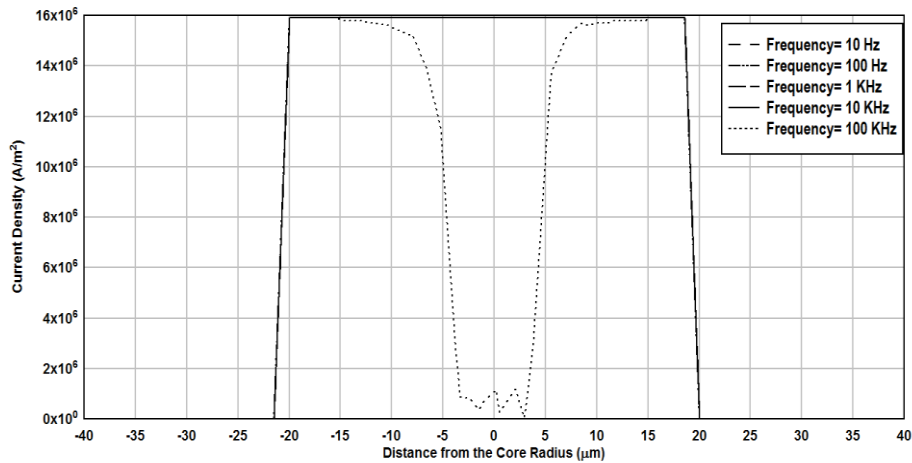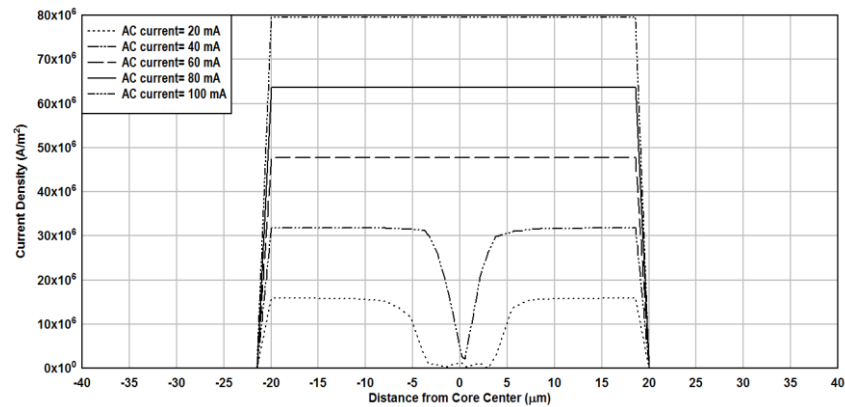
(a)
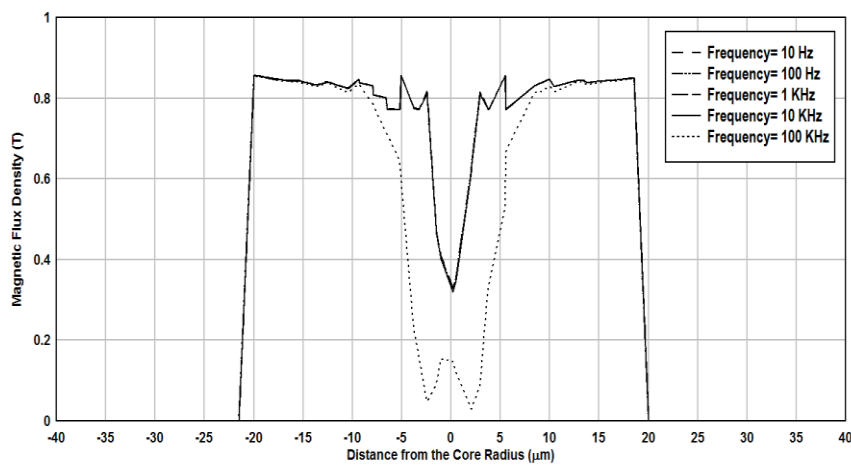
(b)

Figure 5-2: (a) Current density, and (b) Magnetic flux density radial distributions computed for different excitation frequencies

As seen in *Figure 5-2 (a)*, As the frequency increases from 10 Hz to 10 KHz, the current density distribution along the core cross section is closely similar. However, when the excitation frequency reaches 100 KHz, the current starts to drain from the central part of the core to the outer shell of the core. This phenomenon is defined as the skin effect, which describes the limitation of the magnetic flux onto the surface layers of a medium at a relatively "high" frequency. For *Figure 5-2 (b)*, while the excitation frequency increase, the magnetic flux density reduced at the central part of the core, with all the implemented frequencies. This reduction of the magnetic flux density at the central part of the core increases significantly at 100 KHz excitation frequency.

Before proceeding further, it should be highlighted that uniform maximum value of magnetic flux density inside the core is an important need for an adequate functionality of a fluxgate magnetometer. Thus the portion of the core that has relatively lower value of magnetic flux density will degrade the performance of the fluxgate [235].To mitigate such effects, one of the proposed solutions is to increase the excitation current. Thus, in the **second** study, the radius of the magnetic core is kept at 20 μm, and again the core is surrounded by air. However, the current flow through the core's cross section has an

intensity changing from 20 mA to 100 mA at 100 KHz frequency. *Figure 5-3* illustrates the effect of excitation current on current density, and magnetic flux distribution.

(a)
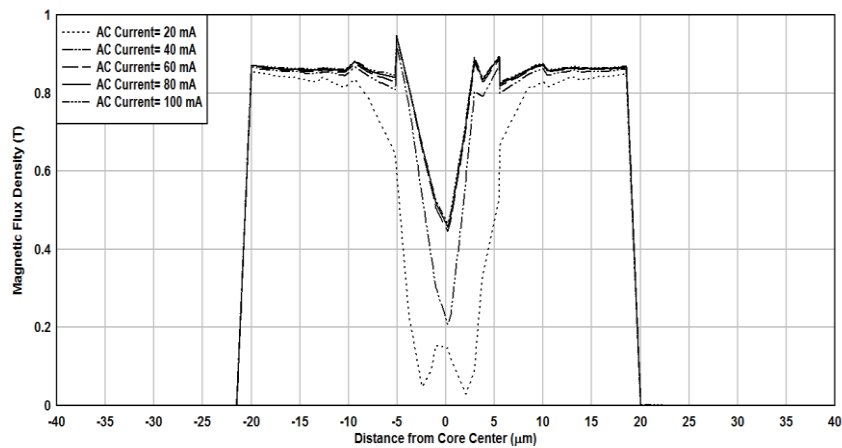
(b)

Figure 5-3: (a) Current density, and (b) Magnetic flux density radial distributions computed for different excitation amplitudes

As shown in *Figure 5-3(a)*, at the beginning, there was a portion in the central part of the core that has a reduced value of current density. However, as the excitation current increases, such portion of the core starts to be reduced until the ac current reaches 60 mA, where at this amplitude, the current density value become constant along the microwire diameter. After that the value of the current density starts to increase homogenously along the wire cross section as the ac current increases. As for *Figure 5-3(b)*, the flux penetration inside the core starts to increase as the ac current amplitude increases from 20 to 60 mA. However, after this value, the portion of the magnetic core that has a reduced flux value remains almost the same as excitation current increases from 60 to 100 mA.

To this extent, it is important to highlight that, it is almost impossible, from the flux density point of view, to uniform the magnetic flux density value inside the wire across its whole cross section, as this practically needs an infinite current to be achived. Instead, increasing the current amplitude at certain frequency will results in reducing the inner portion of the wire, that is unsaturated. However, the geometrical aspect of the unsaturated part of the core depends on both the magnetic core dimensions, and the

excitation frequency [236]. Thus, in our **third** study, the radius of the magnetic core increased from 20 µm to 40 µm , with an air surrounded the core. Again, the current flow through the core's cross section has an intensity changing from 20 mA to 100 mA at frequencies 10 KHz, 100 KHz, and 1 MHz. *Figure 5-4* and *5-5* illustrates the effect of the excitation current at certain frequency on the current density, and the magnetic flux distribution, when the magnetic core geometry increases.

(a)

(b)

(c)
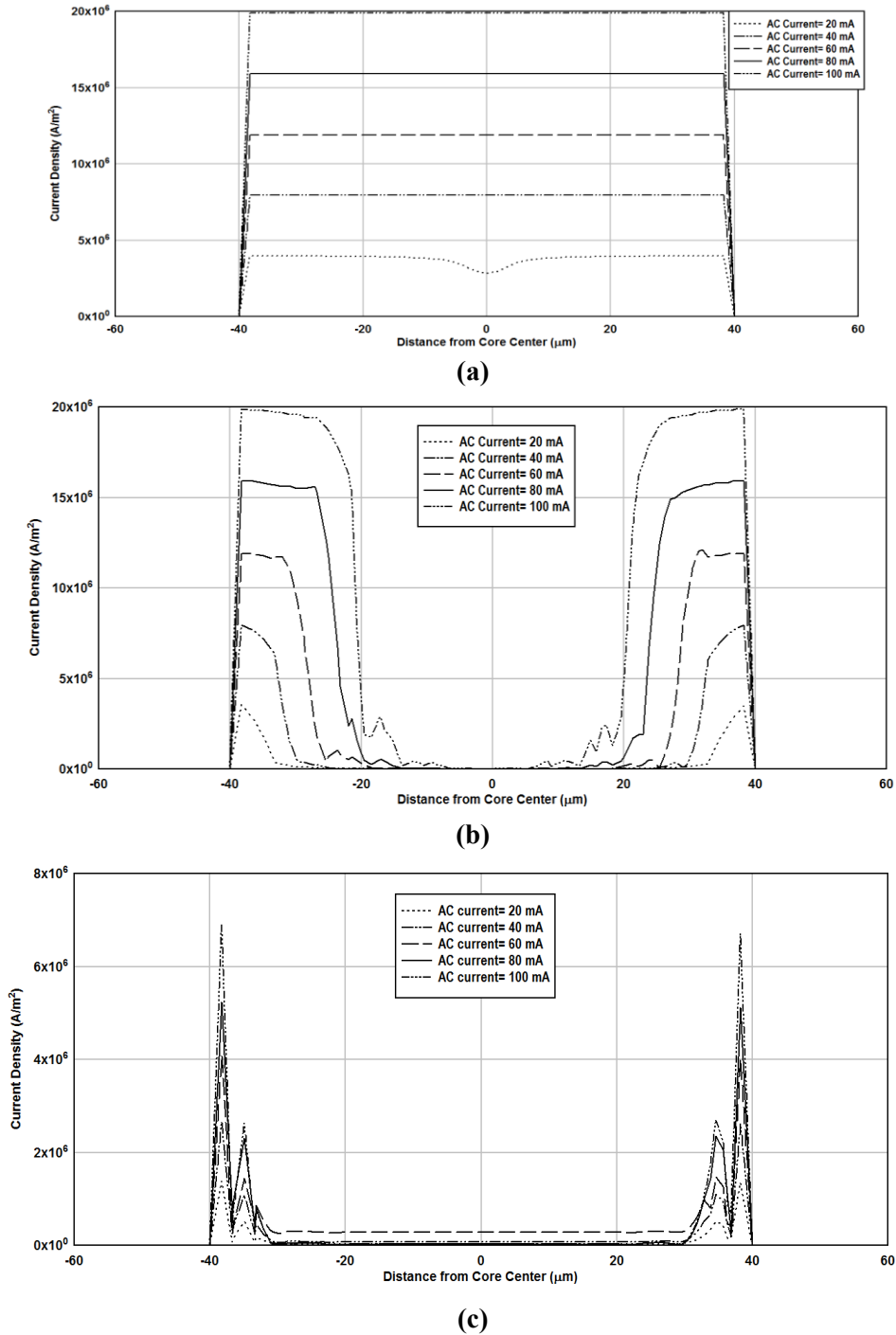
Figure 5-4: Current density radial distribution for different excitation amplitudes for a core with radius 40 µm at (a) 10 KHz, (b) 100 KHz, and (c) 1 MHz

(a)

(b)

(c)

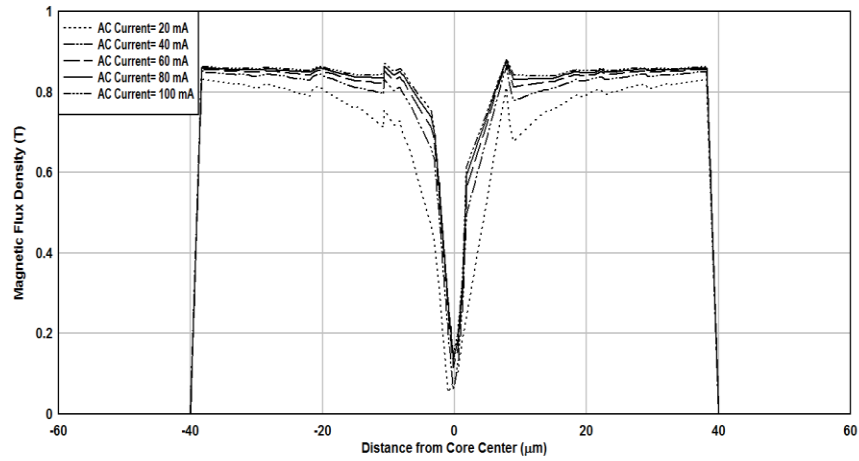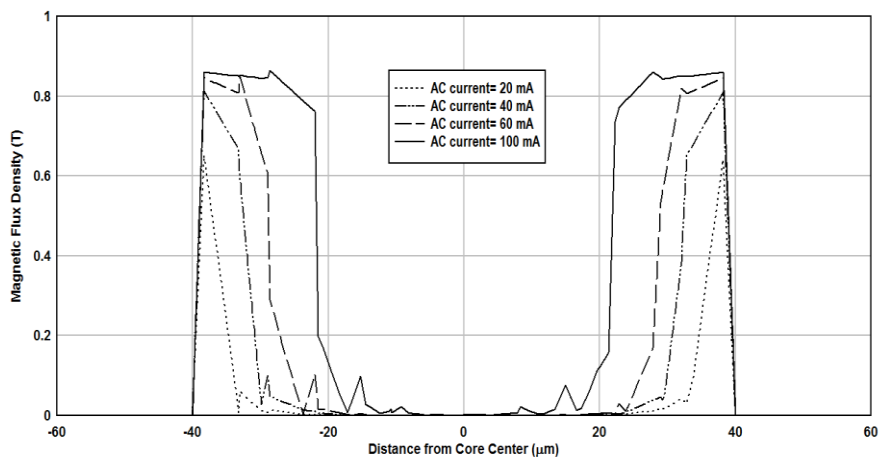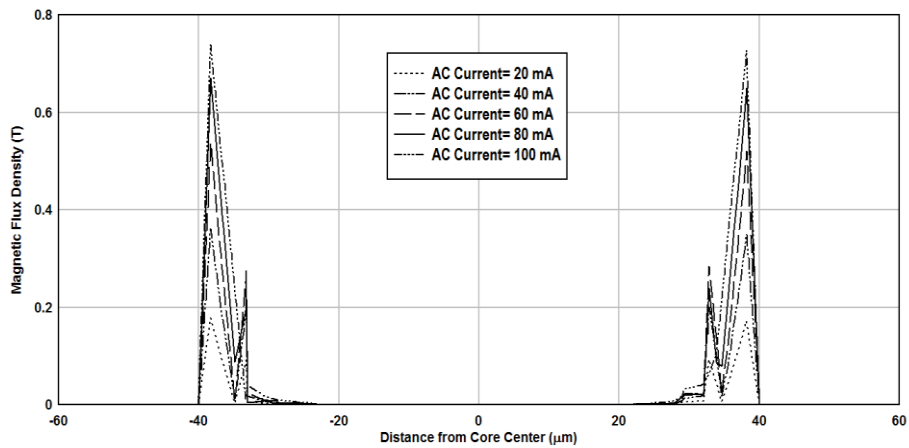**Figure 5-5 Magnetic Flux density radial distribution for different excitation amplitudes for a core with radius 40 µm at (a) 10 KHz, (b) 100 KHz, and (c) 1 MHz**

As presented in *Figure 5-4a*, at 10 KHz, the current density is homogenous along the microwire cross section for excitation amplitude values above 20 mA. This results in reduction of the region with relatively low flux density in the central part of the core

68

as shown in *Figure 5-5a*, with a close geometrical aspect of these regions for the change of current amplitudes from 40 mA to 100 mA.

However, when the frequency raised to be 100 KHz, the current density distribution starts to drain to the outer part of the microwire as displayed in *Figure 5-4b*, and its behavior, with the different excitation currents, changes when compared with *Figure 5-3a*, as a result of core radius increasing from 20 µm to 40 µm. The current penetrates deeper into the magnetic core with higher density values as the intensity increases rom 20 mA to 100 mA. The effect of increasing the core radius reflected also in the flux density distribution at the given frequency as shown in *Figure 5-5b*. The region with lower flux density values increases compared to *Figure 5-3b*. The flux density distribution exhibits the same trend as the current density distribution when the excitation amplitude increases. As the frequency increases to 1 MHz, the current density concentrates more on the outer region of the core as shown in *Figure 5-4c*, leaving the most core region with relatively very low values of current density. This is reflected on the flux density distribution, that keep the same trend with increasing of the flux density values as the current amplitude goes higher.

However, it should be highlighted that the maximum flux density value corresponding to each excitation amplitude decreased at 1 MHz excitation frequency (see *Figure 5-5c)*, compared with 10 KHz, and 100 KHz excitation frequencies. This can be attributed to the inherent characteristic of the magnetic core, which exhibits decrease in permeability µ value with frequency. *Figure 5-6* demonstrates a typical behavior of three different ferromagnetic materials, where µ value still constant as the frequency increases, until a certain frequency value, then it decreases. As a result the produced flux density B decreases as well. The corresponding decrease of the current density values in *Figure 5-5c* is due to increased impedance due to the skin effect [237].
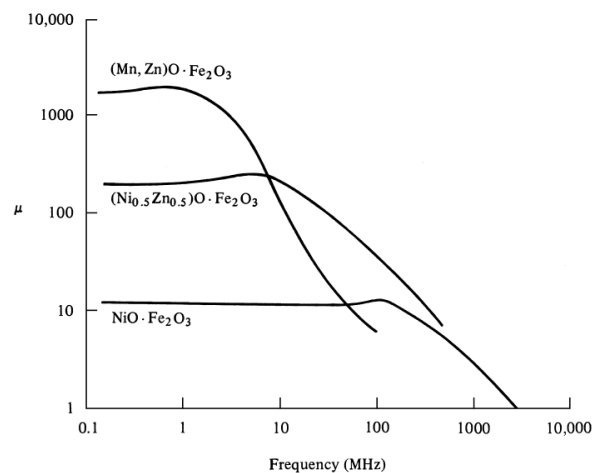
Figure 5-6: Variation of permeability with frequency for three different ferromagnetic materials

As seen from the above results, In addition to excitation frequency and amplitude, the design of the core geometry is a dominant factor in the performance of a miniature fluxgate. As a rule of thumb, a low sensitivity is expected when the amount of soft magnetic material inside the core is low [238]. From this perspective, the **fourth** study in this chapter concerns with including the core cross section effect, while changing the frequency and amplitude of the ac excitation current. Thus, in the fourth study, the

radius of the magnetic core increased from 20 μm to 100 μm , with air surrounded the core. For each core geometry, the microwire core is excited by an ac excitation frequency of 1KHz, 10 KHz, 100 KHz, and 1 MHz. *Figure 5-7a, b, and c* represents the current distribution along the core cross section where the current flow through the core has an intensity of 20 mA, 60 mA, and 100 mA respectively at 1 KHz.
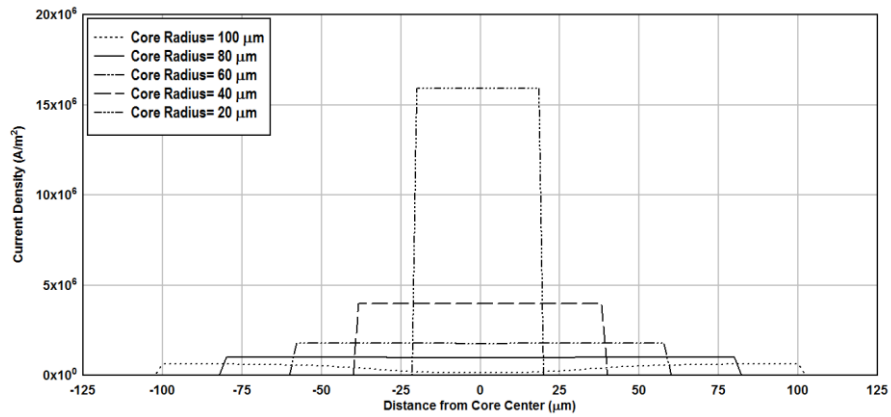
(a)
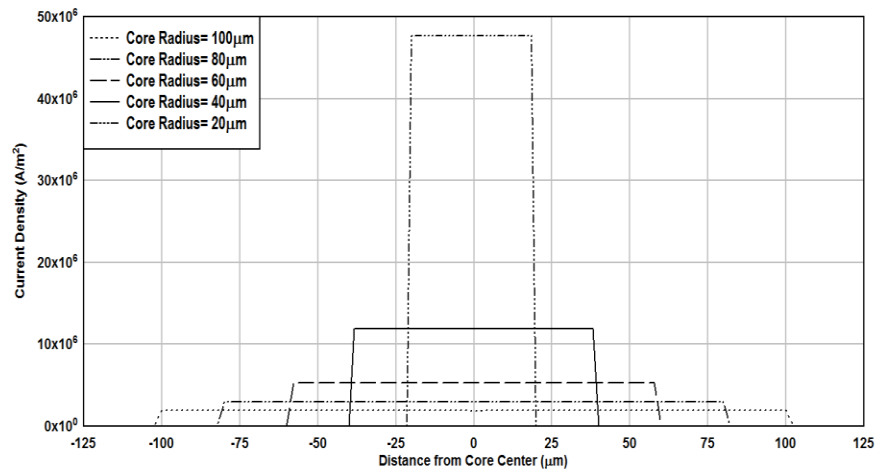
(b)
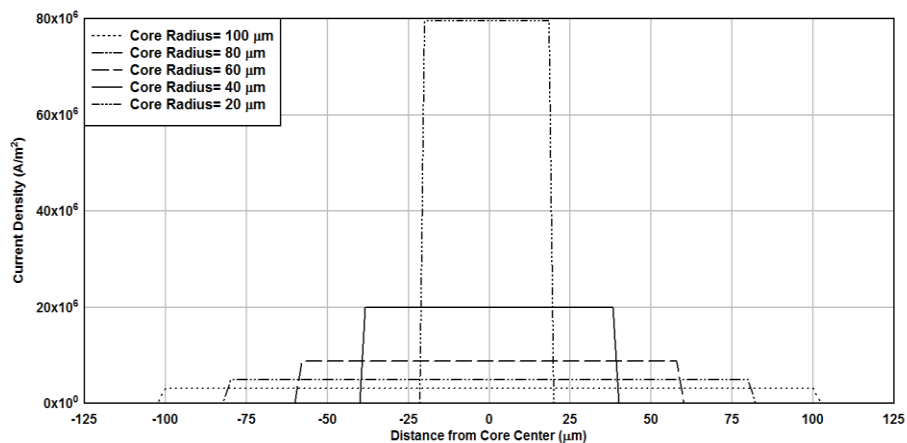
(c)

Figure 5-7: Current density radial distribution for different core diameters excited at 1 KHz with excitation amplitude of (a) 20, (b) 60, and (c) 100 mA

It can be seen that at 1 KHz excitation frequency, the 20 mA current amplitude was enough to homogenize the current density across microwire cores with radii 20, 40, and 60 μm. However, a slight reduction in the current density value appears at the central part of the core with radius 80 μm. This slight decrease become more obvious at the 100 μm radius core. Increasing the excitation current amplitude above 20 mA restores back the homogeneity in current density along all the cross sections of the cores with different radii. And as the current amplitudes goes from 20 mA to 100 mA, the current density values across the core's cross section increases as well. *Figure 5-8 a, b, and c* illustrates the corresponding flux density distributions for the current densities represented in *Figure 5-7a, b, and c* respectively. In *Figure 5-8a*, It can be seen that despite the homogeneity of the current destiny appears in *Figure 5-7a*, the flux density distribution is noticeably different for each core radius. For the 100 μm core, the area with low value of flux density is fairly large relative to the total diameter of the core. After that, as the core radius decreased from 80 μm to 20 μm, this area starts to shrink gradually.

(a)

(b)

(c)

Figure 5-8: Magnetic flux density radial distribution for different core diameters excited at 1 KHz with excitation amplitude of (a) 20, (b) 60, and (c) 100 mA

By increasing the excitation amplitude to 60 mA, the geometrical area representing the low flux density value changes significantly as shown in *Figure 5-8b*, especially for the cores with radii 100 μm, 80 μm, 60 μm, and 40 μm. Also, the flux density values inside these cores become higher compared to the relative values at *Figure 5-8a*. Increasing the excitation amplitude to 100 mA added more to the core with radius 100 μm, as the region with the low flux density values become smaller. The similar regions for the other core radii coincide with relatively close values to each other.

Due to the importance of the "High" frequency of excitation in improving the sensitivity of the sensor, the same (previous) configuration of core radii and excitation amplitudes will be investigated when the excitation frequency increase from 1 KHz to 10 KHz. *Figure 5-9 a, b, and c* represents the current distribution along the core cross section where the current flow inside the core has an intensity of 20 mA, 60 mA, and 100 mA respectively at 10 KHz.
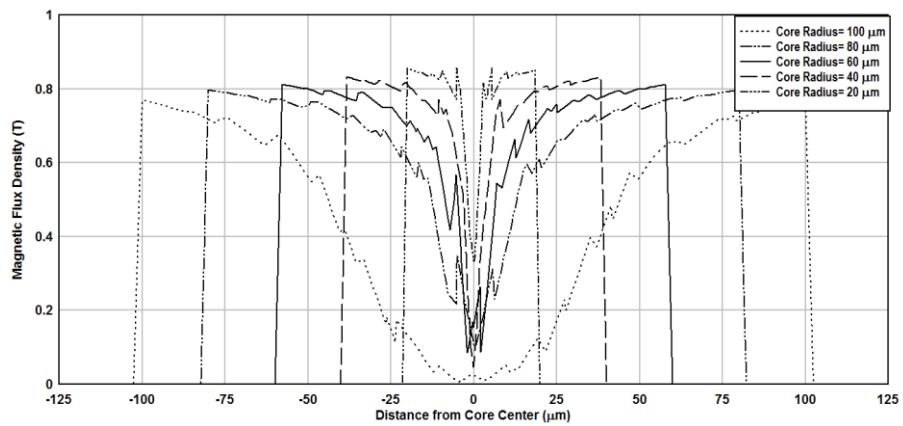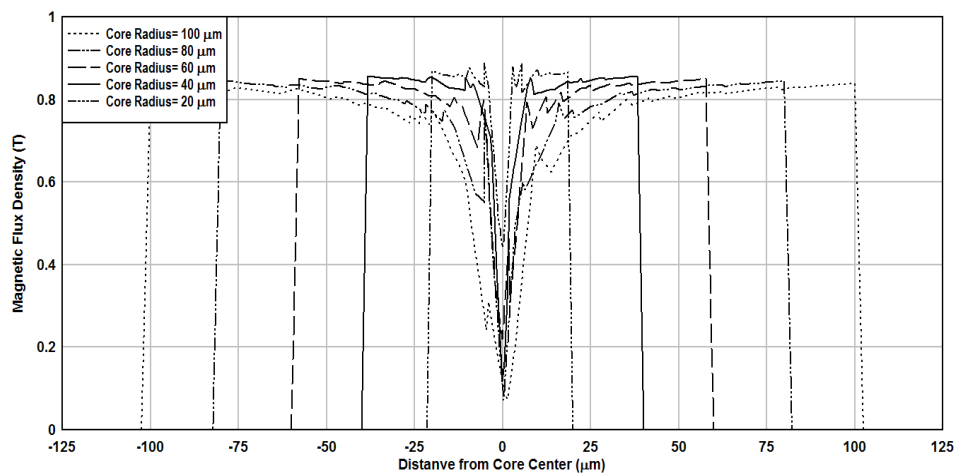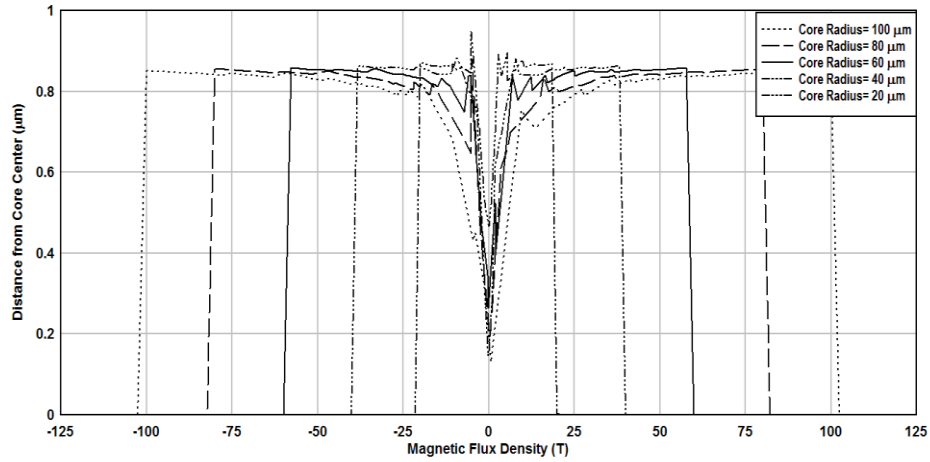

(a)
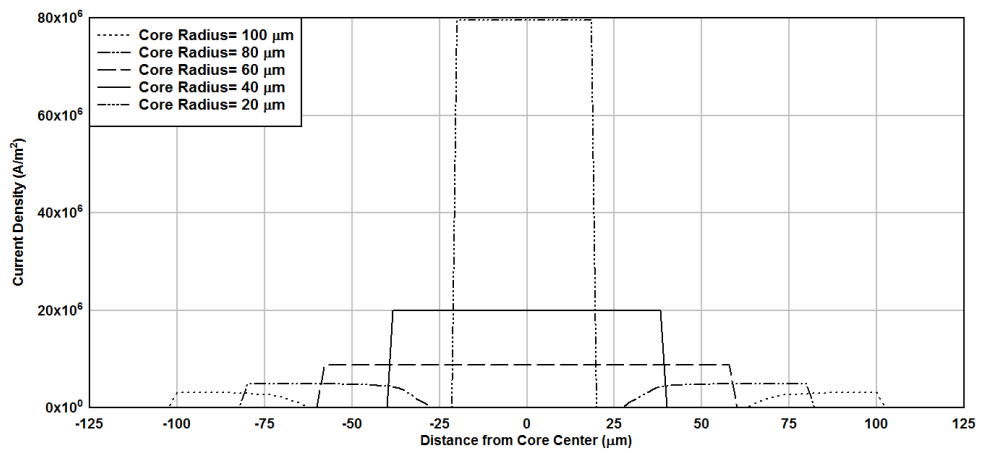
Figure 5-9: Current density radial distribution for different core diameters excited at frequency 10 KHz with excitation amplitude of (a) 20, (b) 60, and (c) 100 mA

From current density perception, homogeneity of current density inside the magnetic core with radius 20 μm didn't affected by increasing the excitation frequency. The other cores with radii 40, and 60 μm restores the homogeneity of the current density along the core's cross when the excitation amplitude reaches 60, and 100 mA respectively. For the cores with radii 40, and 60 μm, increasing the excitation intensity could not reinstate the homogeneity of the current density due to the skin depth effect as a result of employing a higher frequency to those cores.

Looking at the flux density perspective shown in *Figure 5-10*, for 20 mA excitation amplitude, the flux density inside the magnetic cores with radii 60, 80, and 100 μm takes a different pattern compared with *Figure 5-8a*, except the 20 and 40 μm radius cores flux density distributions, which almost remains unchanged with increasing the excitation frequency. As the excitation amplitude increases from 20 mA to 100 mA, the flux density distribution of the 60 μm radius core shrinks gradually to gain similar region of low flux density as the ones possessed by 20 and 40 μm radius cores. However, the region of the 60 μm radius core has a deeper tip in the vertical direction rather than the corresponding regions of 20 and 40 μm radius cores.

73
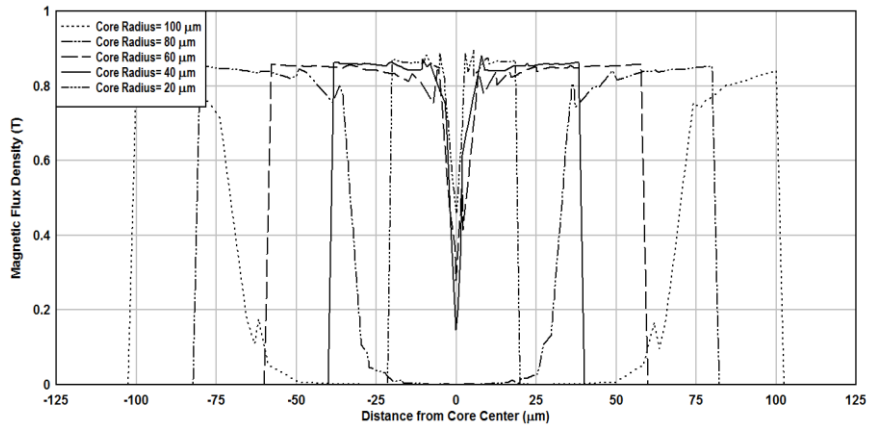
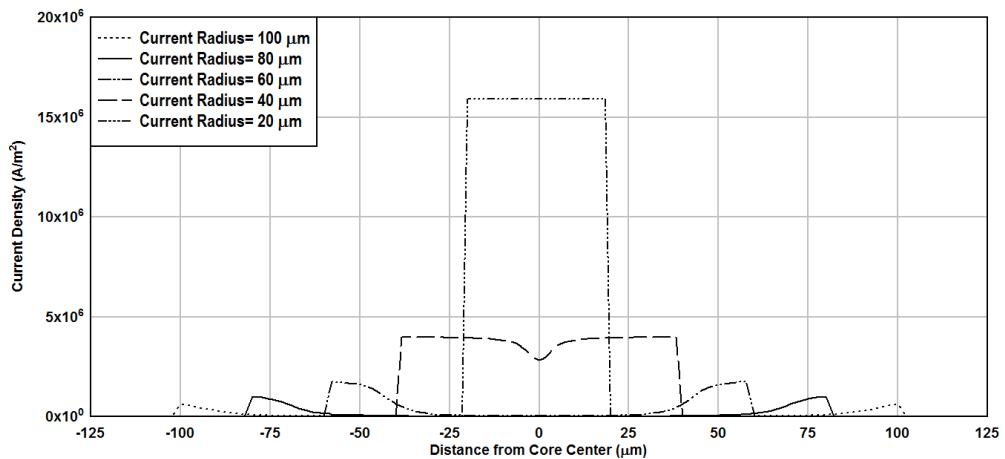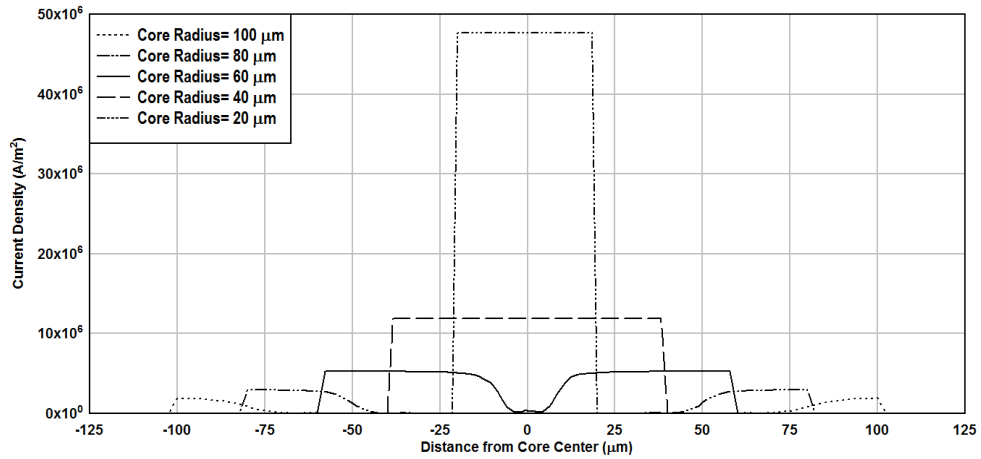**Figure 5-10: Magnetic flux density radial distribution for different core diameters excited at 10 KHz with excitation amplitude of (a) 20, (b) 60, and (c) 100 mA**

After that, further increase of the excitation frequency from 10 KHz to 100 KHz is examined for the same (previous) configuration of core radii and excitation amplitudes. *Figure 5-11 a, b, and c* represents the current distribution along the core cross section where the current flow inside the core has an intensity of 20 mA, 60 mA, and 100 mA respectively at 100 KHz.
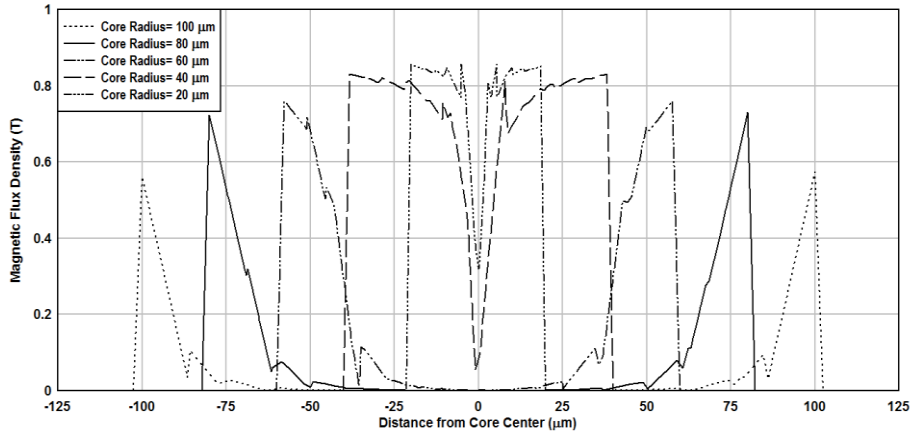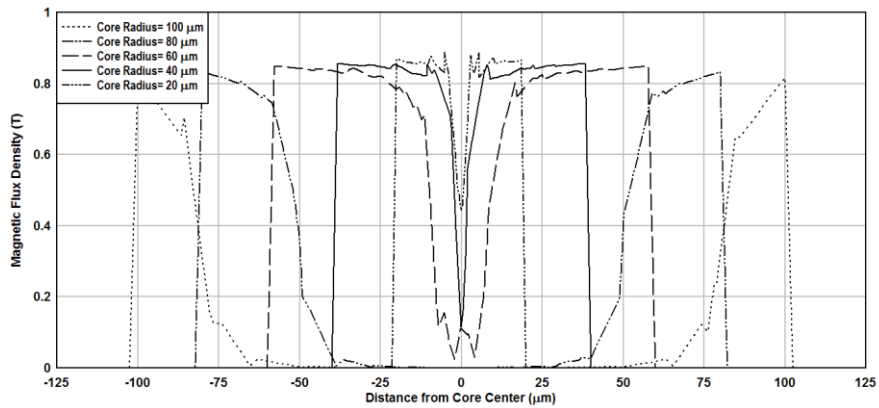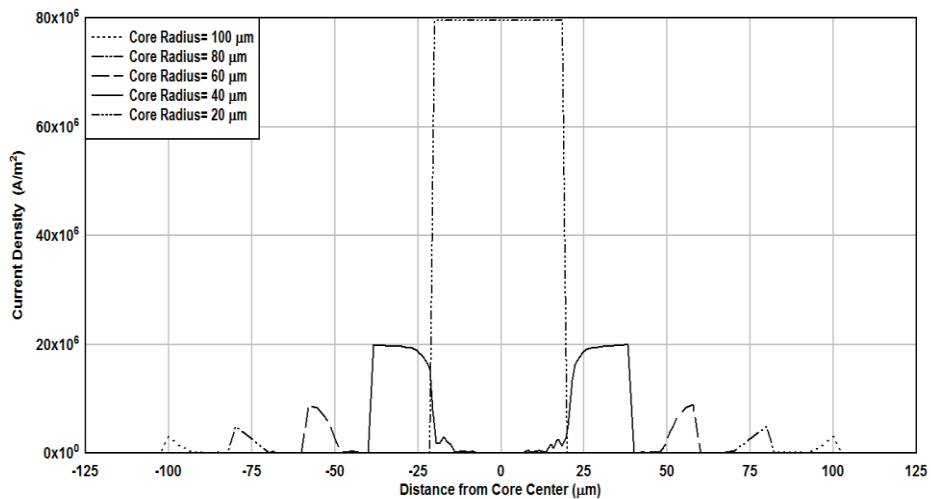
Figure 5-11: Current density radial distribution for different core diameters excited at 100 KHz with excitation amplitude of (a) 20, (b) 60, and (c) 100 mA

Increasing the excitation intensity from 20 mA to 60 mA succeeds in restoring the homogeneity of the current density along the core's cross section of the 20 μm radius core only. Further increase of the current amplitude to 100 mA fails to oppose the skin depth effect of increasing the excitation frequency. Furthermore, the maximum current density value decreases dramatically with core radius increase for the same excitation intensity. The flux density distribution standpoint is revealed in *Figure 5-12*, where the flux density distribution pattern changed drastically as compared to the lower excitation frequencies. Increasing the excitation frequency to 100 KHz contributes in reducing the maximum flux density value, for the same excitation amplitude, as the core radius increases from 20 μm to 100 μm. However, increasing the excitation amplitudes from 20 mA to 60 mA participates in raising the maximum flux density values for each core radius respectively. Furthermore, as the excitation amplitude increases, the low flux density region inside the core decreases as well, but didn't reach the same geometrical aspect of the previously 10 KHz excited cores, except for the 20 μm radius core. However, even for the 20 μm radius core, the geometrical aspect of the low flux density region changes significantly when the excitation current increases from 100 KHz to 1 MHz, as depicted in *Figure 5-13*. In this case, increasing the excitation amplitude has a least effect in minimizing the low flux density region compared to the lower excitation frequencies cases.

(a)

(b)

(c)

Figure 5-12: Magnetic flux density radial distribution for different core diameters excited at 100 KHz with excitation amplitude of (a) 20, (b) 60, and (c) 100 mA.
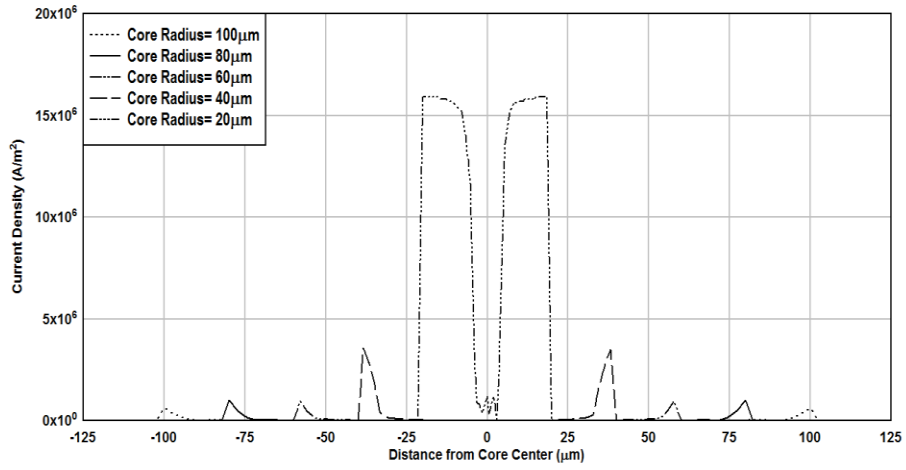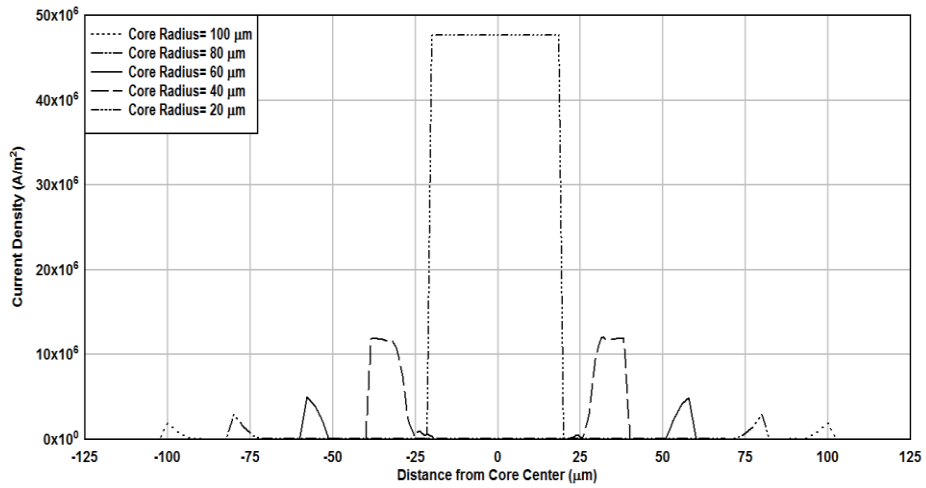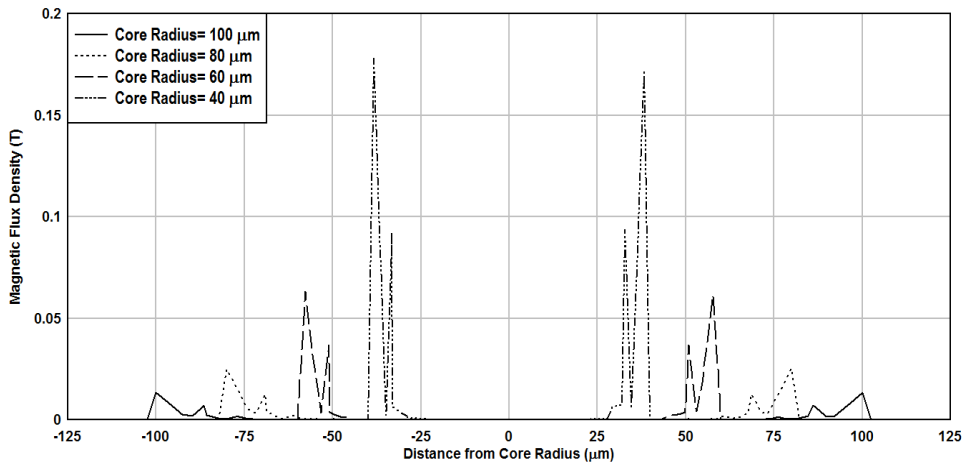

(a)
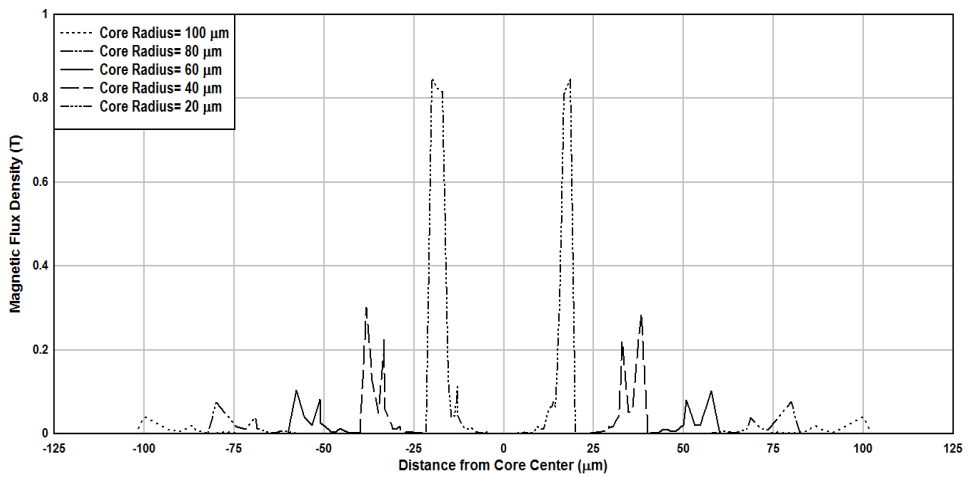
(b)
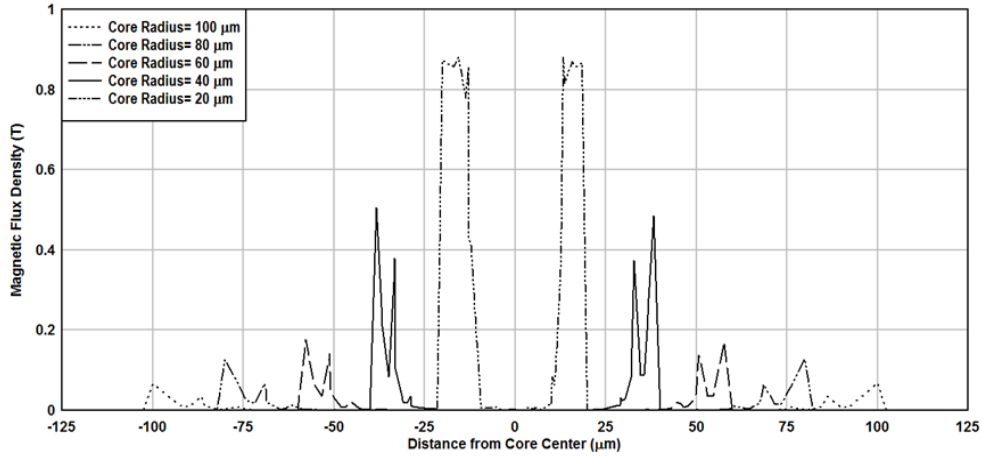
(c)

Figure 5-13 Magnetic flux density radial distribution for different core diameters excited at 1 MHz with excitation amplitude of (a) 20, (b) 60, and (c) 100 mA
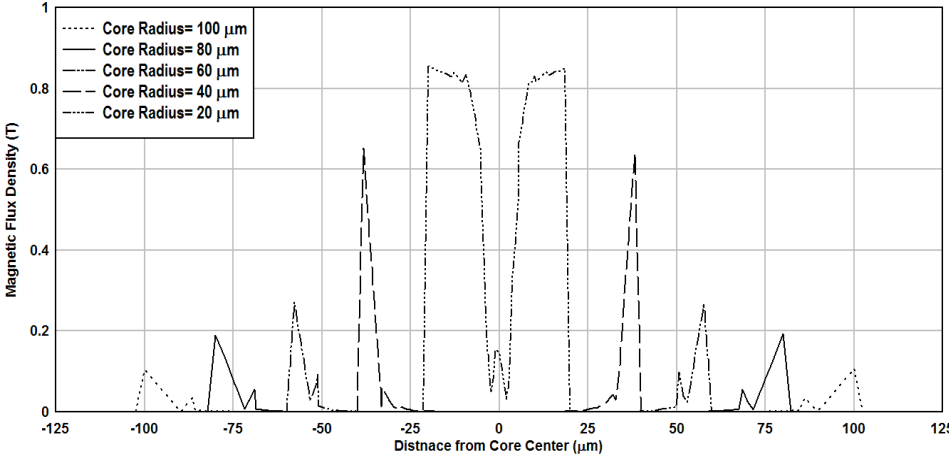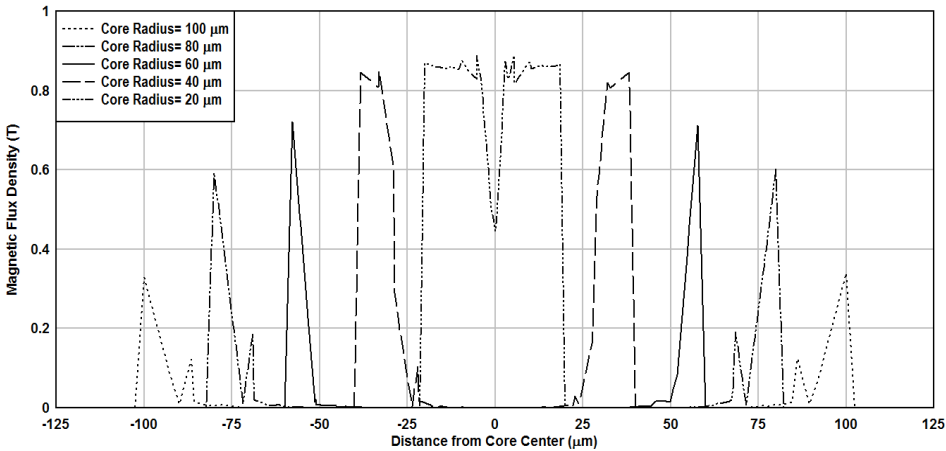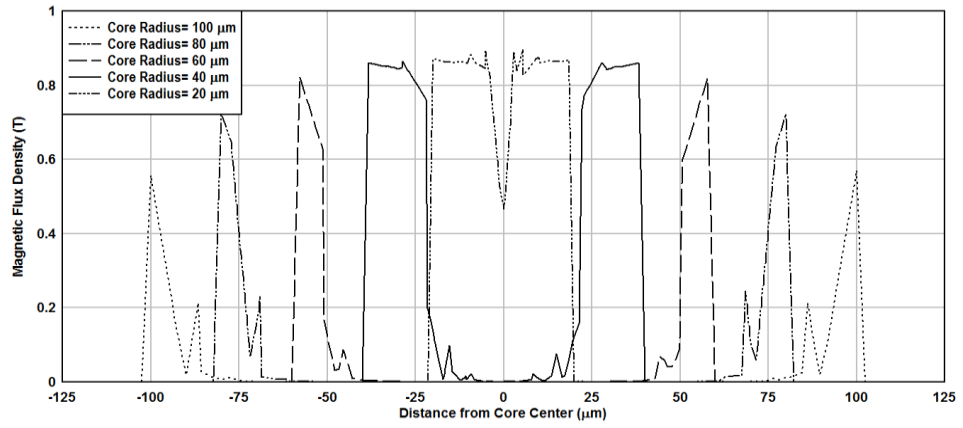
As it can be concluded from the previous studies, increasing the ac current contributes in decreasing the region of the low flux density inside the magnetic core, and hence, enhances its sensitivity. But, on the other hand, increasing the ac current participates in increasing the Barkhausen noise originated, as a result of magnetic domain dynamics, during the movement of magnetization from one dynamic state to the other [239]. One of the solutions to overcome the magnetic core noise is to add dc bias to the ac excitation current to establish another operation mode where magnetization varies mostly by coherent rotation, and thus the noise from magnetization is kept minimal. Also, it turns out that the dc bias amplitude relies on the hysteresis curve of the microwire core [240]. So, in this new mode of operation, minimum noise is obtained by proper selection of the excitation parameters I_{ac}, and I_{dc} . However, the choice of I_{dc} and I_{ac} is not a straightforward as one might think. It was found that the sensitivity decreases when the dc bias increases while the amplitude of the ac current is fixed [241]. This is because a higher dc bias causes the magnetization M to rotate toward the circumferential axis, reducing the amplitude of M oscillation. This means that M will become more attracted by $H_{dc} + H_{ac}$, resulting in smaller M_z variation. On the other side, sensitivity increases, as the ac current increases, while the dc bias is fixed. This is because as we increase H_{ac}, the angle ϱ swings to a greater extent resulting in a larger variation of M_z [242]. Looking from another prospective, the proper pair of I_{ac}, and I_{dc} depends on minimizing the region of low flux density value inside the core. Therefore, the **fifth** study in this chapter, concerns with tuning the amplitude of I_{ac} and I_{dc} for a given frequency and core radius to obtain the desired requirement. *Figure 5-14a, b, and c* illustrate the change in current distribution along a 40 μm radius core, as a result of dc bias, where the ac current flows through the core has an intensity of 20 mA, 60 mA, and 100 mA respectively at 10 KHz.
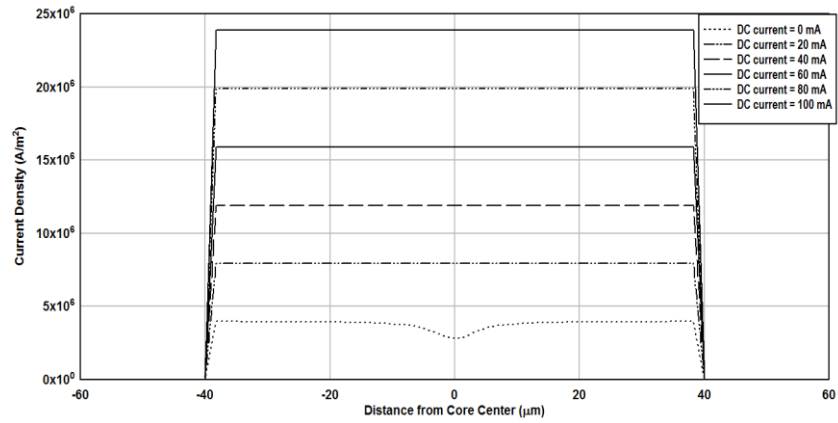
(a)
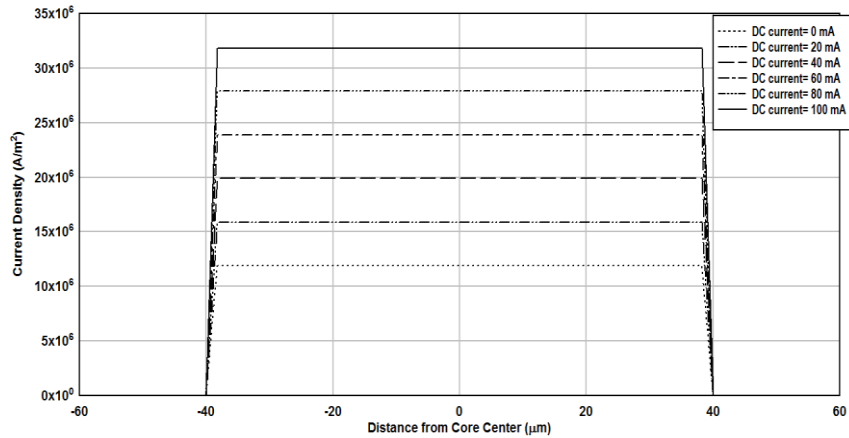
(b)
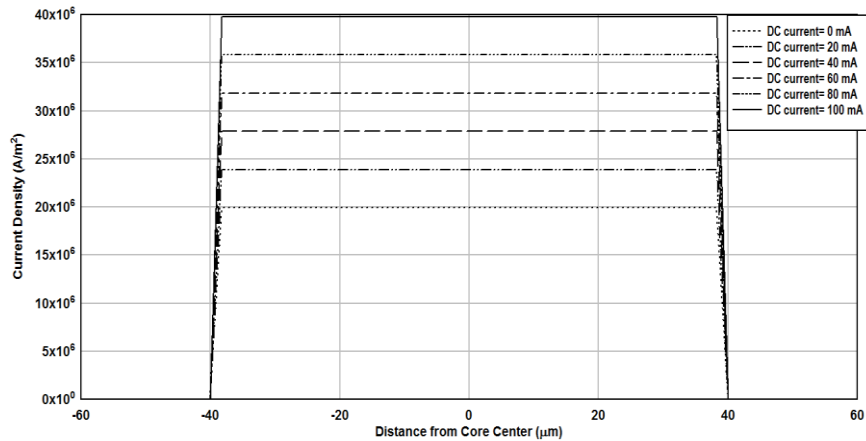
(c)

Figure 5-14 Current density radial distribution for different dc bias values for a 40 μm radius core excited at 10 KHz with ac excitation amplitude of (a) 20, (b) 60, and (c) 100 mA

It can be seen that adding the dc bias does not contribute in the homogeneity of the current density value along the core cross section, However, increasing the dc bias value for each ac excitation amplitude, causes only an increase in the level of current density inside the core. Furthermore, the effect of the dc bias on the flux density

distribution is relatively insignificant in reducing the low flux value region inside the core, as shown in *Figure 5-15*.

(a)
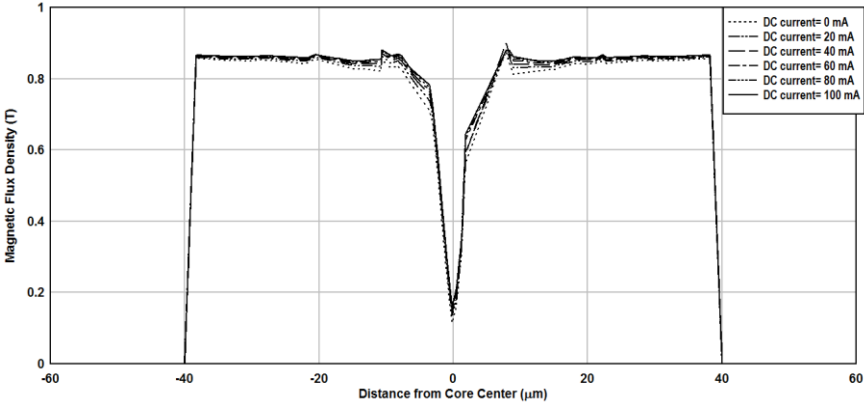
(b)
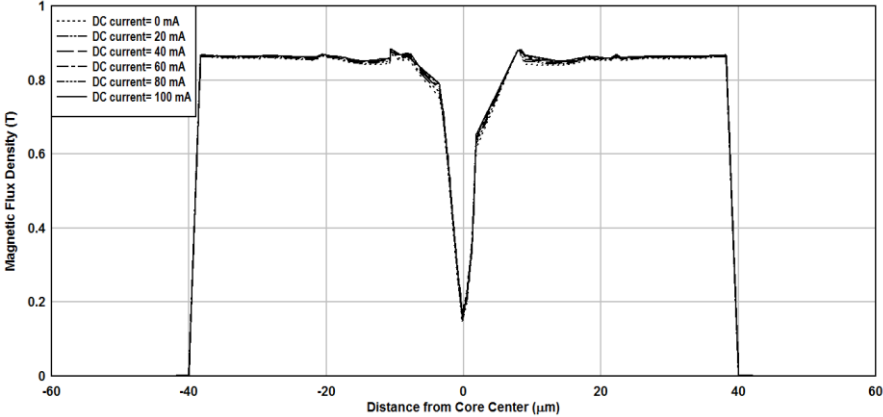
(c)

Figure 5-15 Magnetic flux density radial distribution for different dc bias values for a 40 μm radius core excited at 10 KHz with ac excitation amplitude of (a) 20, (b) 60, and (c) 100 mA

In the next step, another important parameter will be investigated which is the ac excitation frequency. In this case, another tradeoff will be added to study between low frequency that returns a low sensitivity, and high frequency that let the current affected by the skin effect. In this context, *Figure 5-16* depicts the influence of change in dc bias, when ac frequency become 100 KHz, on the current distribution along a 40 μm radius core, where the ac current flows through the core has an intensity of 20 mA, 60 mA, and 100 mA respectively.
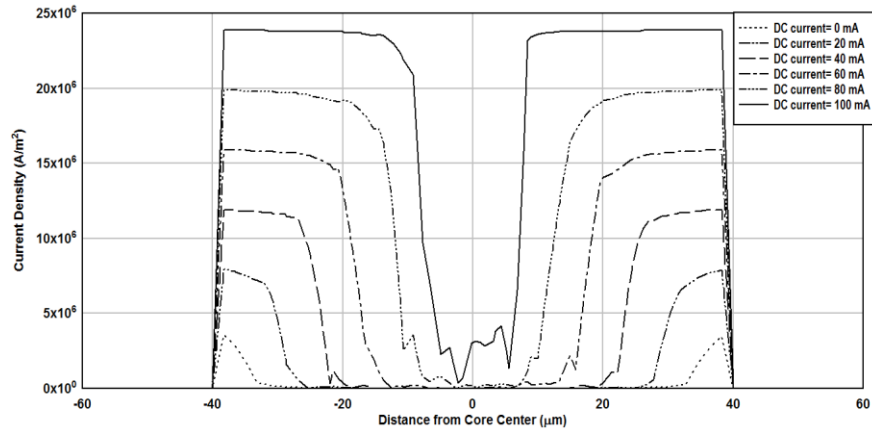
(a)
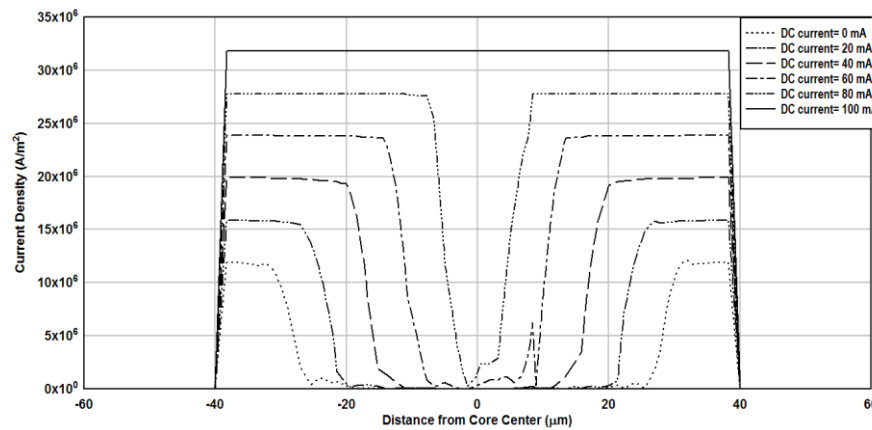
(b)
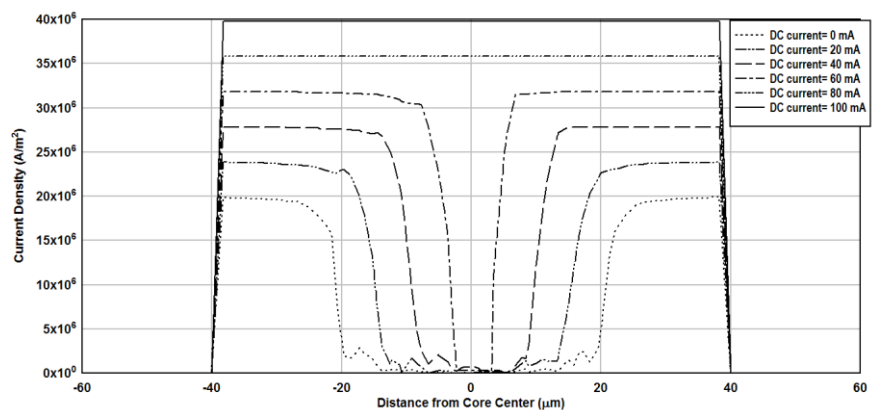
(c)

Figure 5-16: Current density distribution for different dc bias values for 40 μm radius core excited at 100 KHz with ac amplitude of (a) 20, (b) 60, and (c) 100 mA

It can be seen, from *Figure 5-16a*, that the skin effect starts to influence the current density distribution along the core cross section, leading to relatively low current density values in the central part of the core. However, as the ac current increases from 20 mA to 60 mA, the dc bias starts to counterpart the skin effect, and the current density values of the core's central part starts to increase, until a homogeneity along the core cross section is occurred at dc bias value of 100 mA as shown in *Figure 5-16b*. Further increase in the ac current to 100 mA, leads to a lower value of dc current "i.e. 80 mA" to uniform the current density along the magnetic core. On the other hand, as shown in *Figure 5-17*, even with increasing the ac current from 60 mA (*Figure 5-17b*) to 100 mA (*Figure 5-17c*), still a higher value of dc current "i.e. 100 mA" is needed to achieve similar low flux density area inside the core. Thus, It was thought that a higher value of I_{ac}, with proper value of I_{dc} can finally lead to very small region of low flux density. However, it has been shown that there is a limit to the I_{ac} values, and after that increasing it has relatively negligible effect.
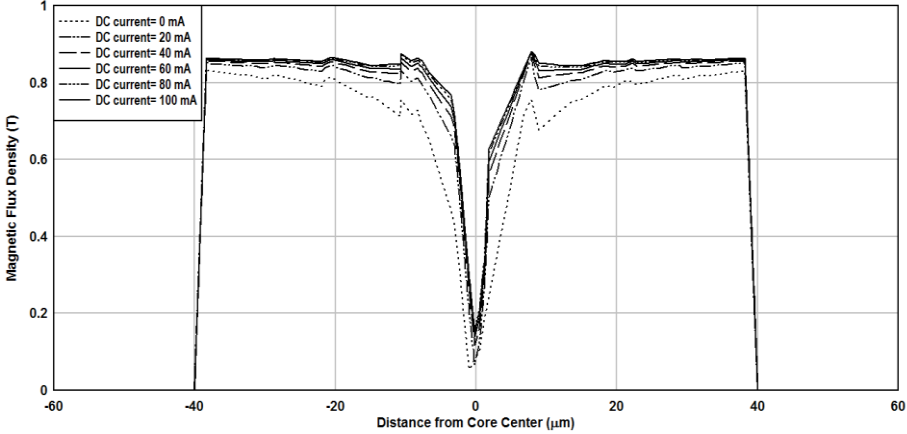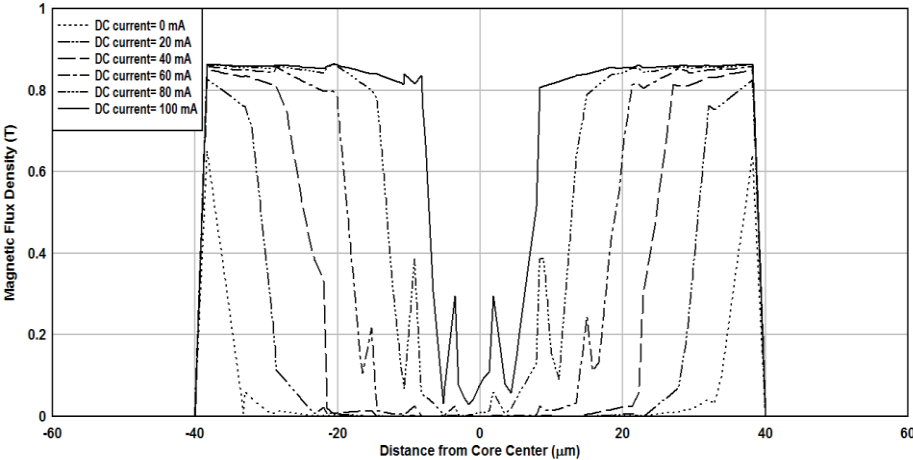

(a)
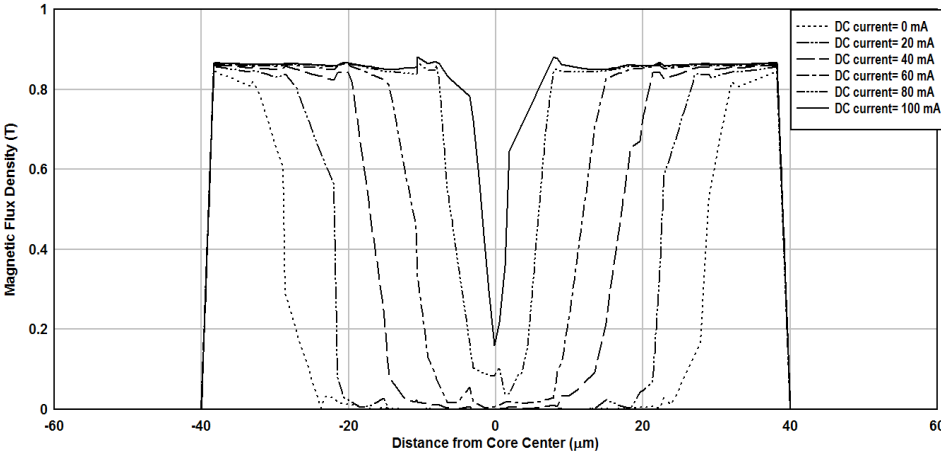
(b)
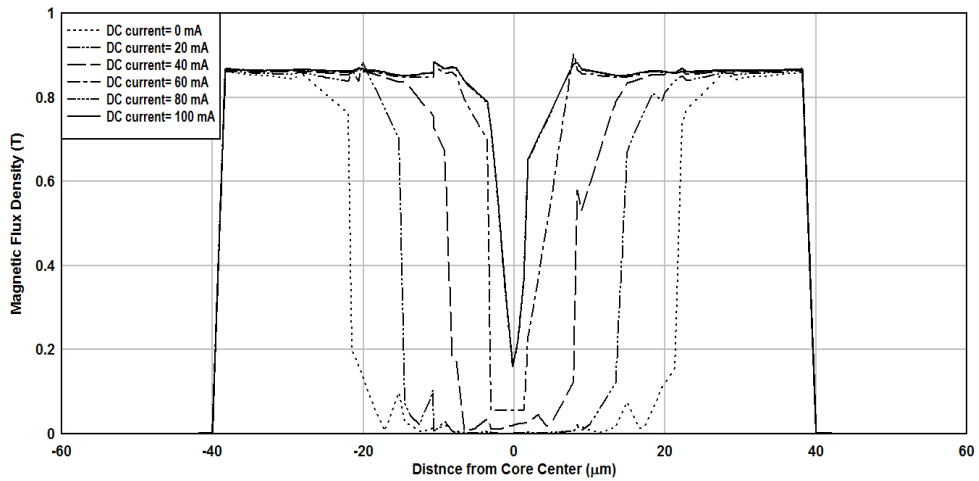
(c)

Figure 5-17: Magnetic flux density radial distribution for different dc bias values for a 40 µm radius core excited at 100 KHz with ac excitation amplitude of (a) 20, (b) 60, and (c) 100 mA

So far we considered only the case when the core radius is constant when tuning the values of ac current intensity and the dc bias. Therefore, the next step involves the impact of the core radius on the necessary values of ac current intensity and dc bias to reach the smallest portion of the core with low flux density values under a given frequency. In this context, *Figure 5-18a, b, c, d, and e* represents the current distribution along magnetic cores with radii 40, 60 ,80 , and 100 µm, excited at 10 KHz, where the Both the ac current and the dc bias passing through the core having an amplitude of 20, 40, 60, 80, and 100 mA respectively.
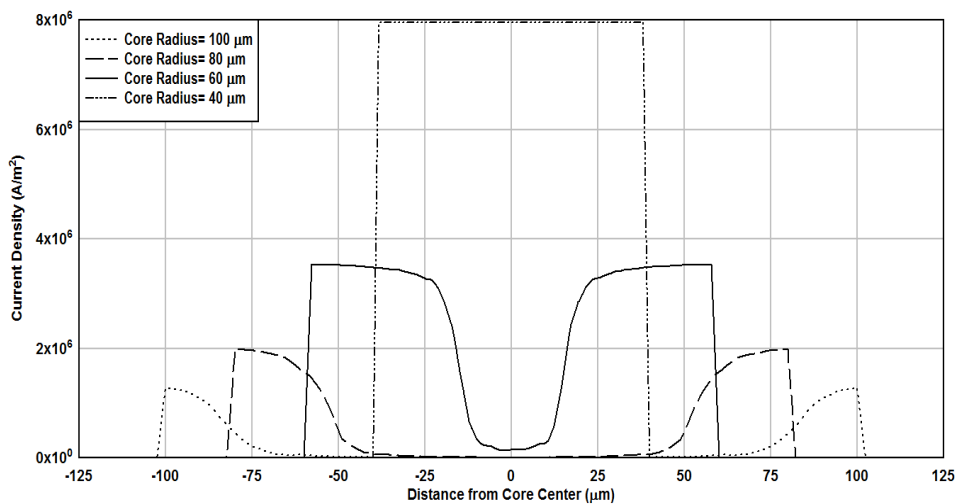
(a)
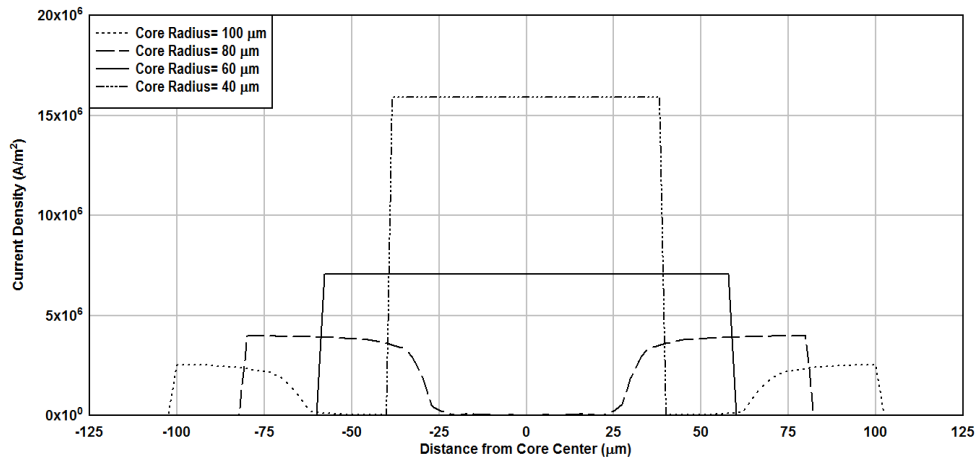
(b)
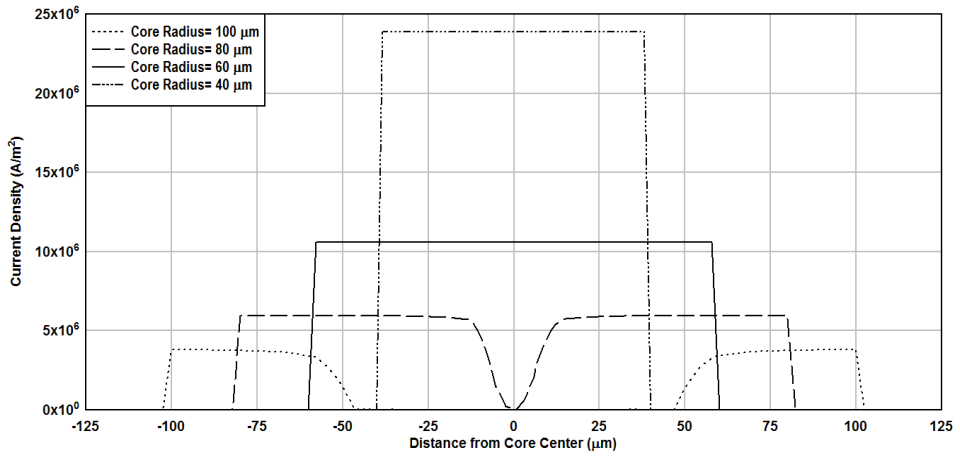
(c)
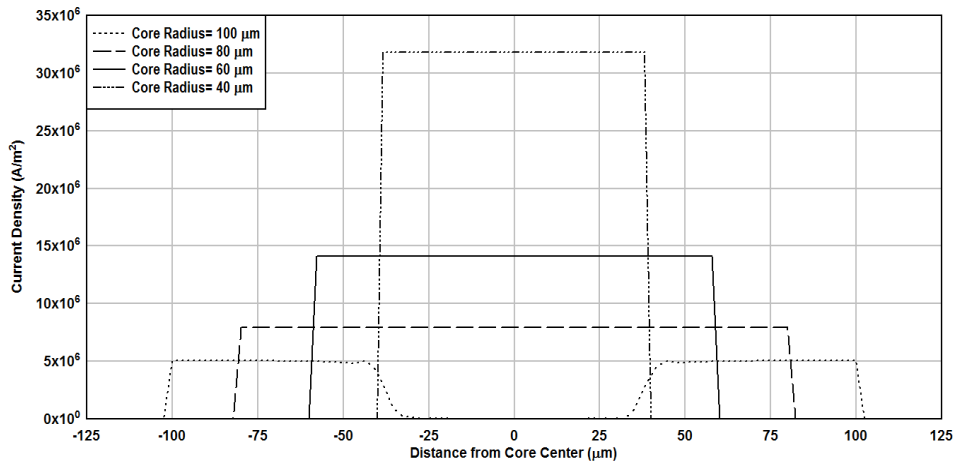
(d)
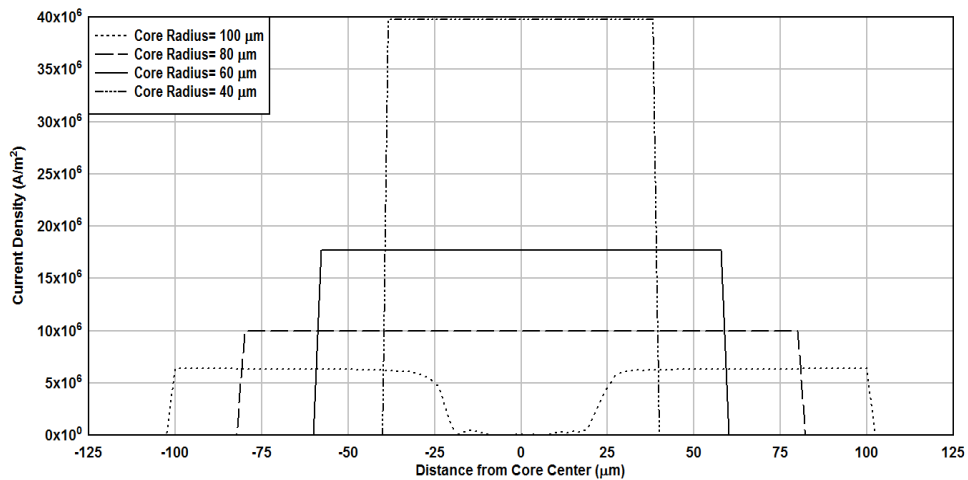
(e)

Figure 5-18: Current density radial distribution for different core radii for a core excited at 10 KHz with both an ac excitation, and dc bias amplitudes of (a) 20, (b) 40, (c) 60, (d) 80, and (e) 100 mA

It can be seen that when the cores are excited with 20 mA ac current, and 20 mA dc bias, the homogeneity in the current density occurs only for the 40 μm radius core, while the rest of the cores suffer from the skin effect, with a noticeable difference between the current density values of 40 μm radius core and the others, as shown in *Figure 5-18a*. However, when both ac current and dc bias increases to be 40 mA, the maximum current density values for all the investigated cores, increased considerably as shown in *Figure 5-18b*. Furthermore, the 60 μm radius core possess a homogenous current density value along its cross section beside the 40 μm radius core. Increasing both the ac current and dc bias to 60 mA contributes in minimizing the region of the low current density for the 60 μm radius core. Moreover, as shown in *Figure 5-18c*, the maximum current density values increases progressively, for each of the investigated cores, when compared to *Figure 5-18b*. Further increase in both the ac current and dc bias to 80 mA, participates in the current density homogeneity in the 80 μm radius core with increase in its maximum value as well as shown in *Figure 5-18d*. However, rising both the ac current and dc bias to 100 mA succeeds only in mitigating the skin effect inside the 100 μm radius core, with the increment of the maximum current density values for the rest of the examined cores as shown in *Figure 5-18e*.

From the flux density distribution perception, it can be observed, for the excited cores with 20 mA ac current, and 20 mA dc bias, that as core radius increases, the flux density drifts more to the border of the microwire, leaving the middle part with low values of flux density, as shown in *Figure 5-19a*. Also, the maximum flux density value for the examined core decreases gradually as the core radius increases. Intensify both the ac current and dc bias to 40 mA, participates in making the maximum flux density values for the examined cores relatively close to each other. However, the smallest sections of low flux density values can be found for the 40, and 60 μm radius cores as shown in *Figure 5-19b*. Further increase for both the ac current and dc bias to 60 mA contributes in shrinking the inner low flux density portion of the 80 μm radius core considerably as shown in *Figure 5-19c*. Further minimization of the inner low flux density segment of the 80 μm radius core achieved when both the ac current and dc bias

85

rises to 80 mA, as seen in *Figure 5-19d*. Finally, increasing both the ac current and dc bias to 100 mA, provides a more close values of the maximum flux density for all the investigated cores. However, as seen in *Figure 5-19e*, the enhancement in reducing the low flux density region of the 100 μm radius core, is not comparable to the other studied cores, even for the lower values of ac current and dc bias illustrated in *Figure 5-19d*.

(a)
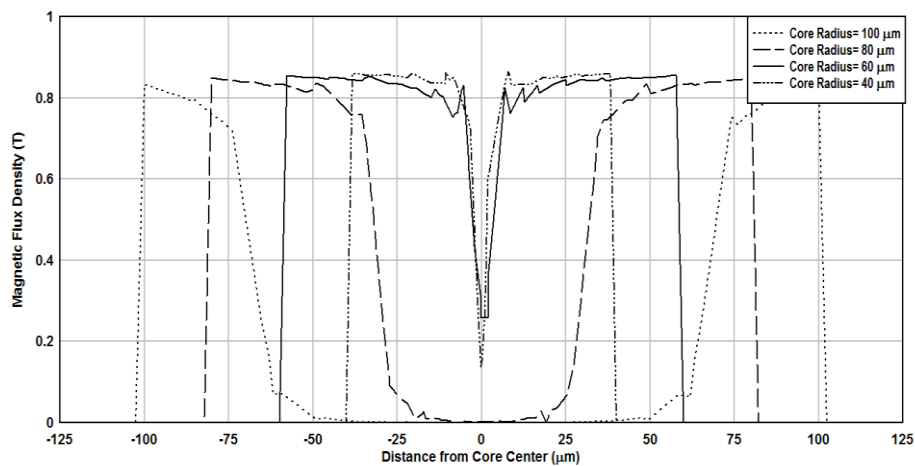
(b)
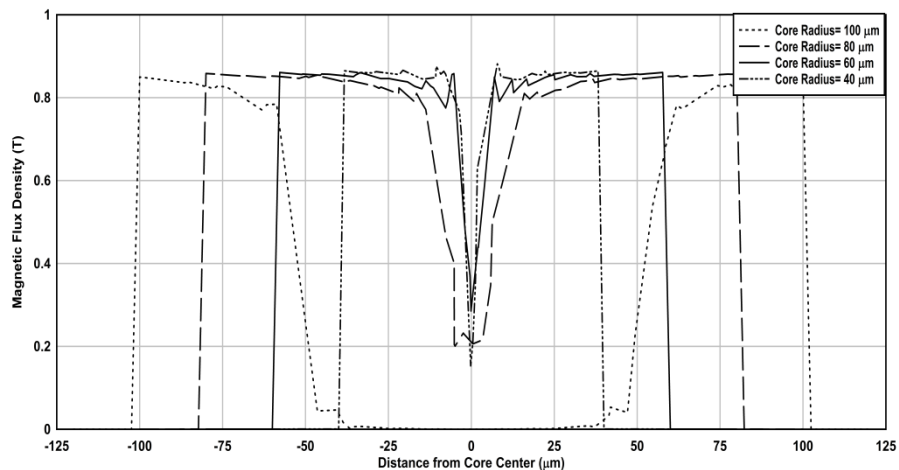
(c)
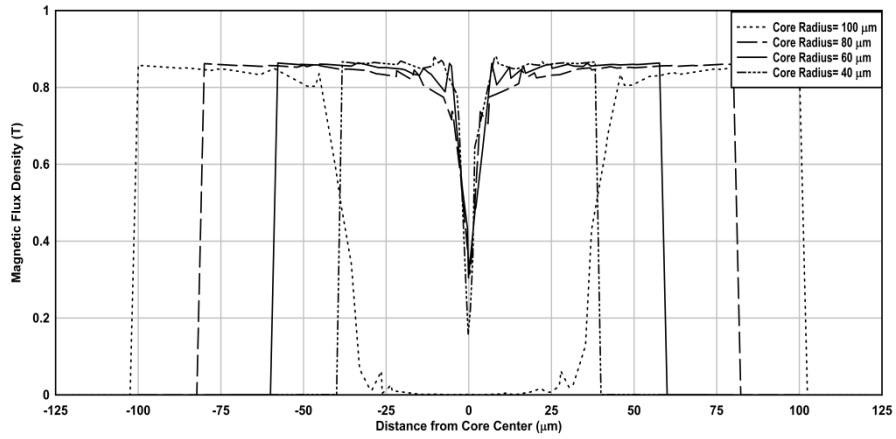
(d)
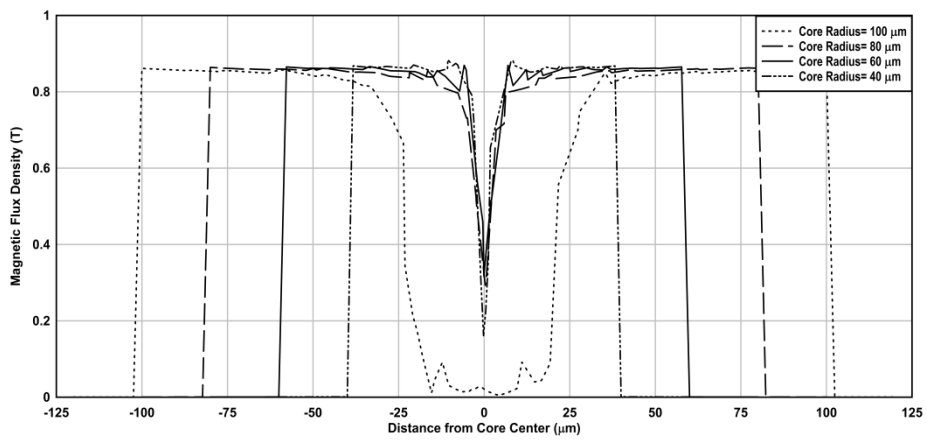
(e)

Figure 5-19: Magnetic flux density radial distribution for different core radii for a core excited at 10 KHz with both an ac excitation, and dc bias amplitudes of (a) 20, (b) 40, (c) 60, (d) 80, and (e) 100 mA

Moving forward, the current density behavior along the examined cores, for values of both ac current and dc bias of 60, 80, and 100 mA respectively, where the excitation frequency increases from 10 KHz to 100 KHz, is investigated in *Figure 5-20*.
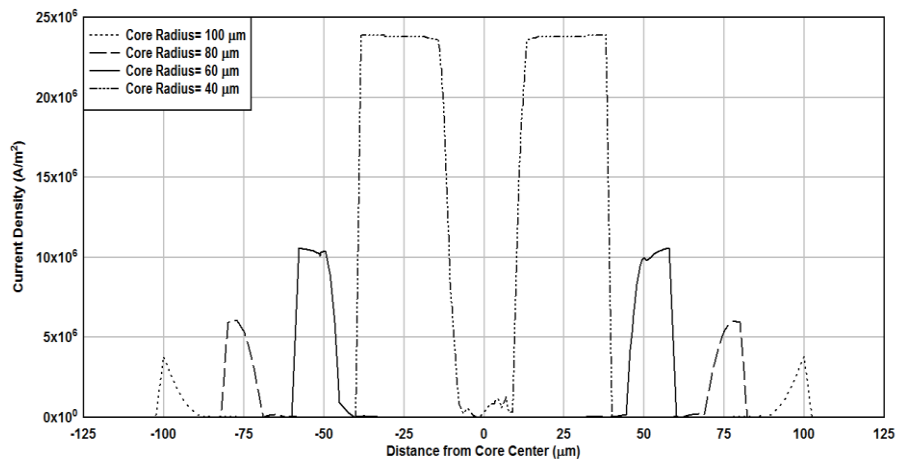
(a)
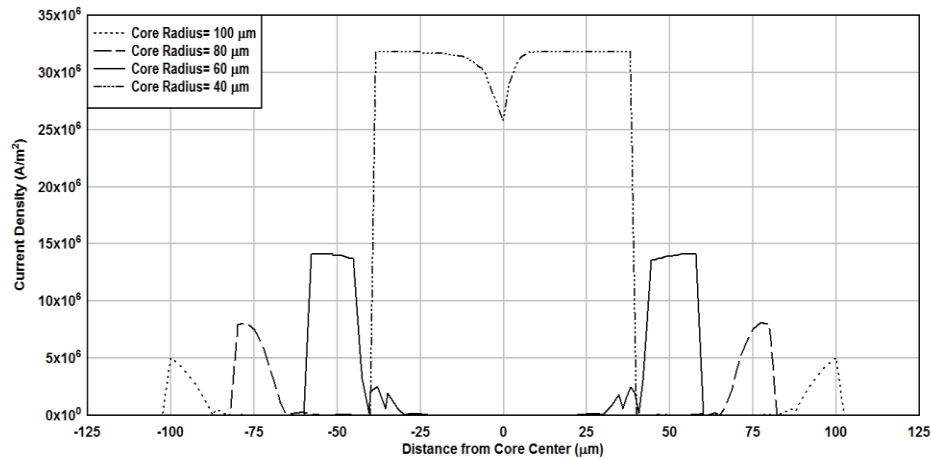
(b)
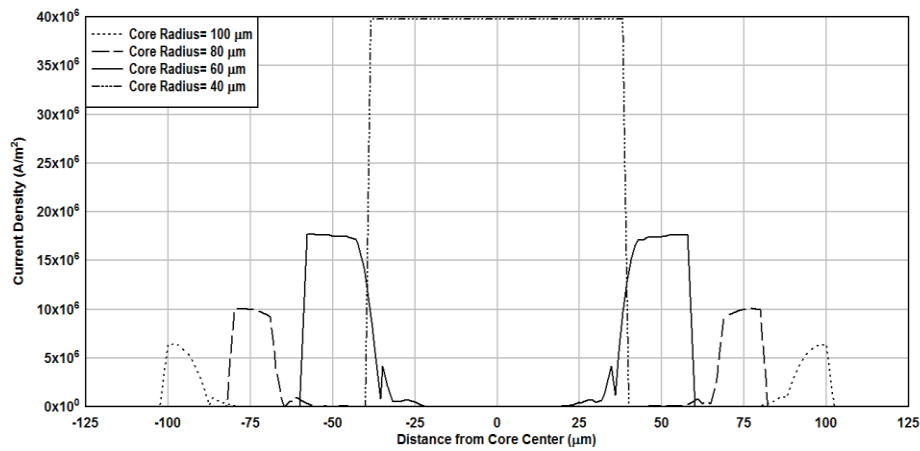
(c)

Figure 5-20: Current density radial distribution for different core radii for a core excited at 100 KHz with both an ac excitation, and dc bias amplitudes of (a) 60, (b) 80, and (c) 100 mA

It can be seen in *Figure 5-20a*, that when both ac current and dc bias is 60 mA, the skin effect noticeably affect all the examined cores. As the core radius increases, the current density inside the core drifts more toward the core's borders. Furthermore, the maximum current density values decreases as the core radius increases.

As both ac current and dc bias increases to 80 mA, the maximum current density values for each core increases remarkably. However, the low current density area in the core's central part becomes relatively minimal for the 40 μm radius core only. The improvement in minimizing the skin effect for the other cores is limited as shown in *Figure 5-20b*. Increasing both ac current and dc bias to 100 mA, enhances the current density homogeneity greatly for the 40 μm radius core only. However, these high values of ac and dc currents failed to oppose the skin effect due to increasing the frequency, as shown in *Figure 5-20c*. From flux density distribution standpoint, increasing both the ac current and dc bias from 60 mA to 80 mA contributes in minimizing the low flux density region in the 40 μm radius core center, compared to the corresponding region for the same core in *Figure 5-21a*. However, for the rest of studied cores, the area of low flux density in the middle of the core is relatively large as

seen in *Figure 5-21b*. Further increase of both ac current and dc bias from 80 mA to 100 mA, did not enhance the consequence of the skin effect for all the studied cores. However, increasing both the I_{ac} and I_{dc} currents, causes a slight increase in the maximum flux density values for all the investigated cores as shown in *Figure 5-21c*.
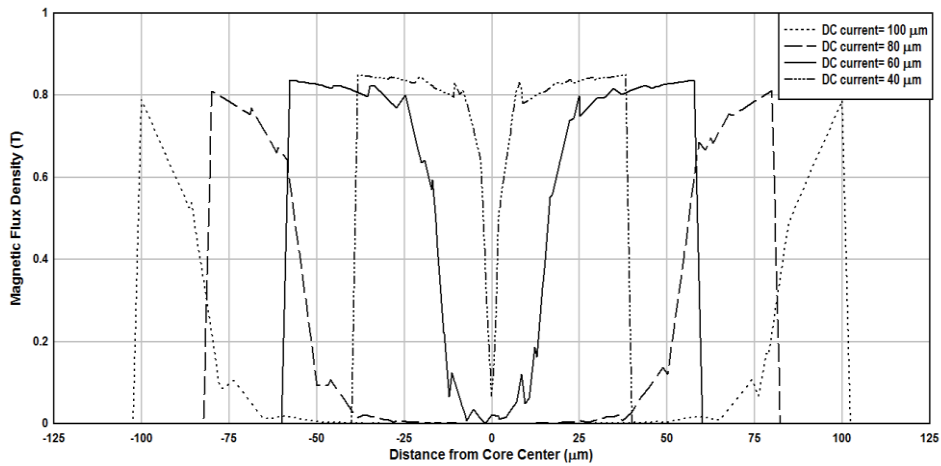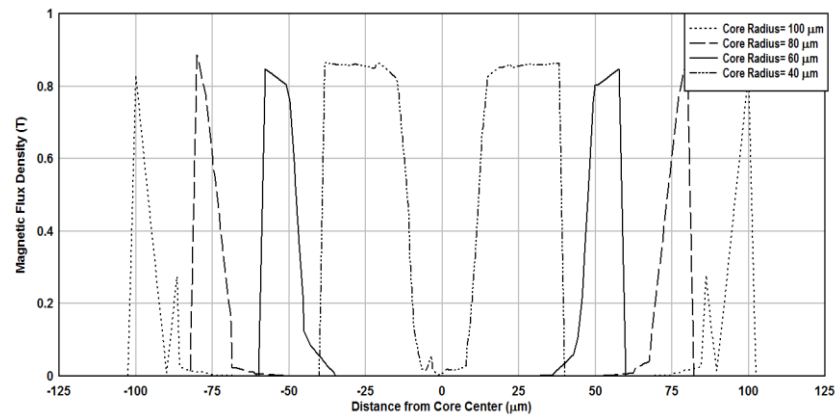

(a)
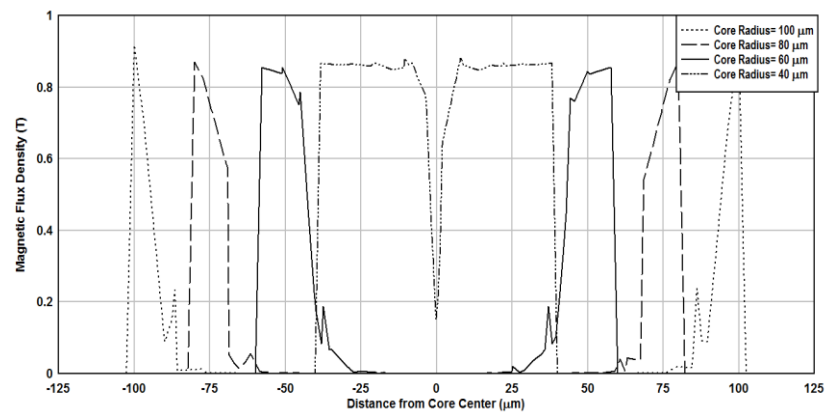
(b)
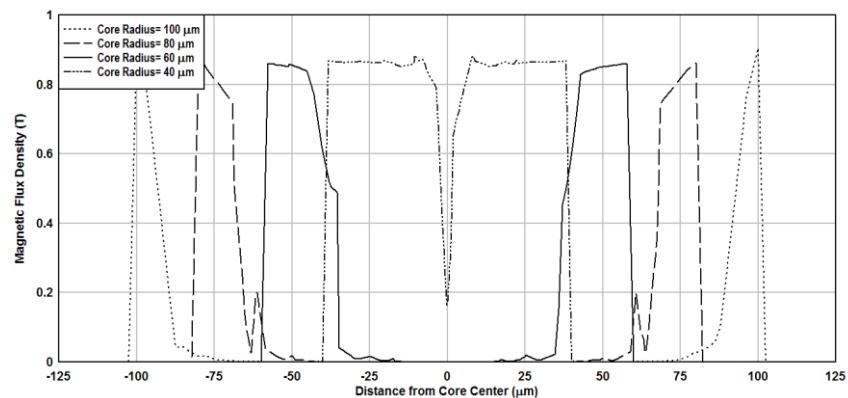
(c)

Figure 5-21: Magnetic flux density radial distribution for different core radii for a core excited at 100 KHz with both an ac excitation, and dc bias amplitudes of (a) 60, (b) 80, and (c) 100 mA.

5.4. Summary

Table 5.1 summarizes the results in this chapter. The first study tested the effect of frequency from 10 Hz to 100 KHz on a 20 μm radius core, excited by 20 mA ac current. The skin depth appears clearly at 100 KHz excitation frequency. However in the second study, for the 20 μm radius core, increasing the ac current at the 100 KHz frequency contributes in existence of flux desnisty, starting from 60 mA.

For the third study, increasing the core radius from 20 μm to 40 μm results in having flux density inside the core at 10 KHz. As ac current increase to 100 mA, the flux density for the 20 μm radius core at 100 KHz, could not be achieved for the 40 μm radius core.

The fourth study shows the effect of the core radius. At 1 KHz increasing the ac current helps in having flux inside cores with values up to 80 μm. Increasing the excitation frequency to 10 KHz decreases the core radius value to be up to 60 μm. At 100 KHz the core radius value that has flux density is 20 μm only. The flux density was not presented for any of the core radii, when a 1 MHz excitation frequency is used.

The fifth study is about the effect of adding dc bias . It was found that the dc bias helps in adding the 80 μm core radius with flux density at 10 KHz.

 Moreover, the dc bias participates in the addition of the 40 μm core radius, beside the 20 μm core radius, to have flux density at 100 KHz.

Table 5-1: Summary of the first configuration results

Mode	Core Radius	Excitation Frequency	AC Current	DC Bias
2nd Harmonic	20 μm	1 KHz	20 mA	
2nd Harmonic	40 μm	1 KHz	60 mA	
2nd Harmonic	60 μm	1 KHz	100 mA	
2nd Harmonic	80 μm	1 KHz	100 mA	
2nd Harmonic	20 μm	10 KHz	20 mA	
2nd Harmonic	40 μm	10 KHz	60 mA	
2nd Harmonic	60 μm	10 KHz	100 mA	
2nd Harmonic	20 μm	100 KHz	60 mA	
Fundamental	40 μm	10 KHz	20 mA	20 mA
Fundamental	60 μm	10 KHz	40 mA	40 mA
Fundamental	80 μm	10 KHz	80 mA	80 mA
Fundamental	40 μm	100 KHz	80 mA	80 mA

Chapter 6 : Composite Microwire Based Orthogonal Fluxgate Core: Simulations and Results

During the previous chapters, it has been understood that the orthogonal fluxgate sensor that uses a soft magnetic microwires as a core has an advantage by the ability to excite the core directly with a current flows inside the microwire. Thus, there is no need to have an excitation coil, which simplifies the fluxgate structure. However, the main problem of using this fluxgate core configuration is that magnetic flux density in the central part of the wire is relatively small. In previous chapter, several attempts to optimize the core parameters succeeded in reducing the area with the small magnetic flux density value considerably. But, as seen from the obtained results, there will always be an inner part of the core with a minimum magnetic flux density value. To avoid the existence of this undesired region, an alternative model for the fluxgate core is presented in this chapter. First, the proposed fluxgate core is modeled numerically using finite element analysis method. Then, different design factors have been tested through conducted simulations to reveal the effect of each design parameter on the relative assumptions adopted by the proposed fluxgate sensing element.

6.1. Background

Soft magnetic microwire based orthogonal fluxgate gained an interest because of the increasing demand for miniature magnetic field sensors. However, this kind of structure for the fluxgate core still has issues that might lead to unwanted consequences which affect the performance of the fluxgate magnetometer. The main concern comes from the behavior of magnetic flux density as the current injected directly into the soft magnetic material. As observed from the results of the previous chapter, the magnetic flux starts to be minimum at the center of the soft magnetic core and then it increases up to the maximum value at the borders of the wire. The first effect of this behavior is that only the outer part of the core will act as a fluxgate while inner part of the core will not participate in fluxgate mode.

One might think that the only impact of this effect is that the amount of the soft magnetic material participating in the fluxgate mode will be limited. Actually, this not the only problem, as such portion of microwire can be magnetized in another direction rather than circumferential one. The result of such magnetization will be a constant magnetic field that will act, at all extent, as a sensed field. Therefore this field will be added to the measured field generating an offset on the output characteristic of the fluxgate sensor [243].

Furthermore, adopting this configuration as a fluxgate's core will make the sensor, to some extent, is vulnerable to the perming effect, i.e., a change in fluxgate's output characteristic when relatively high magnetic field is present [244]. If the value of field is high enough, it may reverse the inner part magnetization, results in a variable offset at the fluxgate's output characteristic. In this context, the applied excitation field will not always be high enough to restore this portion of the microwire to its original state [245]. Additionally the excitation current that pass directly through the microwire core may increase the core temperature and could induce thermal treatment inside the soft magnetic core, and results in permanent change in the core's magnetic properties.

During the previous chapter, optimization of the core parameters succeeds, to some extent in reducing the portion of the core which has relatively low flux density values. However, based on Ampere's law, it is almost impossible to have a soft magnetic wire with uniform flux density values across the whole cross-section of the microwire, as, this, theoretically, could need an infinite excitation current [246].

To avoid the previously mentioned effects, an alternative design for the fluxgate core is presented in this chapter. The proposed structure suggests that the fluxgate core consists of a non-ferromagnetic part (excitation part) electroplated by a soft magnetic shell (sensing part). The main idea is that a material like copper as the excitation component of the core has low resistivity (~17 nΩ•m) compared to the resistivity of many soft magnetic materials (~200 nΩ•m) [247]. Thus, adopting such structure as a sensing element will pave the way for the necessary excitation current to flow mainly through the low resistivity way in the center of the core, and at the same time avoid any existence of regions with low magnetic flux density values inside soft magnetic part of the core. For this proposed structure it is assumed that, with a proper excitation current profile, the whole excitation current will flow inside the copper core leaving the magnetic layer with uniform magnetization. However, this assumption depends on actual current distribution that can significantly change the magnetic flux density. Therefore, throughout this chapter, several simulations will be conducted to validate the presented assumption, and examine the effect of different design parameters on the response of the proposed composite fluxgate core.

6.2. Composite Wire Based Fluxgate Core: Modeling and Simulation

In the second model in this thesis, the fluxgate composite microwire core consists of an inner rod of copper surrounded by an outer layer of soft magnetic material. The excitation current is injected directly (i.e., flows) into the copper rod, generating the circumferential magnetic field inside the soft magnetic shell. As in this thesis, we don't address the noise and sensitivity prospective, our problem includes describing the current density J, and magnetic flux B inside the whole composite microwire core. This is obtained through the calculation of electric and magnetic fields inside the geometry using finite element models developed in COMSOL Multiphysics. For evaluating the proposed design behavior, the excitation current profile, the diameter of the excitation part of the core, the thickness of the sensing part of the core, and the frequency are the main factors that was examined during simulations.

For the proposed composite core, The Jiles-Atherton hysteresis model with its five descriptive parameters is chosen to reproduce the magnetic hysteresis behavior of the soft magnetic part of the fluxgate core. The current density distribution inside the composite core was modeled when an ac current feed the copper part of the core with different amplitudes and frequencies to demonstrate the response of the different parts of the composite core against the excitation current profiles. Furthermore, the effect of adding dc bias with different amplitudes to the ac excitation mechanism was investigated to illustrate how this will affect the distribution of fields inside the composite core.

In this thesis, as the fluxgate core's structure has no geometrical variation in the direction orthogonal to the plane of study, this provides the problem to be solved with less physical memory and processing power of the personal computer. This is why we didn't apply 3D geometries simulations in this thesis. Instead, the use of two-

dimensional description was adopted to model the fluxgate core. Thus, we take the solution domain as a 2D planar circle that corresponds to the microwire cross section as illustrated in *Figure 6-1*. Also, a region outside the materials' domains is defined as a free air surrounding the composite core. After modeling the geometry of the core, *Magnetic Fields* interface is added under the *AC/DC* branch for the physics selection of the model. After adding physics for the model, we assign boundary conditions to the core. The magnetic continuity is employed for all boundaries except for boundaries at the edges of the solution medium, which are defined as magnetically insulated. After defining the governing physics and boundary conditions, a mesh is generated for the whole model in order to discretize the domain geometry of the core into triangular elements. After building the model, FEM simulations were conducted with different core radius values that are submitted to different excitation current amplitudes, and different frequencies to show the effect of design parameters on the field's density distribution along the entire composite wire cross section. The detailed analysis of fields due to the investigated design factors is presented in the next sections.
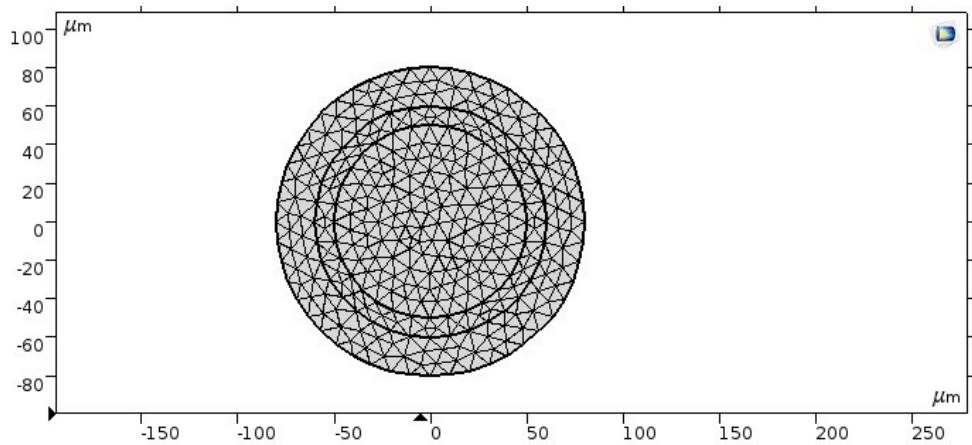
Figure 6-1: COMSOL solution domain for the second configuration

6.3. Analysis of the Results

In the first glance, it should be highlighted that during assessment of the composite core performance the aim of the conducted simulations is to adjust the different operating conditions, along with the core dimensions to illustrate mutual effect of the design factors on each other. One of the most common factors to be investigated for the fluxgate core design is the excitation current. Thus, the first study to be conducted in this chapter is the effect of excitation current on the composite microwire core. At the beginning, the radius of the excitation part of the composite core is chosen to be 25 µm, and the thickness of the soft magnetic part of the composite core is chosen to be 10 µm. The whole composite core is surrounded by air, and the total current passing through the cross section of the excitation part of the core was defined as an ac current having a total intensity changing from 20 mA to 100 mA, with no dc bias, at 50 KHz frequency. *Figure 6-2* depicts effect of the ac excitation current on current density, and magnetic flux distribution.

(a)

(b)

Figure 6-2: (a) Current density radial, and (b) Magnetic flux density radial distributions for composite core excited at 50 KHz with different ac excitation amplitudes

As shown in *Figure 6-2(a)*, the current density distribution along the excitation part of the core is homogenous, while the current density value increases as the ac excitation current increases from 20 mA to 100 mA. However, at each ac current value, the current density starts to drain from the copper part of the core to the soft magnetic shell, with a decrease in the current density amplitude until it is minimum at the outer order of the soft magnetic shell. This behavior reflected on the magnetic flux density response inside the soft magnetic shell, as it contributes in reducing the magnetic flux density values. As shown in *Figure 6-2(b)*, Flux density value is maximum at the inner border of the soft magnetic shell, and starts to drop until it reaches a lower value at the outer border of the soft magnetic shell. Furthermore, as the ac excitation current increases, the maximum value of the flux density increases as well. However, this increment did not contribute in uniform the amplitude of the flux inside the shell.

In the next step, another important parameter will be investigated which is the dc bias. Thus, the second study in this chapter, concerns with adjusting the amplitude of I_{ac} and I_{dc} for a given frequency and core radius to obtain better response. *Figure 6-3* illustrates the change in current, and flux distributions, as a result of dc bias, along a composite core with excitation part of 25 μm radius, and a soft magnetic shell of 10 μm thickness. The ac current passing through the excitation part of the core increases

compared to the previous study to have an intensity of 40 mA at 50 KHz. From *Figure 6-3(a)* it can be observed that as the dc bias value increases from 0 mA to 100 mA, the current density value increases, with a uniform value inside the excitation part of the core. Furthermore, compared with *Figure 6-2(a)*, the same trend of decaying in the current density value at the border between the copper part, and the soft magnetic shell is observed for all the investigated values of dc bias.

(a)
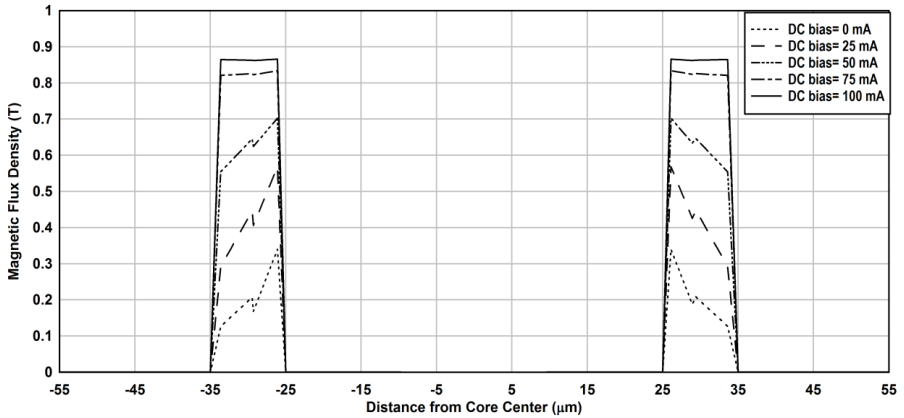
(b)

Figure 6-3: (a) Current density, and (b) Magnetic flux density radial distributions for a composite core excited at 50 KHz with ac excitation amplitude 40 mA at different dc bias values

Figure 6-3(b) illustrates the corresponding flux response against the change in the dc bias value. As the dc bias increase from 0 mA to 50 mA, the flux density distribution inside the soft magnetic shell follow the same trend seen in *Figure 6-2(b)*. Interestingly, a further increase of the dc bias to be 75 mA helps to restore the uniformity of the flux density along the magnetic shell cross section. Furthermore, a higher value of flux density, with more homogenous pattern, is achieved as the dc bias reaches 100 mA. However, this was obtained with a higher current density value inside the excitation part of the core. Before proceeding further, it should be noted that the common selection of the excitation mechanism involves a high value of the ac current in order to reduce the noise, and also a high dc bias value that should be enough to allow the increase of the ac current value, but at the same time not too high to avoid a drop of

sensitivity [248]. Staring form this standpoint, the next step in our analysis is to increase the ac current value for the tested configuration. *Figure 6-4* shows the influence of change in the dc bias, when the ac current increase to be 60 mA at 50 KHz, on the current and flux density distribution along the core cross section. The composite core is surrounded by air where the radius of the excitation part of the core is kept at 25 μm, and the soft magnetic shell thickness is kept at 10 μm.
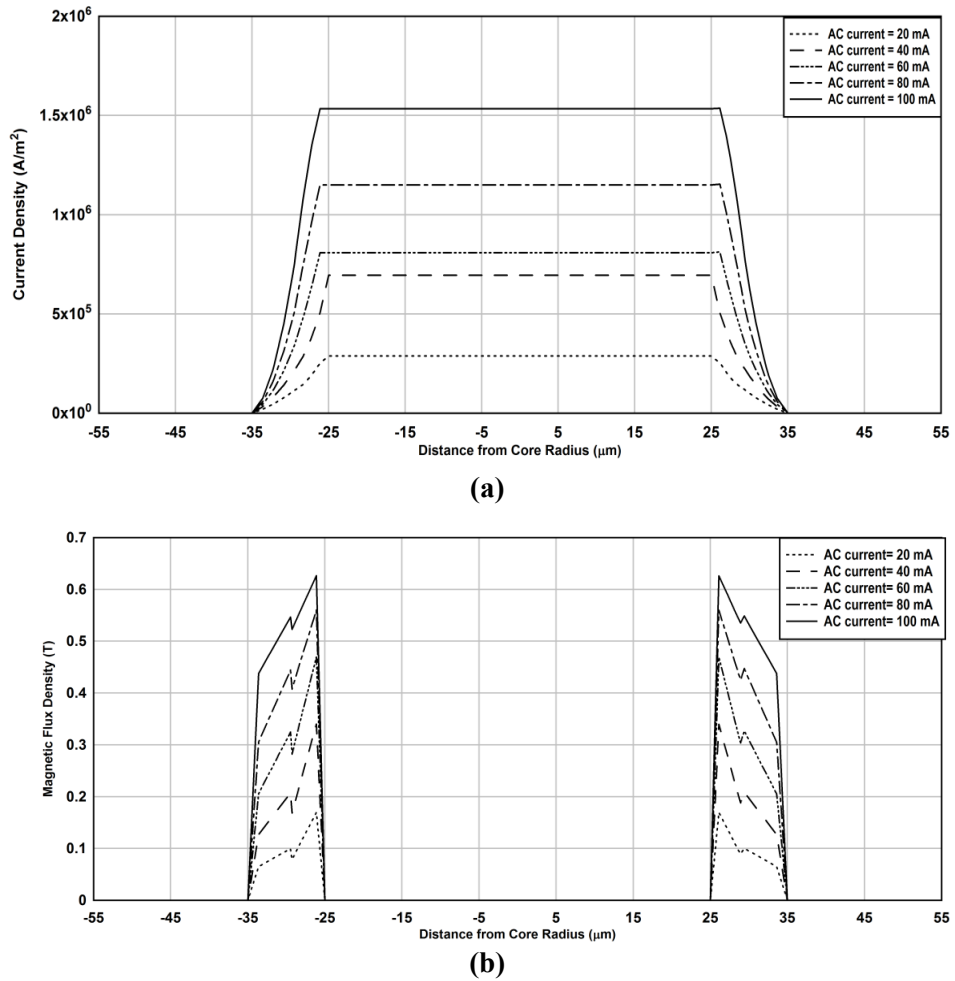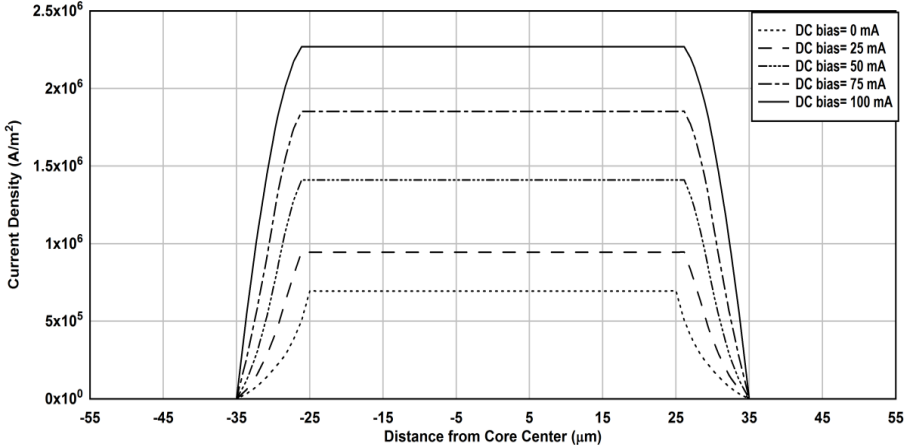

(a)

(b)
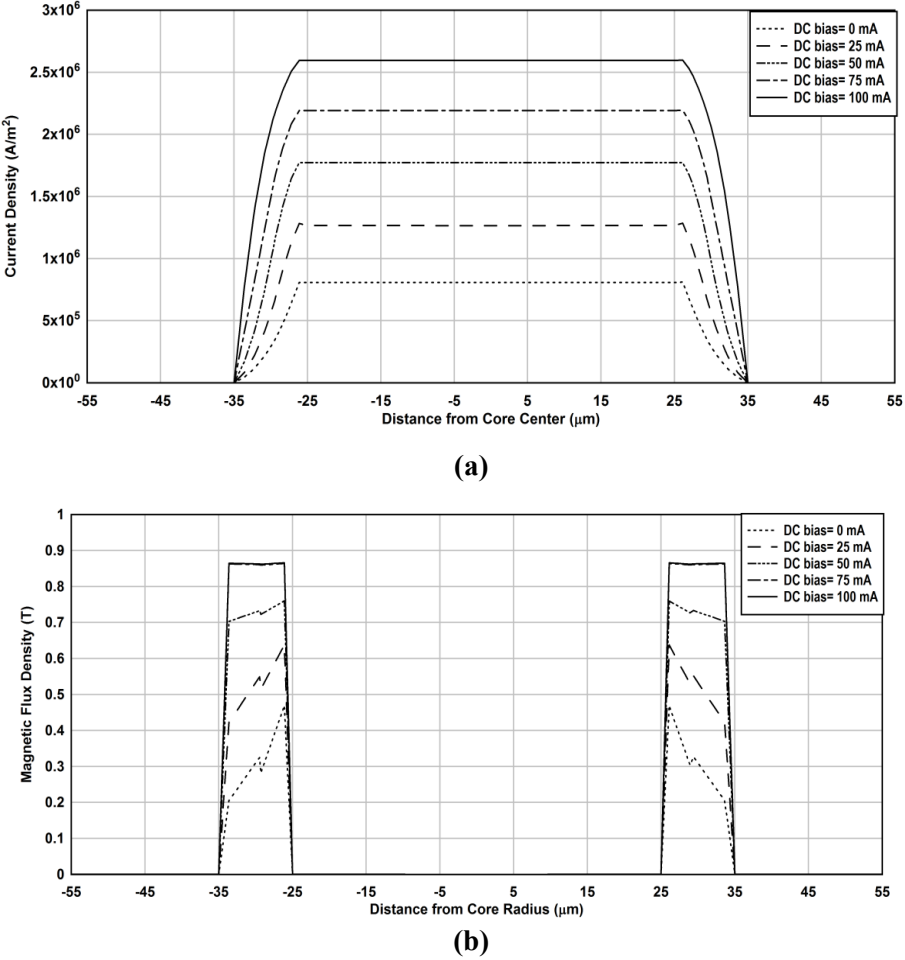
Figure 6-4: (a) Current density, and (b) Magnetic flux density radial distributions for a composite core excited at 50 KHz with ac excitation amplitude 60 mA at different dc bias values

It is shown from *Figure 6-4(a)* that the current density distribution adopts the same trend of increase as the dc bias value increase, but with a relatively higher current density values, compared with *Figure 6-3(a)*, for each corresponding dc value. Furthermore, for the increase of the ac current to 60 mA, the magnetic flux density distribution shows a slight effect against the increment of the dc bias values from 0 mA to 50 mA as shown in *Figure 6-4(b)*. However, as the dc bias reaches 75 mA, compared with *Figure 6-3(b)*, a higher value of flux density is achieved inside the soft magnetic shell, with a uniform pattern as well. Moreover, increasing the dc bias to 100 mA does not contribute in further increase in the value of magnetic flux density. Therefore, it is observed that increasing ac current gives opportunity to achieve a better flux density response with a relatively lower value of dc bias. In this context, the current and flux density behavior along the examined composite core, for a further increment of the ac

96

current to be 80 mA at 50 KHz, and a dc bias change from 0 mA to 100 mA, is investigated in *Figure 6-5*. As shown in *Figure 6-5(b)*, a uniform and relatively high value of magnetic flux density could be obtained inside the soft magnetic part of the core at 50 mA dc bias. Furthermore, compared with *Figure 6-4(a)*, the desired flux density response was achieved with a lower current density values inside the excitation part of the core, as shown in *Figure 6-5(a)*. Besides, a further increase in the dc bias to 75, and 100 mA contribute in a minor increase of the flux density, with almost identical values, inside the soft magnetic shell, as indicated in *Figure 6-5(b)*.
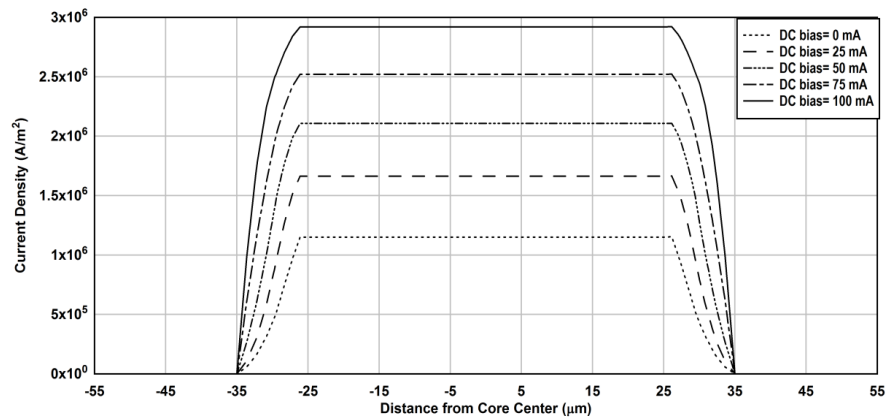
(a)
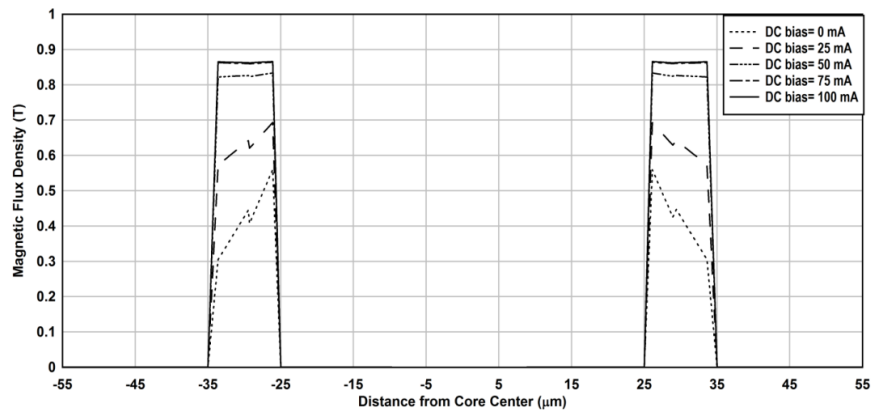
(b)

Figure 6-5: (a) Current density, and (b) Magnetic flux density distributions for a composite core at 50 KHz with ac amplitude 80 mA at different dc bias values

After obtaining the results from the above analysis, we will move forward to another factor to be studied which is the frequency of the ac excitation. As mentioned before in the previous chapter, it is always favorable to increase the excitation frequency to increase the sensitivity [249]. However, there will always be a limit for such an increment based on the fluxgate core response. In this context, the third study to be conducted in this chapter is the effect of frequency on the composite microwire core. *Figure 6-6 (a), (b)*, and *(c)* shows the influence of change in the dc bias, when the excitation frequency increases to 100 KHz, on the magnetic flux distribution along the composite core cross section. The radius of the excitation part of the core kept at 25 µm, and the soft magnetic shell thickness kept at 10 µm, where the ac current flows

inside the excitation part of the core has an intensity of 40 mA, 60 mA, and 80 mA respectively. In *Figure 6-6(a)* it can be observed that as dc value increase, magnetic flux density values along the soft magnetic part of the core increase as well. However, compared with *Figure 6-3(b)*, the homogeneity of the flux density values could not be restored even with the higher values of dc bias. Increasing the ac current values to 60 mA, and 80 mA causes insignificant increase in the maximum magnetic flux density value inside the sot magnetic shell, compared to the 40 mA ac current case. Furthermore, the accompanying increment in the dc values, for each of the investigated ac values, did not succeed in restoring the uniformity of the magnetic flux along the magnetic shell cross section.
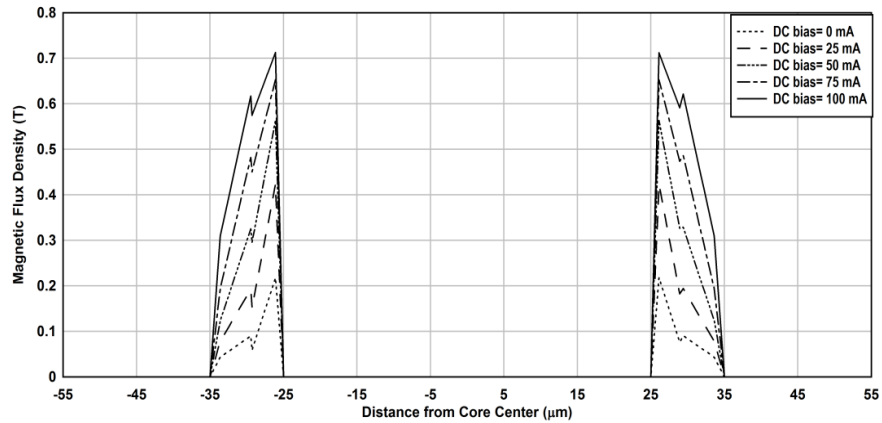
(a)
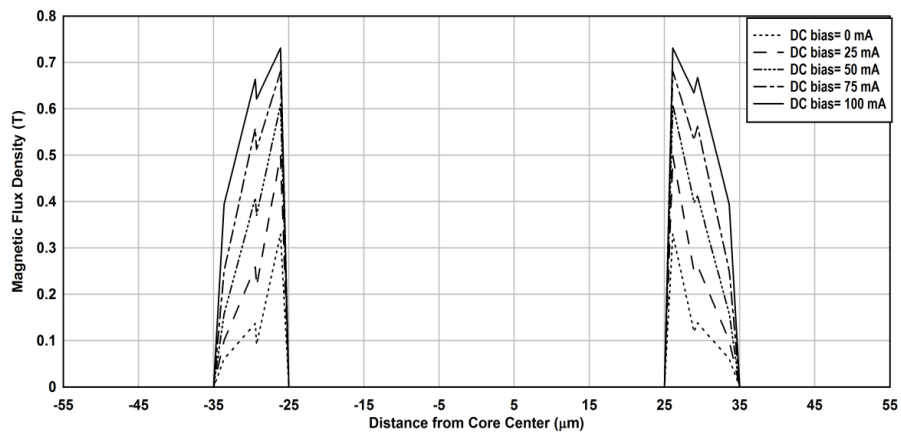
(b)
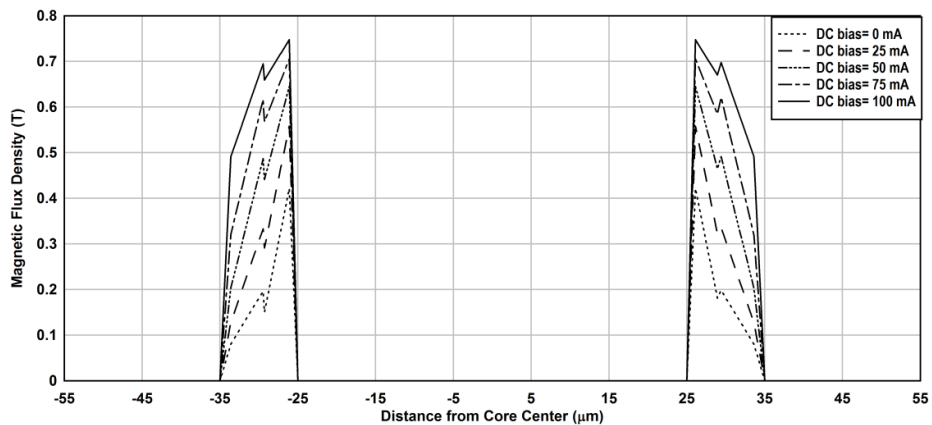
(c)

Figure 6-6 Magnetic flux density radial distribution for different dc bias amplitudes for a composite core excited at frequency 100 KHz with excitation amplitude of (a) 40, (b) 60, and (c) 80 mA

From the above results it can be seen that the route of increasing the frequency to increase the sensitivity resulted in distortion in the desired flux homogeneity inside the magnetic shell. Another possible idea to increase sensitivity of measurements is to increase amount of soft magnetic material within the composite core. Thus, the fourth study in this chapter will deal with the impact of thickness of the soft magnetic shell on the core's excitation mechanism at certain frequency. At the beginning, the radius of the excitation part of the core is kept at 25 μm, and the excitation frequency will be lowered from 100 KHz to 10 KHz. *Figure 6-7*, *6-8*, and *6-9* investigate the necessary values of ac current intensity and dc bias to reach the desired flux density pattern for a magnetic shell thickness of 10 μm, 20 μm, and 30 μm respectively.
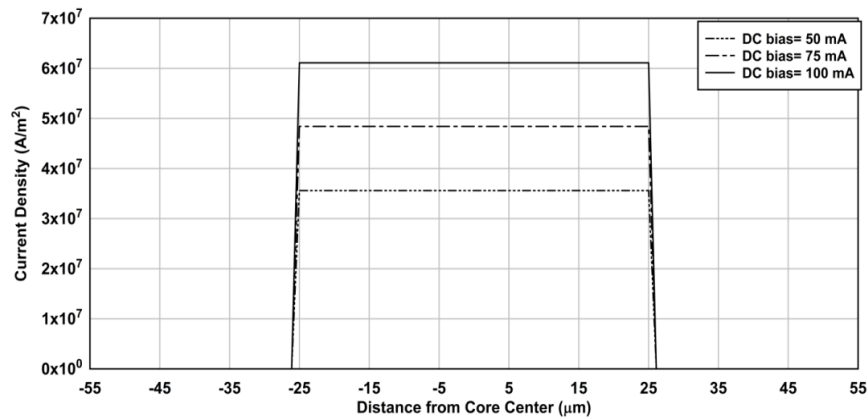
(a)
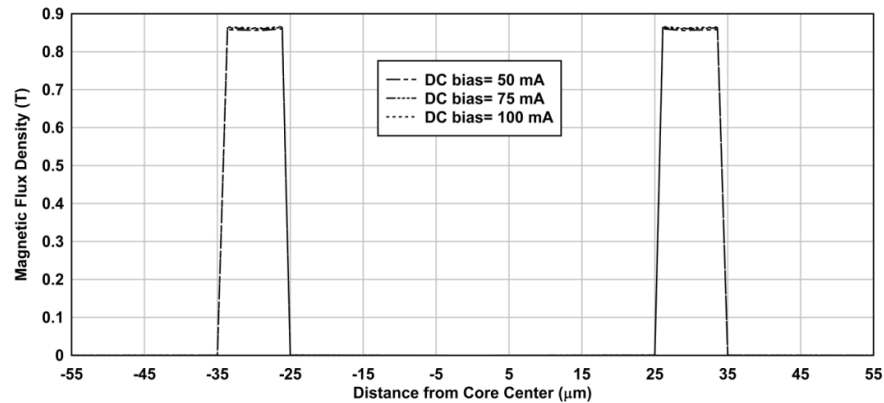
(b)

Figure 6-7 (a) Current density, and (b) Magnetic flux density radial distributions for different dc bias amplitudes for a composite core with 10 μm magnetic shell, excited at 10 KHz with ac excitation amplitude 20 mA, and 25 μm excitation part radius

As seen in *Figure 6-7(b)*, starting from 50 mA dc bias, it needs only an ac current intensity of 20 mA to achieve a uniform flux density value inside the 10 μm soft magnetic shell. Increasing the dc value to 75 and 100 mA has an insignificant effect on

the flux density value inside the magnetic shell. But, on the other hand, the increase in the dc bias values can cause unnecessary increase in the current density value inside the excitation part of the core. Increasing the soft magnetic shell to 20 μm at 10 KHz frequency and 25 μm excitation part radius, causes a change in the current excitation mechanism as shown in *Figure 6-8*. For *Figure 6-8(b)*, it turns out that an ac current intensity of 60 mA, beside at least 50 mA dc bias, was needed to achieve a uniform flux density value inside the 20 μm soft magnetic shell. Again, increasing the dc bias to 75 and 100 mA has the least influence on the flux density values inside the shell. From the current density perception, comparing *Figure 6-8(a)* to *Figure 6-7(a)*, it is found that achieving the desired flux density pattern for the larger soft magnetic thickness contributes in a considerable increase in the current density values inside the excitation part of the core for each of the investigated dc bias values.

(a)

(b)

Figure 6-8: (a) Current density, and (b) Magnetic flux density radial distributions for different dc bias amplitudes for a composite core with 20 μm magnetic shell, excited at 10 KHz with ac excitation amplitude 60 mA, and 25 μm excitation part radius.

Having the same frequency, and excitation part radius, it is found that as the thickness of the soft magnetic shell increases to 30 μm, an additional increase in the ac current is needed to get the desired flux pattern. This is illustrated in *Figure 6-9(b)*

where an ac current intensity of 100 mA, with at least 50 mA dc bias succeeded in uniform the flux density values across the whole magnetic shell cross section. Furthermore, as shown in *Figure 6-9(a)*, increasing the dc bias values to 75 mA and 100 mA causes an increase in current density values, but it did not affect the flux density behavior inside the shell.

(a)

(b)

Figure 6-9: (a) Current density, and (b) Magnetic flux density radial distributions for different dc bias amplitudes for a composite core with 30 μm magnetic shell, excited at 10 KHz with ac excitation amplitude 100 mA, and 25 μm excitation part radius

Moving forward, to investigate the frequency effect, the excitation frequency will be increased from 10 KHz to 50 KHz with air surrounding the whole composite core. Again, the soft magnetic thickness will be increased from 10 μm to 20 μm, and the radius of the excitation part of the core is kept at 25 μm. *Figure 6-10(a), (b), (c), (d), (e)* and *(f)* illustrate the effect of dc bias on magnetic flux distribution across the composite core geometry, when the ac current flows inside the excitation part of the core has an intensity of 40 mA, 60 mA, and 80 mA, 100 mA, 125 mA, and 150 mA respectively. As shown in *Figure 6-10(a), (b), (c), (d)*, for each of investigated ac currents, it can be seen that the dc bias increment contributes significantly in the enlargement of the flux density region inside the sot magnetic shell. Moreover, for each of the investigated dc currents, a slight increase in the flux density values is observed as the ac current value increases. Nonetheless, the homogeneity of the flux inside the shell was not nearly

restored without the influence of a higher ac current as shown in *Figure 6-10(e)*, and *(f)*. However, this involves another perspective to be taken into consideration, which is the temperature.

(a)

(b)
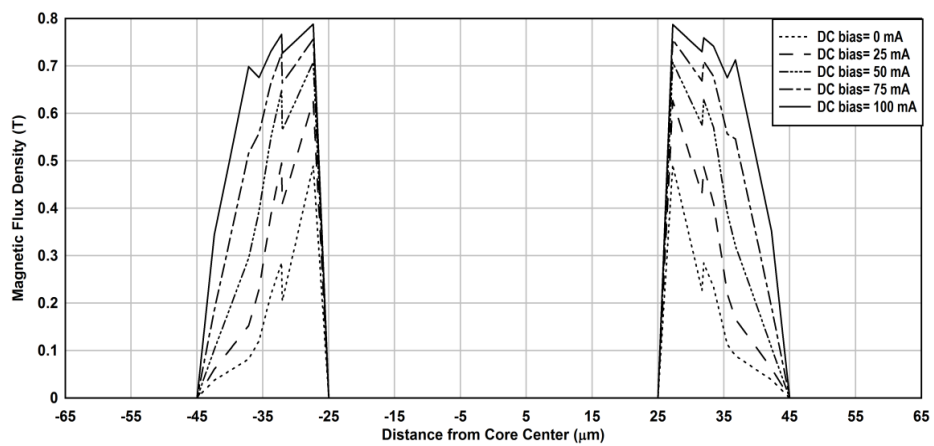
(c)
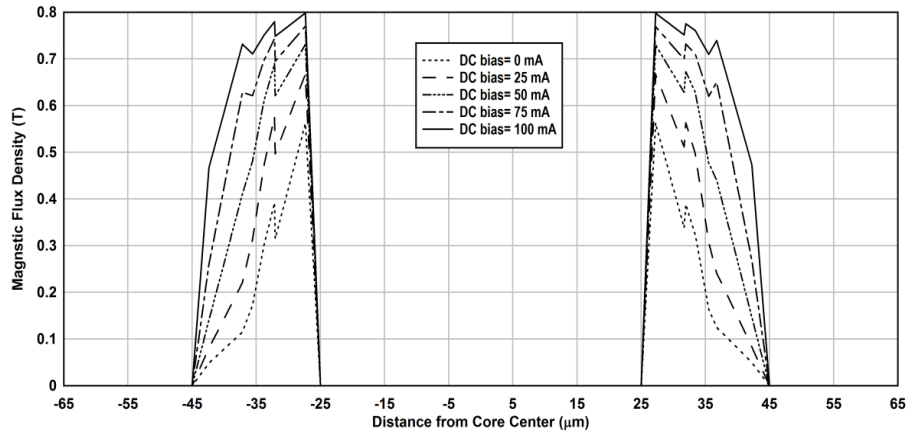
(d)
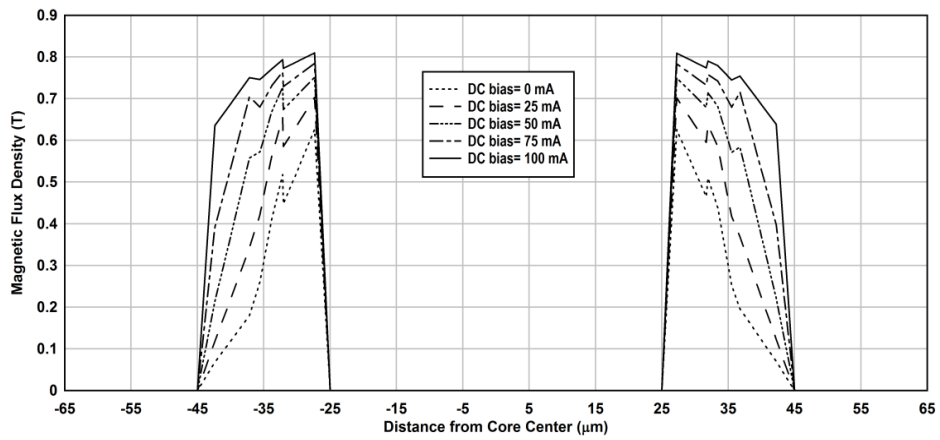
(e)
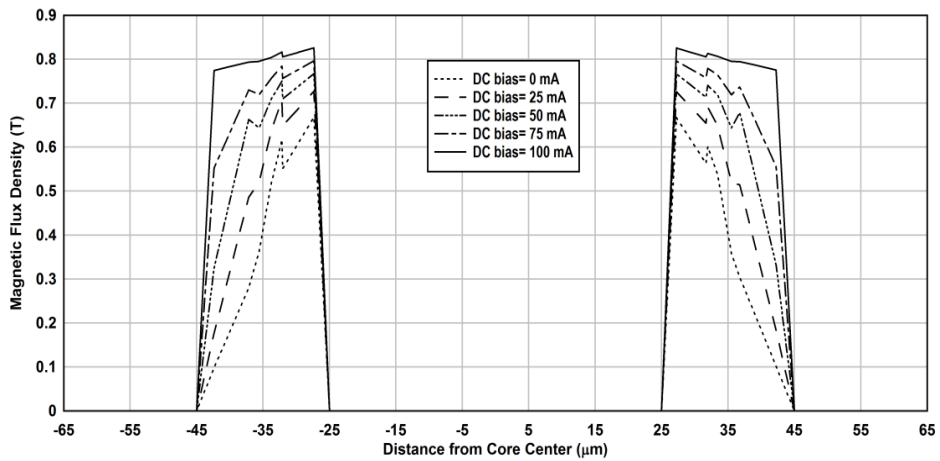
(f)

Figure 6-10: Magnetic flux density radial distribution for different dc bias amplitudes for a composite core, with 20 μm magnetic shell excited at frequency 50 KHz with excitation amplitude of (a) 40, (b) 60, (c) 80, (d) 100, (e) 125, and (f) 150 mA

Large current density inside the core can induce heat, and such heat may cause mechanical stresses inside the core, which could be a possible source of noise at the fluxgate output [250]. This prospective will initiate the fifth study in this chapter to investigate the impact of the radius of the excitation part of the core on the current, and flux density distributions. *Figure 6-11*, *6-12* and *6-13* illustrate the impact of ac current, and dc bias change on the current and flux density behavior through the cross section of the composite core, where the magnetic shell thickness is 10 μm, 20 μm and 30 μm respectively. In this analysis, for all the investigated shell thicknesses, the radius of the excitation part of the core is increased from 25 μm, to 50 μm. The excitation frequency is chosen to be 10 KHz, and the whole composite core is surrounded by air.
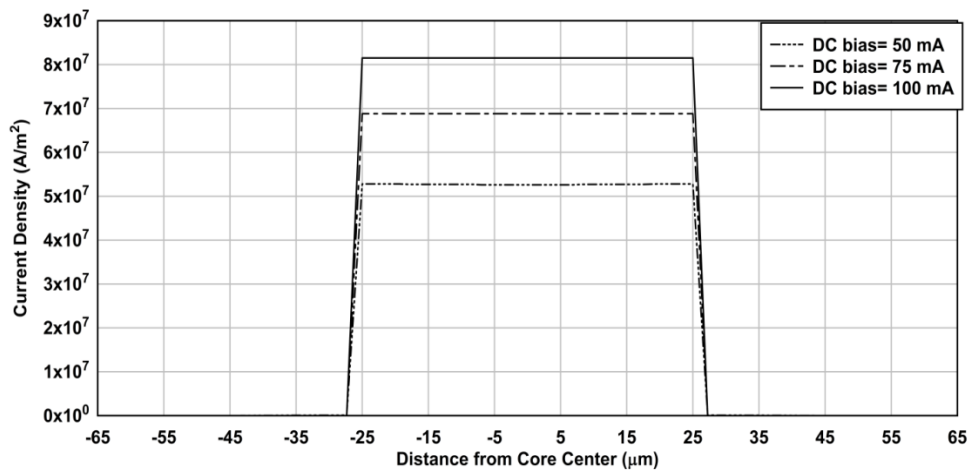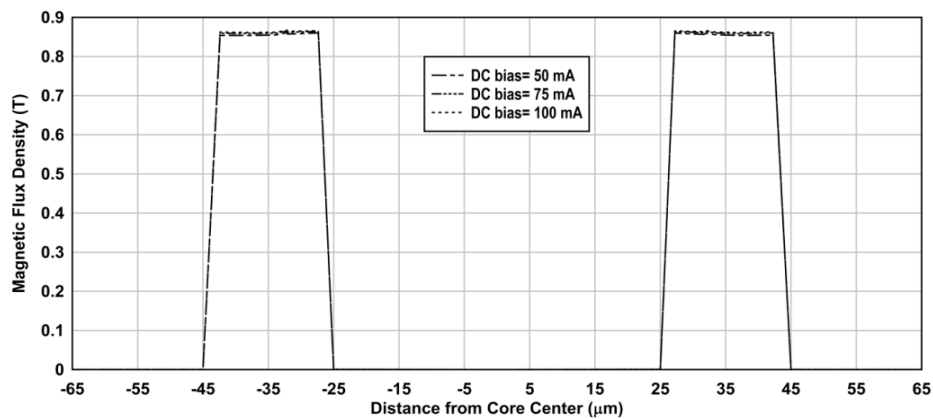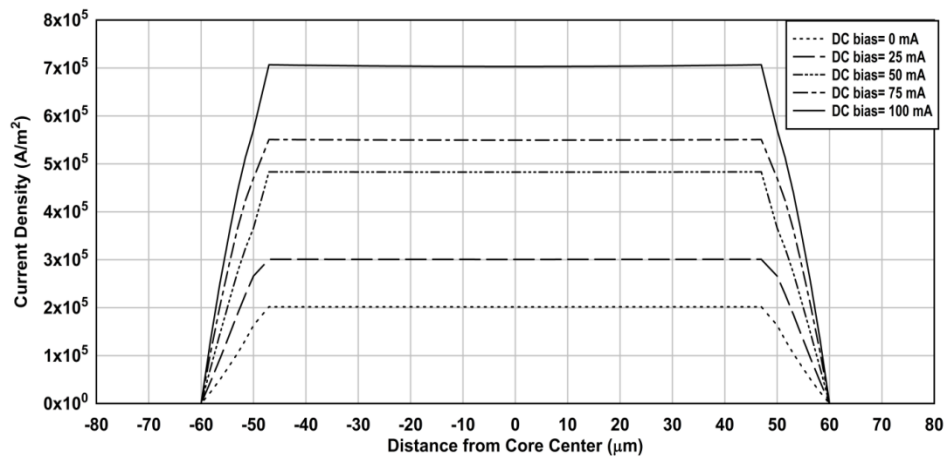

(a)
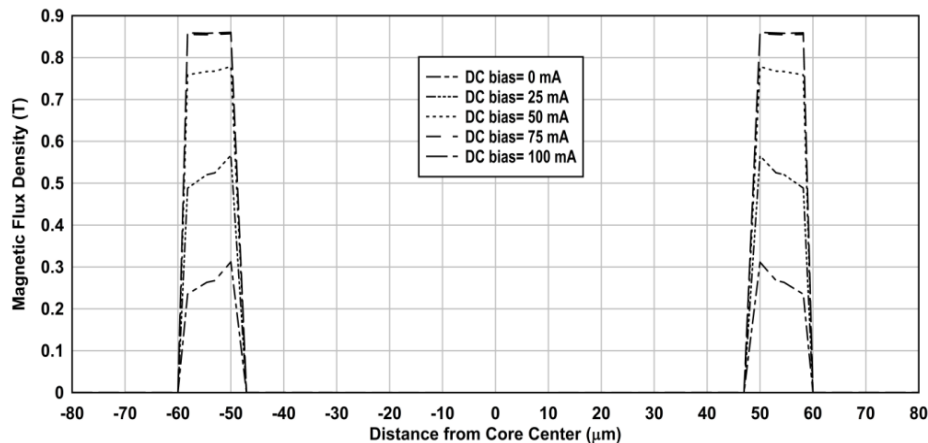
(b)

Figure 6-11: (a) Current density, and (b) Magnetic flux density radial distributions for different dc bias amplitudes for a composite core with 10 μm magnetic shell, excited at 10 KHz with ac excitation amplitude 40 mA, and 50 μm excitation part radius.

As seen in *Figure 6-11*, compared to *Figure 6-7*, a uniform flux density value inside the 10 μm soft magnetic shell could be achieved only by increasing both the ac current to 40 mA, and the dc bias to 75 mA. However, as shown in *Figure 6-11(a)*, this increase could be obtained with a relatively lower current density values, compared with *Figure 6-7(a)*. Increasing the dc value to 100 mA has unnoticeable effect on the

104

flux density values inside the magnetic shell. But, on the other hand, the increase in the dc bias values causes unnecessary increase in the current density value inside the excitation part of the core. For the 20 μm soft magnetic shell case in *Figure 6-12*, using the 50 μm excitation part radius causes an increase in ac current to be 100 mA, compared with a 60 mA value for the 25 μm excitation part radius case in *Figure 6-8*, to get the same result. Furthermore, an increase in the dc bias to 100 mA was needed as well to homogenous the flux density values inside the 20 μm shell. Again, these relatively larger excitation values were realized with a relatively lower current density values inside the excitation part of the core. This could be translated to a relatively lower heat generation inside the sensing element, and consequently, a lower noise at the sensor output. To attain the same flux response for the 30 μm soft magnetic shell case in *Figure 6-13*, the ac current increases to be 150 mA. However, even with the use of dc bias values up to 100 mA, the homogeneity of the flux density inside the soft magnetic shell could not be restored as shown in *Figure 6-13(b)*.

(a)

(b)

Figure 6-12 (a) Current density, and (b) Magnetic flux density radial distributions for different dc bias amplitudes for a composite core with 20 μm magnetic shell, excited at 10 KHz with ac excitation amplitude 100 mA, and 50 μm excitation part radius

(a)

(b)

Figure 6-13: (a) Current density, and (b) Magnetic flux density radial distributions for different dc bias amplitudes for a composite core with 30 μm magnetic shell, excited at 10 KHz with ac excitation amplitude 150 mA, and 50 μm excitation part radius

From the previous analysis it was found that the same response could be attained, for certain magnetic shell thicknesses, with a relatively lower current density values when the radius of the excitation part of the core increases to 50 μm. From this standpoint, the next step is to investigate the excitation frequency prospective. *Figure 6-14*, and *6-15* reveals the impact of the dc bias change on the current and flux density behavior through the cross section of composite core, where radius of excitation part of the core is 25 μm, and 50 μm respectively. For both investigated radiuses, the ac current intensity inside the excitation part of the core is chosen to be 100 mA at 50 KHz. Also, the magnetic shell thickness for both the investigated radiuses is kept as 10 μm, and the whole composite core is surrounded by air.
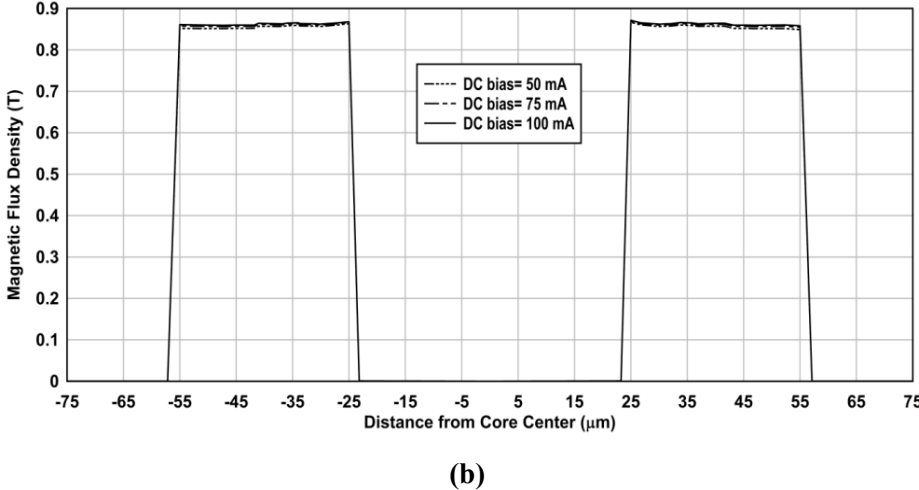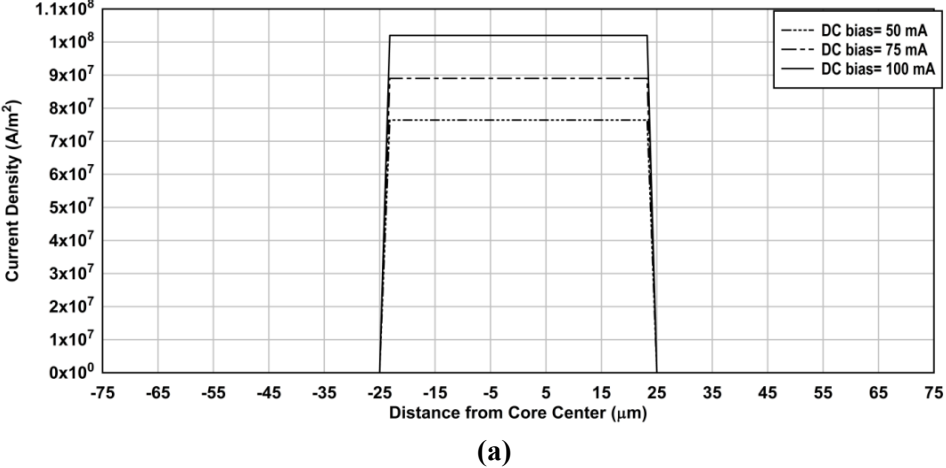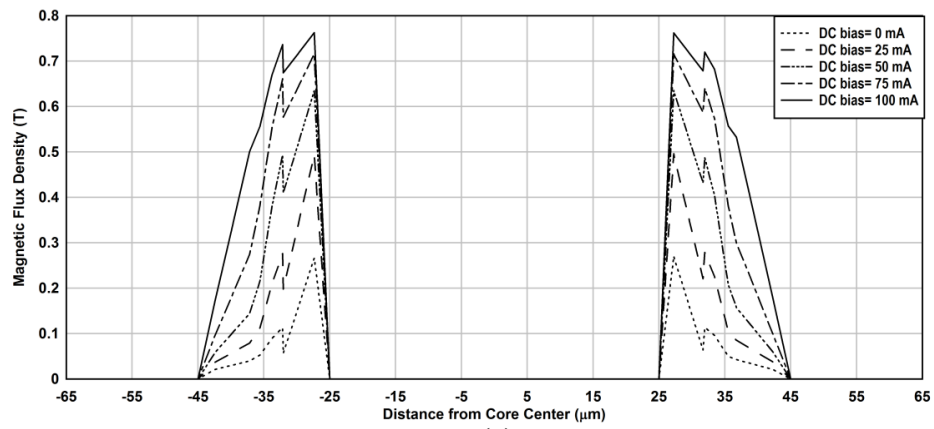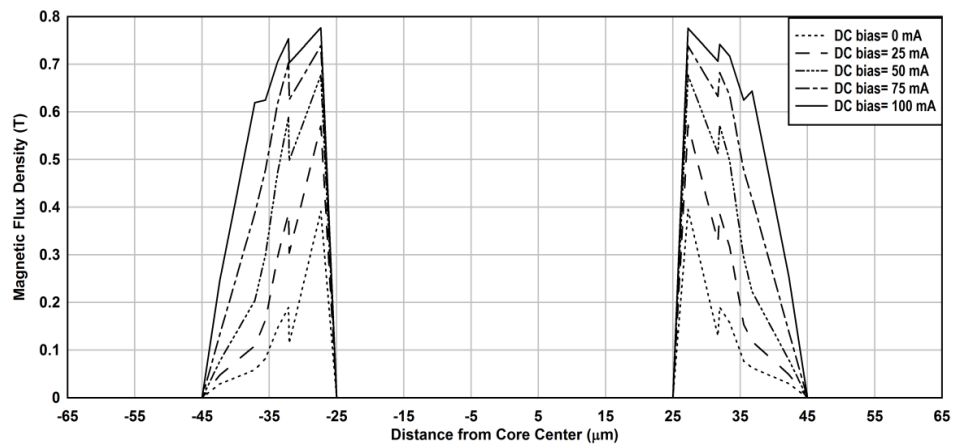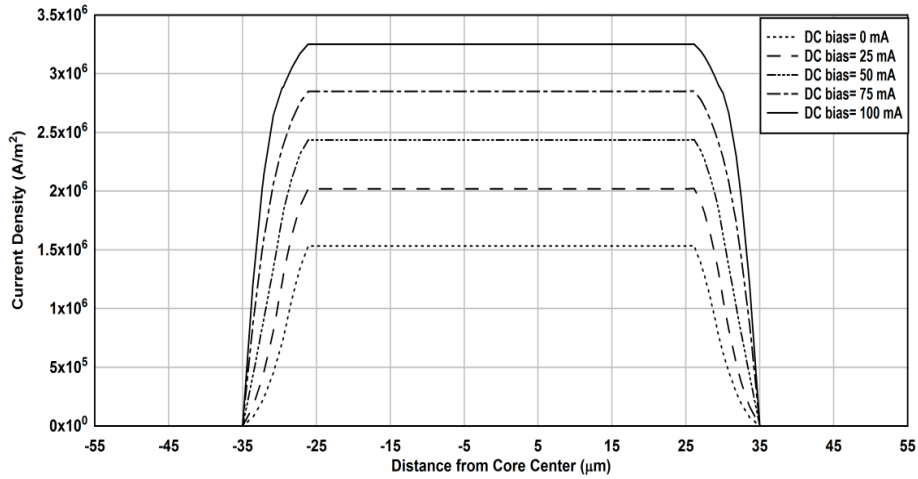
(a)
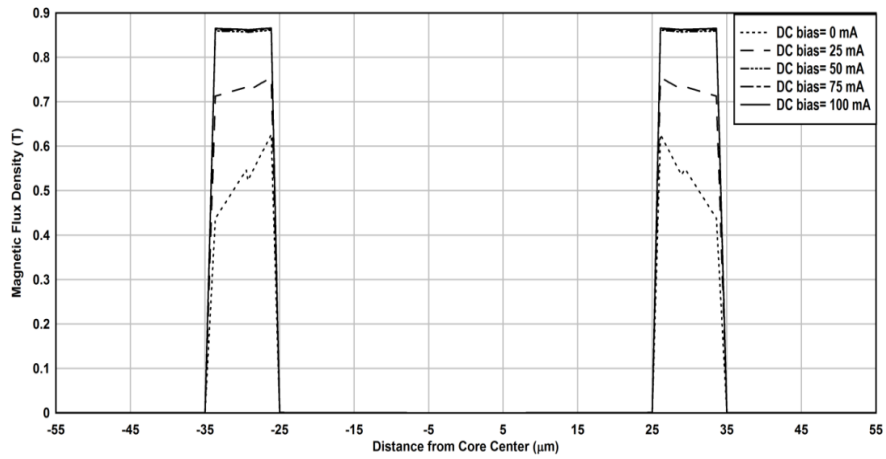
(b)

Figure 6-14: (a) Current density, and (b) Magnetic flux density radial distributions for different dc bias amplitudes for a composite core with 10 μm magnetic shell, excited at 50 KHz with ac excitation amplitude 100 mA, and 25 μm excitation part radius.
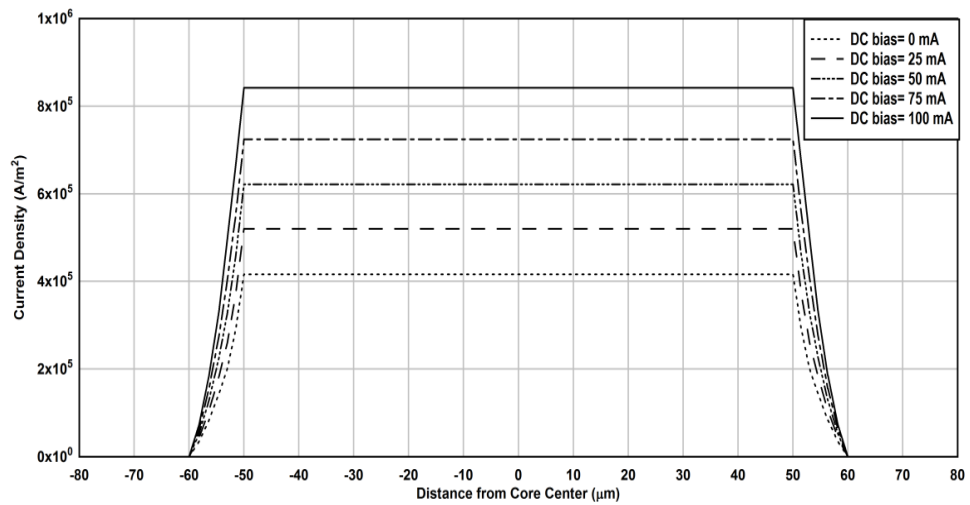
(a)
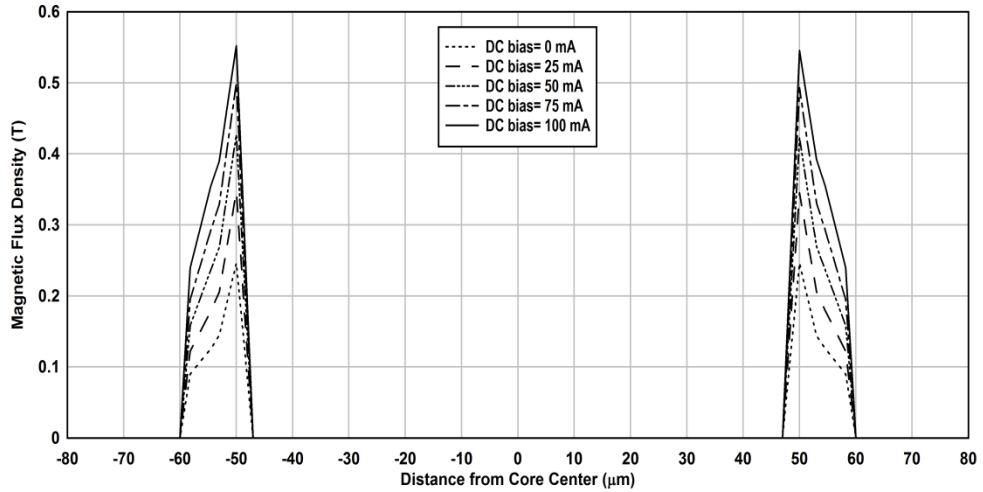
(b)

Figure 6-15: (a) Current density, and (b) Magnetic flux density radial distributions for different dc bias amplitudes for a composite microwire with 10 μm magnetic shell, excited at 50 KHz with ac excitation amplitude 100 mA, and 50 μm excitation part radius

Comparing *Figure 6-14*, and *6-15*, it can be seen that at dc bias values of 0 mA, and 25 mA, the magnetic flux density follows the same trend for both excitation part radiuses. However, as shown in *Figure 6-14(b)*, and *6-15(b)*, maximum value of magnetic flux density inside the magnetic shell decreased in the 50 μm radius compared with the 25 μm radius case, as a result of a corresponding decrease in the current density values observed at *Figure 6-14(a)*, and *6-15(a)*. In *Figure 6-14(b)*, as the dc bias value reaches 50 mA, the magnetic flux density values become homogenous inside the magnetic shell. On the other hand, as shown in *Figure 6-15(b)*, the 50 mA dc bias value causes only an increase in the maximum magnetic flux density value inside the shell, without considerable effect on the geometrical destruction of the flux. A further increase in the dc value to 75 mA, and 100 mA results in non-significant effects on both the flux density value and its geometrical footprint for the 25 μm radius case, as seen in *Figure 6-14(b)*.

Instead, in *Figure 6-15(b)*, same increase in the dc values results in only an increase in the maximum flux density values for the 50 μm radius case, without noticeable effect on the geometrical aspect of the flux distribution. From the above analysis, it can be concluded that although that the increase of the excitation part radius contributes in a significant decrease in the current density values inside the core, this causes unwanted consequences on the flux density behavior inside the sot magnetic shell at 50 KHz frequency. Thus, an attempt to compensate for these consequences is done through increasing the ac current.

Figure 6-16 and *6-17* illustrates the effect of the dc bias at certain core geometry on the current density, and the magnetic flux distributions, when the ac excitation current increases to 125 mA, and 150 mA respectively. The radius of the excitation part of the core is kept as 50 μm and the frequency is kept as 50 KHz. Also, the magnetic shell thickness is kept as 10 μm, and the whole composite core is surrounded by air. In *Figure 6-16*, it can be seen that increasing the ac current to 125 mA causes an increase in the current density values inside the excitation part of the core, for each of the considered dc values. Compared to *Figure 6-15(b)*, the reflection on magnetic flux density distribution was a small increase in the maximum flux density values, while following the same trend of flux distribution inside the soft magnetic shell. Increasing

the ac current to 150 mA causes a slight enhancement in geometrical footprint of magnetic flux distribution. Yet, as shown in *Figure 6-17(b)*, this increase in the current density did not manage to restore the uniformity of the flux along the cross section of the soft magnetic shell.
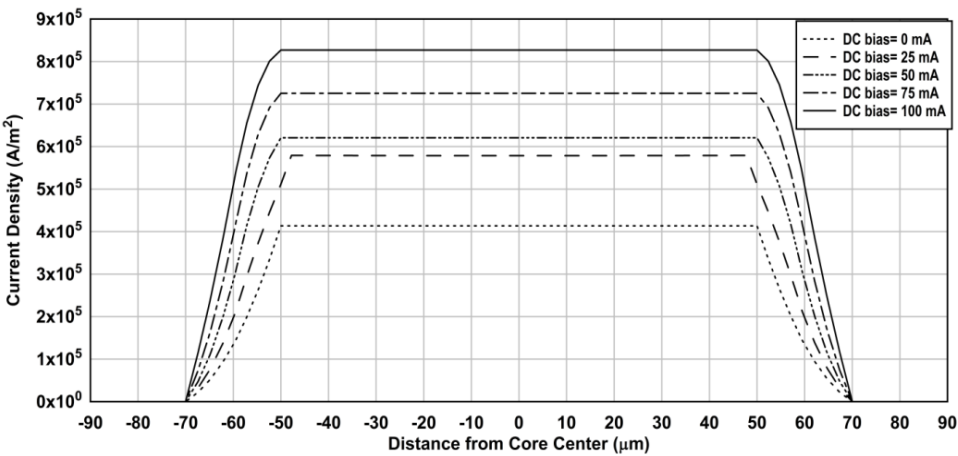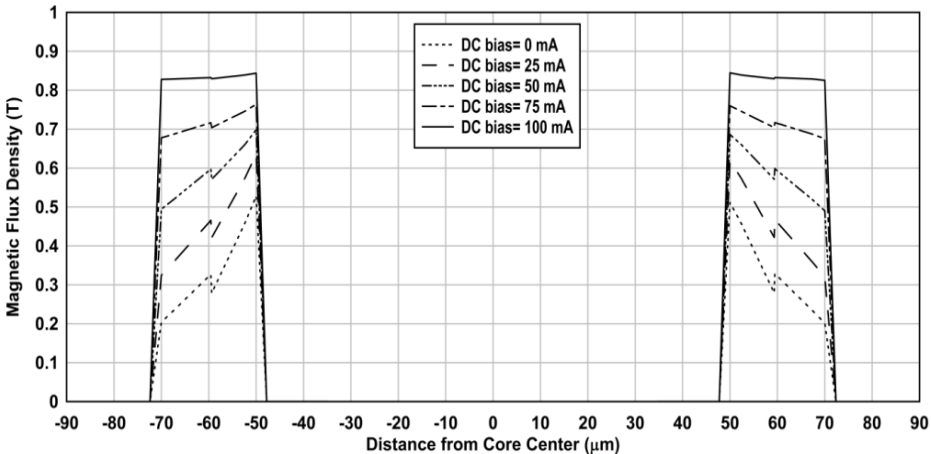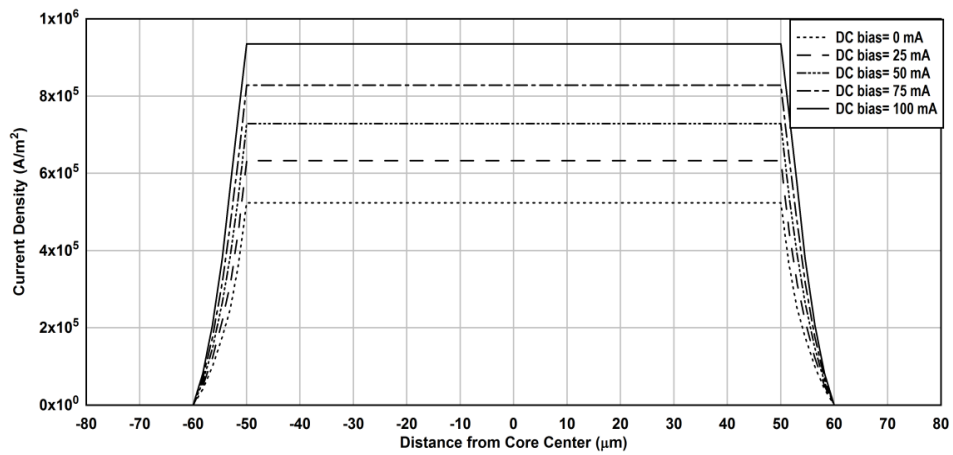

(a)
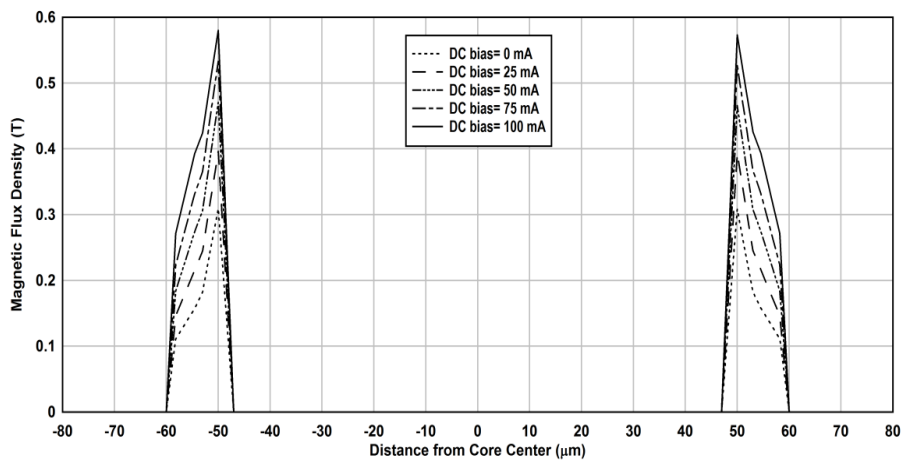
(b)

Figure 6-16: (a) Current density, and (b) Magnetic flux density radial distributions for different dc bias amplitudes for a composite core with 10 μm magnetic shell, excited at 50 KHz with ac excitation amplitude 125 mA, and 50 μm excitation part radius.
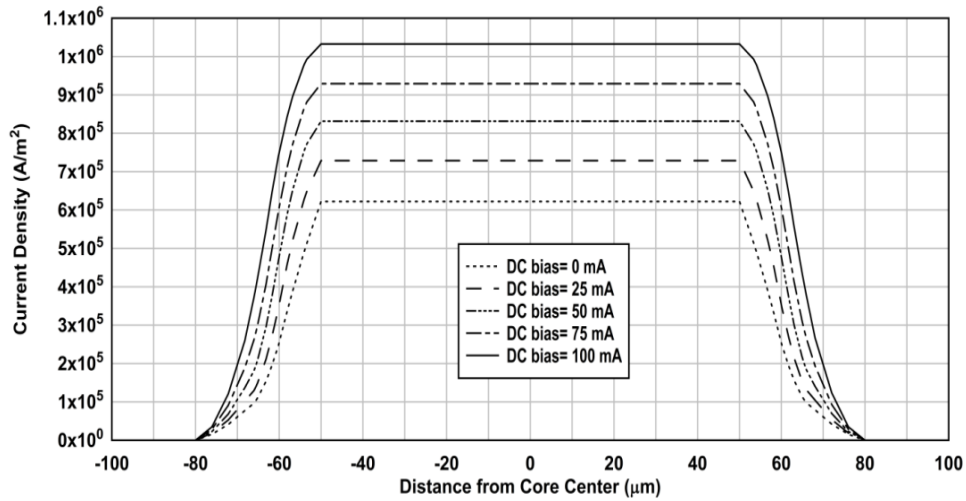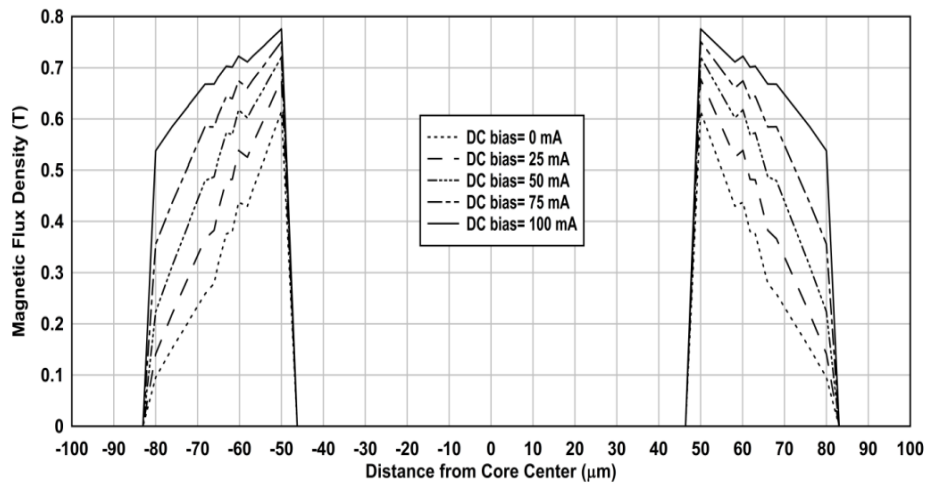

(a)

109
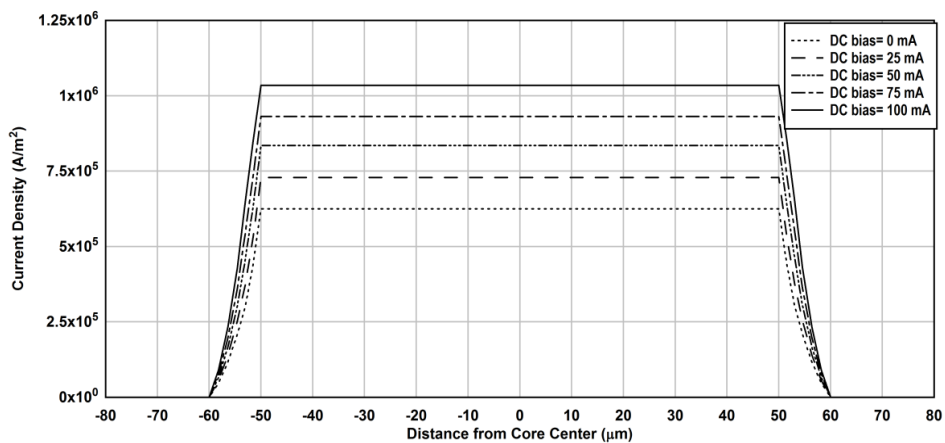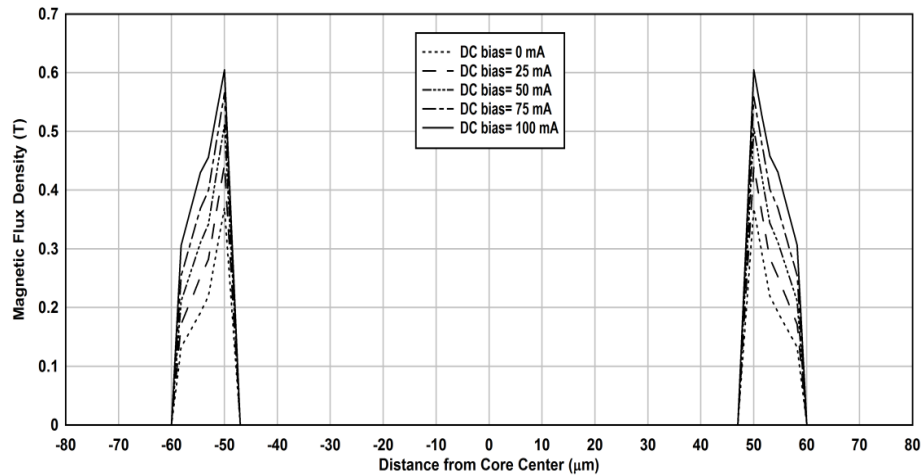
(b)

Figure 6-17: (a) Current density, and (b) Magnetic flux density radial distributions for different dc bias amplitudes for composite core with 10 μm magnetic shell, excited at 50 KHz with ac excitation amplitude 150 mA, and 50 μm excitation part radius

6.4. Summary

Table 6.1 summarizes the results in this chapter. The first study shows that the ac current values were not enough to uniform the flux inside a 10 μm magnetic shell excited at 50 KHz. Therefore, the second study shows the effect of the dc bias on the core response. It was found that adding the dc bias contributes in achieving a uniform flux density inside a 10 μm magnetic shell excited at 50 KHz. Furthermore, it was found that increasing the ac current causes to have the same result al lower dc value. As the excitation frequency increases to 100 KHz in the third study, the uniformity of the flux could not be done inside the 10 μm shell.

The fourth study was done to illustrate the effect of magnetic shell thickness, on the core. At 10 KHz, as the magnetic shell thickness increases, a higher ac current is needed to achieve a uniform flux density inside the shell. A uniform magnetic flux density could be realized for a magnetic shell of thickness 30 μm, with ac current of 100 m, and dc bias of 50 mA. However, as frequency increases to 50 KHz, an ac current up to 150 mA, and dc bias up to 100 mA could not restore the flux uniformity.

In the fifth study, the radius of the excitation part of the core was studied. At 10 KHz, increasing the excitation part's radius, from 25 μm to 50 μm, causes an increase in the necessary ac current and dc bias to achieve flux uniformity along magnetic shell of 10 μm thickness. A higher values of ac current and dc bias is needed for the flux uniformity along magnetic shell of 20 μm thickness. an ac current up to 150 mA, and dc bias up to 100 mA could not restore the full uniformity of the flux along a magnetic shell of 30 μm thickness. As the frequency increase to 50 KHz, an ac current up to 150 mA, and dc bias up to 100 mA could not restore the full uniformity of the flux along a magnetic shell of 10 μm thickness.

110

Table 6-1: Summary of the second configuration results

Mode	Copper Rod Radius	Magnetic Shell Thickness	Excitation Frequency	AC Current	DC Bias
Fundamental	25 µm	10 µm	10 KHz	20 mA	50 mA
Fundamental	25 µm	20 µm	10 KHz	60 mA	50 mA
Fundamental	25 µm	30 µm	10 KHz	100 mA	50 mA
Fundamental	25 µm	10 µm	50 KHz	80 mA	50 mA
Fundamental	50 µm	10 µm	10 KHz	40 mA	75 mA
Fundamental	50 µm	20 µm	10 KHz	100 mA	100 mA

Chapter 7 : Conclusions and Future Work

7.1. Design Considerations

The main results in this thesis are listed in the following paragraphs. For the first design in this thesis, where a soft magnetic microwire is considered, it is found that, at 1 KHz, the desired response could be achieved for 20 μm radius core with 20 mA ac current. For a 40 μm radius core, 60 mA ac current was enough to get desired response. The desired response for both the 60 μm and 80 μm radius cores was attained only at 100 mA ac current. As the frequency increases to 10 KHz, the desired response for the 20 μm, 40 μm, and 60 μm radii cores could be done. However, the desired response for the 80 μm radius core could not be done with 100 mA ac current at 10 KHz frequency. An increase in the frequency to 100 KHz limits the response to the 20 μm radius core with 60 mA ac current. More increase in the excitation frequency to 1 MHz makes it difficult to have the desired response even for the 20 μm radius core.

For the dc bias effect, at 10 KHz, the desired response for 40 μm radius core was achieved with 20 mA ac current, and 20 mA dc bias. Desired response for 60 μm radius core was achieved with 40 mA ac current, and 40 mA dc bias. Desired response for the 80 μm radius core could be realized for the first time at this frequency with 80 mA ac current, and 80 mA dc bias. At100 KHz, the desired response for the 40 μm radius core exists with 80 mA ac current, and 80 mA dc bias.

For the second design in this thesis, where a composite microwire is considered as the fluxgate core, at 10 KHz excitation frequency and 25 μm copper rod radius, the desired response for a 10 μm magnetic shell was done with 20 mA ac current, and 50 mA dc bias. Getting the same desired response for a 20 μm magnetic shell requires a 60 mA ac current, and 50 mA dc bias. The desired response for a 30 μm magnetic shell was done with 100 mA ac current, and 50 mA dc bias. As the frequency increases to 50 KHz, the desired response for a 10 μm magnetic shell was done with 80 mA ac current, and 50 mA dc bias. The desired response could be done partially for a 20 μm magnetic shell with 150 mA ac current, and 50 mA dc bias. The desired response could not be done for the 30 μm magnetic shell at 50 KHz frequency.

Increasing the copper rod radius from 25 μm to 50 μm, at 10 KHz, helps in having the desired response for the 10 μm magnetic shell with 40 mA ac current, and 75 mA dc bias. The desired response for the 20 μm magnetic shell done at the same frequency with 100 mA ac current, and 100 mA dc bias. The desired response could be done partially for the 30 μm magnetic shell with 150 mA ac current, and 100 mA dc bias.

Table 7-1: Summary of thesis results

First Configuration Results				
Mode	**Core Radius**	**Excitation Frequency**	**AC Current**	**DC Bias**
2nd Harmonic	20 µm	1 KHz	20 mA	
2nd Harmonic	40 µm	1 KHz	60 mA	
2nd Harmonic	60 µm	1 KHz	100 mA	
2nd Harmonic	80 µm	1 KHz	100 mA	
2nd Harmonic	20 µm	10 KHz	20 mA	
2nd Harmonic	40 µm	10 KHz	60 mA	
2nd Harmonic	60 µm	10 KHz	100 mA	
2nd Harmonic	20 µm	100 KHz	60 mA	
Fundamental	40 µm	10 KHz	20 mA	20 mA
Fundamental	60 µm	10 KHz	40 mA	40 mA
Fundamental	80 µm	10 KHz	80 mA	80 mA
Fundamental	40 µm	100 KHz	80 mA	80 mA

Second Configuration Results					
Mode	**Core Radius**	**Magnetic Shell**	**Excitation Frequency**	**AC Current**	**DC Bias**
Fundamental	25 µm	10 µm	10 KHz	20 mA	50 mA
Fundamental	25 µm	20 µm	10 KHz	60 mA	50 mA
Fundamental	25 µm	30 µm	10 KHz	100 mA	50 mA
Fundamental	25 µm	10 µm	50 KHz	80 mA	50 mA
Fundamental	50 µm	10 µm	10 KHz	40 mA	75 mA
Fundamental	50 µm	20 µm	10 KHz	100 mA	100 mA

7.2. Conclusions

Increasing the excitation frequency is an important condition for the enhancement of a fluxgate response. However, the main drawback of increasing the frequency inside the wire-based core is that the current density will not be uniform along the cross section of the core. For the first studied configuration in this thesis, the skin effect, resulted from increasing the frequency, is significantly influence the area of the core under which the amplitude of the magnetic flux is relatively small. Eventually, the excitation frequency has to be chosen as compromise between a higher frequency, and a desired low flux density section. Another solution to compensate for the imperfections is to increase the ac excitation current. For the first design, the higher is the excitation field, the lower is the area has a lower flux density values. For the second design increasing the ac excitation current results in increasing the magnetic flux density values.

From the operation mode prospective, the fundamental mode operation, that is fulfilled when dc bias is added to ac current, contributes in enhancing performance. For the first design, adding a dc bias contributes to overcome the skin effect. For the second design, excitation of the core with enough dc bias participates in increasing the flux density section.

Furthermore, it is always favorable to have a larger amount of magnetic material inside the core in order to enhance its response. For the first design, the magnetic flux profile is affected by the distance from the center of the wire. Thus, optimizing core radius is needed to compensate for the skin effect resulted from increasing the

frequency. For the second design, a larger magnetic layer needs higher excitation current to avoid a disturbed flux profile at the outer portion of the core.

7.3. Future work

For the micro fluxgate magnetometer, the proper design is achieved when the main noise appearing at fluxgate's output is the magnetic core noise, as this means that the electronic components of the device have been well designed. While magnetic noise is the one that originating from core's magnetic material, another significant noise source for fluxgate magnetometer is the excitation noise that is superimposed on the excitation current. With the various attempts to increase the excitation frequency, tiny disturbances in the excitation waveform will influence the detection limit and the signal stability of the micro fluxgate magnetometer. Another source of noise comes from the demodulator employed for extracting the desired harmonic from the induced voltage in the sensing coil. Any noise in the demodulator leads to a sensitivity changes at fluxgate output. Therefore, a suggested future work in this thesis is to investigate the required electronics complications resulted from different micro fluxgate structures. For instance, designs of precise current source and a very low noise demodulator can be proposed. Also, as the magnetic material of the fluxgate's core influences its performance, an investigation of other magnetic materials, and a study of their effects on the performance of the sensor can be conducted as well as part of the suggested future work.

References

1. Boll, R., and Overshott, K. J., 2008, Sensors, Magnetic Sensors, Vol. 5, Wiley-VCH, N.J., USA.

2. Weiss, E., and Alimi, R., 2018, Low-Power and High-Sensitivity Magnetic Sensors and Systems, Artech House, Norwood, MA, USA.

3. Ripka, P., and Tipek, A., 2007, Modern Sensors Handbook, ISTE Ltd: Wiltshire, UK.

4. Brauer, J.R., 2014, Magnetic Actuators and Sensors, 2nd edition, Wiley-IEEE Press: New Jersey, USA.

5. Velasco, Q.G., Román, L.M., Conesa, R. A. and Jeréz, F., 2011, "Design of a Low Consumption Fluxgate Transducer for High Current Measurement Applications," IEEE Sensors Journal, Vol. 11, Issue 2, pp. 280-287.

6. Ferri, M., Surano, A., Rossini, A., Malcovati, P., Dallago, E., and Baschirotto, A., 2009, "Low Voltage Fluxgate Magnetic Current Sensor Interface Circuit with Digital Output for Portable Applications," Proceedings of the IEEE Sensors Conference, Christchurch, New Zealand, pp. 79-82.

7. Waheed, O.T., and Rehman, A., 2011, "Design and Development of a Fluxgate Magnetometer for Small Satellites in Low Earth Orbit," Journal of Space Technology, Vol. 1, No.1, pp.78-82.

8. Zhang, Y., Steiger, M., Hibbs, A.D., Grimm, R.E., and Sprott, T.A., 2010, "Dual-Mode Fluxgate Induction Sensor for UXO Detection and Discrimination," Journal of Environmental Engineering and Geophysics, Vol. 15, Issue 2, pp.51–64.

9. Benyosef, L.C., Stael, G.C., and Bochner, M., 2008, "Optimization of the Magnetic Properties of Materials for Fluxgate Sensors," Materials Research, Vol. 11, No. 2, pp. 145-149.

10. Jiles, D.C., and Lo, C.C.H., 2003, "The Role of New Materials in the Development of Magnetic Sensors and Actuators," Sensors and Actuators A: Physical, Vol. 106, pp. 3–7.

11. Ripka, P., 2008, "Sensors Based on Bulk Soft Magnetic Materials: Advances and Challenges," Journal of Magnetism and Magnetic Materials, Vol. 320, pp. 2466‐2473.

12. Can, H., Svec, P., Bydzovsky, J., Svec, P., Aktas, B., Szeri, H., and Topal, U., 2017, "Fabrication of Fluxgate Sensor Heads by Milling with a Circuit Board Plotter and Influence of Core Annealing Conditions on Sensor Performance", Journal of Superconductivity and Novel Magnetism, Vol. 30, No.11, pp.3257-3261.

13. Brauer, P., Risbo, T., Merayo, J.M.G. and Nielsen, O.V., 2000, "Fluxgate Sensor for the Vector Magnetometer Onboard the 'Astrid-2' Satellite," Sensors and Actuators A: Physical, Vol. 81, pp. 184–8.

14. Rühmer, D., Ludwig, F. and Schilling, M. 2016, "A Shielded Fluxgate Sensor for Spatially Resolved Measurements of Magnetic Dipole Fields," Sensors and Actuators A: Physical, Vol. 238, No.1, pp. 229-233.

15. Snoeij, M.F., Schaffer, V., Udayashankar, S., and Ivanov, M.V., 2015, "An Integrated Fluxgate Magnetometer for use in Closed Loop/Open Loop Isolated Current Sensing," Proceedings of the 41st European Solid-State Circuits Conference (ESSCIRC), Graz, Austria, pp. 263–266.

16. Heidari, H., and Nabaei, V., 2019, Magnetic Sensors for Biomedical Applications. 1st edition, Wiley-IEEE Press: New Jersey, USA.

17. Delevoye, E., Audion, M., Beranger, M., Cuchet, R., Hida, R., and Jager, T., 2008, "Microfluxgate Sensors for High Frequency and Low Power Applications," Sensors and Actuators A: Physical, Vol. 145, pp. 271–277.

18. Kaluza, F., Gruger, A., and Gruger, H., 2003, "New and Future Applications of Fluxgate Sensors," Sensors and Actuators A: Physical, Vol. 106, pp. 48-51.

19. Forslund, A., Belyayev, S., Ivchenko, N., Olsson, G., Edberg, T., and Marusenkov, A., 2008, "Miniaturized Digital Fluxgate Magnetometer for Small Spacecraft Applications," Measurement Science and Technology, Vol. 19:015320.

20. Poletkin, K., and Francis, L.A., 2018, Magnetic Sensors and Devices: Technologies and Applications, CRC Press: NY, USA.

21. Majlis, N., 2007, The Quantum Theory of Magnetism, 2nd Edition, World Scientific: Singapore.

22. Spaldin, N.A., 2011, Magnetic Materials: Fundamentals and Applications, Cambridge Uni. Press, UK.

23. Mattis, D.C., The Theory of Magnetism Made Simple, 2006, World Scientific: Singapore

24. Nolting, W., and Ramakanth, A., 2009, Quantum Theory of Magnetism, Springer-Verlag: Berlin Heidelberg.

25. Lacheisserie, E.T., Gignoux, D., and Schlenker, M., 2005, Magnetism Fundamentals Springer: Boston, USA.

26. Getzlaff, M., 2008, Fundamentals of Magnetism, Springer-Verlag: Berlin Heidelberg.

27. Buschow, K.H.J., 2015, Handbook of Magnetic Materials, Vol. 24, Oxford: UK.

28. Blundell, S., 2001, Magnetism in Condensed Matters, Oxford: New York, USA.

29. O'handley, R.C., 2000, Modern Magnetic Materials: Principles and Applications, John Wiley& Sons: New York, USA.

30. Goldman, A., 1999, Handbook of Modern Ferromagnetic Materials, Springer: New York, USA.

31. Bruck, E., 2016, Handbook of Magnetic Materials, Vol. 25, North-Holland: UK.

32. Chikazumi, S., 2005, Physics of Ferromagnetism, Oxford: New York, USA.

33. Aharoni, A., 2001, Introduction to the Theory of Ferromagnetism, Oxford University Press, Oxford.

34. Pop, N.C., 2019, "A Model for Magnetic Hysteresis," The European Physical Journal Plus, Vol. 134: 567.

35. Takacs, J., Kovacs, G., and Varga, L.K., 2008, "Hysteresis Reversal," Physica B: Condensed Matter, Vol. 403, Issue. 13-16, pp. 2293-2297.

36. Fabrizio, M., Giorgi, C., and Morro, A., 2009, "A Thermodynamic Approach to Ferromagnetism and Phase Transitions," International Journal of Engineering Science, Vol. 47, pp. 821-839.

37. Wlodarski, Z., Wlodarska, J., and Brykalski, A., 2006, "Experimental Verification of Hysteresis Models," Physica B: Condensed Matter, Vol. 372, Issue. 1-2, pp. 160-163.

38. Chwastek, K., 2012, "Modelling Hysteresis Loops in Thick Steel Sheet with the Dynamic Takács Model", Physica B: Condensed Matter, Vol. 407, pp. 3632-3634.

39. Dautovic, S., Samardzic, N., and Juhas, A., 2020, "Takacs Model of Hysteresis in Mathematical Modeling of Memristors," Radioengineering, Vol.29, Issue.1, pp. 147- 158.

40. Wlodarski, Z., 2007 "Extraction of Hysteresis Loops from Main Magnetization Curves," Journal of Magnetism and Magnetic Materials, Vol. 308, pp. 15-19.

41. Halbert, D., Etien, E., and Champenois, G., 2004, "An Inversible Model for Hysteresis Characterization at Constant Flux Amplitude," Journal of Electrical Engineering, Vol. 55, No. 11-12, pp. 319-323.

42. Dupré, L., Sablik, M.J., Van Keer, R.,and Melkebeek, J.A.A., 2002, "Modelling of Microstructural Effects on Magnetic Hysteresis Properties," Journal of Physics D: Applied Physics, Vol. 35, pp. 2086-2090.

43. Sablik, M.J., and Landgraf, F.J.G., 2003, "Modeling Microstructural Effects on Hysteresis Loops with the Same Maximum Flux Density," IEEE Transactions on Magnetics, Vol. 39, pp. 2528-2530.

44. Hauser, H., Melikhov, Y., and Jiles, D.C., 2007, "Including Effects of Microstructure and Anisotropy in Theoretical Models Describing Hysteresis of Ferromagnetic Materials," Applied Physics Letters, Vol. 91, 172512.

45. Takacs, J., 2001, "A Phenomenological Mathematical Model of Hysteresis," COMPEL-The International Journal of Computation and Mathematics in Electrical and Electronic Engineering, Vol.20, No.4, pp. 1002-1015.

46. Wlodarski, Z., 2007, "Modeling Hysteresis by Analytical Reversal Curves," Physica B: Condensed Matter, Vol. 398, Issue.1, pp. 159-163.

47. Chwastek, K., Szczygłowski, J., and Wilczyński, W., 2010, "Mathematical Modelling Of Ferromagnetic Hysteresis In Soft Magnetic Materials", Proceedings of The Sixth International Conference on Mathematical Modeling and Computer Simulation of Material Technologies, (MMT-2010), Ariel, Israel.

48. Mayergoyz, I., 1991, Mathematical Models of Hysteresis, Springer Verlag, New York.

49. Wlodarski, Z., 2007, "Classical and Hyperbolic Approximation of Hysteresis Loops," Physica B: Condensed Matter, Vol. 389, Issue.2, pp. 347-350.

50. Krasnoselskii, M.A., and Pokrovskii, A.V., 1989, Systems with Hysteresis, Springer-Verlag: Berlin-Heidelberg.

51. De Leon, F., and Semleon, A., 1995, "A Simple Representation of Dynamic Hysteresis Losses in Power Transformers," IEEE Transactions on Power Delivery, Vol.10, pp. 315–321.

52. Takács, J., Mathematics of Hysteretic Phenomena, 2003, Wiley-VCH, Weinheim, USA.

53. Goldsztein, G., Broner, F., and Strogatz, S.H., 1997, "Dynamical Hysteresis without Static Hysteresis: Scaling Laws and Asymptotic Expansions," SIAM Journal of Applied Mathematics, Vol. 57, pp. 1163-1187.

54. Visintin, A., 1994, Differential Models of Hysteresis, Springer-Verlag, New York, USA.

55. Voros, J., 2009, "Modeling and Identification of Hysteresis using Special Forms of the Coleman-Hodgdon Model," Journal of Electrical Engineering, Vol. 60, No.2, pp. 100-105.

56. Stadler, A., 2010, "A Generalized Model for Rate-Independent Ferromagnetic Hysteresis Phenomena," Proceedings of 5th International Workshop on Multi-Rate Processes and Hysteresis, Pecs, Hungary.

57. Wang, L.J., 2006, "The Curve of Magnetic Hysteresis Loop of the Polynomial Fitting Ferromagnetic Material," Phys. Exp. Coll., Vol. 19, pp. 58-61.

58. Heslop, D., and Muxworthy, A.R., 2005, "Aspects of Calculating First-Order Reversal Curve Distributions," Journal of Magnetism and Magnetic Materials, Vol. 288, pp. 155-167.

59. Raulet, M.-A., Sixdenier, F., Guinand, B., Morel, L., and Goyet, R., 2008, "Limits and Rules of Use of a Dynamic Flux Tube Model," COMPEL-The International Journal of Computation and Mathematics in Electrical and Electronic Engineering, Vol. 27, No. 1, pp. 256 – 265.

60. Raulet, M.A., Ducharne, B., Masson, J.P., and Bayada, G., 2004, "The Magnetic Field Diffusion Equation Including Dynamic Hysteresis: A linear Formulation of the Problem," IEEE Transactions on Magnetics, Vol. 40, pp. 872–875.

61. Bertotti, G., 1998, Hysteresis in Magnetism, Academic Press, Boston.

62. Bertotti, G., 2008, "Connection between Microstructure and Magnetic Properties of Soft Magnetic Materials," Journal of magnetism and Magnetic Materials, Vol. 320, pp. 2436-2442.

63. Chwastek, K., 2010, "Problems in Descriptions of Hysteresis," Przegląd Elektrotechniczny, Vol. 4 pp. 24-27.

64. Liorzou, F., Phelps, B., and Atherton, D.L., 2000, "Macroscopic Models of Magnetization," IEEE Transactions on Magnetics, Vol. 36, pp. 418-428.

65. Bertotti, G., Mayergoyz, I.D., and Serpico, C., 2006, "Identification of the damping coefficient in Landau-Lifschitz equation," Physica B: Condensed Matter, Vol. 306, pp. 102-105.

66. Wiele, B.V., Dupré, L., and Olyslager, F., 2006, "Memory Properties in a Landau-Lifshitz Hysteresis Model for Thin Ferromagnetic Sheets," Journal of Applied Physics, Vol. 99: 08G101.

67. Atherton, D.L., and Beattie, J.R., 1990, "A Mean Field Stoner-Wohlfarth Hysteresis Model," IEEE Transactions on Magnetics, Vol. 26, pp. 3059-3063.

68. Landau, D.P., 2007, Theory of Magnetic Phase Transitions, Chapter in: Kronmüller H., Parkin St. (Eds.) Handbook of Magnetism and Magnetic Materials, Vol. 1 Fundamentals and theory, J. Wiley & Sons: New York, USA.

69. Torre, E.D., Oti, J., and Kádár, Gy., 1990, "Preisach Modeling and Reversible Magnetization," IEEE Transactions on Magnetics, Vol. 26, pp. 3052-3058.

70. Kádár, Gy., 2005, The Preisach-Type Model of Ferromagnetic Hysteresis, in Iványi A. (Ed.), Preisach Memorial Book, Akadémiai Kiadó, Budapest.

71. Visintin, A., 2000, "A Weiss-Type Model of Ferromagnetism," Physica B: Condensed Matter, Vol. 275, pp. 87-91.

72. Sablik, M.J., and Jiles, D.C., 1993, "Coupled Magnetoelastic Theory of Magnetic and Magnetostrictive Hysteresis," IEEE Transactions on Magnetics, Vol. 29, pp. 2113-2123.

73. Benabou, A., Clenet, S., and Piriou, F., 2003, "Comparison of Preisach and Jiles-Atherton Models to Take into Account Hysteresis Phenomenon for Finite Element Analysis," Journal of Magnetism and Magnetic Materials, Vol. 261, Issue. 1-2, pp. 139-160.

74. Szewczyk, R., Bienkowski, A., and Salach, J., 2008, "Extended Jiles-Atherton Model for Modeling the Magnetic Characteristics of Isotropic Materials," Journal of Magnetism and Magnetic Materials, Vol. 320, pp. e1049- e1052.

75. Bergqvist, A.J., 1997, "Magnetic Vector Hysteresis Mode with Dry Friction-Like Pinning," Physica B: Condensed Matter, Vol. 233, pp. 342-347.

76. Jiles, D.C., 2002, "Hysteresis Models: Non-Linear Magnetism on Length Scales from the Atomistic to the Macroscopic," Journal of Magnetism and Magnetic Materials, Vol. 242, pp. 116-124.

77. Jiles, D., 2016, Introduction to Magnetism and Magnetic Materials, 3rd. ed., CRC Press: New York, USA.

78. White, R.M., 2007, Quantum Theory of Magnetism: Magnetic Properties of Materials, 3rd. Ed., Springer-Verlag: Berlin Heidelberg.

79. Krishman, K.M., 2016, Fundaments and Applications of Magnetic Materials, 1st. ed., Oxford, UK.

80. Zirka, S.E., Moroz, Y.I., Harrison, R.G., and Chwastek, K., 2012, "On Physical Aspects of the Jiles-Atherton Hysteresis Models," Journal of Applied Physics, Vol. 112: 043916.

81. Ramesh, A., Jiles, D.C., and Roderik, J., 1999, "A Model of Anisotropic Anhysteretic Magnetization," IEEE Transactions on Magnetics, Vol. 32, pp. 4234–4236.

82. Raghunathan, A., Melikhov, Y., Snyder, J.E., and Jiles, D.C., 2009, "Generalized form of Anhysteretic Magnetization Function for Jiles-Atherton Theory of Hysteresis," Applied Physics Letters, Vol. 95: 172510.

83. Pop, N.C., and Caltun, O.F., 2011, "Jiles-Atherton Magnetic Hysteresis Parameters Identification," Acta Physica Polonica A, Vol. 120: 491.

84. Cheng, P., and Szewczyk, R., 2018, "Modified Description of Magnetic Hysteresis in Jiles-Atherton Model," Advances in Intelligent Systems and Computing, Vol. 743, pp. 648–654.

85. Li, Z., Li, Q., Li, C., Sun, Q., and Lou, J., 2011, "Queries on the J-A Modeling Theory of the Magnetization Process in Ferromagnets and Proposed Correction Method," Proceedings of Chinese Society of Electrical Engineering, Vol. 31, pp. 124–131.

86. Li, X., Peng, Q., Li, J., Wen, X., and Lu, H., 2012, "Parameter Identification of Hysteresis Loop Model for Transformer Core," Power Systems Technology, Vol. 36, pp. 200–205.

87. Hernandez, E.M., Muranaka, C.S., and Cardoso, J.R., 2000, "Identification of the Jiles-Atherton Model Parameters using Random and Deterministic Searches," Physica B: Condensed Matter, Vol. 275, pp. 212-215.

88. Hamimid, M., Feliachi, M., and Mimoune, S.M., 2010, "Modified Jiles-Atherton Model and Parameters Identification using False Position Method," Physica B: Condensed Matter, Vol. 405, pp. 1947- 1950.

89. Szewczyk, R., 2014, "Computational Problems Connected with Jiles-Atherton Model of Magnetic Hysteresis," Advances in Intelligent Systems and Computing, pp. 267- 275.

90. Padilha, J.B., Kuo-Peng, P., Sadowski, N., Leite, J.V., and Batisela, N.J., 2017, "Restriction in the Determination of the Jiles-Atherton Hysteresis Model Parameters," Journal of Magnetism and Magnetic Materials, Vol. 442, pp. 8-14.

91. Wang, X., Thomas, D.W.P., Sumner, M., Paul, J., and Cabral, S.H.L., 2009, "Numerical Determination of Jiles-Atherton Model Parameters", The International Journal for Computation and Mathematics in Electrical and Electronic Engineering, Vol. 28 No. 2, pp. 493-503.

92. Szewczyk, R., 2016, "Assessment of Uncertainty of Determination of Parameters of Jiles-Atherton Model of Hysteresis Loops of Isotropic Materials," *Przegląd Elektrotechniczny*, a A, 1000, pp. 162-165.

93. Chwastek, K., and Szczyglowski, J., 2006, "Identification of a Hysteresis Model Parameters with Genetic Algorithms," Mathematics and Computers in Simulation, Vol. 71, pp. 206–211.

94. Marion, R., Scorretti, R., Siauve, N., Raulet, M., and Krähenbühl, L., 2008, "Identification of Jiles-Atherton Model Parameters Using Particle Swarm Optimization," IEEE Transactions on Magnetics, Vol. 44, pp. 894–897.

95. Coelho, L., Mariani, V.C., and Leite, J.V., 2012, "Solution of Jiles-Atherton Vector Hysteresis Parameters Estimation by Modified Differential Evolution Approaches," Expert Systems with Applications, Vol. 39, Issue 2, pp. 2021–2025.

96. Bai, B., Wang, J., and Zhu, K., 2011, "Identification of the Jiles-Atherton Model Parameters using Simulated Annealing Method," Proceedings of the International Conference on Electrical Machines and Systems (ICEMS), Beijing, China, pp. 1–4.

97. Jiang, W., Shi, Y., Zhao, W., and Wang, X., 2016, "Parameters Identification of Fluxgate Magnetic Core Adopting the Biogeography-Based Optimization Algorithm," Sensors, Vol.16: 979.

98. Naghizadeh, R. A., Vahidi, B., and Hosseinian, S.H., 2012, "Parameter Identification of Jiles-Atherton Model using SFLA," COMPEL: The International Journal for Computation and Mathematics in Electrical and Electronic Engineering, Vol. 31, No. 4, pp. 1293-1309.

99. Kwapulinski, P., Rasek, J., Stoklosa, Z., and Haneczok, G., 2003, "Magnetic Properties of $Fe_{74}Cu_1Cr_xZr_{3\ x}Si_{13}B_9$ Amorphous Alloys," Journal of Magnetism and Magnetic Materials, Vol. 254–255, pp. 413–415.

100. Jia, Y., Wang, Z., Wang, F., Zhang, L., and Duan, H., 2018, "Effect of Ti on Structure and Soft Magnetic Properties of Si-rich Finemet-Type Nanocrystalline $Fe_{73.5}Cu_1Nb_{3-x}Si_{17.5}B_5Ti_x$ Alloys," Materials Research Bulletin , Vol. 106, pp. 296-300.

101. Shokrollahi, H., and Janghorban, K., 2007, "Different Annealing Treatments for Improvement of Magnetic and Electrical Properties of Soft Magnetic Composites," Journal of Magnetism and Magnetic Materials, Vol. 317, pp.61–67.

102. Leary, A.M., Ohodnicki, P.R., and McHenry, M.E., 2012, "Soft Magnetic Materials in High-Frequency, High-Power Conversion Applications," The Journal of The Minerals, Metals & Materials Society, Vol. 64, pp.772–781.

103. Hamler, A., Gorican, V., Sustarsic, B., Sirc, A., 2006, "The Use of Soft Magnetic Composite Materials in Synchronous Electric Motor," Journal of Magnetism and Magnetic Materials, Vol. 304, pp. e816–e819.

104. Borrego, J.M., Conde, A., Roth, S., and Eckert, J., 2003, "Soft Magnetic Properties of FeCoSiAlGaPCB Amorphous Alloys," Journal of Magnetism and Magnetic Materials, Vol. 254–255, pp. 444–446.

105. Mohapatra, J., Zeng, F., Elkins, K., Xing, M., Ghimire, M., Yoon, S., Mishra, S.R., and Liu, J.P., 2018, "Size-Dependent Magnetic and Inductive Heating Properties of Fe3O4 Nanoparticles: Scaling Laws across the Superparamagnetic Size," Physical Chemistry Chemical Physics, Vol. 20, No.18, pp. 12879—12887.

106. Anderson, C., 2015, Magnetic Sensors: Fundamentals and Applications, NY Research Press, New York, USA.

107. Lenz, J.E., 1990, "A Review of Magnetic Sensors," Proceedings of IEEE, Vol. 78, No. 6, pp. 973–989.

108. Reininger, T., Welker, F., and Zeppelin, M.V., 2006, "Sensors in Position Control Applications for Industrial Automation," Sensors and Actuators A: Physical, Vol. 129, No. 1, pp.270- 274.

109. Tumanski, S., 2007, "Induction Coil Sensors—A Review" Measurements, Science and Technology, Vol. 18, R31–R46.

110. Korepanow, V.E., 2003, "The Modern Trends in Space Electromagnetic Instrumentation," Advances in Space Research, Vol. 32, pp. 401–406.

111. Seran, H.C., and Fergeau, P., 2005, "An Optimized Low-Frequency Three-Axis Search Coil Magnetometer for Space Research," Review of Scientific Instruments, Vol. 76, pp. 1–10.

112. Huang, Q., Khawaja, A.H., Chen, Y., and Li, J., 2019, Magnetic Field Measurement with Application to Modern Power Grids, 1st edition, Wiley-IEEE Press: New York, USA.

113.   Popovic, R.S., 2014, "High Resolution Hall Magnetic Sensors," Proceedings of IEEE 29th International Conference on Microelectronics, MIEL, Belgrade, Serbia.

114.   Oh, S., Jang, B.J., and Chae, H., 2018, "Sensitivity Enhancement of a Vertical-Type CMOS Hall Device for a Magnetic Sensor," Journal of Electromagnetic Engineering and Science, Vol. 18, No. 1, pp. 35-40.

115.   Sander, C., Leube, C., and Paul, O., 2016, "Compact Two-Dimensional CMOS Hall Sensor based on Switched Configurations of Four Three-Contact Elements," Sensors and Actuators A: Physical, Vol. 248, pp. 281-289.

116.   Popovic R.S., 2004, Hall Effect Devices, Institute of Physics: London, U.K.

117.   Tumanski, S., 2001, Thin Film Magnetoresistive Sensors, Institute of Physics: London, U.K.

118.   Freitas, P.P., Ferreira, R., Cardoso, S., and Cardoso, F., 2007, "Magnetoresistive Sensors," Journal of Physics: Condensed Matter, Vol.19, No. 16: 165221.

119.   Su, W., Wang, Z., Wen, T., Hu, Z., Wu, J., Zhou, Z., and Liu, M., 2019, "Liner Anisotropic Magnetoresistive Sensor without Barber-Pole Electrodes," IEEE Electron Device Letters, Vol. 40, Issue 6, pp. 969-972.

120.   Dimitrova, P., Andreev, S., and Popova, L., 2008, "Thin Film Integrated AMR Sensor for Linear Position Measurements," Sensors and Actuators A: Physical, Vol. 147, Issue. 2, pp. 387-390.

121.   Vcelák, J., Ripka, P., Platil, A., Kubík, J., and Kaspar, P., 2006, "Errors of AMR Compass and Methods of Their Compensation," Sensors and Actuators A: Physical, Vol. 129, pp. 53–57.

122.   Wang, Z., Wang, X., Li, M., Gao, Y., Hu, Z., and Nan, T., 2016, "Highly Sensitive Flexible Magnetic Sensor Based on Anisotropic Magnetoresistance Effect," Advanced Materials, Vol. 28, pp. 9370- 9377.

123.   Hadjigeorgiou, N.G., and Sotiriadis, P.P., 2020, "Parasitic Capacitances, Inductive Coupling, and High Frequency Behavior of AMR Sensors," IEEE Sensors Journal, Vol. 20, Issue 5, pp. 2339-2347.

124.   Hirota, E., Sakakima, H., and Inomata, K., 2002, Giant Magneto-Resistance Devices, Vol. 40, Springer Series in Surface Sciences, Springer: Berlin, Germany.

125.   Yan, S., Cao, Z., Guo, Z., Zheng, Z., Cao, A., Qi, Y., Leng, Q., and Zhao, W., 2018, "Design and Fabrication of Full Wheastone-Bridge-Based Angular GMR Sensors," Sensors, Vol. 18, No. 6:1832.

126.   Beltran, M.D.C., Reig, C., Madrenas, J., Marcellis, A.D., Santos, J., Cardoso, S., and Freitas, P., 2016, "Integration of GMR Sensors with Different Technologies," Sensors, Vol. 16, No. 6:939.

127.   Cubells-Beltra, M.D., Reig, C., Marcellis, A.D., Figueras, E., Fera, A.Y., Zadov, B., Paperno, E., Cardoso, S., and Freitas, P.P., 2014, "Monolithic Integration of Giant Magnetoresistance (GMR) Devices onto Standard Processed CMOS Dies," Microelectronics Journal, Vol. 45, No. 6: 702.

128.   Paz, E., Ferreira, R., and Freitas, P.P., 2016, "Linearization of Magnetic Sensors with a Weakly Pinned Free-Layer MTJ Stack using a Three-Step Annealing Process," IEEE Transactions on Magnetics, Vol. 52, Issue 7,pp. 1-4.

129.   Lei, Z.Q., Li, G.J., Egelhoff, W.F., Lai, P.T., and Pong, P.W.T., 2011, "Review of Noise Sources in Magnetic Tunnel Junction Sensors," IEEE Transactions on Magnetics, Vol. 47, Issue 3, pp. 602-612.

130.   Jin, Z., Oogane, M., Fujiwara, K., and Ando, Y., 2017, "Magnetic Sensor Based on Serial Magnetic Tunnel Junctions for Highly Sensitive Detection of Surface Cracks," Journal of Applied Physics, Vol. 122: 174502.

131.   Ouyang, Y., He, J., Hu, J., Zhao, G., Wang, Z., and Wang, S.X., 2015, "Prediction and Optimization of Linearity of MTJ Magnetic Sensors Based on Single-Domain Model," IEEE Transactions on Magnetics, Vol. 51, Issue 11.

132.   Jin, F., Tu, X., Wang, J., Yang, B., Dong, K., Mo, W., Hui, Y., Peng, J., Jiang, J., Xu, L., and Song, J., 2020, " Noise Modeling and Simulation of Giant Magnetic Impedance (GMI) Magnetic Sensor," Sensors, Vol. 20, No.4:960.

133.   Zidi, M., Asfour, A., and Yonnet, J.P., 2014, "GMI Magnetic Sensor Operating with a Direct Digital Synthesizer," Proceedings of IEEE International Instrumentation and Measurement Technology Conference, Montevideo, Uruguay.

134.   NazariNejad, S., Fomani, A.A., and Mansour, R., 2013, "Giant Magneto-Impedance Thin Film Magnetic Sensor," IEEE Transactions on Magnetics, Vol. 49, Issue 7, pp. 3874-3877.

135.   Silva, E.C., Gusmao, L.A.P., Barbosa, C.R.H., and Monteiro, E.C., 2008, "Magnetic Field Transducers Based on the Phase Characteristics of GMI Sensors and Aimed at Biomedical Applications," Proceedings of 13th International Conference on Biomedical Engineering, pp. 652-656, Singapore.

136.   Yin, J., Yan, P., Chen, H., Yu, L., Jiang, J., Zhang, M., and Ruan, S., 2017, "All-Fiber-Optic Vector Magnetometer Based on Anisotropic Magnetism-Manipulation of Ferromagnetism Nanoparticles," Applied Physics Letters, Vol. 110, Issue. 23, pp. 10.1063.

137.   Pai, P., Chen, L., and Azar, M.T., 2014, "Fiber Optic Magnetometer with Sub-Pico Tesla Sensitivity for Magneto-Encephalography," Proceedings of IEEE Sensors Conference, Valencia, Spin.

138.   Candiani, A., Margulis, W., Sterner, C., Konstantaki, M., Childs, P., and Pissadakis, S., 2011, "A Vectorial Magnetometer Utilizing a Microstructured Optical Fibre Bragg Grating Infiltrated by a Ferrofluid," Proceedings of The European Conference on Lasers and Electro-Optics, Munich, Germany.

139.   Wang, Y., Li, J., and Viehland, D., 2014, "Magnetoelectrics for Magnetic Sensor Applications Status, Challenges, and Perspectives," Materials Today, Vol. 17, Issue 6, pp. 269-275.

140.   Li, M., Dong, C., Zhou, H., Wang, Z., Wang, X., Liang, X., Lin, Y., and Sun, N.X., 2017, "Highly Sensitive DC Magnetic Field Sensor Based on Nonlinear ME Effect," IEEE Sensors Letters, Vol. 1, Issue 6, pp. 1-4.

141.   Shen, Y., Ma, D., and Gao, J., 2018, "A Man-Portable Magnetoelectric DC Magnetic Sensor with Extremely High Sensitivity," IEEE Electron Device Letters, Vol. 39, Issue 9, pp. 1417-1420.

142. Rao, C.N., Dua, P., Kuchhal, P., Lu, Y., Kale, S.N., and Cao, P., 2019, "Enhanced Sensitivity of Magneto-Optical Sensor using Defect Induced Perovskite Metal Oxide Nanomaterials," Journal of Alloys and Compounds, Vol. 797, pp. 896-901.

143. Rogachev, A.E., Vetoshko, P.M., Gusev, N.A., Kozhaev, M.A., Prokopov, A.R., Popov, V.V., Dodonov, D.V., Shumilov, A.G., Shaposhnikov, A.N., Berzhansky, V.N., Zvezdin, A.K., and Belotelov, V.I., 2016, "Vector Magneto-Optical Sensor based on Transparent Magnetic Films with Cubic Crystallographic Symmetry," Applied Physics Letters, Vol. 109:162403.

144. Garcia, R., Blanco, E., and Dominguez, M., 2016, "Development of a Magneto-Optical Sensor Prototype to Measure Current by Means of the Induced Magnetic Field," Sensors and Actuators A: Physical, vol. 249, pp. 231-241.

145. Phetchakul, T., Luanatikomkul, W., Yamwong, W., and Poyai, A., 2012, "The Mechanism of Dual Schottky Magnetodiode," Proceedings of 9th International Conference on Electrical Engineering, Electronics, Computer, Telecommunications and Information Technology, Phetchaburi, Thialand.

146. Phetchakul, T., and Junkamkaw, S., 2009, "Dual Magnetodiode," Proceedings of the 12th International Symposium of Integrated Circuits, Singapore.

147. Tikhonov, R.D., 2005, "Sensors on Bipolar Magnetotransistors with the Base in the Well," Soild-State Electronics, Vol. 49, Issue 8, pp. 1302-1308.

148. Leepattarapongpan, C., Phetchakul, T., Penpondee, N., Pengpad, P., Chaowicharat, E., Hruanun, C., and Poyai, A., 2010, "Magnetotransistor based on the carrier recombination-deflection effect," IEEE Sensors Journal, Vol. 10, Issue 2, pp. 294-299.

149. Tikhonov, R.D., 2009, "An Integrated Magnetoresistor Sensor," Measurement Techniques, Vol. 52, pp. 410-415.

150. Clarke, J., and Braginski, A.I., 2006, The SQUID Handbook, Wiley-VCH: New York, USA.

151. Enpuku, K., Hirakawa, S., Tsuji, Y., Momotomi, R., Matsuo, M., Yoshida, T., and Kandori, A., 2011, "HTS SQUID Magnetometer using Resonant Coupling of Cooled Cu Pickup Coil," IEEE Transactions on Applied Superconductivity, Vol. 21, issue 3, pp. 514-517.

152. Chwala, A., Kingman, J., Stolz, R., Schmelz, M., Zakosarenko, V., Linzen, S., Bauer, F., Starkloff, M., Meyer, M., and Meyer, H.G., 2013, "Noise Characterization of Highly Sensitive SQUID Magnetometer Systems in Unshielded Environments," Superconductor Science and Technology, Vol. 26, No.3, 035017.

153. Adachi, Y., Miyamoto, M., Kawai, J., Uehara, G., Ogata, H., Kawabata, S., Sekihara, K., and Kado, H., 2011, "Improvement of SQUID Magnetometer System for Extending Application of Spinal Cord Evoked Magnetic Field Measurement," IEEE Transactions on Applied Superconductivity, Vol. 21, Issue 3, pp. 485-488.

154. Schmelz, M., Stolz, R., Zakosarenko, V., Schonau, T., Anders, S., Fritzsch, L., Muck, M., and Meyer, H.G., 2011, "Field-Stable SQUID Magnetometer with Sub-ft /Hz Resolution based on Sub-Micrometer Cross-Type Josephson Tunnel Junctions," Superconductor Science and Technology, Vol. 24, No.6, 065009.

155.   Bagherinia, M., Bruggi, M., Corigliano, A., Mariani, S., and Lasalandr, E., 2014, "Geometry Optimization of a Lorentz Force, Resonating MEMS Magnetometer," Microelectronics Reliability, Vol. 54, Issue 6-7, pp. 1192-1199.

156.   Wu, G.Q., Xu, D.H., Xiong, B., Che, L.F., and Wang, Y.L., 2016, "Design, Fabrication and Characterization of a Resonant Magnetic Field Sensor Based on Mechanically Coupled Dual-Microresonator," Sensors and Actuators A: Physical, Vol. 248, pp. 1–5.

157.   Laghi, G., Dellea, S., Longoni, A., Minotti, P., Tocchio, A., Zerbini, S., and Langfelder, G., 2015, "Torsional MEMS Magnetometer Operated off-Resonance for In-plane Magnetic Field Detection," Sensors and Actuators A: Physical, Vol. 229, pp. 218–226.

158.   Herrera-May, A.L., García-Ramírez, P.J., Aguilera-Cortés, L.A., Martínez-Castillo, J., Sauceda-Carvajal, A., García-González, L., and Figueras-Costa, E., 2009, "A Resonant Magnetic Field Microsensor with High Quality Factor at Atmospheric Pressure," Journal of Micromechanics and Microengineering, vol. 19, 015016.

159.   Kumar, V., Sebdani, S.M., and Pourkamali, S., 2017, "Sensitivity Enhancement of a Lorentz Force MEMS Magnetometer with Frequency Modulated Output," Journal of Microelectromechanical Systems, Vol. 26, Issue. 4, pp. 870-878.

160.   Ghosh, S., and Lee, J.E., 2017, "A Lorentz Force Magnetometer Based on a Piezoelectric-on-Silicon-Radial-Contour Mode Disk," Proceedings of the 19th International Conference on Solid-State Sensors, Acutators and Microsystems (TRANSDUCERS), Kaohsiung, Taiwan.

161.   Wickenden, D.K., Champion, J.L., Osiander, R., Givens, R.B., Lamb, J.L., Miragliotta, J.A., Oursler, D.A., and Kistenmacher, T.J., 2003, "Micromachined Polysilicon Resonating Xylophone Bar Magnetometer," Acta Astronautica, Vol. 52, pp. 421-425.

162.   Park, B., Li, M., Liyanage, S., and Shafai, C., 2016, "Lorentz Force Based Resonant MEMS Magnetic-Field Sensor with Optical Readout," Sensors and Actuators A: Physical, Vol. 241, pp.12-18.

163.   Bahreyni, B., and Shafai, C., 2007, "A Resonant Micromachined Magnetic Field Sensor," IEEE Sensor Journal, Vol. 7, pp. 1326-1334.

164.   Said, M.H., Tounsi, F., Gkotsis, P., Mezghani, B., and Francis, L.A., 2017, "A Resonant Microstructure Tenability Analysis for an Out-of-Plane Capacitive Detection MEMS Magnetometer," Microsystem Technologies, vol. 23, pp. 2599-2608.

165.   Ripka, P., and Kawahito, S., 1999, "Processing of the Fluxgate Output Signal," Imeko World Congress, Osaka, Japan, pp. 75-80.

166.   Geiler, A.L., Harris, V.G., Vittoria, C., and Sun, N.X., 2006, "A Quantitative Model for the Nonlinear Response of Fluxgate Magnetometers," Journal of Applied Physics, Vol. 99, No. (8), pp.08B316.

167.   Ripka, P., 2000, "New Directions in Fluxgate Sensors," Journal of Magnetism and Magnetic Materials, Vol. 215-216, pp. 735-739.

168.   Ripka, P., and Janosek, M., 2010, "Advances in Magnetic Field Sensors," IEEE Sensors Journal, Vol. 10, pp. 1108–1116.

169.   Topal, U., Can, H., Celik, O.M., Narman, A., Kamis, M., Citak, V., Cakrak, D., Sozeri, H., and Svec, P., 2019, "Design of Fluxgate Sensors for Different Applications from Geology to Medicine," Journal of Superconductivity and Novel Magnetism, Vol. 32, pp. 839-844.

170.   Quesada, G.V., Lumbreras, M.R., Roca, A.C., and Jerez, F., 2011, "Design of Low-Consumption Fluxgate Transducer for High Current Measurement Applications," *IEEE Sensors Journal*, Vol. 11, issue 2, pp. 280-287.

171.   Gemmel, C., Heil, W., Karpuk, S., Lenz, K., Ludwig, C., Sobolev, Y., Tullney, K., Burghoff, M., Killian, W., Gruneberg, S.K., Muller, W., Schnabel, A., Seifert, F., Trahms, L., and Barbler, S. , 2010 , " Ultra-Sensitive Magnetometry based of Free Precession of Nuclear Spins," The European Physical Journal D, Vol. 57, pp. 303-320.

172.   Denisov, A.Y., Sapunov, V.A., and Rubinstein, B., 2014, "Broadband Mode in Proton-Precession Magnetometers with Signal Processing Regression Methods," Measurement Science and Technology, Vol. 25, No. 5, pp.055103.

173.   Denisov, A.Y., and Khomutov, S.Y., 2006, "Measurement Quality Estimation of Proton-Precession Magnetometers," Earth Planets and Space, Vol. 58, No. 6, pp. 707-710.

174.   Haobin, D., and Changda, Z., 2010, "A Further Review of the Quantum Magnetometers," Chinese Journal of Engineering Geophysics, Vol. 4, pp. 13-27.

175.   Budker, D., and Romalis, M., 2007, "Optical Magnetometry," Nature Physics, vol. 3, pp. 227–234.

176.   Kitching, J., Knappe, S., and Donley, E.A., 2011, "Atomic Sensors – A Review," IEEE Sensors Journal, Vol. 11, No. 9, pp. 1749-1758.

177.   Chalupczak, W., Godun, R.M., Pustelny, S., and Gawlik, W., 2012, "Room Temperature Femtotesla Radio-Frequency Atomic Magnetometer," Applied Physics Letters, Vol. 100, No. 24:242401.

178.   Bevilacqua, G., Biancalana, V., Chessa, P., and Dancheva, Y., 2016, "Multichannel Optical Atomic Magnetometer Operating in Unshielded Environment," Applied Physics B, Vol. 122, No. 4, pp.103.

179.   Alxendrov, E.B., Evgeny, B., and Bonch-Bruevich, V.A., 1992, "Optically Pumped Atomic Magnetometers after Three Decades," Optical Engineering, Vol. 13, No. 4, pp. 711-718.

180.   Aktham, A., 2017, Magnetic Sensors: Development Trends and Application, In-Tech.

181.   Vopálenský, M., Ripka, P., and Platil, A., 2003, "Precise Magnetic Sensors," Sensors and Actuators A: Physical, Vol. 106, pp. 38–42.

182.   Ripka, P., and Kaspar, P., 1998, "Portable Fluxgate Magnetometer," Sensors and Actuators A: Physical, Vol. A68, pp. 286–289.

183. Henrotte, F., Nicolet, A., and Hameyer, K., 2006, "An Energy-Based Vector Hysteresis Model for Ferromagnetic Materials," International Journal for Computation and Mathematics in Electrical and Electronic Engineering, Vol. 25, No. 1, pp. 71-80.

184. Henrotte, F., and Hameyer, K., 2006, "A Dynamical Vector Hysteresis Model based on an Energy Approach," IEEE Transactions on Magnetics, Vol. 42, pp. 899-902.

185. Della Torre, E., 1999, Magnetic Hysteresis, IEEE Press, Piscataway, USA.

186. Andò, B., Baglio, S., Bulsara, A.R., and Sacco, V., 2005, "Residence Times Difference Fluxgate Magnetometers," IEEE Sensors Journal, Vol. 5, No. 5, pp. 895-904.

187. Ando, B., Ascia, A., Baglio, S., Bulsara, A.R., Neff, J.D., and In, V., 2008, "Towards an Optimal Readout of a Residence Times Difference (RTD) Fluxgate Magnetometer," Sensors and Actuators A: Physical, Vol.142, pp. 73–79.

188. Ando, B., Bulsara, A., Baglio, S., and Sacco, V., 2005, "Effects of Driving Mode and Optimal Material Selection on a Residence Times Difference based Fluxgate Magnetometer," IEEE Transactions on Instrumentation and Measurement, Vol. 54, No.4, pp. 1366–1373.

189. Ando, B., Baglio, S., Caruso, V., Sacco, V., and Bulsara, A., 2006, "Multilayer based Technology to Build RTD Fluxgate Magnetometer, Sensors and Transducers, Vol. 65, No.3, pp. 509–514.

190. Ando, B., Baglio, S., Pitrone, N., Sacco, V., and Bulsara, A., 2005, "Noise Effects in RTD-Fluxgate," IEEE Sensors Journal, pp. 935–938.

191. Ripka, P., 1992, "Review of Fluxgate Sensors," Sensors and Actuators A: Physical, Vol. 33, pp. 129-141.

192. Belyayev, S., and Ivchenko, N., 2018, "Effect of Second Harmonic in Pulse Width Modulation Based DAC for Feedback of Digital Fluxgate Magnetometer," Measurement Science and Technology, Vol. 29, No. 4, pp. 045008.

193. Cao, J., Zhao, J., and Cheng, S., 2019, "Research on the Simplified Direct Current Fluxgate Sensor and Its Demodulation," Measurement Science and Technology, Vol. 30, pp. 1–8.

194. Wang, X., Wang, T., Jiang, W., Zhao, W., and Shi, Y., 2015, "A Design of excitation system for fluxgate based on sine wave," Proceedings of Fifth International Conference on Instrumentation and Measurement, Computer, Communication and Control, Qinhuangdao, China, pp. 1090-1093.

195. Cerman, A., Kuna, A., Ripka, P., and Merayo, J.M.G., 2005, "Digitalization of highly precise fluxgate magnetometers," Sensors and Actuators A: Physical, Vol. 121, pp. 421–429.

196. Cerman, A., and Ripka, P., 2003, "Towards Fully Digital Magnetometer," Sensors and Actuators A: Physical, Vol. 106, pp.34–37.

197. Yuan, Z., Zhang, Y., Wang, D., Jiang, Y., and Guo, R., 2020, "Research on the Orthogonal Fundamental Mode Fluxgate Sensor Circuit," IEEE Access, Vol. 8, pp. 150665-150671.

198. Baschirotto, A., Dallago, E., Malcovati, P., Marchesi, M., Melissano, E., Morelli, M., Siciliano, P., and Venchi, G., 2009, "An integrated micro-fluxgate magnetic sensor with front-end circuitry," IEEE Transactions on Instrumentation and Measurement, Vol.58, No.99, pp. 3269-3275.

199. Kawahito, S., Cerman, A., Aramaki, K., and Tadokoro, Y., 2003, "A Weak Magnetic Field Measurement System using Microfluxgate Sensors and Delta-Sigma Interface," IEEE Transactions on Instrumentation and Measurement, Vol. 52, pp. 103–110.

200. Iguchi, K., and Matsuoka, A., 2014, "A Digital Type Fluxgate Magnetometer using a Sigma-Delta Digital-to-Analog Converter for a Sounding Rocket Experiment," Measurement Science and Technology, Vol. 25, No. 7, pp.075803.

201. Butta, M., Janosek, M., and Ripka, P., 2010, "Field-Programmable Gate Array-Based Fluxgate Magnetometer with Digital Integration," Journal of Applied Physics, Vol. 107, 09E714.

202. Belyayev, S., and Ivchenko, N., 2015, "Digital Fluxgate Magnetometer: Design Notes," Measurement Science and Technology, Vol. 26, 12590.

203. Jiles, D., 1991, Introduction to Magnetism and Magnetic Materials, Chapman & Hall, London, UK.

204. Wei, S., Liao, X., Zhang, H., Pang, J., and Zhou, Y., 2021, "Recent Progress of Fluxgate Magnetic Sensors: Basic Research and Application," *Sensors*, 21, 1500.

205. Dezuari, O., Belloy, E., Gilbert, S.E., and Gijs, M.A.M., 2000, "Printed Circuit Board Integrated Fluxgate Sensor," Sensors and Actuators A: Physical, Vol. 81, pp. 200–203.

206. Bulsara, A.R., In, V., Kho, A., Palacios, A., Longhini, P., and Baglio, S., 2008, "Exploiting Nonlinear Dynamics in a Coupled Core Fluxgate Magnetometer," Measurement Science and Technology, Vol. 19, No. 7, pp. 075203-1-075203-12.

207. Choi, W.Y., Hwang, J.S., and Choi, S.O., 2004, "The Microfluxgate Magnetic Sensor Having Closed Magnetic Path," IEEE Sensors Journal, Vol. 4, No. 6, pp. 768- 771.

208. Liu, S., 2006, "Study on Low Power Consumption of Racetrack Fluxgate," Sensors and Actuators A: Physical, Vol. 130-131, pp. 124-128.

209. Butta, M., and Ripka, P., 2008, "Two Domain Model for Orthogonal Fluxgate," IEEE Transactions on Magnetics, Vol. 44, No.11, pp. 3992–3995.

210. Ripka, P., 2001, Magnetic Sensors and Magnetometers, Artech House Inc.: Norwood, MA, USA.

211. Djamal, M., Sanjaya, E., Yulkifli, Y., and Ramli, R., 2011, "Development of Fluxgate Sensors and its Applications," Proceedings of International Conference on Instrumentation, Communication, Information Technology and Biomedical Engineering , Bandung, Indonesia.

212. Lenz, J., and Edelstein, A.S., 2006, "Magnetic Sensors and Their Applications," IEEE Sensors Journal, Vol. 6, No. 3, pp. 631-649.

213. Vazquez, M., Chiriac, H., Zhukov, A., Panina, L., and Uchiyama, T., 2011, "On the State-of-the Art in Magnetic Microwires and Expected Trends for Scientific and Technological Studies," Physica Status Solidi (a), Vol. 208, Issue 3, pp. 493-501.

214. Drljaca, P.M., Kejik, P., Vincent, F., Piguet, D., Gueissaz, F., and Popovic, R.S., 2004, "Single Core Fully Integrated CMOS Micro-Fluxgate Magnetometer," Sensors and Actuators A: Physical, Vol. 110, pp. 236–241.

215. Robbes, D., 2006, "Highly Sensitive Magnetometers—a Review", Sensors and Actuators A: Physical, Vol. 129, pp.86–93.

216. Terashima, Y., and Sasada, I., 2002, "Magnetic Domain Imaging using Orthogonal Fluxgate Probes," Journal of Applied Physics, Vol. 91, Issue 10, pp. 8888-8890.

217. Sasada, I., 2002, "Symmetric Response Obtained with an Orthogonal Fluxgate Operating in Fundamental Mode", IEEE Transactions on Magnetics, Vol. 38, No. 5, pp.3377-3379.

218. Sasada, I., and Kashima, H., 2009, "Simple Design for Orthogonal Fluxgate Magnetometer in Fundamental Mode," Journal of the Magnetics Society of Japan, Vol. 33, No.2, pp. 43-45.

219. Smith, R.C., Dapino, M.J., Braun, T.R., and Mortensen, A.P., 2006, "A Homogenized Energy Framework for Ferromagnetic Hysteresis," IEEE Transactions on Magnetics, Vol. 42, Issue 7, pp. 1747-1769.

220. Han, F., Harada, S., and Sasada, I., 2014, "Beat Interferences in Fundamental Mode Orthogonal Fluxgates," IEEE Transactions on Magnetics, Vol. 50, Issue 7, pp. 1-5.

221. Buschow, K.H.J., and de Boer, F.R., 2003, Physics of Magnetism and Magnetic Materials, Kluwer Academic, New York, USA.

222. Morrish, A.H., 2001, The Physical Principles of Magnetism, Institute of Electrical and Electronics Engineers: New York, USA.

223. Yamaguchi, M., and Tanimoto, Y., 2006, Magneto-Science: Magnetic Field Effects on Materials, Springer-Verlag, Berlin Heidelberg, Germany.

224. Johnson, C., 2009, Numerical Solution of Partial Differential Equations by the Finite Element Method, Dover Publications, Dover, USA.

225. Prohl, A., 2001, Computational Micromagnetism, 1st edition, Teubner Verlag, Berlin, Germany.

226. Pryor, R.W., 2011, Multiphysics Modeling Using COMSOL: a First Principles Approach, Jones and Bartlett Publishers, UK.

227. Kuczmann, M., and Ivanyi, A., 2008, "The Finite Element Method in Magnetics," Akademiai Kiado, Budapest.

228. Leite, J.V., Benabou, A., Sadowski, N., Clenet, S., Bastos, J.P.A., and Piriou, F., 2008, "Implementation of an Anisotropic Vector Hysteresis Model in a 3-D Finite-Element Code," IEEE Transactions on Magnetics, Vol. 44, Issue 6, pp. 918-921.

229. Takács, J., 2006, "Mathematical Proof of the Definition of Anhysteretic State," Physica B, Vol. 372, pp. 57-60.

230. Ivanyi, A., 1997, Hysteresis Models in Electromagnetic Computation, Akademiai Kiado, Budapest.

231. Zorlu, O., Kejik, P., and Popovic, R.S., 2007, "Fluxgate-Type Magnetic Microsensors for Wide Linear Measuring Range," Proceedings of IEEE Sensors Applications Symposium, San Diego, California USA.

232. Zhi, S., Feng, Z., and Lei, C., 2019, "Improved Performance of Fundamental Mode Orthogonal Fluxgate using a Micro-Patterned Meander Shaped Ribbon Core," Sensors, Vol. 19, 5058.

233. Korepanov, V., and Marusenkov, A., 2012, "Flux-Gate Magnetometers Design Peculiarities," Survey Geophysics, Vol. 33, pp.1059-1079.

234. Ripka, P., Butta, M., Jie, F., and Li, X.P., 2010, "Sensitivity and Noise of Wire Core Transverse Fluxgate," IEEE Transactions on Magnetics, Vol. 46, No.2, pp.654–657.

235. Ripka, P., and Hurley, W.G., 2006, "Excitation Efficiency of Fluxgate Sensors," Sensors and Actuators A: Physical, Vol. 129, pp. 75–79.

236. Baranov, P., Baranova, V., Kolomeytsev, A., and Zatonov, I., 2018, "Drive Signal Waveform for a Fluxgate," Journal of Physics: Conference Series, Vol. 1065, No. 5, 052020.

237. Setiadi, R.N., and Schilling, M., 2018, "Inductance Analyzer based on Auto Balanced Circuit for Precision Measurement of Fluxgate Impedance," Measurement science and Technology, Vol. 29, No.5, pp. 1-8.

238. Weiss, E., Paperno, E., and Plotkin, A., 2010, "Orthogonal Fluxgate Employing Discontinuous Excitation," Journal of Applied Physics, Vol. 107, Issue 9, pp. 09E717.

239. Guo, B., Liu, S., Yang, S., Li, G., Li, J., and Sun, X., 2015, "Orthogonal Micro-Fluxgate with S- Shape Excitation Wire and 3D Solenoid Detection Coil," Microsystems Technology, Vol. 21, pp. 1579–1586.

240. Butta, M., and Sasada, I., 2013, "Orthogonal Fluxgate with Annealed Wire Core," IEEE Transactions on Magnetics, Vol. 49, No.1, pp.62–65.

241. Butta, M., and Sasada, I., 2021, "New Aspects on the Performance of a Fundamental Mode Orthogonal Fluxgate Magnetometer Based on Amorphous Wire Cores," AIP Advances, Vol. 11, pp. 015113.

242. Sasada, I., 2002, "Orthogonal Fluxgate Mechanism Operated with DC Biased Excitation," Journal of Applied Physics, Vol. 91, pp. 7789.

243. Ripka, P., Pribil, M., and Butta, M., 2014, "Fluxgate Offset Study," IEEE Transactions on magnetics, Vol. 50, No. 11, pp. 4006804- 4006804.

244. Ripka, P., 2003, "Advances in Fluxgate Sensors," Sensors and Actuators A: Physical, Vol. 106, pp. 8–14.

245. Bazinet, R., Jacas, A., Confalonieri, G.A.B., and Vazquez, M., 2014, "A Low Noise Fundamental Mode Orthogonal Fluxgate Magnetometer," IEEE Transactions on Magnetics, Vol. 50, No. 5, pp. 6500103 - 6500103.

246. Ando, B,. Baglio, S., La Malfa, S., Trigona, C., and Bulsara, A.R., 2010, "ROC Analysis for RTD Fluxgate Magnetometers," Proceedings of IEEE Instrumentation and Measurement Technology Conference, Austin, TX, USA.

247. Shokrollahi, H., and Janghorban, K., 2007, "Soft Magnetic Composite Materials (SMCs)," Journal of Materials Processing Technology, Vol.189, pp. 1-12.

248. Butta, M., and Sasada, I., 2012, "Noise Correlation in Fundamental Mode Orthogonal Fluxgate," Journal of Applied Physics, Vol. 111, no.7, pp.07E517.

249. Snoeij, M.F., Schaffer, V., Udayashankar, S., and Ivanov, M.V., 2016, "Integrated Fluxgate Magnetometer for Use in Isolated Current Sensing," IEEE Journal of Solid-State Circuits, Vol. 51, pp. 1684–1694.

250. Butta, M., and Sasada, I., 2012, "Sources of Noise in a Magnetometer Based on Orthogonal Fluxgate Operated in Fundamental Mode," IEEE Transactions on Magnetics, vol. 48, issue 4, pp.1508–1511.

الملخص

يمكن إن تقسم أجهزة قياس المغناطيسية طبقا لحساسيتها الى ثلاثة تصنيفات رئيسية:
منخفضة الحساسية، متوسطة الحساسية، وعالية الحساسية. وبناء على التطبيقات التى يستخدم
فيها جهاز قياس المغناطيسية، فإنه يمكن إعتبار مستشعر الفيض المغناطيسى أحد أفضل
المستشعرات فى مدى قياس النانو تسلا. إن مستشعرات الفيض المغناطيسى تستخدم فى قياس
شدة المجال المغناطيسى المستمر أو ذو التردد المنخفض فى إتجاه معين. تعتمد نظرية التشغيل
لمستشعر الفيض المغناطيسى على إستغلال الخواص اللاخطية للمادة المغناطيسية الموجوة
بعنصر الاستشعار بالجهاز، والتى تقاد الى التشبع عن طريق محفز تيار ثنائى القطبية، وذلك
لتوليد جهد كهربى مكافىء لقيمة المجال المغناطيسى الخارجى المراد قياسه. ولذا يعتبر عنصر
الاستشعار هو المكون الاساسى والاهم داخل مستشعر الفيض المغناطيسى. وحيث أن الخواص
اللاخطية للمادة المغناطيسية المكونة لعنصر الاستشعار لها تأثير لا يمكن تجاهله، وبالتالى فإن
إختيار نموذج دقيق لهذه الخواص يعتبر مهما للحصول على تنبؤ دقيق بأداء عنصر الاستشعار
عند ظروف التشغيل المختلفة. ولذا فإنه تم إختيار نموذج جيلس– إيثرتون فى هذه الرسالة
لتمثيل الخواص اللاخطية لعنصر الاستشعار.

أما عن الهدف الرئيسى لهذه الرسالة تقديم محاكاة لدراسة أداء عنصر الاستشعار
لمستشعر الفيض المغناطيسى. وتهدف هذه المحاكاة الى بيان مدى إعتمادية توزيع شدة التيار
والفيض المغناطيسى داخل عنصر الاستشعار على كلا من محددات التصميم المختلفة
والخواص المغناطيسية لعنصر الاستشعار. حيث تم فى هذه الرسالة إستخدام طريقة العناصر
المنتهية لتحليل طريقة توزيع كلا من شدة التيار والفيض لمغناطيسى داخل عنصر الاستشعار
ذو الخواص المغناطيسية اللاخطية. كما تم فى هذه الرسالة إنشاء نموذجين لتصميمين مختلفين
لعنصر الاستشعار لمستشعر الفيض المغناطيسى. وتم أيضا فى هذه الرسالة إنجاز دراسة
متكاملة لكلا من التصميمين المقترحين، لبيان تأثير عناصر التصميم مثل الية التغذية والتردد
وأبعاد عنصر الاستشعار، على توزيع كلا من شدة التيار والفيض المغناطيسى داخل عنصر
الاستشعار. ومن ثم تم فى هذه الرسالة دراسة التحكم فى هذه العناصر للوصول الى إعتبارات
التوزيع الامثل للفيض المغناطيسى داخل عنصر الاستشعار بما يساهم فى تحسين الاستجابة
لكلا من التصميمين المقترحين، وكذلك تبيان محددات عناصر التصميم المختلفة.

ولذا تلبى هذه الرسالة الطلب على توفير بيئة محاكاة دقيقة، ومن ثم توفير خريطة أداء لفهم كيفية إستجابة عنصر الاستشعار لمعاملات التشغيل المختلفة، مما يساهم فى تعديل وإبتكار تصميمات متعددة لمستشعر الفيض المغناطيسى بالطريقة المثلى ويقلل الفجوة ما بين النظريات والتصنيع بدون الحاجة الى إهدار الوقت والمال على تنفيذ نماذج فعلية.

أما عن محتوى الرسالة فإنها تتكون من سبعة فصول. الفصل الاول يعطى مقدمة لموضوع البحث وأهدافه، وفى الفصل الثانى يتم شرح المبادىء الاساسية للمغناطيسية وتصنيف المواد المغناطيسية وخصائصها. بينما فى الفصل الثالث تتم مناقشة نظريات العمل للعديد من أجهزة قياس المغناطيسية. أما الفصل الرابع فيختص بتناول موسع لنظرية عمل مستشعر الفيض المغناطيسى وأنواعه المختلفة. بينما يتم فى الفصل الخامس إنشاء نموذج للتصميم الاول لعنصر الاستشعار وإتمام دراسة متكاملة عن أداء هذا التصميم وتأثير عناصر التصميم المختلفة وعرض النتائج الخاصة بهذا التصميم. وفى الفصل السادس يتم إنشاء نموذج للتصميم الثانى لعنصر الاستشعار وتحليل إستجابة هذا التصميم لعوامل التشغيل المختلفة وتبيان مدى فاعلية التعديل الذى تم إقتراحه فى هذا التصميم وعرض النتائج الخاصة به. أما الفصل السابع فإنه يعرض نتائج البحث وتوصيات لاعتبارات ومحددات التصميم المختلفة كما يعرض النقاط المقترحة لتطوير البحث.

دراسة إعتبارات التصميم لقياس المجال المغناطيسى

اعداد

محمود سيد ياسين

رسالة مقدمة إلى كلية الهندسة — جامعة القاهرة
كجزء من متطلبات الحصول على درجة
ماجستير العلوم
في
المواد المتقدمة

كليــة الهندســة ـ جامعــة القاهـرة
الجيــزة ـ جمهوريـة مصـر العربيـة
2021